



RAPIDITY DEPENDENCE OF THE SINGLE INCLUSIVE JET CROSS
SECTION IN $p\bar{p}$ COLLISIONS AT $\sqrt{s} = 1.8$ TeV WITH THE DØ DETECTOR

by

Levan Babukhadia

A Dissertation Submitted to the Faculty of the
DEPARTMENT OF PHYSICS
In Partial Fulfillment of the Requirements
For the Degree of
DOCTOR OF PHILOSOPHY
In the Graduate College
THE UNIVERSITY OF ARIZONA

1 9 9 9

Rapidity Dependence of the Single Inclusive Jet Cross Section in $p\bar{p}$ Collisions at
 $\sqrt{s} = 1.8$ TeV with the DØ Detector

Levan Babukhadia, Ph.D.
The University of Arizona, 1999

A Dissertation Submitted to the Faculty of the
DEPARTMENT OF PHYSICS
In Partial Fulfillment of the Requirements
For the Degree of
DOCTOR OF PHILOSOPHY
In the Graduate College
THE UNIVERSITY OF ARIZONA

Approved by the Examination Committee:

Dr. Michael A. Shupe (Dissertation Director)
Dr. Gerald C. Blazey (Dissertation Co-Director)
Dr. Bruce R. Barrett
Dr. Douglas J. Donahue
Dr. Kenneth Johns
Dr. Michael D. Scadron

STATEMENT BY AUTHOR

This dissertation has been submitted in partial fulfillment of requirements for an advanced degree at The University of Arizona and is deposited in the University Library to be made available to borrowers under rules of the library.

Brief quotations from this dissertation are allowable without special permission, provided that accurate acknowledgment of source is made. Requests for permission for extended quotation from or reproduction of this manuscript in whole or in part may be granted by the head of the major department or the Dean of the Graduate College when in his or her judgment the proposed use of the material is in the interests of scholarship. In all other instances, however, permission must be obtained from the author.

SIGNED: _____

ACKNOWLEDGEMENTS

I was extremely lucky with the advisors and friends I gained in graduate school.

I would like to thank from the bottom of my heart my advisor at the University of Arizona, Michael Shupe for teaching me how to be an experimental high energy physicist. I am indebted to him for connecting me with both DØ and ATLAS experiments, thereby opening avenues for me to gain experience in doing physics analysis as well as hardware work. His vast knowledge, deep insights, ability to approach problems from different perspectives, but always in connection with fundamental physics, and his tremendous experience were laid out in front of me to learn from; and I did my best to not let such unique opportunity pass by.

Special thanks to my co-advisor Jerry Blazey. He put me on track for doing this analysis—one of the most exciting roller coaster rides of my life so far. His deep knowledge and experience, applied always to the point, kept me focused on the main path. It was through him and thanks to him that I met many people in DØ without actually living at Fermilab. He was always there when I needed advice in moments of the toughest decisions I faced.

I am immensely grateful to Daniel Elvira for all his support and help throughout the ups and downs of the analysis. His understanding of DØ jet systematics is unmatched. Many thanks to Freedy Nang. With him I could discuss many issues that some avoid discussing in the open, be it physics or anything else. His technical knowledge was always astounding to me.

This work would not have been possible without thorough discussions and input from many people in the DØ QCD group. In particular, I would like to personally thank Iain Bertram, John Krane, Bob Hirosky, Mrinmoy Bhattacharjee, and Anna Goussiou. Thanks to the QCD group conveners with whom I worked: Nikos Varelas, Heidi Schellman, Greg Snow, and Andrew Brandt, for they supported my efforts to do this analysis remotely, from Tucson, and because they had confidence in my ability to meet schedules that were at times overly optimistic.

Tremendous thanks to the entire Arizona group here, in Tucson. In particular, I would like to thank Peter Loch for numerous discussions of many physics and technical questions in great depth and detail. He taught me almost everything I know about PAW, Unix, and LaTeX; his friendship is dear to me. Thanks to Ken Johns; his temperament and dedication to work were always inspiring. Thanks to John Rutherford for many discussions at the core of the physics topics. I learned a lot from him during the ATLAS FCal testbeam; his enthusiasm always amazed. Thanks to Leif Shaver with whom I could discuss various engineering and hardware issues; most recently our offices were next to each other, which also made us especially close. Thanks to Sasha Savin for interesting, at times heated, discussions. Thanks to Teresa Embry for all the help she could offer; her efficiency still surprises. Many thanks go to Dan Tompkins who helped me with the electronics project for the CERN testbeam. My sincere thanks go to fellow students with whom I could always share: Kevin Davis, Pete Johnson, Deb Koolbeck, Igor Koruga, Rob McCrosky, Ronnie Norton, Jason Seely, and now-postdoc Dave Fein.

A special thank you to Michael Scadron, my first, theoretical physics advisor here in Arizona, who set me on the right track. Thanks to Bruce Barrett and Doug Donahue for serving on my defense Committee. Last but not least, many thanks to graduate secretaries, Iris Wright and Lisa Shapouri who always so eagerly and effectively helped with all the paperwork.

DEDICATION

To my parents and sister whose ingenious support is continuously heartfelt despite
the distance.

To Nata, my wife, a friend and a partner, who loves and always stands by me.

To Mariam, our daughter, our future, who fills with joy and inspires.

TABLE OF CONTENTS

LIST OF FIGURES	9
LIST OF TABLES	16
ABSTRACT	17
1 INTRODUCTION	18
1.1 The Constituents of Matter: Leptons and Quarks	20
1.2 The Quanta of Interactions: Bosons	23
1.3 Putting It All Together—The Standard Model	25
1.4 Jets—The Tools for Studying Quarks and Gluons	28
2 THEORETICAL INTERLUDE	34
2.1 The Standard Model	42
2.1.1 The Gauge Symmetries	44
2.1.2 Quantization, and Feynman Diagrams	46
2.1.3 Divergences, Regularization, and Renormalization	49
2.1.4 The Glashow-Salam-Weinberg Model	51
2.1.5 Quantum Chromodynamics	57
2.2 Jet Cross Sections—A Test of the Standard Model	65
2.2.1 Description of Jet Production	68
2.2.2 The Single Inclusive Jet Cross Section	77
3 THE EXPERIMENT	82
3.1 The Fermilab Accelerators	84
3.2 Overview of the DØ Detector	89
3.3 The Central Detector	92
3.3.1 The Vertex Detector	94
3.3.2 The Transition Radiation Detector	95
3.3.3 Central Drift Chamber	97
3.3.4 Forward Drift Chamber	99
3.3.5 Central Detector Readout	100
3.4 The Calorimeter	100
3.4.1 The Central Calorimeter	108
3.4.2 The End Calorimeters	110
3.4.3 Massless Gaps and Intercryostat Detector	111
3.4.4 Calorimeter Readout	113
3.4.5 The Calorimeter Performance	113
3.5 The Muon Spectrometer	115

3.5.1	The Wide Angle Muon Chambers	116
3.5.2	The Small Angle Muon Chambers	118
3.6	The Trigger and Data Acquisition Systems	118
3.6.1	The Level 0 Trigger	119
3.6.2	The Level 1 Trigger	120
3.6.3	The Level 2 Trigger	121
3.7	The Offline Data Processing	122
4	THE DATA SAMPLE AND RECONSTRUCTION	124
4.1	The Inclusive Jet Triggers	124
4.2	Jet Definition	127
4.3	Missing Transverse Energy	132
4.4	The Treatment of Hot Cells	133
4.4.1	Anomalous Isolated Deposit Algorithm (AIDA)	133
4.4.2	Effects of AIDA on Jets	134
4.4.3	AIDA Cell Restoration	141
4.5	The \vec{H}_T Correction	151
4.6	The Total η Bias Correction	152
5	DATA SELECTION AND ASSOCIATED EFFICIENCIES	161
5.1	Determination of Jet Quality Cuts	165
5.1.1	Electromagnetic Fraction Cut	165
5.1.2	Coarse Hadronic Fraction Cut	167
5.1.3	Hot Cell Fraction Cut	169
5.2	Determination of Event Quality Cuts	171
5.2.1	Determination of the R_{MTE} Cut	171
5.2.2	Determination of the Vertex Cut	174
5.3	The Methodology for Cut Efficiency Calculation	174
5.4	The Efficiency of Jet Quality Cuts	175
5.4.1	Electromagnetic Fraction Cut Efficiencies	175
5.4.2	Coarse Hadronic Fraction Cut Efficiencies	177
5.4.3	Hot Cell Fraction Cut Efficiencies	180
5.4.4	Global Jet Quality Cut Efficiencies	180
5.5	The Efficiency of Event Quality Cuts	183
5.5.1	Missing Transverse Energy Fraction Cut Efficiencies	183
5.5.2	The Z-vertex Cut Efficiency	186

6	JET ENERGY SCALE	188
6.1	Determination of the DØ JES	189
6.1.1	The Offset Correction	189
6.1.2	The Response Correction	193
6.1.3	The Showering Correction	199
6.2	Independent Closure Test of the JES	205
6.2.1	The Method	205
6.2.2	Systematics	209
6.2.3	The Results for CAFIX 5.1 and CAFIX 5.2	219
7	LUMINOSITY STUDIES	223
7.1	Luminosity Matching	223
7.2	Luminosity Dependence of the Cross Sections	224
7.2.1	Shape Studies	225
7.2.2	Normalization Studies	231
8	THE OBSERVED INCLUSIVE JET CROSS SECTIONS	235
9	JET ENERGY RESOLUTIONS AND UNFOLDING	240
9.1	Determination of Jet Energy Resolutions	243
9.2	Effects of Nonzero Vertex Resolution	249
9.3	Unfolding of the Cross Sections	251
10	RESULTS AND CONCLUSIONS	256
10.1	Experimental and Theoretical Uncertainties	260
10.2	Data and Theory Comparison	270
10.3	Conclusions	283
	REFERENCES	285

LIST OF FIGURES

2.1	A few QED Feynman rules in the momentum representation.	48
2.2	One loop linear and quadratic divergences in QED.	49
2.3	A cartoonist's view of jet production in $p\bar{p}$ collisions.	66
2.4	The CTEQ3M family of PDF's of the light quarks and gluons inside proton at $Q^2 = 30$ GeV. The left plot shows PDF's themselves, while the right plot illustrates Bjorken x weighted PDF's to better highlight the differences among them.	71
2.5	Some of the QCD $2 \rightarrow 2$ processes contributing to the order α_s^2 . . .	73
2.6	Some of the QCD $2 \rightarrow 3$ processes contributing to the order α_s^3 . . .	75
2.7	A lego $\eta - \varphi$ plot of the real dijet event in the DØ calorimeter. . . .	77
2.8	A three-jet event observed in the DØ calorimeter.	78
2.9	Inclusive differential jet cross section ($ \eta < 0.9$) using the PAPAGENO leading order generator with different values of Λ_c , as indicated. . .	80
3.1	The Fermilab accelerator complex—a schematic overview, not drawn to scale. Although the Tevatron and the Main Ring have the same radius, they are separated here for clarity.	85
3.2	A cutaway isometric view of the Run 1 DØ detector.	90
3.3	The Central Detectors.	92
3.4	A quadrant of the Vertex detector—end view.	94
3.5	A section of the Transition Radiation Detector.	97
3.6	End view of a section of the Central Drift Chamber.	98
3.7	Exploded view of one of the two FDC packages illustrating the Φ module sandwiched by the two Θ modules.	99
3.8	General view of DØ LAr calorimeters.	105
3.9	Schematic view of the DØ calorimeter unit cell.	106
3.10	Side view of calorimeter trigger towers.	107
3.11	Side view of calorimeter modules, intercryostat detectors, and massless gaps.	109
3.12	Calorimeters and muon system interaction lengths as a function of θ . . .	112
3.13	Elevation view of the DØ Detector including the muon system. . . .	115
3.14	Extruded aluminum section for B and C layers. The A layer has four decks of cells instead of three.	116
4.1	The ΔR distributions for jets with $0.0 \leq \eta_d < 1.0$ and E_T of 100–120 GeV (left) and with $1.5 \leq \eta_d < 3.0$ and E_T of 40–60 GeV (right). Overwhelming majority of AIDA cells are found in a close vicinity of the jet centroid, well within the jet cone radius of 0.7. . .	135

4.2	The ΔR distributions for simulated THCC's with packed integer ID's of +075701 (left) and +251517 (right).	136
4.4	Different scatter plots of the AIDA cells in layer 15: ieta vs. iphi (top left), ieta vs. ΔR (top right), iphi vs. ΔR (bottom left), and a “lego” plot of ieta vs. iphi (bottom right). The THCC's can clearly be identified due to their high frequency of appearance.	142
4.5	The ΔR distributions of two THCC candidates among the cell removed by AIDA with packed integer ID's of -192315 (left) and -134917 (right). Difference between the two is apparent—the cell -192315 is most likely a jet-belonging cell incorrectly removed by AIDA while the cell -134917 has the ΔR distribution very much alike of that of the THCC.	143
4.6	The ΔR distributions for jets with $0.0 \leq \eta_d < 1.0$ and E_T of 100–120 GeV (left) and with $1.5 \leq \eta_d < 3.0$ and E_T of 40–60 GeV (right) after the removal of the THCC's.	145
4.7	The f_{E_T} distributions for jets with $0.0 \leq \eta_d < 1.0$ and E_T of 80–100 GeV (left) and with $1.5 \leq \eta_d < 3.0$ and E_T of 40–60 GeV (right) after the removal of the THCC's.	146
4.8	The distributions of change of the missing E_T of the event (left) and the jet E_T (right) due to ACRA. Note the logarithmic scales. . . .	149
4.9	The distributions of change of the pseudorapidity η (left) and azimuth φ of a jet due to ACRA. Note the logarithmic scales.	150
4.10	Correlation between the event \cancel{E}_T and the \mathcal{H}_T . The sample with the MR and hot cells removed clearly shows that the two quantities are highly correlated (top right). Choosing the correct vertex lowers the cross section by about 5% on average (bottom right).	152
4.11	Possible biases in any jet quantity due to reconstruction and algorithm differences.	154
4.12	Biases in jet η due to differences in jet angle definitions (top squares and upward triangles) and due to the reconstruction (bottom squares and downward triangles). Filled circles show the <i>total</i> η bias. . . .	157
4.13	Closure of the parameterization of the <i>total</i> η bias correction as a function of $D\emptyset$ jet η for all energies (left) and as a function of energy for all pseudorapidities (right).	158
5.1	The third moment about the mean \mathcal{M}_3 of the EMF distributions of Normal jets as a function of jet η_d for jet E_T of 40–60 GeV. Only the vertex cut $ Z < 50$ cm has been applied.	163
5.2	The EMF distributions of Normal jets in the CEN region for jet E_T of 100–120 GeV with only the Z cut applied (left) and with the Z and the R_{MTE} cuts applied (right). Vertical lines indicate the low and the high EMF cuts.	166
5.4	The CHF distributions of Normal jets in the CEN region for jet E_T of 100–120 GeV with and without the R_{MTE} cut superimposed on top of each other (left). The ratio of these two distributions is also shown (right). Vertical line indicates the CHF cut.	168

5.6	The HCF distributions of Normal jets in the CEN region for jet E_T of 100–120 GeV with (right) and without (left) the R_{MTE} cut. Vertical line indicates the HCF cut.	170
5.9	The vertex distributions for four jet triggers during Run 1B are centered at about $Z = 0$ cm and have a characteristic <i>rms</i> of about 30 cm.	173
5.11	The fits to the EMF distributions. The left plot shows the fit to the high end of the EMF distribution in the ICR for jet E_T of 50–60 GeV. The right plots shows fits to the low and the high ends of the EMF distributions in the FOR region for jet E_T of 80–100 GeV. Normal and Restored jets are combined. Vertical lines indicate the EMF cuts.	176
5.12	The CHF distributions in the CEN region for jet E_T of 100–120 GeV excluding the Main Ring region (left) and for the bottom half of the calorimeter only (right). Normal and Restored jets are combined. Vertical line indicates the CHF cut.	178
5.14	The fits to the HCF distributions in the ICR for jet E_T of 60–80 GeV (left) and in the FOR region for jet E_T of 80–100 GeV. Normal jets only. Vertical line indicates the HCF cut.	179
5.15	ε_{glob} as a function of un-corrected jet E_T in three η_d regions for Normal jets. Error bars shown are combined statistical and systematic uncertainties. The error band on the fitted model is also indicated.	181
5.16	The nominal (left) and the systematic (right) fits to the $1/R_{MTE}$ distribution in the CEN region for leading jet E_T of 100–120 GeV. Vertical line indicates the R_{MTE} cut.	184
5.17	ε_{MTE} as a function of un-corrected leading jet E_T in three η_d regions. Error bars shown are combined statistical and systematic uncertainties. The error band on the fitted model is also indicated. The upper error band is truncated at 100%.	185
6.3	Parametric simulation of the R_{jet} measurement. A fit to R_{jet} “measured” from the simulated data, when binned in terms of E' to remove resolution effects, agrees very well with the input response (top). The agreement between the fit and the input function is also excellent given different reasonable assumptions for the E_T dependence of the γ cross section, such as E_T^{-5} , E_T^{-4} , and E_T^{-2} (bottom).	195
6.4	R_{jet} versus jet energy on a semi-logarithmic (top) and linear (bottom) energy scales for the 0.7 cone jet algorithm. The outer band corresponds to the uncertainty in R_{jet} equivalent to the 68% confidence region (a volume defined by the $\chi^2 \leq \chi^2_{min} + 3.5$ surface) in the correlated three (fit) parameter space.	198
6.5	The parameterization of the showering correction (actually, S^{-1}) as a function of the response corrected jet energy in two intermediate pseudorapidity regions. The dashed lines indicate 1σ total uncertainty band.	201
6.6	The parameterization of the showering correction (actually, S^{-1}) as a function of the response corrected jet energy in two forward-most pseudorapidity intervals considered. The dashed lines indicate 1σ total uncertainty band.	202

6.7	The parameterization of the showering correction (actually, S^{-1}) as a function of jet pseudorapidity for different jet energies of 100, 130, 160, 200, 250, 300, and 600 GeV, from top to bottom. For all energies, the correction for $ \eta \leq 1.75$ corresponds to the fit for jet mid-energy considered, 160 GeV. The energy dependence is allowed for $ \eta > 1.75$. No discontinuities are present at $ \eta = 1.75$	203
6.9	\mathbf{R}_{jj} as a function of \bar{E}' is shown in three pseudorapidity regions. Data points from γ -jet data are overlayed for the purpose of qualitative comparison—note that the jet-jet data here are not corrected for the UCE. In both data samples, jet energy scale correction used is CAFIX 5.1.	211
6.10	\mathbf{R}_{jj} as a function of \bar{E}' is shown in three pseudorapidity regions. Data points from γ -jet data are overlayed for the purpose of qualitative comparison—note that the jet-jet data here are not corrected for the UCE. In both data samples, jet energy scale correction used is CAFIX 5.1.	212
6.11	Illustration of the jet E_T resolution bias on \mathbf{R}_{jj} from jet-jet data: when binned in terms of E^{FOR} (E'), \mathbf{R}_{jj} is biased high (low), but is unbiased when binned in terms of \bar{E}'	213
6.12	The HERWIG particle level MC shows no resolution bias (top plot). However, as soon as the MC particle jets are smeared by the jet energy resolutions (bottom plot), bias appears when binned in either E^{FOR} or E' but binned in \bar{E}' remains unbiased. Even when the forward energy resolutions are artificially lowered by additional 20%, binning in \bar{E}' stays unbiased (open squares in the bottom plot). . .	214
6.13	Illustration of the derivation of the unclustered energy correction in jet-jet data.	215
6.14	\mathbf{R}_{jj} as a function of \bar{E}' is shown in three pseudorapidity regions after the unclustered energy correction is applied.	217
6.15	\mathbf{R}_{jj} as a function of \bar{E}' is shown in three pseudorapidity regions after the unclustered energy correction is applied.	218
6.16	\mathbf{R}_{jj} as a function of \bar{E}' is shown in three pseudorapidity regions after the unclustered energy correction is applied.	220
6.17	\mathbf{R}_{jj} as a function of \bar{E}' is shown in three pseudorapidity regions after the unclustered energy correction is applied.	221
7.1	R_{low}^{tot} is fit to three models: P0 (solid line), P1 (dashed line), and P2 (dotted line). Shown here are fits in $ \eta < 0.5$ and $1.5 \leq \eta < 2.0$ pseudorapidity regions.	226
7.2	R_{low}^{vhi} is fit to three models: P0 (solid line), P1 (dashed line), and P2 (dotted line). Shown here are fits in $ \eta < 0.5$ and $1.5 \leq \eta < 2.0$ pseudorapidity regions.	227
7.3	Distributions of the instantaneous luminosity for each jet trigger. Note that plotted is dimensionless luminosity, which must be scaled by a factor of $10^{30} \text{ cm}^{-2}\text{s}^{-1}$ to obtain a proper value of \mathcal{L}	228

7.4	Plots on the left show R_{low}^{tot} obtained from the Jet_85 data only. The ratios are fitted (dashed line) to a constant (model P0) in the E_T range of interest. Shown here are fits in $ \eta < 0.5$ and $1.5 \leq \eta < 2.0$ pseudorapidity regions. The plot on the right shows the fitted constants and their uncertainties (inner error bars represent statistical errors due to the fit alone, while outer error bars have systematic uncertainty added in quadrature). For all five η regions there is fairly good agreement with 1.	233
8.1	Observed inclusive jet cross sections in the two central pseudorapidity regions with the nominal, high, and low jet energy scale (CAFIX 5.2) corrections.	236
8.2	Observed inclusive jet cross sections in the two intermediate pseudorapidity regions with the nominal, high, and low jet energy scale (CAFIX 5.2) corrections.	237
8.3	Observed inclusive jet cross section in the forward-most pseudorapidity region with the nominal, high, and low jet energy scale (CAFIX 5.2) corrections.	238
9.1	Finite energy resolution of the detector distorts the measured energy of monoenergetic jets of energy E_0 (left). In contrast with non-hermetic and non-linear calorimeters, such smearing is Gaussian when calorimeters are nearly hermetic and linear, such as the DØ calorimeters. Even though the energy smearing is Gaussian in DØ, it still distorts the steeply falling energy spectra for various cross section measurements by “smearing them up”. A cartoonist’s view of the effect on the hypothetical cross section is indicated in the plot on the right.	241
9.3	Illustration of the third jet E_T cut extrapolation for $1.5 \leq \eta < 2.0$ and $95 \leq \langle E_T \rangle < 150$ GeV bin with CAFX 5.2.	246
9.5	The ratios of the JETRAD cross sections smeared by the effective vertex resolution of 7.5 cm and the true cross sections. Effect of nonzero σ_z is in the order of 1–2% in all pseudorapidity regions. Therefore, no correction due to this effect is applied to the data. . .	250
9.6	The illustration of the jet cross section unfolding method on the example of the two pseudorapidity regions.	252
9.7	Derived unfolding correction factors in all pseudorapidity regions along with the total uncertainty bands. The correction becomes large at the highest E_T ’s because of the increase in the slope of the cross sections as they approach the kinematic limit in a given η interval. On the other hand, the increase in R_{unf} at lowest E_T ’s is attributed to the degraded energy resolutions.	254
10.1	Final, unfolded single inclusive jet cross sections corresponding to the nominal jet energy scale correction (CAFIX 5.2) from all five pseudorapidity regions considered (up to $ \eta = 3.0$) with statistical errors only.	257

10.2	Fractional experimental uncertainties on the cross sections in the two central pseudorapidity regions. Errors originating from the different sources are distinguished. The jet energy scale error dominates the total uncertainty in the cross sections.	263
10.3	Fractional experimental uncertainties on the cross sections in the two intermediate pseudorapidity regions. Errors originating from the different sources are distinguished. The jet energy scale error dominates the total uncertainty in the cross sections.	264
10.4	Fractional experimental uncertainties on the cross section in the forward-most pseudorapidity region. Errors originating from the different sources are distinguished. The jet energy scale error dominates the total uncertainty in the cross section.	265
10.5	The illustration of the uncertainties in the theoretical pQCD predictions calculated with JETRAD for the central pseudorapidity region ($ \eta < 0.5$). The uncertainties become larger at higher η 's. They are generally in the order of the systematic experimental uncertainties.	269
10.6	The comparison between the $D\bar{O}$ single inclusive jet production cross sections, $\langle d^2\sigma/(dE_T d\eta) \rangle$, as a function of jet E_T in the two central pseudorapidity regions and the α_s^3 QCD predictions calculated by JETRAD with the CTEQ3M PDF and the input parameters $\mu_R = \mu_F = E_T^{max}/2$ and $\mathcal{R}_{sep} = 1.3$	271
10.7	The comparison between the $D\bar{O}$ single inclusive jet production cross sections, $\langle d^2\sigma/(dE_T d\eta) \rangle$, as a function of jet E_T in the two intermediate pseudorapidity regions and the α_s^3 QCD predictions calculated by JETRAD with the CTEQ3M PDF and the input parameters $\mu_R = \mu_F = E_T^{max}/2$ and $\mathcal{R}_{sep} = 1.3$	272
10.8	The comparison between the $D\bar{O}$ single inclusive jet production cross section, $\langle d^2\sigma/(dE_T d\eta) \rangle$, as a function of jet E_T in the forward-most pseudorapidity region and the α_s^3 QCD prediction calculated by JETRAD with the CTEQ3M PDF and the input parameters $\mu_R = \mu_F = E_T^{max}/2$ and $\mathcal{R}_{sep} = 1.3$	273
10.9	The comparison between the $D\bar{O}$ single inclusive jet production cross sections, $\langle d^2\sigma/(dE_T d\eta) \rangle$, as a function of jet E_T in all five pseudorapidity regions (up to $ \eta = 3.0$) and the α_s^3 QCD predictions calculated by JETRAD with the CTEQ4M PDF and the input parameters $\mu_R = \mu_F = E_T^{max}/2$ and $\mathcal{R}_{sep} = 1.3$	274
10.10	The comparison between the $D\bar{O}$ single inclusive jet production cross sections, $\langle d^2\sigma/(dE_T d\eta) \rangle$, as a function of jet E_T in all five pseudorapidity regions (up to $ \eta = 3.0$) and the α_s^3 QCD predictions calculated by JETRAD with the CTEQ4HJ PDF and the input parameters $\mu_R = \mu_F = E_T^{max}/2$ and $\mathcal{R}_{sep} = 1.3$	275
10.11	The comparison between the $D\bar{O}$ single inclusive jet production cross sections, $\langle d^2\sigma/(dE_T d\eta) \rangle$, as a function of jet E_T in all five pseudorapidity regions (up to $ \eta = 3.0$) and the α_s^3 QCD predictions calculated by JETRAD with the MRST PDF and the input parameters $\mu_R = \mu_F = E_T^{max}/2$ and $\mathcal{R}_{sep} = 1.3$	276

- 10.12 The comparison between the $D\bar{O}$ single inclusive jet production cross sections, $\langle d^2\sigma/(dE_T d\eta) \rangle$, as a function of jet E_T in all five pseudorapidity regions (up to $|\eta| = 3.0$) and the α_s^3 QCD predictions calculated by JETRAD with the MRSTg \uparrow PDF and the input parameters $\mu_R = \mu_F = E_T^{max}/2$ and $\mathcal{R}_{sep} = 1.3$ 277
- 10.13 The comparison between the $D\bar{O}$ single inclusive jet production cross sections, $\langle d^2\sigma/(dE_T d\eta) \rangle$, as a function of jet E_T in all five pseudorapidity regions (up to $|\eta| = 3.0$) and the α_s^3 QCD predictions calculated by JETRAD with the MRSTg \downarrow PDF and the input parameters $\mu_R = \mu_F = E_T^{max}/2$ and $\mathcal{R}_{sep} = 1.3$ 278

LIST OF TABLES

1.1	The fundamental constituents of matter in the Standard Model. . .	26
1.2	The fundamental interactions, their carriers, and relative strengths.	27
2.1	All possible $2 \rightarrow 2$ QCD subprocesses and their invariant amplitudes (q and q' denote different quark flavors).	74
4.1	Run 1B inclusive jet trigger configurations.	125
4.2	THCC's found among the cells removed by AIDA.	144
5.1	Parameterization of the global jet quality cut efficiencies for Normal and Restored jets and for all η_d regions.	183
5.2	Parameterization of the R_{MTE} cut efficiencies in three η_d regions. . .	183
5.3	ε_Z for each jet trigger.	187
7.1	Subsamples with different \mathcal{L} cuts.	227
7.2	Summary of fit parameters, χ^2 values, degrees of freedom (ndf), and confidence levels (CL). Pseudorapidity regions are numberd in ac- cending order according to increasing η , i.e. region 1 corrsponds to the central-most ($ \eta < 0.5$) interval, while region 5 is forward-most ($2.0 \leq \eta < 3.0$) interval.	232
7.3	Integrated luminosities for different subsamples of Jet_85 data. . . .	233
10.1	Single inclusive jet cross section in $ \eta < 0.5$	258
10.2	Single inclusive jet cross section in $0.5 \leq \eta < 1.0$	259
10.3	Single inclusive jet cross section in $1.0 \leq \eta < 1.5$	260
10.4	Single inclusive jet cross section in $1.5 \leq \eta < 2.0$	261
10.5	Single inclusive jet cross section in $2.0 \leq \eta < 3.0$	262
10.6	Results of the χ^2 test for the full dynamic range.	279
10.7	Results of the χ^2 test in the central ($ \eta < 0.5$) region only.	279
10.8	Results of the χ^2 test in the pseudorapidity region $ \eta < 1.0$	280
10.9	Results of the χ^2 test in the pseudorapidity region $ \eta < 1.5$	280
10.10	Results of the χ^2 test in the pseudorapidity region $ \eta < 2.0$	281

ABSTRACT

We have made a precise measurement of the rapidity dependence of inclusive single jet production cross section $d^2\sigma/(dE_T d\eta)$ in $p\bar{p}$ collisions at $\sqrt{s} = 1.8$ TeV. The measurement is based on integrated luminosity of 92 pb⁻¹ data collected by the DØ detector at the Tevatron Collider, Fermi National Accelerator Laboratory. The cross sections are reported as a function of jet transverse energy in five pseudorapidity (η) intervals up to $\eta = 3.0$. The experimental results are in good agreement with the theoretical predictions from next-to-leading order perturbative quantum chromodynamics.

CHAPTER 1

INTRODUCTION

“He knows the facts, but He does not know this version of the facts.”
(Leo Szilard)

Physics, or Natural Philosophy, as it had been known over the centuries, is an empirical science with the ambitious goal to satisfy our never ending and ever increasing quest for understanding Nature. Its impressive progress over hundreds of years, and in the 20th century in particular, has led to invaluable applications that undeniably have had tremendous impact on the well-being of humanity. Offshoots of Natural Philosophy developed into separate branches of science, allowing us to harvest its fruits in many exotic varieties. In various epochs, however, including, unfortunately, the present day, it has not been evident to many how mankind might benefit from the progress of physics, and from science in general. And each time we doubt its ability to pay back, it has proved to be unpredictably and unprecedentedly profitable in more ways than could have been imagined, fully justifying our faith to invest in science... At the dawn of the new millennium, with the hope that we will not deviate from this path, this dissertation has been inspired, and is presented here.

In this work we deal with the smallest and the most fundamental constituents of matter and energy found to the present day. To the best of our knowledge, they may be further indivisible and are, therefore, the best candidates for

the smallest building blocks of the Nature. They are unimaginably tiny, less than 10^{-18} meters (m) in extent and, perhaps, they have no detectable size. They are the subject of study of one of the most visionary (and at the same time very realistic) intellectual activities of our times known as “elementary particle physics”, or “high energy physics”, and the reason for its latter name should become evident as our story unfolds.

The general idea that *all* big things are made up of *only so many* smaller things is certainly not new, and can be traced back to ancient civilizations tens of centuries ago. Its remarkable, and probably most attractive feature, is that by knowing very well only the few building blocks *and* all the possible ways of putting them together, one could hope to derive, and thereby fully understand, the incredible variety of the surrounding us world. The candidates for the role of these fundamental constituents of Nature have been changing with increasing sophistication of the human thought, spanning from only four substances, or elements: Earth, Air, Fire, and Water to ephemeral indivisible particles, or atoms—a purely philosophical concept at the time of their first introduction. It is interesting to note that in these early, rudimentary attempts it always seemed easier to come up with different candidates for the building blocks than to explain how they could actually be put together to yield everything else. Today, we call the ways of putting constituents together the “interactions” among them. And even today, the understanding of the interactions remains as the hardest part of the puzzle.

Although such ideas were crucial to the development of philosophical thought, they clearly had little or no effect on everyday life over the many centuries. For one thing, there were many competing ideas around, and nobody really knew

which of them corresponded to the reality they all pretended to describe. It was the birth of the experimental science that gave us the powerful tool to discriminate among many logically plausible candidate theories by directly testing their predictions in real-life experiments. Only after overwhelming experimental evidence had been collected did the ancient concept of atoms gain a second life and become a part of our general knowledge. Experiment became not only the ultimate judge, but also a lighthouse to guide theoretical searches toward a true model of Nature.

While Galileo Galilei's experiments at the turn of the 17th century can be considered to be the starting point of systematic experimentation in physics, it was the discovery of the electron at the end of the 19th century that gave birth to experimental elementary particle physics as we know it today. But where do we stand today in our search for the building blocks of matter and energy? As a result of striking progress in particle physics throughout the 20th century the following, experimentally confirmed, picture has emerged. The tiny particles—leptons, quarks, and bosons—are the smallest building blocks of the universe. While the first two are the constituents of matter, the bosons are the corpuscles, or quanta, carrying the interactions among them, responsible for holding together everything in the universe, ourselves included.

1.1 The Constituents of Matter: Leptons and Quarks

The longest studied of the lepton family of particles is the electron (denoted by e), discovered in 1897 by J. J. Thompson in intriguing cathode ray experiments at Cavendish Laboratory, University of Cambridge. Still, to the present day we have not been able to detect any substructure in the electron. It is now known to be

less than 10^{-18} meters (m) in size, a perfect justification to be called a “point-like” particle. It carries negative electric charge, and its quantity has become the natural unit for expressing electric charge because of the major role the electron plays in electromagnetic phenomena.

The two other charged leptons, the muon (μ) and the tau (τ), at first glance seem to be unnecessary heavier duplications of the electron with masses respectively about 200 and 3500 times that of the electron. It is for this reason that out of the leptons only electron exists in the atoms of our natural world.

In addition, each of these three leptons has an electrically neutral partner: particles called electron, muon, and tau neutrinos (ν_e , ν_μ , and ν_τ), respectively. These elusive particles are famous for their inability to interact with almost anything—they can penetrate through large blobs of mass, such as the earth, without experiencing a single interaction. For decades they have been considered to be massless particles traveling at the speed of light, but very recent experimental evidence suggests they may in fact have non-zero but, comparatively speaking, rather small masses.

The quarks show no size down to the smallest currently accessible scale of 10^{-19} m. They come in six distinct variates, or flavors. Their names have been abbreviated for daily use to the first letter: up (u), down (d), charm (c), strange (s), top (t), and bottom (b) quarks. They carry fractions of the electron’s electric charge. In addition, they also carry another type of a charge, whimsically christened color. It has nothing to do with the ordinary color. In the same way as an electric charge is a measure of the strength of the electromagnetic force between two electrically charged particles, the color is the charge of color force that quarks can

experience. It is the color charge that allows them to interact much more strongly than would be possible via their electric charge so that they can bind together in various combinations to create hundreds of other composite particles similar to those in the nuclei of the atoms: protons and neutrons.

However, quarks are not part of the hadrons or mesons in the same way as atom is made up of neutrons and protons with electrons orbiting them. One distinct characteristic of quarks is that they do not exist in an isolated form in Nature, very much unlike leptons, for instance.

While an electric charge can be positive or negative, the quark color charge can be of three types. In the same way as the equal and the opposite electrical charges give an electrically neutral state (like an atom being overall neutral but made up of positively charged nucleus and negatively charged electrons), the combination of all the three different colors gives a color-neutral, or a “white” state.

Since a label is needed to specify the three color charges, in keeping with the etymology, the three quark colors are conventionally called “red”, “blue”, and “green”, or, for that matter, any other three colors from an artist’s palette that would yield white when mixed. Each color also has an *anticolor* associated with it so that when the two are put together, once again, a colorless state emerges. In this sense, color and anticolor are the analogues of positive and negative electric charges in QED. For reasons not quite understood even today, it is *only* these white states of bound quarks that can be observed isolated in Nature, making study of the properties of quarks much more challenging than that of other elementary particles.

1.2 The Quanta of Interactions: Bosons

No story about building blocks of the universe would be complete without mentioning the corpuscles carrying the interactions, or the forces, among them that they all are destined to obey. There are four forces responsible for all types of interactions around us. At the same time, they are believed to be the manifestations of only one, unified interaction although today we surely lack any description of this hypothetical interaction. The four forces we distinguish today are: the electromagnetic, gravitational, weak, and strong forces. All forces have designated particles to be the messengers, or carriers, of the interactions. These particles are collectively called bosons, the most well-known of which is the *photon*, or a quantum of light.

The photon is the carrier of the electromagnetic force responsible for the overwhelming majority of the phenomena we experience daily, be it our ability to see, hear, talk, or even walk. The classical description of electromagnetism was discovered by James Clark Maxwell in the middle of the 19th century. His famous equations made it clear that electricity and magnetism are two aspects of a single phenomenon—electromagnetism. They also suggested that the action of this unified electromagnetic force propagated with a finite velocity we now call the speed of light. Dealing with the understanding of so called “black body radiation”, Max Planck pioneered the idea that radiation—an entity of intertwined electric and magnetic fields—may indeed be composed of small quanta of energy. At the time, this was such a revolutionary idea that it scared off even its author from developing it any further. It was Albert Einstein who realized the importance of the concept of quantization of radiation and successfully applied it to describe the photoelectric effect. It was for this work that Einstein received his Nobel prize—the highest award

for scientific achievement—rather than for his theory of relativity, probably the most celebrated breakthrough of the 20th century. This was the first indication that light was made up of particles (photons). It took a few more years to finally confirm the quantum (particle) nature of the electromagnetic field in *X-ray* experiments by Arthur Compton. The photon is a massless particle and therefore, in the absence of any other matter, or in vacuum, travels at the incredibly high speed of 10^8 meters per second, mediating an electromagnetic force at infinite distances.

Another well known force, gravitation, has also been known for centuries. Johannes Kepler and Sir Isaac Newton understood how to describe the motion of planets in the solar system, which is governed by gravitation. The unique feature of gravity is that, as Newton proposed first, *everything* in the universe is subject to its influence. Its “charge” is mass, and since mass and energy are equivalent, as it was first realized by Einstein when building his theory of special relativity ($E = mc^2$), everything, even massless particles, experience gravity. On the one hand, it is the dominant force in the macroscopic world, determining the large scale structure of the post-big-bang expanding universe, but on the other hand it is the weakest of the four forces in the micro world of the elementary particles (with their tiny masses). To date, only a classical, relativistic description of the gravitation is available, built upon the foundations laid out once again by Einstein in his theory of general relativity. Every attempt to reveal the quantum content of the theory, thereby connecting it to quantum mechanics, has so far failed. Despite this, gravity is believed to be mediated by *gravitons*, massless and chargeless bosons. The range of the gravitational force, like that of the electromagnetic, is infinite. Unlike electromagnetism, however, it is always attractive.

The weak force was not known before the 20th century. It first showed up in the mysterious β -decays of nucleons. It is mediated by heavy vector bosons: the charged W^\pm and the neutral Z^0 . Their existence was first predicted theoretically *en passant* the attempts to unify electric and weak forces in the 1960's and was experimentally confirmed about twenty years later. Because the mediating particles are massive, the range of the weak force is limited.

The strong, or the color force too is a discovery of the 20th century. It binds colored quarks inside the composite particles: hadrons and mesons. This force is mediated by eight colored agents called gluons. The gluons are massless particles, but despite this the strong force has limited range for reasons to be discussed in coming chapters. As with quarks, the gluons are elusive in that they too have never been seen directly, i.e. isolated. If our current understanding of the strong force is correct, gluons and quarks will never be seen isolated, as they are destined to play their role of perpetually unseen constituents concealing their existence from the world in the act of comprising it.

1.3 Putting It All Together—The Standard Model

The Standard Model of fundamental particles and their interactions is a grand achievement of the 20th century. Based on the mathematical language of local field theories guided by various symmetry principles, the most celebrated of them being the local phase, or gauge symmetries, the Standard Model gives the full description of all the constituents of matter and the interactions among them (with only one notable exception of gravitation).

The Constituents of Matter — Fundamental Fermions							
Leptons				Quarks			
Flavor		Mass (GeV)	Electric Charge	Flavor		Mass (GeV)	Electric Charge
The First Generation	e electron	0.0005	−1	u up		0.003	2/3
	ν_e electron neutrino	$< 10^{-8}$	0	d down		0.006	−1/3
The Second Generation	μ muon	0.106	−1	c charm		1.3	2/3
	ν_μ muon neutrino	$< 10^{-4}$	0	s strange		0.1	−1/3
The Third Generation	τ tau	1.777	−1	t top		175	2/3
	ν_τ tau neutrino	< 0.02	0	b bottom		4.3	−1/3

Table 1.1: The fundamental constituents of matter in the Standard Model.

Hadrons and mesons are built of invisible quarks (q) and gluons (g). For example, the most stable hadrons, neutrons (n) and protons (p) have the following quark composition: $p = (uud)$ and $n = (udd)$, while the longest-lived meson pion (π) is made up of a quark and an antiquark: $\pi^+ = (u\bar{d})$, $\pi^- = (\bar{u}d)$, and $\pi^0 = (u\bar{u} - d\bar{d})/\sqrt{2}$. The neutrons and protons, in their turn, make up the nucleus of the atom. The electrons rotate around the atomic nucleus creating neutral atoms which make up all ordinary matter around us. It has been observed that all known leptons and quarks can be arranged in generations, as indicated in Table 1.1, which summarizes all known fundamental fermions, their masses and electric charges based on reference [1]; this list certainly must be complemented by the corresponding anti-particles. It appears that the first generation of these constituents creates the ordinary matter that we see every day. The members of higher generations have

been only momentarily observed in man-created particle reactions or in cosmic rays from the outer space.

Force	Carrier		Mass (GeV)	Range (cm)	Charge (e)	Spin	Strength
Electromagnetic	γ	photon	0	∞	0	1	1
Gravitational	G	graviton	0	∞	0	2	10^{-40}
Weak	W^{\pm}	boson	80	10^{-16}	± 1	1	10^{-11}
	Z^0		91		0		
Strong	g	gluon	0	10^{-13}	0	1	10^2

Table 1.2: The fundamental interactions, their carriers, and relative strengths.

In addition to the constituents of matter, the Standard Model also sorts out all the interactions among them. The four fundamental forces along with their corresponding carriers are summarized in Table 1.2 [1]. The carriers of the forces are known to be bosons of the corresponding gauge symmetry groups (except perhaps for the graviton whose quantum nature is yet to be explained). In 1960's it was demonstrated that quantum electrodynamics, the relativistic quantum field theory of electromagnetic interactions, can be unified with the weak interactions by postulating the symmetry group $SU(2) \times U(1)$, the first group in this direct product, for the weak force and the second one, for the electromagnetic. Although these two interactions are not unified in the strict sense of this word, they appear to be so much tied up with each other that they are often said to be unified. Quantum Chromodynamics, the modern theory of strong interactions, has underlying $SU(3)$ gauge symmetry, eight generators of which are the massless, spin 1, colored gluons. It is believed that gravity is mediated by gravitons of spin 2 but so far no experimental evidence of this exists.

There is one unique boson, called the Higgs boson, predicted by the Standard Model which also awaits discovery. However, unlike the other gauge bosons, it has a completely different origin and is not the mediator of the four known forces in the same sense as the bosons listed in Table 1.2. Yet, the role of the Higgs boson is hard to underestimate: It is needed to create, or “generate”, the masses of all the other bosons as well as of all the fundamental fermions in the gauge theories of the Standard Model via the mechanism of spontaneous symmetry breaking—the only known way of introducing masses without violating the gauge symmetries and other properties of the interactions.

1.4 Jets—The Tools for Studying Quarks and Gluons

After the discovery of the electron by J. J. Thompson, several theories were put forth to suggest the structure of the atom. The cathode rays were originating from the neutral matter which was already known to be made up of indivisible neutral atoms—the evidence supported by the studies in Chemistry. The negatively charged cathode ray electrons were coming from the atoms, hence the electron had to be a part of an atom. But what was the other ingredient of atom? There had to be a positively charged “something else” which, together with negative electrons, could yield a neutral atom. And, not surprisingly, it was the subject of many speculations. J. J. Thompson himself put forth the so called “plum-pudding” model of the atom which stated that an atom was a blob of positively charged paste in which negatively charged, raisin-like electrons were sprinkled around.

Various models of atoms were soon put to a test by the exceptional experimental physicist Ernest Rutherford. Under his guidance, Hans Geiger and Ernest

Marsden studied the angular distribution of the energetic heavy alpha particles deflected by a gold foil. Quite unexpectedly, they found that there were significant number of alpha particles scattering at very large angles from their original direction, and several of them even deflected backwards. In the words of Rutherford himself [2]: “It was about as credible as if you had fired a fifteen inch shell at a piece of tissue paper and it came back and hit you”. This was only possible if the entire positive charge inside the atom was concentrated in even smaller but a rather dense nucleus. Thus a planetary model of the atom was born with a positive charge in the center, like the sun in the solar system, and tiny electrons moving around it in orbits, like the planets orbiting the sun. However, it was known that an accelerating charge, like an electron in the circular orbit, should radiate and thus lose its energy. So, the electrons in the planetary model of atom should very quickly run out of the energy and drop onto the nucleus, destroying the atom. Yet, matter and, consequently, the atoms were stable. There was something terribly wrong with this simple model. Who could then imagine that the understanding of the mind-dazzling act the electron has to perform in order to survive and not fall onto the atom’s center would occupy the greatest minds of the 20th century for many years to come to discover how very much different the atom actually is from the solar system, or, for that matter, from everything else known to us?

However, the Rutherford experiment gave us the *method* for studying the substructure of matter at the tiniest distances. The size of an atom is about 10^{-10} m. The human eye can distinguish objects as small as one-tenth of a millimeter, or 10^{-4} m. With the aid of an optical microscope one could see much smaller objects, perhaps 1000 times smaller, i.e. of the size of about 10^{-7} m. But the atom is 1000 times smaller than that. Electron microscope shows pictures of complex molecules,

and a field ion microscope can produce individual images of atoms. But constituents of atoms (protons, for instance) are one hundred thousand times smaller than atoms themselves! How does one study the structure of the atom? Or in the present day, how does one study the structure of the proton whose constituents—quarks and gluons—are at least another factor of ten thousand smaller, with a size of less than 10^{-19} m?

The method is based on the principle of the “scattering microscope” demonstrated by Ernest Rutherford. The target of interest is bombarded by highly energetic elementary particles, and a careful analysis of the ways they deflect from the target allows the experimenter to deduce a picture of the underlying internal structure. The higher the energy, the shorter the distances which can be probed. As a next step, one could consider smashing the two composite particles against each other and letting them probe each other as deeply as possible. In fact, this is exactly what is done at the Fermilab Tevatron, where protons and antiprotons are accelerated to extremely high energies and collided head-on. Each hard collision results in the conversion of beam particle energy into dozens of outgoing particles, and the only way to extract information from this type of scattering microscope is to carefully study the “debris”. By placing a detector around the interaction point, one can measure all the emerging particles. The analysis of their behavior may lead to better understanding of the proton’s constituents.

As the energy of the hadron collisions increases, however, a new phenomenon appears. Because of the way quarks and gluons are bound inside the hadron, their scattering at large angles most often results in the appearance of two highly energetic, collimated sprays of particles, that have come to be known as

“jets”. Studying of these jets—the direct manifestations of quarks and gluons—and their cross sections gives us invaluable information about the underlying interactions among quarks and gluons, about the structure of the colliding hadrons, and, if it exists, about the substructure of quarks and gluons themselves.

The first undeniable evidence of hadronic jet production was found in e^+e^- colliders in 1975. The jet signature in the final state began to emerge at the center-of-mass (CM) energies of the collisions of 6–8 GeV, but became a dominant pattern as the CM energy reached 30 GeV. The observed angular distribution of jet polar angle θ of the form $1 + \cos^2(\theta)$ was a clear indication that quarks are a spin 1/2 fermions. In 1982, hadronic jets were observed in hadron-hadron collisions ($p\bar{p}$) at CERN¹ at center-of-mass energies of 540–630 GeV. The first hadron collider studies of jet properties and direct tests of QCD were done by the UA1 and UA2 experiments at CERN [3, 4]. In 1985, the Fermilab Tevatron $p\bar{p}$ Collider began operation at energies of 1.8 TeV in the CM. These high energies provided a rich environment for producing hadronic jets in abundance and for studying their various cross sections and characteristics.

The DØ (D Zero) experiment is one of two collider experiments at the Tevatron. It is an international collaboration of over 500 physicists armed with the state-of-the-art DØ detector designed for studying physics at the Tevatron energies. For the first time, the DØ detector provides the ability to trigger and measure jets at very low angles (about 5°) with respect to the beam line. This allows the first time precise determination of the differential cross section for inclusive single jet production as a function of pseudorapidity. This measurement provides stringent

¹European Laboratory for Particle Physics, Geneva, Switzerland.

test of the QCD over the largest dynamic range to date. It also gives a reliable understanding of jets as a dominant source of background or as tagging objects at the Tevatron, as well as at the next generation Large Hadron Collider experiments.

This chapter is followed by a theoretical introduction, and then by the description of the experimental apparatus, the DØ detector. The remainder of the dissertation is a detailed discussion of the methods and techniques used in the data analysis leading to the extraction of the physical quantities of interest. At the end, the experimental results are compared to theoretical predictions.

A Word on the Units and Notation

Throughout this dissertation, unless otherwise noted, we use the so called natural system of physical units, most appropriate to particle physics. We set both Planck's constant: $\hbar \equiv h/(2\pi) = 1.055 \times 10^{-34}$ J·sec and the speed of light in the vacuum: $c = 2.998 \times 10^8$ m/sec to unity, i.e. $\hbar = c = 1$. The most convenient energy unit turns out to be 1 GeV $\equiv 10^9$ eV, for the energy scale is set, roughly speaking, by the proton mass of about 1 GeV. Thus the mass, energy, and momentum are all measured in the same energy units, while distances and times are given in units of inverse energy. Throughout, $-e$ is the rationalized charge of the electron, so that the asymptotic (low energy) value of the fine structure constant is $\alpha = e^2/4\pi \simeq 1/137$.

Bold letters usually denote the three-vectors. When using the four-vector notations, Greek indices run over the four space-time coordinate labels 0, 1, 2, and 3, with x^0 being the time coordinate. The raising and lowering of indices is accomplished by the metric tensor $g_{\mu\nu}$ (which has on the diagonal: $g_{00} = 1$, $g_{11} = g_{22} = g_{33} = -1$, and the off-diagonal components all are zeros), in the

following way: $x_\mu = g_{\mu\nu} x^\nu$ and $x^\mu = g^{\mu\nu} x_\nu$. Repeated indices are generally summed, unless otherwise indicated. A shorthand notation for the derivatives is frequently used with $\partial_t \equiv \partial/\partial t$, and similarly for the space derivatives.

CHAPTER 2

THEORETICAL INTERLUDE

“Gentlemen, we must bow to nature.”
(Julian Schwinger)

A few months after Werner Heisenberg’s success in describing quantum mechanics with matrix equations, Erwin Schrödinger published a single wave equation purporting to explain almost all aspects of electron behavior in terms of de Broglie waves, rather than the matrices:

$$i\partial_t\psi = H\psi. \quad (2.1)$$

The Schrödinger wave equation, Eq. (2.1), with the classical field $\psi(\mathbf{x}, t)$ and the classical Hamiltonian $H = T + V(\mathbf{x}) = \mathbf{p}^2/2m + V(\mathbf{x})$, with $V(\mathbf{x}) = 0$ for a free particle, was easier to use than the matrix equations of Heisenberg. Physicists knew how to deal with wave equations. It was relatively simple to describe atomic levels by solving one wave equation instead of dealing with somewhat cumbersome matrices. Using his equation, Schrödinger successfully calculated the Balmer lines and their intensities for the hydrogen. His derivations were straightforward and easy to follow, while Heisenberg’s methods were difficult to understand. To make matters worse, as it turned out, the followers of the matrix approach had papered over difficulties in their mathematics [5]. Very soon, however, Wolfgang Pauli, and to a lesser extent Schrödinger himself, demonstrated that the two approaches were identical. Quantum Mechanics was born.

By that time, Albert Einstein’s special relativity was a well established

theory, according to which, time and space were to be considered together and not separately, as was customary in Newtonian classical mechanics. In order to obey the principles of relativity theory, time and space coordinates had to transform similarly when changing the frame of reference from one inertial system to another, or, equivalently, to form a four-vector with respect to the Lorentz transformations. The Schrödinger equation was, however, explicitly not Lorentz covariant. It has been shown that the correspondence between classical and quantum equations can be formally established by substituting the differential operators for the classical energy (E) and momentum (\mathbf{p}) in the following manner: $E \rightarrow i\partial_t$ and $\mathbf{p} \rightarrow -i\nabla$. Thus, the Schrödinger equation, Eq. (2.1), for a free particle can be rewritten in the following form:

$$i\partial_t\psi = \frac{1}{2m}\nabla^2\psi, \quad (2.2)$$

explicitly showing that the space and time derivatives enter differently, thereby clearly demonstrating its non-Lorentz covariance. If Quantum Mechanics was to describe Nature accurately, this problem had to be fixed.

Special relativity not only demonstrated the equivalence of space and time, but also demanded that energy and momentum also form a four-vector with a Lorentz invariant “length” $E^2 - \mathbf{p}^2 = m^2$. Taking this Lorentz invariant expression and substituting E and \mathbf{p} with their quantum counterparts, gave a free particle relativistic wave equation known as the Klein–Gordon equation:

$$\left(\partial_t^2 - \nabla^2 + m^2\right)\phi = 0. \quad (2.3)$$

Although manifestly Lorentz invariant, the Klein–Gordon equation suffered from its own difficulties. The first was the property that the standard relativistic relation between the energy and momentum implied that for each \mathbf{p} , there were two possible

solutions—one with positive, and one with negative, energy: $E = \pm\sqrt{\mathbf{p}^2 + m^2}$. This classical result was also true for the wave solutions of Eq. (2.3). The problem could be avoided in case of a free particle in much the same way as it could be done in classical physics. It would be postulated that only particles with positive energies are real physical particles. The existence of a finite energy gap of $\pm m$ between the positive and negative energy states allows this, for neither a classical nor a free quantum particle can overcome the energy gap. It however had disastrous consequences as interactions were introduced into the quantum theory. A particle from the positive energy spectrum could radiate enough energy to make a transition into the negative energy states, after which there would be nothing to stop it from rolling down to infinite negative energy states, emitting infinite amounts of energy. This certainly does not happen in the Nature.

The second problem was related to the fact that the Lorentz invariant probability density, the time component of a four-vector probability current j^μ ,

$$j^0 \equiv \rho = \frac{i}{2m} (\phi^* \partial_t \phi - \phi \partial_t \phi^*) , \quad (2.4)$$

unlike the corresponding quantity $\rho = \phi^* \phi$ for the non-relativistic Schrödinger equation, was not positive definite. In a second order differential equation, such as the Klein–Gordon equation, ϕ and $\partial_t \phi$ could be fixed arbitrarily at a given time so that ρ of Eq. (2.4) could be made negative. It was not clear how to interpret the negative probabilities and, therefore, the Klein–Gordon equation had to be abandoned as a good candidate for the correct single-particle relativistic wave equation.

Soon after Niels Bohr pioneered his quantization rules semi-classically solving for the hydrogen atomic levels, it was realized that, as a result of quantization, particles could be described by a *complete* set of *quantum numbers*. For instance,

in hydrogen atom, the electron energy levels could be described by the principle quantum number, n , which took values from 1 to infinity as electron moved from its first, closest-to-the-nucleus orbit, to basically continuous energy spectrum of a loosely bound particle at the outskirts of atom. A complete set of quantum numbers fully determined the state of the particle, and thus two identical particles with identical quantum numbers could not be distinguished. Although Bohr's semi-classical approach worked very well in describing the relatively simple line emission patterns of hydrogen, it was much harder to understand the spectrum of more complex, heavier elements. As one example, Alkaline-earth metals produced spectral lines which were slightly separated doublets of almost identical frequencies. To explain this, in addition to the three quantum numbers introduced by Pauli to describe orbiting electrons (energy, angular momentum, and orientation in space), he suggested a fourth quantum number, which he called *Zweideutigkeit*—two-valuedness.

George Uhlenbeck and Samuel Goudsmit thought this quantum number could be explained by imagining an electron rotating around its own axis like a toy top with quantized values of the corresponding angular momentum. If the angular momentum associated with this spin had a value of $1/2$ ($\hbar/2$ in the SI units), it could provide two slightly different energy levels depending on the two ways the electron could rotate with respect to its orbital motion. When they showed this idea to Uhlenbeck's teacher, Paul Ehrenfest, he told them to have it checked by Hendrik Lorentz. Lorentz's verdict was severe: he showed that with such a spin electron had to rotate ten times faster than the light itself could travel! However, Ehrenfest, conceivably having liked the idea very much, and as if he himself suspected the possible problem with it, went ahead and sent the Uhlenbeck–Goudsmit paper for publication, not awaiting Lorentz's criticism. As a result, despite the failure of the

original spinning electron model, this new quantum number is still referred to as “spin”.

Pauli also postulated that no two electrons with the same complete sets of quantum numbers could exist. Subsequently, Pauli’s exclusion principle was formalized by requiring that the wave function of multi-electron state be completely antisymmetric in all quantum numbers of all the electrons. Enrico Fermi and Paul Dirac introduced this idea into thermodynamics and thus the particles obeying Pauli exclusion principle are said to obey Fermi–Dirac statistics, or, more simply, are called *fermions*. In much the same way, the particles like photons, for which the wave function is symmetric, are called *bosons* as they obey Bose–Einstein statistics. It was only later that the deep connection between particle’s spin and statistics was mathematically established in the framework of the relativistic quantum theory of fields, showing that all the particles of half integer spin are fermions, and all the particles with integer spin are bosons. In the meantime, however, it was realized that both the Schrödinger and Klein–Gordon equations were for spinless particles. Obviously, this was yet another problem if these equations made a pretense to describe the spin $1/2$ electron.

Dirac tried to attack all these problems at once by deriving a new relativistic equation for spin $1/2$ particles. In order to avoid negative probability densities, he realized that the equation had to be a differential equation first order in time. In order to be Lorentz-invariant, the equation’s time and space derivatives had to enter in the same way. Dirac thus wrote down the general form of such a linear equation and required it to be identical to the Klein–Gordon equation when “squared”. Basically, the whole procedure was equivalent to the linearization of the Klein–Gordon

equation. This approach gave him a free particle matrix equation:

$$(i\gamma^\mu \partial_\mu - m)\psi = 0, \quad (2.5)$$

with a four-component column-vector of wave function ψ , or a *spinor*, and 4×4 matrices γ^μ obeying an anticommutation relation:

$$\{\gamma^\mu, \gamma^\nu\} \equiv \gamma^\mu \gamma^\nu + \gamma^\nu \gamma^\mu = 2g^{\mu\nu}, \quad (2.6)$$

with the usual metric tensor $g_{\mu\nu}$. The Dirac equation was linear in time and space derivatives, and it was demonstrated to be Lorentz invariant. The conserved current now had a form $j^\mu = \bar{\psi}\gamma^\mu\psi$, with adjoint spinor $\bar{\psi} = \psi^\dagger\gamma^0$, ψ^\dagger being a row-vector, hermitian conjugate of ψ . Its time component, j^0 was positively defined, $j^0 \equiv \bar{\psi}\gamma^0\psi = \psi^\dagger\psi \geq 0$, and thus well-suited to the traditional quantum-mechanical interpretation as a probability density.

By following “minimal prescription”, $i\partial_\mu \rightarrow i\partial_\mu + eA_\mu$, to introduce the interaction of an electron of charge e with an arbitrary external electromagnetic field A_μ , Dirac showed that the conserved angular momentum of the electron indeed had two terms: one due to its orbital motion and the other, due to its “spin”. And the spin eigenvalues were correct: $\pm 1/2$. Furthermore, direct solution of his equation for the hydrogen atom gave an exact formula for the energy levels which had the fine structure splitting in it. It became crystal clear that the Dirac equation was indeed a correct relativistic equation for spin 1/2 particles.

However, Dirac’s equation did not solve the other problem of the Klein–Gordon equation, that of the negative energies. And this was not surprising as, classically speaking, the equation was derived by the linearization of the quadratic equation $E^2 = \mathbf{p}^2 + m^2$, unavoidably introducing negative energies. More precisely,

for a given momentum \mathbf{p} , out of the four spinor components of the free particle Dirac equation solution, two corresponded to the positive energy $+\sqrt{\mathbf{p}^2 + m^2}$ while the other two—to the negative energy $-\sqrt{\mathbf{p}^2 + m^2}$ (two because each spin state had one positive and one negative energy state associated with it). But unlike the Klein–Gordon equation, the Dirac equation described fermions—particles of spin $1/2$, which were believed to obey Pauli exclusion principle. Dirac made use of this characteristic of fermions and made a bold suggestion that almost all negative energy states were already filled with electrons. Since no two electron could be in exactly the same quantum state, this picture of the “Dirac sea” rescued electrons from “falling” into the already-occupied infinitely negative energy states. The few available negative energy states, or “holes” behaved just like an electron with opposite quantum numbers: positive energy and positive charge. This was the prediction for the existence of *antiparticles*. The prediction was brilliantly confirmed when, in cosmic ray tracks observed in a Wilson cloud chamber, Carl D. Anderson found a particle of exactly the same mass but equal and positive electric charge as an electron: a *positron*.

The Dirac theory still had some problems. If the credibility of the quantum theory indeed depended on giving positively defined probabilities—one of the motivations that led Dirac to derive his equation—then the existence of the spinless particles would have to be ruled out, for the Dirac’s analysis did not solve the problem of negative probabilities in the Klein–Gordon equation (the only relativistic equation available for spin zero particles). Examples of spin zero particles were already known by then: the hydrogen atom in its ground state, and alpha particles. While it could have been argued that these were composite rather than elementary particles, it was not clear how the idea of elementarity was embedded in Dirac’s

equation.

Furthermore, Dirac's solution of an infinite sea of fermions certainly could not work for bosons, as there is no exclusion principle for particles obeying Bose-Einstein statistics. Thus the prediction of antiparticles for charged bosons could not have been made based on Dirac's analysis.

Finally, although giving the correct magnetic moment of the electron was regarded as one of the triumphs of the Dirac's theory, it could not unequivocally follow from the line of Dirac's arguments. Having introduced electromagnetic interaction into the Dirac equation, it was noted that there is no reason why a term proportional to $[\gamma^\mu, \gamma^\nu] \psi F_{\mu\nu}$ could not be included as well, since it does not violate any invariance principles (here the brackets [...] indicate usual quantum mechanical commutator, while $F_{\mu\nu} = \partial_\mu A_\nu - \partial_\nu A_\mu$ is the electromagnetic field tensor). Then, by choosing an arbitrary constant in front of this term, additional contributions to the magnetic moment of the electron would arise. Therefore, apart from pure simplicity, there was no reason to expect any particular value of the electron's magnetic moment from the considerations that led to the derivation of the Dirac equation.

It took the relativistic quantum theory of fields to solve all the problems of relativistic quantum mechanics. The concept of single-particle equations describing Nature had to be abandoned, giving a way to the quantization of the fields which formally obeyed the same equations. Quantization yielded the particle content of the theory, and instead of the probabilistic interpretation of the square of the wave function, the $|\psi|^2$ turned out to be a measure of the number of particles. The concepts of the probability density and probability current were replaced by the charge and current densities, and so on. And the above-discussed arbitrary term to

spoil the prediction of the electron magnetic moment by the Dirac equation would ultimately be ruled out based on the requirement of the renormalizability of the corresponding quantum field theory.

2.1 The Standard Model

The dynamics of a classical field is fully described by its equation of motion. The examples of such equations are Maxwell's equations of classical electrodynamics. They are often presented as the four coupled equations of the electric (\mathbf{E}) and magnetic (\mathbf{B}) fields and their sources, the charges and currents. The Maxwell equations are Lorentz-invariant, but this is not apparent when presented in terms of \mathbf{E} and \mathbf{B} fields. Therefore, a better way of to present them in explicitly Lorentz-covariant form is to introduce the four-vector potential $A_\mu = (\varphi, \mathbf{A})$, the asymmetric field strength tensor $F_{\mu\nu} = \partial_\mu A_\nu - \partial_\nu A_\mu$, and the source current four-vector $j^\mu = (\rho, \mathbf{j})$. One may then write down Maxwell's equations in a rather compact, and, above all, a Lorentz-covariant form:

$$\partial_\mu F^{\mu\nu} = j^\nu \quad \text{and} \quad \partial_\mu \tilde{F}^{\mu\nu} = 0, \quad (2.7)$$

with the dual tensor $\tilde{F}^{\mu\nu}$ defined by $\tilde{F}^{\mu\nu} = \frac{1}{2}\varepsilon^{\mu\nu\rho\lambda}F_{\rho\lambda}$.

Equivalently, one could start from the classical Lagrangian density of the electromagnetic field $\mathcal{L}(A_\mu, \partial_\mu A_\nu)$ which can be constructed by writing down the most general form of the fields and their derivatives satisfying all the general invariance principles that the theory should obey. Then the requirement that the action functional $S[A_\mu]$,

$$S[A_\mu] = \int d^4x \mathcal{L}(A_\mu, \partial_\mu A_\mu) \quad (2.8)$$

be stationary with respect to small variations in the fields, i.e. $\delta S[A_\mu] = 0$, will yield the field equations. The most general classical Lagrangian density for the electromagnetic (EM) field can be written in the following way:

$$\mathcal{L} = -\frac{1}{4}F^{\mu\nu}F_{\mu\nu} + j^\mu A_\mu, \quad (2.9)$$

with the first term representing the EM field itself (“kinetic” term) and the second term its interaction with the source j^μ . The requirement that the action corresponding to this Lagrangian be stationary yields Maxwell equations, Eq. (2.7).

In the quantum theory of fields, the fields are linear operators. They act in the infinite dimensional linear Hilbert space which has desirable features not present in an arbitrary linear space, among others, the existence of the positively defined norm, or “length”, of its elements, or vectors. A vector in Hilbert space corresponds to the state of a physical system with a definite number of particles N , that is to say, it is an N -particle state. States with different numbers of particles form an orthonormal representation of the Hilbert space. The Field operators which obey formally same-looking “field” equations as in relativistic quantum mechanics, are then quantized. This introduces an interpretation of the field as a creation or annihilation operator of the corresponding type of particle. Thus, the number of particles in any given state can be changed by simply acting on it with a desired combination of the field operators: the N -particle state will transform into the M -particle, generally a different state, and the initial and the final, as well as all the intermediate states will always remain inside the Hilbert space of the theory. One of the biggest problems of the single particle equations in relativistic quantum mechanics, namely, their inability to adequately describe the particle number non-conservation in variety of experimentally observed processes, or reactions, is thus

successfully overcome.

2.1.1 The Gauge Symmetries

As in the classical theory of fields, in quantum theory the Lagrangian density \mathcal{L} is the most general combination of terms with fields and their derivatives that would respect the requirements of all the invariance principles. With the development of the quantum theory of fields a new type of symmetry emerged as the symmetry of Nature. It is called the local phase, or *gauge* symmetry. Combined with the requirement of Lorentz invariance, it significantly limits possible terms for the Lagrangian.

Let us consider the Lagrangian density for the Dirac field ψ :

$$\mathcal{L} = \bar{\psi}(i \not{\partial} - m)\psi, \quad (2.10)$$

where, for any quantity a_μ , we introduce the standard shorthand notation $\not{a} \equiv \gamma^\mu a_\mu$. Using the principle of stationary action, it is straightforward to show that it indeed gives the Dirac equation of Eq. (2.5), as well as its hermitian conjugate equation for $\bar{\psi}$. The fact that the physics results do not generally depend on the phase of the complex number is somewhat familiar from usual quantum mechanics. The phase transformation of the Dirac field $\psi \rightarrow e^{i\alpha}\psi$, with a real and constant phase α , will leave the Dirac Lagrangian invariant as the phases from ψ and $\bar{\psi}$ will be equal and have opposite signs, canceling each other in both terms of the Lagrangian (2.10). This is the same as saying that the Lagrangian in Eq. (2.10) is invariant under the unimodular unitarity group $U(1)$. It has been realized by Emmy Noether that any such symmetry of the Lagrangian implies a conserved current. In the case of the Dirac equation this yields a conservation of the quantity $\bar{\psi}\psi$, a time component of

the conserved current. When fields are quantized, $\bar{\psi}\psi$ becomes an operator for the total number of particles and antiparticles. Conservation of this total number means the conservation of the electric charge in the system, which becomes apparent the moment the interaction of the electron with an electromagnetic field is introduced in the free fermion Dirac Lagrangian.

Consequences of the symmetries of the Lagrangian under phase transformations become even more dramatic as one further requires invariance under the *local* gauge transformations. That is, under the transformations when the phase itself is a function of space-time coordinate x , i.e. transformations of the type: $\psi \rightarrow e^{i\alpha(x)}\psi$. Imagine adjusting phases of the fields in *every* space-time location *independently* of each other and requiring not a single measurement to be sensitive to such arbitrary redefinition of fields. It is indeed a very demanding requirement and, as a result, the theories obeying it attain many attractive, and, more importantly, realistic physical features.

It is clear that the Dirac free field Lagrangian of Eq. (2.10) is *not* invariant under the local gauge symmetry because the transformation of the field derivative

$$\partial_\mu\psi \rightarrow e^{i\alpha(x)}\partial_\mu\psi + ie^{i\alpha(x)}\psi\partial_\mu\alpha, \quad (2.11)$$

gives rise to an extra term, $-\bar{\psi}\psi\partial_\mu\alpha$, in the Lagrangian, spoiling the gauge invariance. It is remarkable that this can be cured by introducing into the theory a vector field A_μ which under the local gauge transformations changes as $A_\mu \rightarrow A_\mu + \frac{1}{e}\partial_\mu\alpha$. If this vector field is implemented in the Lagrangian via the term $e\bar{\psi}\gamma^\mu\psi A_\mu$ then the theory becomes invariant under local gauge transformations as the term $-\bar{\psi}\psi\partial_\mu\alpha$, arising from the fermion field derivative transformation, is exactly canceled by $\bar{\psi}\psi\partial_\mu\alpha$ originating from the transformation of the newly introduced interaction term

between the vector field A_μ and the Dirac field ψ : $e\bar{\psi}\gamma^\mu\psi A_\mu \rightarrow e\bar{\psi}\gamma^\mu\psi A_\mu + \bar{\psi}\psi\partial_\mu\alpha$. This new interaction term is precisely the well-known coupling between the photon and the charged current of classical electrodynamics. Thus, the requirement of local gauge invariance of the Dirac free field Lagrangian forces introduction of the electromagnetic field into the theory, thereby generating the full theory of electrodynamics.

To make the theory complete, a gauge invariant “kinetic” term for the electromagnetic field should be added, after which the Lagrangian of Quantum Electrodynamics (QED) emerges:

$$\mathcal{L}_{QED} = \bar{\psi}(i\not{\partial} - m)\psi + e\bar{\psi}\not{A}\psi - \frac{1}{4}F^{\mu\nu}F_{\mu\nu}. \quad (2.12)$$

Although the gauge field “kinetic” term can and should be included in the full \mathcal{L}_{QED} , the same is not true for the usual mass term $m^2 A_\mu A^\mu$, as it would clearly violate the local gauge symmetry. Therefore, another important consequence of the gauge invariance is the requirement that the gauge field itself be *massless*, which certainly is true in the case of QED with its massless photons.

2.1.2 Quantization, and Feynman Diagrams

Once the invariant Lagrangian of the quantum field theory is constructed and the corresponding field equations are derived, the field operators must be quantized. This is done in two equivalent ways. One is the original, canonical formalism with the canonical field commutators, time ordered products, Wick’s expansion, and the S-matrix. The other method is that introduced by Richard Feynman which postulates that the amplitude of the transition is given by the sum (functional integral) over all possible “trajectories” (in phase space) between the initial and

final states taken with weighting factor of the classical action in the exponent $e^{iS} = e^{i\int d^4\mathcal{L}}$. Freeman Dyson showed that the two approaches are completely equivalent, but it turned out that the second method was easier to use in the majority of practical applications.

The ultimate goal of the relativistic quantum theory of fields is to give a prescription for calculating the transition amplitudes or cross sections of various physics processes. After the quantization, the interactions are evaluated by computing a perturbation series expansion of the interaction part of the Lagrangian. This is a lengthy process of bookkeeping of all the terms arising in this power expansion in field operators, and is made particularly tedious by the fact that the fields as operators do not generally commute, unlike the c -numbers. Fortunately, however, this process can *always* be translated into so called “Feynman rules” which are a set of exact prescriptions describing how to construct an invariant amplitude in the theory.

In most physically interesting cases, the Feynman rules can be directly “seen” from the Lagrangian. Strictly speaking, this is not a correct approach in general and always must be checked with the rigorous derivation of the *complete* set of rules from either the canonical or the path integral approach of quantization. In this simplified approach, various terms in the Lagrangian are associated with sets of particle propagators and interaction vertices. This is most easily done in the momentum representation, rather than in the coordinate representation, using a simple correspondence $i\partial_\mu \rightarrow p_\mu$. The free particle propagators are usually obtained from the terms quadratic in the corresponding fields as the inverse of the entire operator enclosed by the fields. For instance, the form of the Dirac Lagrangian

Some of the Feynman Rules for QED

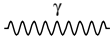
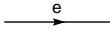
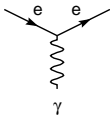
Massless spin 1 boson (photon)		$\frac{ig_{\mu\nu}}{p^2}$
Spin 1/2 fermion		$\frac{i}{\not{p} - m}$
QED vertex		$ie\gamma^\mu$

Figure 2.1: A few QED Feynman rules in the momentum representation.

$\bar{\psi}(i\not{\partial} - m)\psi$ suggests for the fermion propagator a form $i/(\not{p} - m)$ for each virtual fermion line.

The terms in the Lagrangian associated with interactions induce the Feynman rules for the vertices. The vertex is usually given by the coefficient of the interaction term (with proper combinatorial normalization) and the field operators indicating particles entering or leaving the vertex. The rules are also supplemented by the graphical conventional representations of the propagators and vertices, the lines for propagators usually being different (straight line, wiggly, dashed line, etc) for different types of particles. An illustration of some of the QED Feynman rules in the momentum representation is given in Figure 2.1. The central quantity for the quantum field theoretical calculations, the invariant amplitude \mathcal{M} , for a given physics process is then given by the sum of all possible Feynman graphs, or amplitudes. The cross section finally is given by the product of the invariant amplitude squared and the kinematic Lorentz invariant phase space available to the final state of the reaction, $d\sigma \sim |\mathcal{M}|^2 \times d\text{Lips}$.

Some of the Divergences in QED

The figure contains two Feynman diagrams and their corresponding integral representations. The top diagram shows a fermion line with momentum p entering from the left and p exiting to the right. A photon loop with momentum k is attached to the fermion line. The diagram is labeled with γ above the loop and k below it. The integral representation is:

$$\sim \int \frac{d^4 k}{(2\pi)^4} (ie\gamma^\mu) \frac{i}{\not{p} - \not{k} - m} \frac{ig_{\mu\nu}}{k^2} (ie\gamma^\nu) \xrightarrow{k \rightarrow \infty} \int \frac{d^4 k}{k^3}$$

The bottom diagram shows a photon line with momentum p entering from the left and p exiting to the right. A fermion loop with momentum k is attached to the photon line. The diagram is labeled with γ above the loop and $p-k$ below it. The integral representation is:

$$\sim \int \frac{d^4 k}{(2\pi)^4} \text{Tr} \left((ie\gamma^\mu) \frac{i}{\not{k} - m} (ie\gamma^\nu) \frac{i}{\not{p} - \not{k} - m} \right) \xrightarrow{k \rightarrow \infty} \int \frac{d^4 k}{k^2}$$

Figure 2.2: One loop linear and quadratic divergences in QED.

2.1.3 Divergences, Regularization, and Renormalization

Unfortunately, it turns out that many of the possible Feynman diagrams yield results which are divergent. Graphs with closed particle loops require summation, or integration over all possible “running” momenta inside the loop. For example, the one loop correction to the electron propagator in QED is a linearly divergent integral. This is illustrated in the top plot of Figure 2.2. At highest momenta the amplitude corresponding to the graph integral behaves as $\int d^4 k / k^3$ and hence is linearly divergent. Another example of the divergence is the so called photon polarization operator $\Pi^{\mu\nu}$ given by the bottom graph in Figure 2.2 being proportional to the integral expression on the right. It is clear that at high momenta this integral is quadratically divergent. Such divergences appearing at high momenta came to be known as ultraviolet (UV) divergences. Another class of infinities arises when the integrals diverge at lowest momenta, for instance, when the momentum power in the denominator is higher than that of the numerator. In contrast, these are

referred to as infrared (IR) divergences.

The UV divergence is usually “cured” by introducing either a high momentum cutoff or by performing dimensional regularization—the procedure in which the formal integration is performed in arbitrary, not necessarily integer dimensions. Dimensional regularization is often preferred because of its explicit Lorentz invariance. In both cases, after rearranging the amplitudes in various ways the limit is taken by either sending the UV cutoff to infinity or taking a limit of 4 dimensional space-time, respectively. The IR divergences are usually not present for massive theories. Otherwise, they are cured by introducing specific resummation schemes so as to leave the physically measurable quantities free of such divergences.

Certainly, regularization alone is not capable of solving the problem of infinities. It has been noticed that in quantum field theories it is sometimes possible to redefine the measurable physical quantities such as charge, mass, and vertex coupling strengths in such a way that all infinities are taken out. The bare values of these quantities are postulated to be unknown. The only quantities that can actually be observed are their renormalized, or “dressed” values, and it is these values that must be finite for any theory to make sense. The theories in which *all* infinities can be absorbed by redefinition of the *finite* number of physical parameters are said to be the *renormalizable* theories. Strictly speaking, only such theories have a chance of describing physical reality. This is however not necessarily true in cases of the *effective* field theories, with characteristic energy scales much higher than that of the theory under consideration. In the low-energy limit, it is allowable for such theories to contain non-renormalizable terms in their effective Lagrangians.

A physical theory clearly cannot depend on the choice of various possible

schemes used for its regularization and then renormalization. For instance, the final calculations can not depend on the momentum scale, Λ , used for regularizing the integral. The invariance of physical quantities with respect to renormalization method gives rise to the renormalization group equations which often reveal interesting general characteristics of the theory.

2.1.4 The Glashow-Salam-Weinberg Model

The quantum field theory of the electrodynamics, QED, turned out to give the description of all known electromagnetic processes with phenomenal accuracy. The most vivid illustrative example is the prediction of the anomalous magnetic moment of the electron, or, equivalently, its gyromagnetic ratio g , which agrees with the experimental measurement to within eight decimal figures. But the real triumph of the quantum field theoretical approach was perhaps the joining of the QED and theory of weak interactions.

After Antoine-Henri Becquerel’s accidental discovery of *rayonnements invisibles*—which we now know to be the electrons emitted in the β -decay of the neutron, $n \rightarrow pe\bar{\nu}$, from the nucleus of uranium—it took several decades to create a theoretical framework that would describe this, and similar, processes. In order to save the conservation of energy—which seemed to be violated in β -decays—Pauli in 1931 proposed the existence of a new, elusive particle, later dubbed the “neutrino”, which was responsible for carrying away the missing energy. Soon after this, and also taking an advantage of the recently discovered neutron by James Chadwick in 1931, Enrico Fermi in 1933–34, by analogy with QED, proposed a weak interaction Lagrangian with the famous vector-vector (VV) four fermion coupling as the

underlying theory of the β -decay:

$$\mathcal{L}_F = -\frac{G_F}{\sqrt{2}} [\bar{p}\gamma_\mu n] [\bar{e}\gamma^\mu \nu] + \text{hermitian conjugate}, \quad (2.13)$$

where fermion fields are denoted by the first letters of the names of the corresponding particles in the reaction, and the Fermi constant is $G_F \approx 10^{-5}/m_p^2$, with the mass of the proton of about 1 GeV.

In the following years, other weak processes were discovered, such as the weak decays of pions and muons with relatively long (10^{-8} – 10^{-6} s) decay lifetimes. It was becoming evident that this was an entirely new type of interaction. Because lifetimes are inversely related to the couplings, it was clear that the effective coupling of this new type of interaction was much weaker than that of the QED, the latter with the characteristic times scales of interactions of 10^{-16} s (and weaker still than strong interactions with characteristic times of 10^{-23} s).

In the mid 1950's physicists were trying to solve the so called tau–theta puzzle. In cosmic rays, there were seen two particles of suspiciously identical masses and lifetimes, which could be told apart only by their decays. One of them, the theta particle, decayed into the positive parity two pion state, while the other one, the tau particle, decayed into the negative parity three pion state. If these two particles were indeed the same, then it would signal the violation of parity, a discrete symmetry of left and right, at the time believed to be one of the few exact symmetries in Nature. In fact, Tsung-Dao Lee and Chen Ning Yang in their article [6] called for more experimental evidence to solve the tau–theta problem. Soon, in the famous Chien-Shiung Wu's experiment which studied β -transitions of polarized cobalt nuclei $^{60}\text{Co} \rightarrow ^{60}\text{Ni}^* + e^- + \bar{\nu}_e$, parity violation was confirmed [7] by observing an asymmetry: the electrons preferred to be emitted in the direction

opposite to that of the cobalt's nuclear spin.

This unexpected discovery of parity violation suggested a current-current interaction of the type vector $(\bar{\psi}\gamma^\mu\psi)$ minus axial-vector $(\bar{\psi}\gamma^\mu\gamma^5\psi)$, or “ $V - A$ ”, with an effective Lagrangian density much like that of Eq. (2.13):

$$\mathcal{L}_{eff} = -\frac{G_F}{\sqrt{2}}J_\mu^\dagger J^\mu + \text{hermitian conjugate}, \quad (2.14)$$

where the weak current J^μ is the difference between the vector and the axial-vector currents. If split into leptonic and hadronic pieces, the leptonic part of J^μ can be written as (for the first two lepton generations):

$$J^\lambda = \bar{\nu}_e\gamma^\lambda(1 - \gamma_5)e + \bar{\nu}_\mu\gamma^\lambda(1 - \gamma_5)\mu. \quad (2.15)$$

The hadronic part, also having $V - A$ structure, in light of today's Standard Model, contains quarks, coupling them from the same generation as well as allowing quark mixing from one generation to another via relatively suppressed weak interactions. The important consequence of $V - A$ structure is that the helicity projection operator, $(1 - \gamma_5)$, allows *only* left-handed fundamental fermion fields in the theory.

Although $V - A$ theory was very successful in describing the experimental data, it had problems from the point of view of the formal quantum theory of fields: the theory induced by the Lagrangian of Eq. (2.14) was *not* renormalizable. This was signaled first of all by the fact that the weak coupling G_F had the units of the inverse of mass squared. Historically, the search for the correct renormalizable theory of the weak interactions got intertwined with attempts to unify the weak and the electromagnetic forces.

The idea of the unification of electromagnetic and weak interactions was first proposed by Julian Schwinger [8] in 1957, noting the vector nature of the two

interactions. It was Schwinger who first considered the introduction into the theory of two charged vector bosons, which today are known as W^\pm bosons, in an analogy with charge-neutral vector boson (photon) of QED. With the massive vector fields W^μ the Lagrangian of the interaction could be written as:

$$\mathcal{L}_I = g(J_\mu W^\mu + \text{hermitian conjugate}). \quad (2.16)$$

Then the experimentally tested $V - A$ Lagrangian could be considered as the effective, low-energy limit of the theory with the interaction Lagrangian of Eq. (2.16). The equivalence was established via the relation of the coupling constants: $g^2/M_W^2 = G_F/\sqrt{2}$. Thus, the massive vector bosons were necessary in order for the new theory to have the appropriate low-energy behavior of the $V - A$ type. Schwinger did not succeed in developing the full theoretical model, so he suggested to his graduate student, Sheldon Glashow to think about this issue.

By that time, Chen Ning Yang and Robert Mills [9], motivated by the symmetry of the isotopic spin, had already developed a formal gauge theory with the underlying symmetry of the group $SU(2)$, a non-Abelian analog of QED. Glashow was one of the first to realize in 1958 [10] that the key to the weak interaction was to consider it as a local non-Abelian gauge theory in the spirit of the one introduced by Yang and Mills (YM) in a different context. In his 1961 paper [11] Glashow proposed the gauge theory with the underlying $SU(2) \times U(1)$ symmetry as a candidate for the unification of the weak and electromagnetic forces. It was very attractive to consider the weak interactions as a gauge theory *a la* QED. However, as it was discussed above, massive gauge bosons were not allowed in the theory, as their mass term $M_W^2 W_\mu^\dagger W^\mu$ would hopelessly violate local gauge symmetry in exactly the same way as the mass of the photon would in QED. Also, since the group $SU(2)$ has three

generators, it was necessary to introduce a third neutral boson Z^0 , which would indicate the presence of neutral weak currents. Unfortunately, no neutral currents had ever been seen in hundreds of careful experiments carried out to that date. Therefore, Glashow had to speculate that the Z^0 boson was in fact very heavy—the only possible explanation why experimentators had not been able to see it.

Independently, at about the same time, Abdus Salam and John Ward also proposed a unified electroweak theory based on the YM gauge theory and with the neutral Z^0 boson [12]. Inspired by Schwinger, Salam had been working on the theory with only W^\pm and photons for some time. He had proved that such a theory, despite Glashow's hopes, was not and could not be renormalizable. It was clear that the usual mass terms for the vector bosons were banned from the Lagrangians not only because of the requirement of (perhaps purely esthetically desired) local gauge symmetry, but also, and from a more practical point of view, because of the requirement of renormalizability of the theory. Yet, the vector boson masses were needed for the desired low-energy behavior of the theory. This was the biggest problem that the theory of weak interactions had to overcome. Unexpectedly, condensed matter physics came to rescue.

The concept of spontaneously broken symmetry got introduced into the particle physics by Jeffrey Goldstone, a field theorist who had become interested in superconductivity. The essence of this idea is that while the theory itself may have some higher order symmetry associated with it, its ground state may not; hence the symmetry is spontaneously broken when the theory is realized in one of its many possible vacua. The theory of superconductivity, first offered by John Bardeen, Leon N. Cooper, and John R. Schrieffer (BCS) [13], was at first criticized because

of its lack of gauge invariance. By the 1960's it was realized that BCS theory was indeed an example of a broken symmetry. Goldstone suspected that broken gauge symmetry would give a rise to massless particles in the theory [14], but such massless particles had not been seen experimentally. Salam and Steven Weinberg actually took this idea and, in trying to disprove this undesirable feature of spontaneous symmetry breaking, to their big disappointment, came about proving it right in three different ways; and it became to be known as the “Goldstone theorem”.

A remarkable twist in the development of the gauge field theories took place when it was first realized by Peter Higgs that there were no Goldstone bosons in theories with spontaneously broken gauge symmetry [15]. The gist of the argument was that in the theory with three massless $SU(2)$ gauge bosons, when the Goldstone boson appeared, the three bosons would “eat up” the massless particle in such a way that all three of them would acquire masses and there would be no massless particle remaining in the theory. In other words, the Goldstone boson would provide the longitudinal component required to give the three $SU(2)$ bosons mass. This prescription came to be known as the Higgs mechanism. In the Standard Model, not only are the masses of the gauge bosons generated in this way, but also the masses of the fundamental fermions. (Their left-handedness, observed in the weak interactions, does not allow for the corresponding mass terms to be explicitly written in the Lagrangian without violating the local gauge symmetry.)

In 1967, Steven Weinberg [16] reinvented Glashow's $SU(2) \times U(1)$ theory and introduced the Higgs mechanism into it. There was no need to include the gauge invariance violating boson mass terms in the Lagrangian. The necessary gauge boson masses were induced by the spontaneously broken gauge symmetry of

the Higgs scalar field potential. A year later, the same approach independently was described by Salam [17] at a small, relatively insignificant, but impressively named congress held outside Göteborg, Sweden. Thus the unified theory of the weak and electromagnetic interactions was created, which nowadays is often referred to as the Glashow-Salam-Weinberg model. However, it took few more years for this model to become widely accepted. This happened only after Gerardus 't Hooft proved the renormalizability of the Glashow-Salam-Weinberg model with and without spontaneous symmetry breaking in his series of papers in 1971 [18]. About a decade later, in 1983, the theoretically predicted W^\pm and Z^0 gauge bosons were discovered by Carlo Rubbia's group in experiments at CERN's $p\bar{p}$ collider [19]. And the reason for not seeing the weak neutral currents in the experiments at the time when the electroweak theory was being developed, was first understood by Glashow, John Iliopoulos and Luciano Maiani [20]. They proposed a mechanism, today known as the GIM mechanism, which explained that the weak neutral currents were suppressed by destructive interference among the possible quark-lepton amplitudes. For this to happen they however needed "lepton-hadron" symmetry, and the existence of the fourth, charmed quark was thus predicted.

2.1.5 Quantum Chromodynamics

The first significant attempt to explain the nature of the strong force was the "mesotron" theory proposed by Hideki Yukawa in 1934. It suggested that protons and neutrons were bound inside the atomic nucleus by exchanging a relatively light but still massive meson, the Yukawa particle, as a result of which the force had a short range. A good candidate for the Yukawa particle was indeed discovered

in cosmic ray experiments carried out in 1937 and 1946 and came to be known as the “pion”. Later developments in the quantum theory of fields required any meaningful theory to be renormalizable, but the meson theories suffered from the so called “overlapping divergences”. In 1950, however, Abdus Salam proved that the theory of the strong force with spin zero particles could be renormalized to all orders. The Yukawa theory thus lasted until about 1951–52. Then the excited state of the nucleon, the so called delta, was discovered and the strange particles started to be found at about the same time. It was becoming clear that the mesotron theory was inadequate.

During the period from 1947 to 1960, with the first modern particle accelerators starting operation at the Berkeley and Brookhaven laboratories, hundreds of new particles were discovered, including mesons (light-weight) and baryons (heavy-weight). There was a real need for a taxonomic scheme to classify them based on their major characteristics. An inspiring example of the successful classification of the elements was known from Chemistry. In the 19th century, Dmitri Mendeleev had organized all known chemical elements in his periodic table, thereby predicting the existence of three new elements. Particle physicists started to make similar attempts: Fermi and Yang in the US, and physicists at Shoichi Sakata’s school in Japan. No one could find a way that would describe all known properties of the “particle zoo”. The first successful attempt was made by Murray Gell-Mann in 1961. He considered the symmetry group $SU(3)$ for his model. This group has eight generators, two of which can be thought of as a third component of the isotopic spin and the “hypercharge” (the sum of the strangeness and the baryon number of the particle). The other six generators change the values of the isotopic spin and the hypercharge, starting from one particle state with a given set of these quantum

numbers and going to another, with different isotopic spin and hypercharge. It turned out that the known particles could be nicely assigned to the octet and decuplet representations of this group, also making predictions for new particles needed to fill some of the empty spots. In a joking homage to the teaching of Buddha, Gell-Mann called his theory “The Eightfold Way” [21].

A similar picture was proposed by Yuval Ne’eman, who at the time was working with Salam. He had searched for symmetry groups that would incorporate strangeness and isotopic spin but would not introduce further complications. Having considered $SO(5)$, $SO(4)$, $Sp(4)$, $SU(3)$, and G_2 groups, he found out that the it was $SU(3)$ that had all the desirable properties and did not introduce the unwanted transitions. Although Gell-Mann’s and Ne’eman’s attempts were successful, they did not know the reason why such a classification worked. It was hard to understand why the simplest of the $SU(3)$ group representations, the so called fundamental **3** representation, was not to be used in this classification. Indeed, all the higher order representations could be built from the basic **3** representation; yet, no particles could be assigned to it.

It took several years until Gell-Mann 1964 [22] came up with the bold idea that the particles he was trying to classify were made up of even smaller constituents. Searching for a name for these new subparticles, Gell-Mann first called them “quork” to rhyme with *pork*. Later on, as he happened to be re-reading James Joyce’s *Finnegans Wake*, he came across the phrase: “Three quarks for Muster Mark”, and in his models it was three constituents that were making up protons and neutrons. Thus, and in a reaction against pretentious scientific language, he picked the name “quark” for his constituent particles [5]. At about

the same time, another Caltech theorist, George Zweig, then at CERN, came up with exactly the same idea of quarks, except he called them “aces”. Unfortunately, he never published his paper [23] as he resisted the laboratory regulations to publish it in a particular form in the laboratory journal, *Physics Letters* [5].

In Gell-Mann’s picture, the quarks had to have fractional electric charges, $2/3$ and $-1/3$ of that of the electron’s charge. This was already very hard to accept as the amount of the electron’s charge was thought to be the quantum of the electric charge. Also, the quarks had to somehow be bound forever inside hadrons, so as to explain why they had not been seen so far. On the good side, however, the three quarks (up, down, and strange), and their antiquarks, were the ones to form the **3** representation of $SU(3)$. The higher order representations of $SU(3)$, built from the fundamental **3**, accounted for all observed hadrons, and thus explained them as made up from triplets of quarks, along with quark-antiquark pairs comprising mesons.

There was another problem that had to be explained: the wavefunction symmetry of the Δ^{++} resonance, a hadron with a spin $3/2$. As a hadron, it was supposed to be made up of three quarks. Therefore, all three quarks had to have their spins aligned, and thus be in the same quantum state which was not allowed according to the Pauli exclusion principle. Strictly speaking, the exclusion principle was introduced for free particles, and it was not clear if it should also hold for the fermions tightly bound together by the strong force, as it was the case for the quarks. It still served as a motivation for Yoichiro Nambu to be first to introduce another quantum degree of freedom, later to be named *color* by Gell-Mann, and to assume that the quark of each flavor came in three states with different colors. In

this way, the three Δ^{++} quarks with aligned spins, could each still be in a different quantum state.

The fact that the protons and neutrons were composite particles was signaled by their anomalous magnetic moments, which were different from what could be expected from an elementary particle. As a point-like particle, such as the electron, the proton's magnetic moment, μ_p , should have been 1 in units of nuclear magneton (nM), while that of the neutron, μ_n , was supposed to be zero as it carried no electric charge to interact with the magnetic field. The experimental measurements indicated drastically different values, $\mu_p = 2.79$ nM and $\mu_n = -1.91$ nM [24]. Markedly, the absolute *deviations* of measured values of μ_p and μ_n from their expected structureless values were nearly equal in magnitude, 1.79 nM and 1.91 nM for proton and neutron respectively.

The direct experimental evidence of quarks came from deep inelastic electron-proton (ep) scattering experiment at SLAC¹. It indicated the existence of point-like, charged fermionic structure inside the nucleon. Based on current algebra, James Bjorken predicted the phenomenon of scaling, which was explained perhaps in a more intuitive manner by Richard Feynman based on his parton model. The assumption of the parton model was only that there was a substructure inside the proton of nearly free particles which Feynman called partons. This picture alone, without speculations about the dynamics of partons inside the hadron, could explain the experimentally observed Bjorken scaling.

It was in the fall of 1972 that Gell-Mann presented an almost complete picture of the theory of strong interactions at the conference celebrating Fermilab's

¹Stanford Linear Accelerator Center, Palo Alto, California.

opening. The quarks were fractionally charged fermions with an additional quantum number color, the same concept that Nambu had introduced earlier. Most importantly, unlike Nambu's picture, it was a theory with the gauge non-Abelian symmetry of $SU(3)$ group with some resemblance to the existing Yang–Mills theory. The quarks were bound inside hadrons and mesons by the color force and only the color-neutral states existed as stable particles. The mediators of the color force were eight colored gluons corresponding to the eight generators of the underlying $SU(3)$ gauge group. In an analogy with quantum electrodynamics, Gell-Mann christened this theory “Quantum Chromodynamics”, from the Greek word “chromos” for color.

To complete the picture, in 1974, Samuel Ting of Brookhaven and Burton Richter of SLAC observed a very heavy and long-lived meson they called J/ψ [25, 26], which was quickly realized to be the bound state of the charmed quark and antiquark. The existence of this fourth quark had been predicted earlier based on the GIM mechanism. Three years later, at Fermilab, a group lead by Leon Lederman discovered the Upsilon meson (Υ) [27], ten times heavier than the J/ψ , a $q\bar{q}$ bound state of the fifth quark, the b -quark. Finally, in 1995, the CDF [28] and DØ [29] collider experiments at the Fermilab Tevatron announced the discovery of the sixth quark, the top. And the overwhelming evidence of the existence of color came from e^+e^- experiments, where the ratio of the cross sections $R = \sigma(e^+e^- \rightarrow \text{hadrons})/\sigma(e^+e^- \rightarrow \mu^+\mu^-)$ was directly proportional to the number of colors N_c ($R = N_c \sum_{i=1}^{n_f} Q_i^2$), indicating that indeed $N_c = 3$.

In modern quantum field theoretic language, the strong interaction is described as a gauge field with the underlying *exact* symmetry of the color group

$SU(3)$, whose Lagrangian can be written in the following compact way:

$$\mathcal{L}_{QCD} = -\frac{1}{4}F_{\alpha}^{\mu\nu}F_{\alpha\mu\nu} - \sum_n \bar{q}_n \left[\gamma^{\lambda}\partial_{\lambda} - ig\gamma^{\lambda}A_{\alpha\lambda}t_{\alpha} + m \right] q_n, \quad (2.17)$$

where A_{α}^{μ} is the color gauge vector potential; $F_{\alpha}^{\mu\nu}$ is the color gauge-covariant field strength tensor; $g^2 = 4\pi\alpha_s$ is the strong coupling constant; t_{α} are a complete set of generators of color $SU(3)$ in the **3** representation (i.e. Hermitian traceless 3×3 matrices with rows and columns labeled by the three quark colors) normalized so that $\text{Tr}(t_{\alpha}t_{\beta}) = \frac{1}{2}\delta_{\alpha\beta}$; and the subscript n labels quark flavors with quark color indices suppressed. Thus QCD is similar to both QED and the theory of weak interactions in that it is also a quantum field theory with the local gauge symmetry. But, unlike the electroweak interactions, the symmetry of the color group $SU(3)$ is not broken and thus gluons are massless. Also, unlike photons, gluons can interact with each other: as a consequence of its non-Abelian nature, there are the three- and four-gluon vertices present in QCD the analog of which are absent in QED. The Feynman rules are similar to those of QED with additional complication and bookkeeping required for the color indices and combinatorial factors.

One of the remarkable features of QCD is that it turns out to be an asymptotically free gauge field theory meaning that the coupling gets weaker at shorter distance scales, or higher momenta (Q^2). In 1973 Gross and Wilczek [30] and Politzer [31] discovered that in non-Abelian gauge theories of Yang-Mills the coupling strength becomes weak with increasing energy. In QCD, the renormalization group equation (briefly discussed earlier) in the lowest order yields the following dependence of the coupling strength on the momentum scale Q [32]:

$$Q \frac{d}{dQ} g(Q) = -\frac{g^3(Q)}{4\pi^2} \left(\frac{11}{4} - \frac{n_f}{6} \right), \quad (2.18)$$

with n_f being the number of quark flavors. The solution of this differential equation is:

$$\alpha_s \equiv \frac{g^2(Q)}{4\pi} = \frac{12\pi}{(33 - 2n_f)\ln(Q^2/\Lambda^2)}. \quad (2.19)$$

Thus the strong coupling α_s decreases with increasing Q as long as there are no more than 16 quark flavors with masses below the energy scale of interest. Since there appear to be only six flavors of quarks, QCD is an asymptotically free theory. This convinced many physicists that QCD may indeed be the correct theory of the strong interactions as for the first time it allowed doing reliable perturbative calculations of strong interactions, at least at high energies. On the other hand, with the theory of electroweak interactions at hand, it was thought that the mediators of strong interactions should be very heavy bosons to explain why they had not been observed thus far; but unbroken $SU(3)$ gauge symmetry of the QCD suggested that gluons had to be massless. Asymptotic freedom once again came to rescue. The increase of α_s with high energy or short distance implies an increase at low energy or large distance. It was thus suggested as a possibility that at large distances only the color-neutral states can exist since the quarks and gluons will not be able to overcome the increasingly large potential as they are pulled apart to isolate them. This is a somewhat handwaving argument for explaining the color confinement of partons but, although still a hypothesis rather than a theorem, there appears to be little doubt that it is correct.

To summarize: with the exception of the gravitation, all other known particles and interactions appear to be described by the Standard Model, by which we mean the combined theory of Quantum Chromodynamics and the Glashow-Salam-Weinberg model of electroweak interactions. That is to say, down to distances

as small as 10^{-19} m, the correct theory of all known particles and interactions among them seems to be the quantum field theoretical model with the underlying composite local gauge symmetry group of $SU(3) \times SU(2) \times U(1)$, with the exact $SU(3)$ color symmetry of the strong interactions, and the spontaneously broken (down to $U(1)$ of QED) symmetry group $SU(2) \times U(1)$ for the unified electromagnetic and weak interactions.

2.2 Jet Cross Sections—A Test of the Standard Model

The unique feature of Quantum Chromodynamics is its asymptotic freedom: at high enough energies the strong coupling constant of QCD becomes small. As a result, hard scattering processes among quarks and gluons (often collectively called partons), can be calculated using the usual perturbative techniques of the quantum theories of fields. It therefore becomes very intriguing to subject such definitive predictions of perturbative QCD (pQCD) to experimental tests. However, another feature of QCD, the color confinement of partons within color-neutral particles, poses a nontrivial problem for the realization of such tests. If partons are not available in free, isolated states, how can one experimentally study their hard scattering? The answer to this question is as follows: by colliding high energy hadrons instead of ideally desirable, but physically unavailable, isolated partons. High energy hadron collisions will result in the scattering of their constituents, quarks and gluons, which can then be studied in an experiment. Ironically, this somewhat indirect method is at the same time the most direct method available today for experimental testing of pQCD.

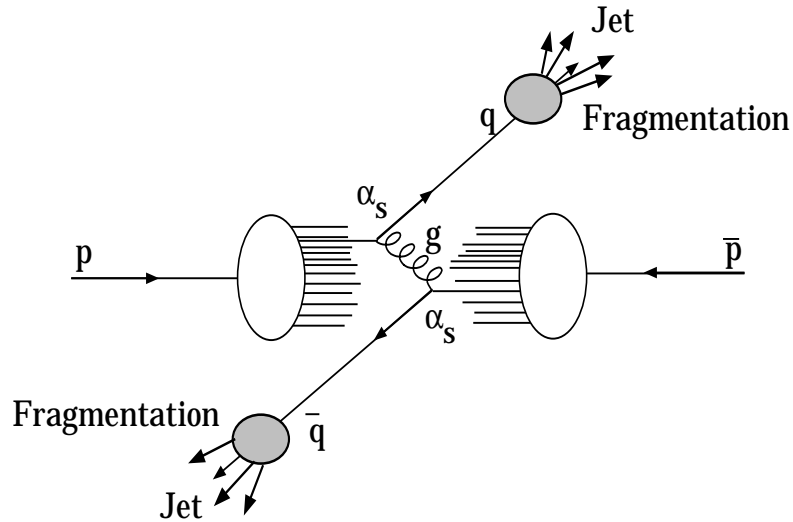


Figure 2.3: A cartoonist's view of jet production in $p\bar{p}$ collisions.

QCD predicts how the final state particles from such high energy hadron-hadron collisions will evolve from collisions of the constituents. Typically only two partons, one from each of the colliding hadrons, undergo the hard scattering. The other partons inside the colliding hadrons do not participate in the hard scattering, and are considered “spectator” partons which form the recoil system. The activity due to the spectator interactions is often referred to as the “underlying event” of the hard scattering. As the separation between the outgoing hard-scattered partons increases (along with that between them and the recoil system) the potential energy of the binding color force also increases trying to prevent partons from escaping into colored isolated states. At some point, as the distances grow, the coupling constant becomes so strong that perturbative methods no longer work, and one must change to large-distance non-perturbative QCD calculations. This latter is currently not very well understood despite impressive progress made in recent years.

In this phase of collisions, one can picture the effect of the non-Abelian gluon interaction causing the lines of color flux to contract into a thin tube, of high

energy density connecting the outgoing partons to each other and to the underlying event. Qualitatively, this picture predicts that the increasing potential energy of the interaction stored in the color field tube will start to materialize itself by emitting gluons which will split into quark-antiquarks pairs, giving rise to a parton cascade, or *shower*.

Partons of different colors in this shower can then form colorless combinations thereby allowing materialization into hadrons and/or mesons—the process known as “dressing of the quarks”, or fragmentation, or hadronization. The energy scale that sets apart the perturbative and non-perturbative QCD descriptions in the process of hard scattering is conventionally called the factorization or fragmentation scale μ_f . All the partons in the shower, as well as their final products of stable, color-neutral particles will have a strong boost in the direction of the original, hard-scattered primary parton. Therefore, in the final state, QCD predicts the appearance of highly collimated sprays of particles, or *jets*, as the manifestations of the hard-scattered partons. A graphical illustration of the process of jet production is shown in Figure 2.3 [33].

The production of the hadronic jets is indeed observed to be the dominant process in hadron–hadron collisions with a center-of-mass energies greater than about 10 GeV. Today, the highest energy hadron collisions in the world are realized at the Tevatron where 900 GeV beams of protons and antiprotons collide to unveil the underlying structure of protons, as well as to test the pQCD predictions for the parton hard scattering.

2.2.1 Description of Jet Production

At high energies, partons inside hadrons behave as nearly free particles. Therefore, highly energetic protons or antiprotons can be considered as a broadened beam of loosely bound partons—quarks, antiquarks, and gluons. The rates for the hard scattering phenomena of the partons are thus entirely determined by the rates of encounters of the partons from two such “beams”. It is this idea of nearly free partons inside an energetic hadron that is the foundation of the parton model, invented by Richard Feynman [34]. The useful kinematic variable turns out to be the fraction of the momentum of the hadron that the parton carries: $x = p_{\text{parton}}/p_{\text{particle}}$. It is often referred to as Bjorken x , after James Bjorken, the discoverer of the scaling laws for the structural form-factors when they are expressed in momentum fractions x . With the fractional incoming momenta of the two hard-scattering partons x_a and x_b , perturbative QCD can be used to calculate the amplitudes of the elementary processes in the momentum representation to a desired order in the QCD coupling strength α_s .

However, the x ’s of the partons are not known a priori. Instead, for a given hadron, the distributions of the momenta of various constituent partons, known as parton distribution functions, or PDF’s, can be measured and calculated. Then, the parton momenta can be integrated over all allowable values for a given hadron at a given energy, and fed into the pQCD matrix elements for the calculation of physical observables of the reactions. To summarize, there are two ingredients required for the calculation of the hadronic cross sections: the PDF’s and the pQCD matrix elements of the contributing elementary subprocesses. Integration over all partons of all momenta from the two hadrons then gives the cross section for the hadronic

process of interest, $a + b \rightarrow c + d$,

$$\sigma(ab \rightarrow cd) \sim \sum_{ij} \int \int dx_a dx_b f_{i/a}(x_a) f_{j/b}(x_b) \hat{\sigma}(ij \rightarrow kl). \quad (2.20)$$

Here, $f_{i/a}$ is the probability of finding constituent i inside particle a with a momentum fraction x_a , and $\hat{\sigma}(ij \rightarrow kl)$ is the cross section of the elementary process leading to the desired final state, cd . In a more formal treatment, such a decomposition into the elementary cross sections and PDF's is supported by the so called factorization theorem, which thereby introduces the factorization momentum scale μ_f which has to be specified when doing direct theoretical pQCD calculations. This expression for the hadronic cross section in the spirit of pQCD and parton model has certainly to be complemented by the non-pQCD description of hadronization giving the evolution of the elementary final states kl into the hadronic final state cd .

We will next briefly discuss proton PDF's and pQCD elementary processes' matrix elements, and then will apply all the ideas of the parton model to write down various jet production cross sections.

The Parton Distribution Functions

The parton distribution functions cannot generally be calculated from the first principles. At a given scale of the momentum transfer Q^2 , however, the PDF's can be measured in deep inelastic (DIS) lepton-hadron scattering reactions. Indeed, the partons were first observed in the DIS processes $ep \rightarrow eX$ at SLAC, the study of which has been continued at higher energies at the HERA Collider in Hamburg, Germany, by the two collider experiments, H1 and ZEUS. According to the parton model, the proton is made up of two up quarks and one down quark, which carry the

flavor quantum numbers of the proton, and are called the “valence quarks”. Many gluons are also present inside the proton. Finally, there are also all other flavors of quarks and antiquarks present inside the proton forming the Dirac sea, and hence are referred to as the sea partons. These sea quarks result from processes such as gluons splitting to virtual quark pairs, which most often reabsorb (analogous to e^+e^- pairs fluctuating in the Coulomb field of hydrogen).

The momentum distribution (PDF) of the valence u quark, for example, can conveniently be denoted by $u_v(x)$, where x is the usual Bjorken variable. The corresponding sea distribution can be written as $u_s(x)$, and the total distribution of the up quark is given by their sum: $u(x) = u_v(x) + u_s(x)$. The corresponding antiquark and other parton distributions can then be denoted according to this scheme. The composition of the proton thus is postulated by requiring that the u_v and d_v distributions satisfy the following sum rules:

$$\int_0^1 dx u_v(x) = 2 \quad \text{and} \quad \int_0^1 dx d_v(x) = 1. \quad (2.21)$$

The quark distributions are empirically determined from the data on electron and neutrino DIS processes in the Q^2 range $5 < Q^2 < 800 \text{ GeV}^2$. The three light quarks, u , d , and s dominate the composition of the proton making the contributions from the heavier quarks negligible when calculating many cross sections. The comparison of the DIS cross sections from muon and neutrino scattering shows the total momentum fraction of the proton carried by the quarks and antiquarks to be:

$$\int_0^1 dx x [u(x) + \bar{u}(x) + d(x) + \bar{d}(x) + s(x) + \bar{s}(x)] \approx 0.5. \quad (2.22)$$

Since the contributions from the heavier quarks are small, this result implies that the other 50% of the momentum is carried by the gluons. The gluon distribution

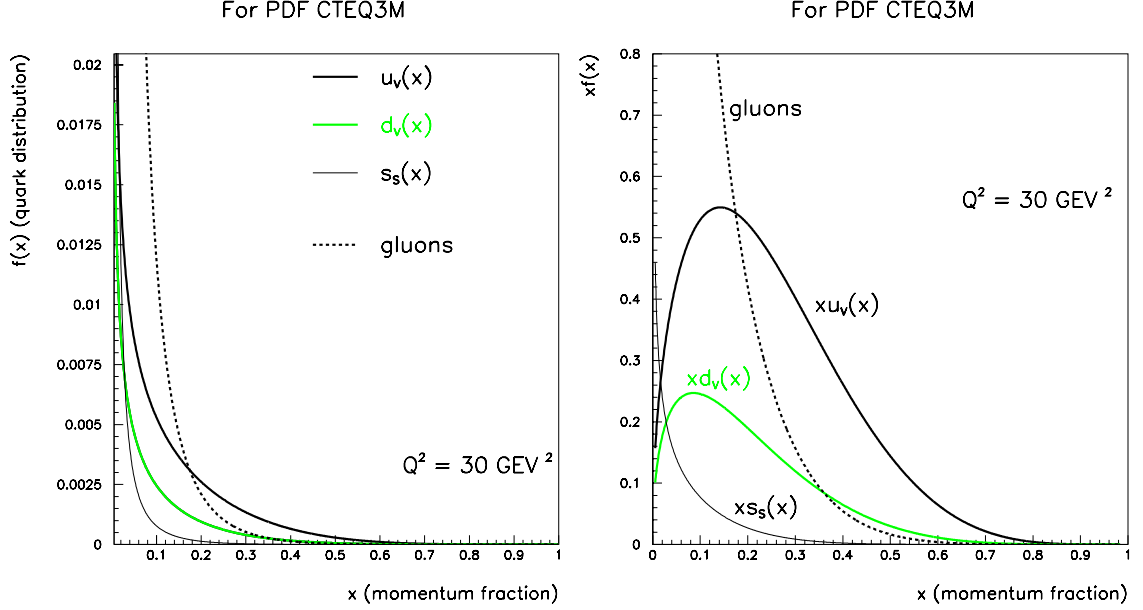


Figure 2.4: The CTEQ3M family of PDF's of the light quarks and gluons inside proton at $Q^2 = 30 \text{ GeV}$. The left plot shows PDF's themselves, while the right plot illustrates Bjorken x weighted PDF's to better highlight the differences among them.

functions can experimentally be obtained from processes such as $pp \rightarrow \gamma + X$ and $pp \rightarrow \psi X$, or by considering the higher order QCD processes in which virtual gluons contribute to DIS. Although it is difficult to measure “soft gluon” distributions, which are currently the most poorly known PDF's for the proton, the current parameterizations suggest that the gluon contribution is dominant at the lower Bjorken x values.

As an illustrative example, the left plot in Figure 2.4 shows the PDF's of the three light quarks and gluons inside the proton at $Q^2 = 30 \text{ GeV}^2$. In order to highlight the differences among the PDF's, the right plot in the same Figure shows the same PDF's at the same Q^2 scale but weighted by the Bjorken x , i.e. $x \cdot f(x)$, which has become a traditional way for presenting these distribution functions. Dealing with $x \cdot f(x)$ is also preferred from the point of view of the theoretical or

phenomenological applications, as it improves numerical convergence in the neighborhood of $x = 0$. It is seen that, inside the proton, gluons dominate at low x values but quark contributions overtake at high x 's.

In the most primitive formulation of the parton model, the PDF's satisfy Bjorken scaling, i.e. do not depend on the scale Q^2 . The QCD-improved parton model allows the consideration of gluon emission by a parton, the probability of which increases with the energy of the parton. This complicates things, as it will cause the depletion in the probability of finding a quark at high x . Thus, generally speaking, the Bjorken scaling is violated. The dependence of the PDF's on the scale Q^2 , or their *evolution*, is described by Dokshitzer-Gribov-Lipatov-Altarelli-Parisi (DGLAP) equations [35]. It was experimentally determined that the distribution functions increase with increasing Q^2 below $x \approx 0.2$ and decrease above that threshold. Since the PDF's can experimentally be measured only at a finite number of Q^2 values, the DGLAP evolution equations provide extrapolation to the PDF's to any desired scale, which is necessary for continuous perturbative cross section calculations.

As a final word on the PDF's, it should be mentioned that there are various groups of physicists who use different methods for obtaining the parameterizations by using different experimental results, fitting methods, and theoretical or phenomenological schemes. We will concentrate on the most widely used PDF sets by the CTEQ [36] and the MRST [37] collaborations.

The Contributing Elementary Subprocesses

The other ingredient needed to calculate the hadronic cross section is the invariant

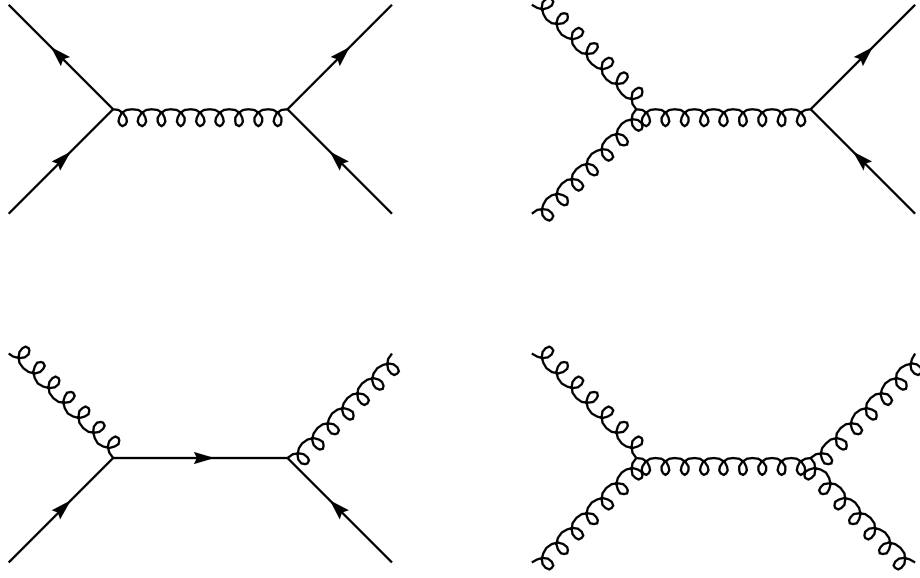


Figure 2.5: Some of the QCD $2 \rightarrow 2$ processes contributing to the order α_s^2 .

amplitudes, or matrix elements \mathcal{M} for all the contributing elementary subprocesses. The elementary subprocess in $p\bar{p}$ collisions is the scattering of all possible combinations of the partons. In tree order, or, in the language of the coupling constant, order α^2 , these are $2 \rightarrow 2$ processes. Some examples of the associated leading-order Feynman diagrams are shown in Figure 2.5. The cross sections of the processes are given by the product of the invariant matrix element and the available final state phase space. Table 2.1 summarizes all the possible QCD $2 \rightarrow 2$ processes and also shows their invariant matrix elements squared calculated to the order α^2 in terms of the usual kinematic Mandelstam variables [38], and for the general scattering process $p_a + p_b \rightarrow p_1 + \dots + p_n$, the expression for the Lorentz invariant phase space is:

$$d\text{Lips} = (2\pi)^4 \delta^4(p_a + p_b - \sum p_i) \prod_i^n \frac{d^3 p_i}{(2\pi)^3 2E_i}. \quad (2.23)$$

In the order α_s^3 , the third jet may be initiated as a result of the gluon bremsstrahlung from either incoming parton lines (*initial state radiation*) or the outgoing, scattered

Subprocess	$ M ^2/16\pi^2\alpha_s^2$	$ M(90^\circ) ^2/16\pi^2\alpha_s^2$
$qq' \rightarrow qq'$	$\frac{4}{9} \frac{\hat{s}^2 + \hat{u}^2}{\hat{t}^2}$	2.2
$q\bar{q}' \rightarrow q\bar{q}'$		
$qq \rightarrow qq$	$\frac{4}{9} \left(\frac{\hat{s}^2 + \hat{u}^2}{\hat{t}^2} + \frac{\hat{s}^2 + \hat{t}^2}{\hat{u}^2} \right) - \frac{8}{27} \frac{\hat{s}^2}{\hat{u}\hat{t}}$	3.3
$q\bar{q} \rightarrow q'\bar{q}'$	$\frac{4}{9} \frac{\hat{t}^2 + \hat{u}^2}{\hat{s}^2}$	0.2
$q\bar{q} \rightarrow q\bar{q}$	$\frac{4}{9} \left(\frac{\hat{s}^2 + \hat{u}^2}{\hat{t}^2} + \frac{\hat{t}^2 + \hat{u}^2}{\hat{s}^2} \right) - \frac{8}{27} \frac{\hat{u}^2}{\hat{s}\hat{t}}$	2.6
$q\bar{q} \rightarrow gg$	$\frac{32}{27} \frac{\hat{u}^2 + \hat{t}^2}{\hat{u}\hat{t}} - \frac{8}{3} \frac{\hat{u}^2 + \hat{t}^2}{\hat{s}^2}$	1.0
$gg \rightarrow q\bar{q}$	$\frac{1}{6} \frac{\hat{u}^2 + \hat{t}^2}{\hat{u}\hat{t}} - \frac{3}{8} \frac{\hat{u}^2 + \hat{t}^2}{\hat{s}^2}$	0.1
$qg \rightarrow qg$	$\frac{\hat{s}^2 + \hat{u}^2}{\hat{t}^2} - \frac{4}{9} \frac{\hat{s}^2 + \hat{u}^2}{\hat{u}\hat{s}}$	6.1
$gg \rightarrow gg$	$\frac{9}{4} \left(\frac{\hat{s}^2 + \hat{u}^2}{\hat{t}^2} + \frac{\hat{s}^2 + \hat{t}^2}{\hat{u}^2} + \frac{\hat{u}^2 + \hat{t}^2}{\hat{s}^2} + 3 \right)$	30.4

Table 2.1: All possible $2 \rightarrow 2$ QCD subprocesses and their invariant amplitudes (q and q' denote different quark flavors).

lines, (*final state radiation*). Examples of Feynman diagrams which describe $2 \rightarrow 3$ subprocesses are shown in Figure 2.6.

Jet Kinematics

In order for the kinematic variables to accurately represent those of the partons, the particles inside the jet must all be summed to give global jet quantities, such as energy and momentum. Although high energy hadron–hadron collisions at symmetric colliders occur in their center-of-mass (CM) frame, the constituent partons

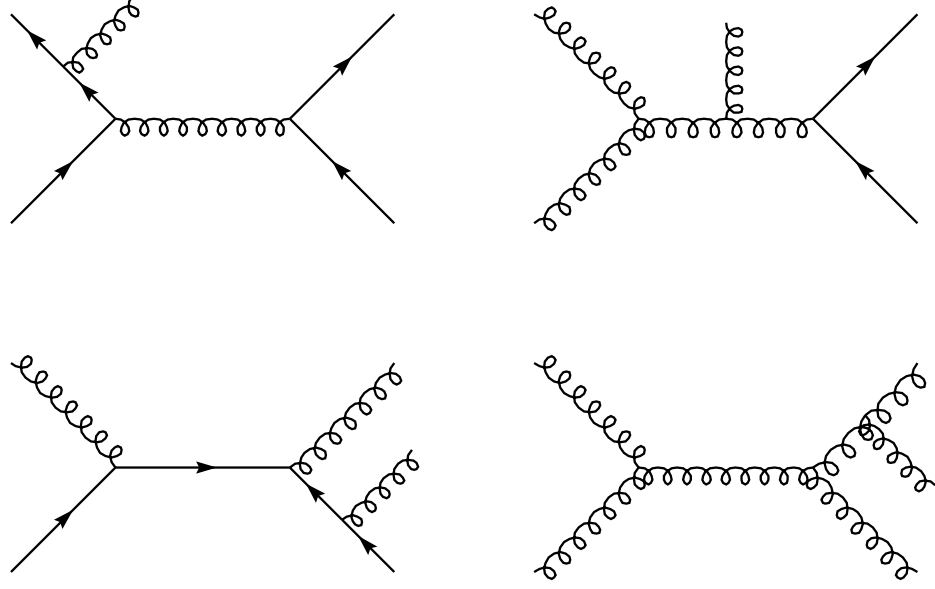


Figure 2.6: Some of the QCD $2 \rightarrow 3$ processes contributing to the order α_s^3 .

undergoing hard interaction are not usually in their CM frame, as they may carry different fractions of the incoming parent hadron's momentum. As a result, the final state emerging from parton-parton scattering is generally boosted along the direction of the colliding hadrons. But motivated to optimize the detection and reconstruction of the jets in the final state, it is desirable to use a set of explicitly Lorentz invariant variables for jet kinematics. The usual choice of these variables is: jet transverse momentum (p_T), azimuthal angle (φ), rapidity (y), and mass (m). The rapidity is defined as:

$$y = \frac{1}{2} \ln \frac{E + p_z}{E - p_z} = \tanh^{-1} \left(\frac{p_z}{E} \right) \quad (2.24)$$

and under a Lorentz boost along the direction of the colliding particles (usually chosen as a direction of the z axis) to a frame with velocity β , it transforms in a simple way: $y \rightarrow y - \tanh^{-1} \beta$, yielding a boost-independent distribution dN/dy . In the limit of high energies, when the mass of the jet can be neglected, the rapidity

is reduced to a more convenient pseudorapidity η which can be written in terms of the polar angle θ :

$$\eta = -\ln \left[\tan \left(\frac{\theta}{2} \right) \right]. \quad (2.25)$$

In the experiment, the directly measured jet quantities are energy (E), pseudorapidity, and azimuth. The transverse momentum of a jet is then calculated as

$$p_T = E/\sin\theta = E\cosh\eta. \quad (2.26)$$

Jet Cross Sections

With all the necessary ingredients at hand, we now are in a position to write down the various jet cross sections resulting from $p\bar{p}$ collisions. The total cross section for two jet, or *dijet*, production is given by:

$$\sigma(p\bar{p} \rightarrow 2jets) = \sum_{ijkl} \int \int dx_p dx_{\bar{p}} f_{i/p}(x_p) f_{j/\bar{p}}(x_{\bar{p}}) \hat{\sigma}(ij \rightarrow kl), \quad (2.27)$$

where the sum runs over all partons, the $2 \rightarrow 2$ elementary subprocesses $\hat{\sigma}$ are calculated in pQCD, $f(x)$ are the corresponding PDF's, and the integration is over all parton momenta. Figure 2.7 is a picture of a real dijet event observed and measured with the DØ detector.

The next-to-leading order parton-parton hard scattering allows for gluon bremsstrahlung in the initial or the final state of the incoming partons. Such events may result in a three jet final state which can be described in the analogous way:

$$\sigma(p\bar{p} \rightarrow 3jets) = \sum_{ijklm} \int \int dx_p dx_{\bar{p}} f_{i/p}(x_p) f_{j/\bar{p}}(x_{\bar{p}}) \hat{\sigma}(ij \rightarrow klm). \quad (2.28)$$

A real three jet event observed by the DØ detector is shown in Figure 2.8.

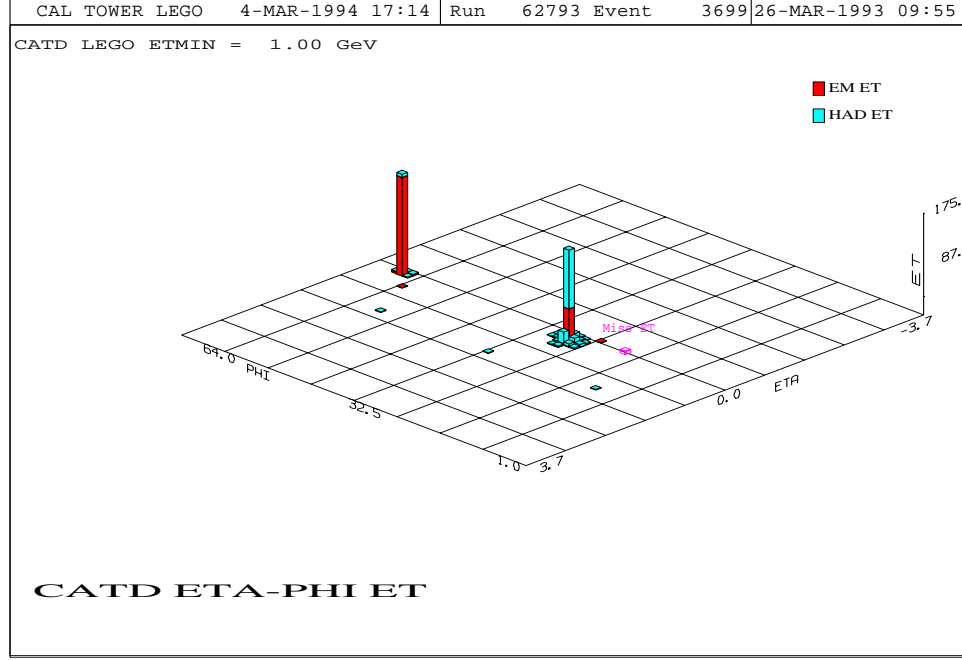


Figure 2.7: A lego $\eta - \varphi$ plot of the real dijet event in the DØ calorimeter.

2.2.2 The Single Inclusive Jet Cross Section

The experimental determination of the inclusive jet cross section in $p\bar{p}$ collisions,

$$p\bar{p} \rightarrow jet + \text{anything} , \quad (2.29)$$

is the most direct test of perturbative QCD and thus of the Standard Model. In the framework of the parton model, the *total* cross section for this reaction is given by:

$$\sigma(p\bar{p} \rightarrow jet + X) = \sum_{ijk} \int \int dx_p dx_{\bar{p}} f_{i/p}(x_p) f_{j/\bar{p}}(x_{\bar{p}}) \hat{\sigma}(ij \rightarrow k + X) , \quad (2.30)$$

where X stands for any number and type of objects, including jets, that could emerge in the final state along with the scattered parton k . Therefore, it is clear that by measuring this cross section experimentally, not only pQCD predictions are tested, but also the structure of the proton, i.e. the parton PDF's. The Fermilab

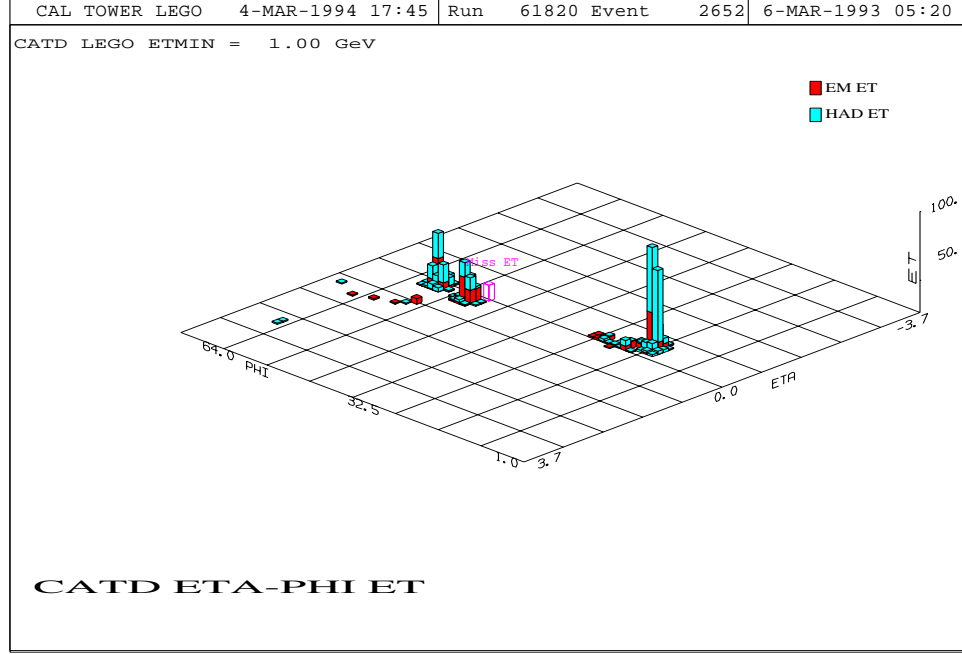


Figure 2.8: A three-jet event observed in the DØ calorimeter.

Tevatron provides the arena for carrying out measurements of a large variety of physics processes involving jets. Recently, the next-to-leading order (NLO) theoretical calculation of the inclusive jet cross section have become available, which add particular interest to this measurement at the Tevatron.

It is, however, nearly impossible to measure the total jet cross section in the experiment. Despite the very good solid angle coverage of the DØ detector, substantial energy escapes undetectable at small angles through the Tevatron beam pipe itself ($|\eta| > 4.7$). Moreover, due to trigger and reconstruction inefficiencies, it is practically impossible to accurately determine the dominating lowest E_T spectrum of the cross section. On the other hand, the determination of the *differential* cross sections is possible in the finite intervals of E_T and pseudorapidity η (above approximately $E_T = 10$ GeV and for $|\eta| < 4.7$). The double differential inclusive

jet cross section, measured with the DØ detector, thus, is defined as:

$$\frac{d^2\sigma}{dE_T d\eta} (p\bar{p} \rightarrow jet + X). \quad (2.31)$$

The measurement is then compared to next-to-leading order theoretical predictions in the wide kinematic range.

To reiterate, in this measurement we test only the perturbative predictions of the QCD that describe parton-parton hard scattering. The theoretical calculations are today available in next-to-leading order, or α_s^3 in QCD coupling strength. They are based on the jet definition at the parton level. Because of the finite, large angular size of the jet (at DØ a fixed cone size of 0.7 is used in $\eta - \varphi$ space to define a jet), non-perturbative processes governing the hadronization and associated fluctuations are not important for any practical purposes.

Some detailed systematic studies in the course of this analysis requiring more fundamental understanding of the jet structure are aided by available Monte Carlo programs, such as HERWIG [39] or PYTHIA [40] which implement several different hadronization schemes. Usually it is found that the results of the measurement reported here are independent of such large scale QCD behavior. Some of the relevant details of the NLO theoretical pQCD calculations to which data are compared will be discussed in the corresponding chapter.

Parton Compositeness

Another question that the measurement of the inclusive jet cross section may help to answer is whether or not the partons themselves are composite particles. It is theoretically possible that quarks and gluons have a substructure governed by some new kind of strong interactions at an energy scale Λ_c much larger than the

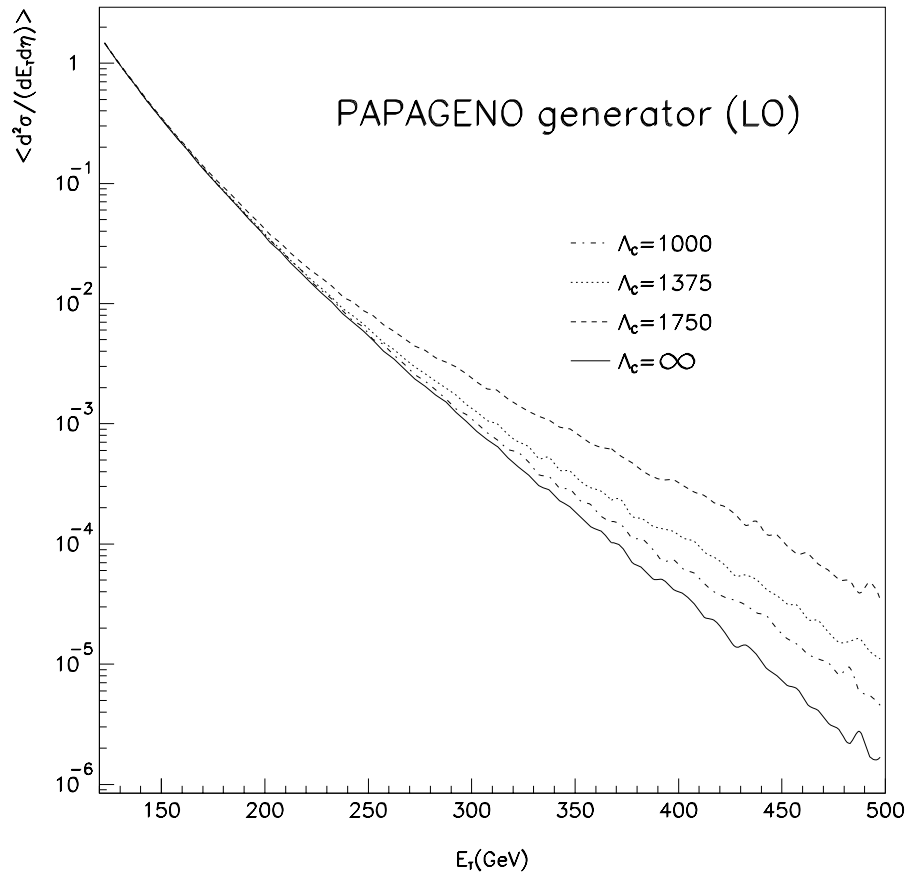


Figure 2.9: Inclusive differential jet cross section ($|\eta| < 0.9$) using the PAPAGENO leading order generator with different values of Λ_c , as indicated.

characteristic scale Λ of QCD. In much the same way as the gauge symmetry of QCD traps quarks and gluons inside hadrons and mesons, there might be some other interaction that would bind together more fundamental fermions, or preons, inside quarks and gluons. This theory would have to be an asymptotically free theory with massless gauge carriers. Otherwise, to bind preons at such small distances, the gauge bosons must be extremely heavy and they would have already been seen in high energy experiments.

At low energies, $E \ll \Lambda$, such an underlying theory can effectively be described by higher order interaction terms, such as $\bar{\psi}\psi\bar{\psi}\psi$. Although clearly unrenormalizable, inclusion of these terms into standard QCD Lagrangian is still allowable, with the realization that they describe an *effective* theory. For instance, one such candidate was proposed in reference [41]:

$$\mathcal{L} = \pm \frac{1}{2\Lambda_c^2} (\bar{u}_L \gamma^\mu u_L + \bar{d}_L \gamma^\mu d_L) (\bar{u}_L \gamma_\mu u_L + \bar{d}_L \gamma_\mu d_L) .$$

The addition of such terms leads to deviations from the expected pQCD behavior at energy scales nearing the characteristic energy scale of the underlying interactions Λ_c . Figure 2.9 shows leading-order predictions of the inclusive jet cross section using PAPAGENO, a Monte Carlo generator which includes the compositeness contact term. Appearance of the rise in the cross section at highest E_T is clear, and, as expected, the deviations from pQCD predictions (corresponding to $\Lambda_c = \infty$ in this Figure) start to appear at lower values of E_T as the value of compositeness scale Λ_c is reduced.

Therefore, the precise measurement of the jet cross section can be used to determine whether or not there is any substructure at the energy scales currently accessible to us. This, of course, is a continuation of the ideas originated in the famous Rutherford scattering experiments of energetic α particles scattering in a gold foil. The excess in the number of deflected α particles at high angles indicated the substructure of the atom. Unfortunately, in jet cross sections, the appearance of the same signature may be due to experimental and/or theoretical uncertainties, e.g. poorly determined PDF's in certain kinematic regions, as they too are experimentally measured with varying degree of accuracy in different areas of the phase space. This makes searches for parton substructure even more challenging.

CHAPTER 3

THE EXPERIMENT

Senator Pastore: *“Is there anything connected with the hopes of this accelerator that in any way involves the security of the country?”*

Dr. Wilson: *“No sir, I do not believe so.” ...*

Senator Pastore: *“It has no value in that respect?”*

Dr. Wilson: *“It has only to do with the respect with which we regard one another, the dignity of men, our love of culture... It has to do with, are we good painters, good sculptors, great poets? ... It has nothing to do directly with defending our country except to make it worth defending.” [42]*

Particle colliders, today the biggest pieces of scientific equipment in the world, have become a well established tool in high energy experimental physics primarily because they can reach the highest collision energies. At the highest energies in the center-of-mass (CM) frame of reference of the colliding particles, experiments are able to probe the smallest distances possible in order to reveal the laws of physics governing the behavior of fundamental constituents of matter. How deep one can probe matter by particle scattering is limited by the de Broglie wavelength $\lambda \sim 1/q$, q being momentum transferred between the two colliding particles. In addition, the highest possible CM energies cross thresholds for the production of the heaviest of the particles, and allow the study of their previously unexplored fundamental properties. Based on the widely accepted big-bang cosmological model of our universe, we now believe that very high energy collisions naturally occurred in the very early moments of the universe. High energy collisions continue to take place in cosmic

ray interactions with matter (as, for instance, in the earth's atmosphere) providing us with useful information. However, the precision of measurements obtainable from these sources is not of comparable quality to that from controlled experiment's setup at colliders which allows systematic experimentation. The complexity of extracting laws of physics from collider experiments can be illustratively compared to trying to understand the precise mechanism of the operation of Swiss watches by smashing them against each other and analyzing the resulting debris.

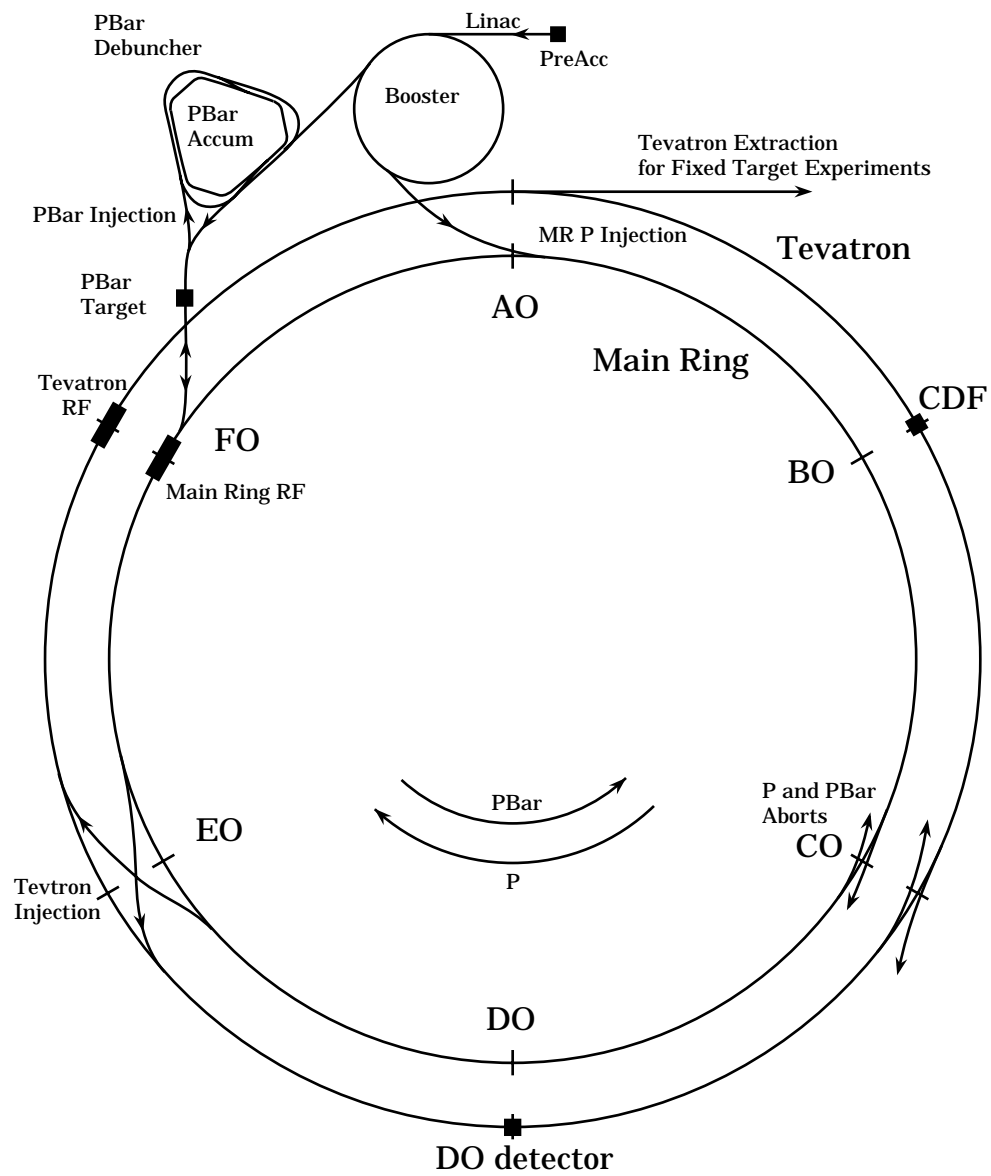
There are two basic ways to create high energy collisions, each with its relative advantages and disadvantages. One way is to direct a beam of energetic particles onto a stationary target (so called a “fixed target” experiment). Another way is to collide particles head-on from two beams moving in opposite directions (collider experiments). The biggest advantage of the collider experiments is that the energy in the CM system increases linearly with the beam energy (assuming the energies of the two colliding beams increase together), while in the fixed target experiments it increases only with the square root of the beam energy. The disadvantage of colliding beam experiments is low event rates, or luminosity \mathcal{L} , generally defined as the product of incident beam flux (particles per second) with mean target density (particle per unit area). Since the cross sections σ of many important non-strong physics processes are small, very high luminosities are needed to give corresponding event rates ($\mathcal{L} \cdot \sigma$) high enough to yield statistically significant data samples. In fixed target experiments, the event rates can be increased more easily by selecting high density target materials and by using long targets. In collider experiments, on the other hand, high event rates are achieved by pinching down the beams to very small size at the crossing points and also (in circular colliders) by circulating the beams to get multiple crossings. In addition, storing particles

in circulating beams poses its own limitations. For example, colliders are limited to beams of charged and stable particles: e^\pm , p , and \bar{p} . These and many other practical difficulties associated with the creation of colliding beams have been successfully overcome. Since the mid 1970's colliders have been a primary tool for studying physics at the energy frontier.

3.1 The Fermilab Accelerators

The Enrico Fermi National Accelerator Laboratory (Fermilab), located about 30 miles west of the “windy city”, Chicago, currently houses the world’s highest center-of-mass (CM) energy proton–antiproton ($p\bar{p}$) colliding beam accelerator, the Tevatron, which started its operation in mid 1980s. It achieved previously unprecedented energies of 1.8 TeV in the CM of colliding particles, and thereby opened a new frontier in high energy physics research. Acceleration of protons and antiprotons to high energies is achieved via a multi-step process employing several distinct accelerators and/or storage rings for different energy ranges. Figure 3.1 schematically shows the entire Fermilab accelerator complex. The Tevatron itself is the last accelerator in this chain. This section describes the basic steps in the acceleration process at Fermilab, as a more detailed discussion lies outside of the scope of this manuscript and can be found elsewhere [43].

The proton beam begins life in the preaccelerator which consists of the magnetron surface-plasma source housed in an electrically charged dome. The magnetron source converts regular hydrogen gas (H_2) to ionized hydrogen gas (H^-). The H^- ions are then allowed to accelerate from the charged dome to the grounded wall through a column across the high accelerating voltage provided by a commercial



Cockroft–Walton generator, a solid state device, that generates high voltage by charging capacitors in parallel and discharging them in series. With five stages of voltage multiplication, the generator boosts the input voltage of 75 kV by a factor of ten, with very little variation. As a result, H^- ions are accelerated to an energy of 750 keV, and they next enter the linear accelerator (Linac). The Linac consists of 14 cylindrical accelerating tanks or cavities arranged colinearly with a total length of approximately 150 m. The H^- ions emerge from the Linac with an energy of 400 MeV and drift an additional 46 m before injection into the Booster, the first circular accelerator, or synchrotron, in the acceleration chain.

Upon entering the Booster, the H^- ions pass through a carbon foil which strips the electrons from the ions, leaving only the proton core. The Booster consists of a series of magnets arranged in a 75 m radius circle, with 17 radio frequency (RF) cavities interspersed, accelerating protons to an energy of 8 GeV. The accelerated proton beam from the Booster can be directed to four different locations depending on the need. These four locations are: the Main Ring (via the 8 GeV line), the 8 GeV line dump (a depository for unneeded beam), the Long 3 dump, and the AP4 line which leads to the antiproton source.

The Main Ring (MR) is a synchrotron 1 km in radius that consists of 1000 conventional copper-coil iron yoke magnets which continually bend and focus the protons. The MR is divided into 6 sections, or sectors, labeled A through F. It has 18 accelerating cavities located at the beginning of the sixth sector (F sector). The MR can accelerate protons from 8 GeV to either 120 or 150 GeV, depending on their next destination. In addition to accepting protons from the Booster, the MR can also accept antiprotons from the antiproton source at 8 GeV and accelerate

them to 150 GeV. Once the proton or antiproton beam in the MR is accelerated to 150 GeV, it can be injected into the Tevatron. The proton beam accelerated to 120 GeV can be sent to the antiproton source.

The antiproton beam is produced in a multi-stage process starting in the MR and involving several different machines. Production starts when a proton bunch is extracted from the Main Ring at 120 GeV. The bunch is directed onto a tungsten target producing \bar{p} 's with wide momentum spread. A strong focusing magnet, the lithium lens, selects \bar{p} 's with a momentum spread of 3% around 8.9 GeV. Then, the \bar{p} 's are injected into a small synchrotron, called the Debuncher, where they circulate for 2 sec while the momentum spread is reduced and transverse betatron emittance is reduced via stochastic cooling [44]. This cooling process is then continued in the accumulator, a storage ring where the \bar{p} 's are accumulated for several hours (stacking) until there are enough of them to transfer to the Main Ring. When that happens, six bunches of \bar{p} 's are extracted from the core of the beam where the energy spread is only 0.05%. Then, they are injected into the Main Ring where they are accelerated to 150 GeV.

In the final stage of the acceleration process, the 150 GeV protons or antiprotons are injected into the Tevatron from the MR. The Tevatron, designed with the constraint of fitting within the existing MR beam tunnel, has the same basic layout and shares the same radiation enclosure as the MR, and is located 65 cm directly below the MR magnets. Such small vertical separation between the Tevatron and the MR would create difficulties for the collider detectors placed at interaction regions of the Tevatron. Each detector would have to have a hole for the MR and also suffer from the losses of the MR protons or antiprotons from time

to time, further complicating the physics analysis. To avoid this, an “overpass” was built for the MR at the interaction region BØ to bypass the CDF (Collider Detector at Fermilab) detector to be placed at that location. This required a major reconstruction of the beam tunnel and separation of 19 feet was achieved. However, the prototype of this overpass was first built at the interaction point DØ but with a separation of only about 89 inches to fit inside the existing tunnel, as there was no second collider detector at that time. As a result of the design of the DØ overpass, the current DØ detector is perforated by the MR pipe.

The Tevatron is the third synchrotron and consists of 1,000 superconducting magnets. To maintain their operating temperature of 4.3 K, the Tevatron is cryogenically cooled by immersing the coils in liquid helium. There are 8 RF cavity accelerating sections in the Tevatron ring. The Tevatron can accept both protons and antiprotons from the MR. Fermilab generally operated the Tevatron with six bunches of protons and antiprotons rotating in the opposite directions. A radio frequency process called cogging is used to adjust the 12 intersection points so that a bunch crossing occurs at each intersection region every $3.5 \mu\text{s}$. Then, all bunches are accelerated to 900 GeV to provide a CM energy of 1.8 TeV.

The instantaneous luminosity, \mathcal{L} , is a measure of the interaction rate. It is given by:

$$\mathcal{L} = \frac{f N_b N_p N_{\bar{p}}}{4\pi\sigma^2}$$

where f is the crossing frequency, N_b the number of bunches, N_p , $N_{\bar{p}}$ the number of p 's and \bar{p} 's and $\pi\sigma^2$ the area or section of the beam. One way to increase the instantaneous luminosity at the collision point is to reduce the transverse beam size

in that region. This is achieved by specially designed strong quadrupole magnets placed on either side of the interaction point to reduce the beam (transverse) spot size to approximately $40\ \mu\text{m}$.

3.2 Overview of the DØ Detector

The DØ detector is a large, multipurpose apparatus designed and constructed to study proton–antiproton collisions in the center-of-mass energy of 2 TeV. Its name derives from its location in the Fermilab Tevatron ring, being operated at one of the six interaction regions, identified as DØ. The first data taking period, or a *run*, with the DØ detector started in August 1992 and lasted through May 1993. The following run started shortly thereafter, in December 1993, and continued through July 1995. These two runs at the $p\bar{p}$ CM energy of 1.8 TeV are collectively referred to as Run 1 for the DØ experiment. To distinguish between the two data sets collected during the first and second periods of Run 1, they are often referred to as Run 1A and Run 1B, respectively. The analysis presented here is based on the Run 1B data sample.

The DØ detector is built to cover a wide spectrum of physics topics by providing accurate measurements to test the Standard Model predictions and to search for new phenomena. This includes, but is not limited to, the search for the top quark, various jet and photon cross section measurements, b -quark production, and the studies of W and Z bosons. Designed to be somewhat complementary to the other, already existing collider detector at the Tevatron, CDF, the emphasis in the DØ detector is on excellent calorimetry. Good measurement of high transverse momentum parton jets by means of finely segmented, hermetic, linear, and

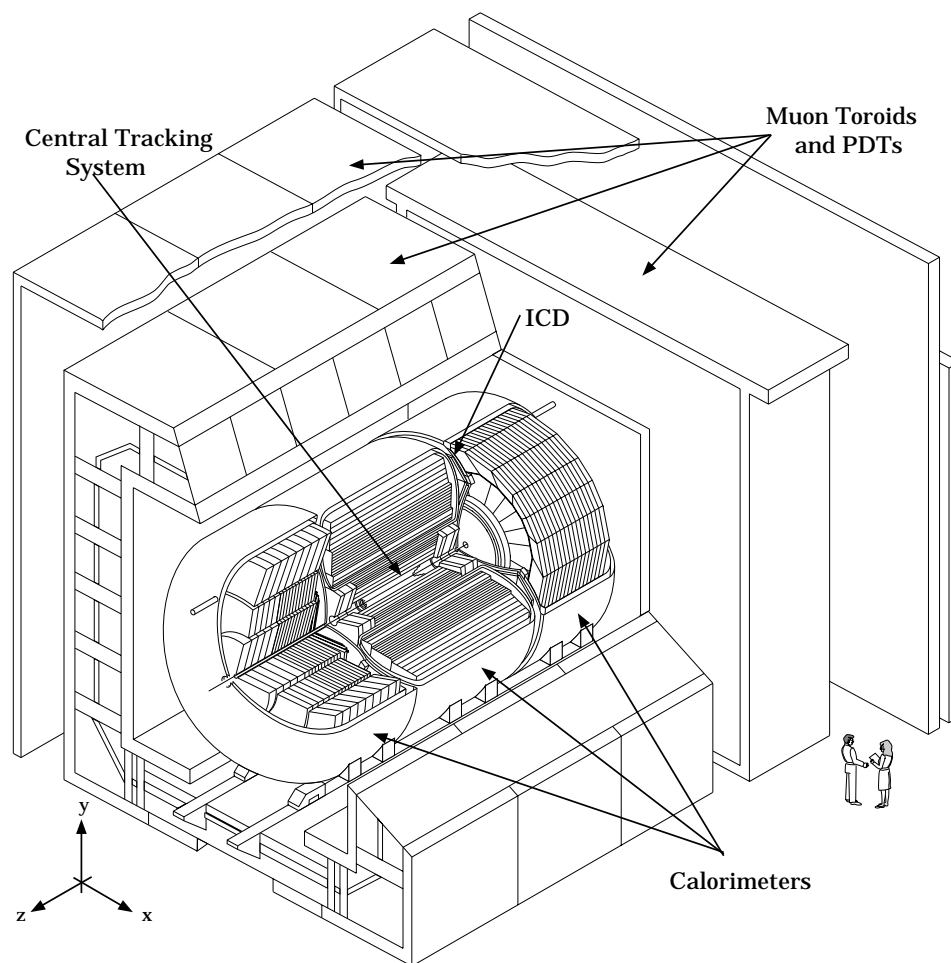


Figure 3.2: A cutaway isometric view of the Run 1 DØ detector.

nearly compensating calorimeters, precise determination of the missing transverse energy (\cancel{E}_T) in the calorimeters as a way of detecting neutrinos and possibly other non-interacting particles, and excellent identification of electrons and muons are the strengths of the DØ detector. In Run 1, little emphasis has been placed on identifying and tracking individual particles within jets, as the details of hadronization are not relevant to the underlying hard scattering. As a result, there was no central tracking magnetic field in DØ Run 1.

In preparation for the Tevatron's next and its second run, the Run 1 DØ detector is undergoing a significant upgrade. The goal is to have improved tracking and vertexing capabilities (primarily with the new Silicon Vertex Detector), better muon identification, and faster and more efficient readout electronics to meet the Tevatron's increased luminosities by an order of magnitude compared to Run 1. The new run should also achieve slightly higher $p\bar{p}$ CM collision energy of 2 TeV, and is scheduled to begin by the end of year 2000.

A general view of the Run 1 DØ detector is shown in Figure 3.2. Fully assembled, it stands approximately 13 m in height, 11 m in width, and 17 m in length, with a total weight of about 5500 tons. Not shown in the figure is the detector support platform on which the entire structure rests. This platform is mounted on twenty 500-ton Hillman rollers so that the entire detector may be rolled along hardened steel tracks from the assembly area to the collision hall. The platform also provides rack space for the detector electronics and other support services.

A right-handed coordinate system is adopted, see Figure 3.2, in which the z -axis is along the proton direction and the y -axis is upward. The angles φ and

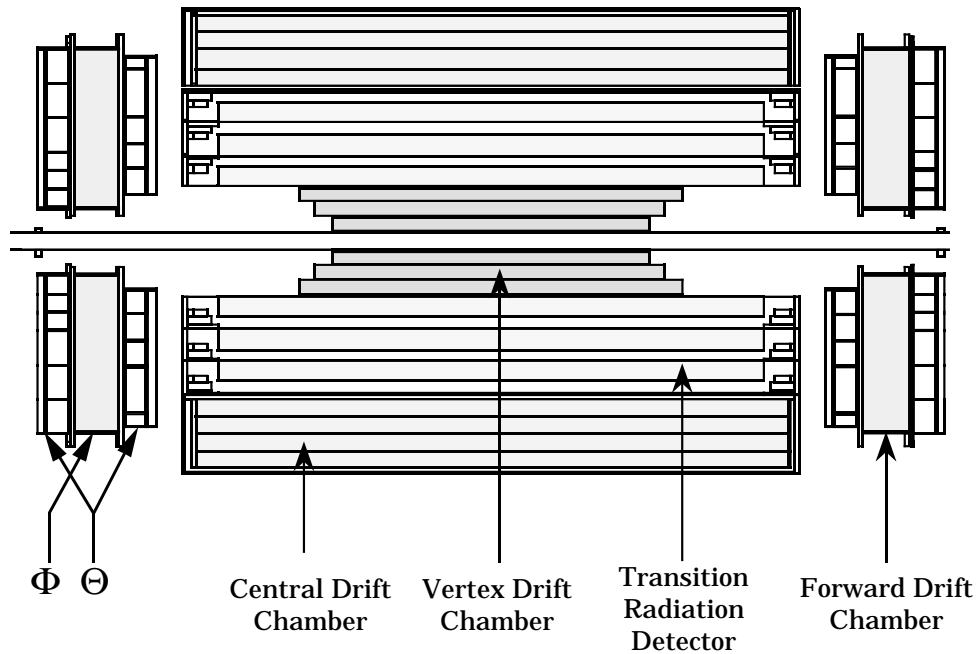


Figure 3.3: The Central Detectors.

θ are the azimuthal and polar angles, respectively. The radial coordinate r is the distance from the beam line.

In the following sections, the different components of the Run 1 DØ detector are described based on reference [45]. From the inside to the outside, the detector consists of three main systems: the central detectors, the calorimeters, and the muon system. Since the DØ calorimeters are the principle tool for the measurement of jets—the central objects of the physics analysis presented in this dissertation—the description of the calorimeters, naturally, is more detailed.

3.3 The Central Detector

The Central Detector, a compact system of concentric tracking and transition radiation detectors illustrated in Figure 3.3, is enclosed in the cylindrical volume between

the Tevatron beam line and the inner cylindrical aperture of the calorimeters. The entire system extends 135 cm along the $\pm z$ -axis, centered at $z = 0$, and is enclosed within a radius of 78 cm in the direction perpendicular to the beam line. The tracking detectors are wire drift chambers. As a charged particle traverses them, it ionizes the chamber active media which usually is gas mixture rather than liquid to avoid any significant disturbance in the particle's path itself. Arrays of many anode or sense wires at sufficiently high potential immersed in the gas create an electric field in which liberated electrons accelerate to high enough energies to initiate secondary ionization, the secondary electrons inducing tertiary ionizations and so on. It is this cascade or avalanche of electrons that amplifies otherwise tiny signal by several orders of magnitude (*gas gain*) allowing its detection and measurement. Knowing the drift velocity of the charge carriers in the media and the time when the particle of interest entered the chamber (in DØ, the first time marker is taken to be the beam crossing time), a position or *hit* of the traversing particle can be measured.

Connecting hits from the several layers of the tracking system, a contiguous *track* of the incoming particle can be reconstructed. The drift chambers also measure the energy loss (dE/dx) of the incoming particles since the measured signal is proportional to its energy. Influenced by the absence of a central tracking magnetic field, the Central Detector system was designed to achieve good spatial resolution of individual particles, good two-track resolving power, high efficiency, and good ionization energy determination for better electron identification. In the following sections, the subdetectors which make up the Central Detector are described, working from the inside, outward.

3.3.1 The Vertex Detector

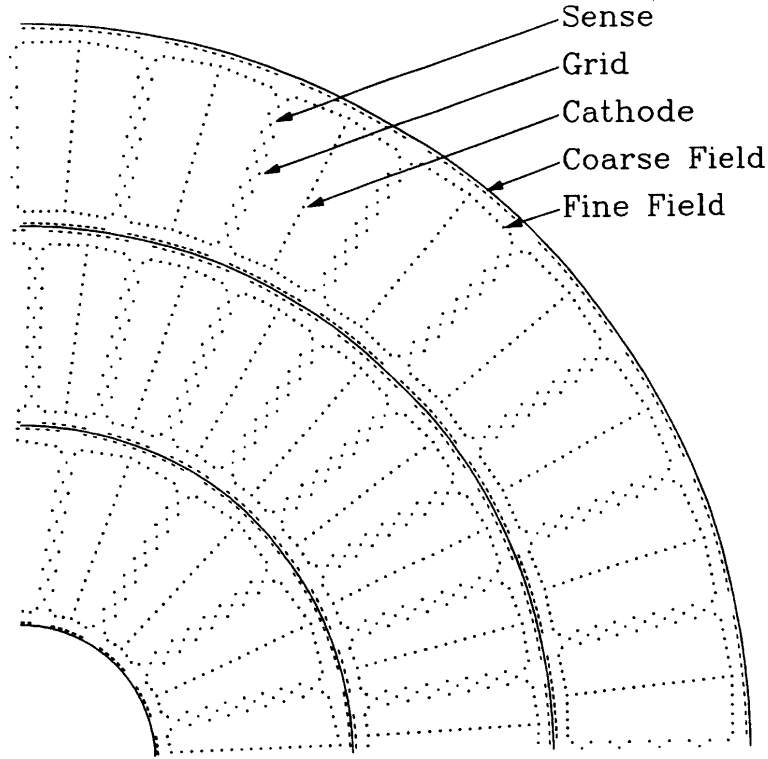


Figure 3.4: A quadrant of the Vertex detector—end view.

The Vertex Chamber (VTX) is the innermost tracking drift chamber and completely surrounds the beam pipe, which consists of a very thin cylinder of beryllium¹ with an outer radius of about 3.7 cm. The outer radius of the Vertex chamber is 16.2 cm. The VTX was designed to reconstruct tracks around the interaction region and measure the vertex position. The vertex and tracking information is essential for non-inclusive jet analysis and for an accurate determination of the jet E_T . The VTX is made of three mechanically independent concentric layers of cells, see Figure 3.4. The innermost layer is 97 cm long and has 16 cells, while each successive layer is 10

¹The beam pipe is needed to maintain the vacuum to minimize interactions of p 's and \bar{p} 's with air molecules and beryllium was chosen to minimize multiple scattering.

cm longer than the preceding one (thus providing total coverage for $|\eta| < 2.3$), and is divided into 32 cells. In each cell, there are 8 sense wires of $1.8 \text{ k}\Omega/\text{m}$ resistivity kept at $+2.5 \text{ kV}$ potential which provide the measurement of $r - \varphi$ coordinate of the hit. They are offset by $\pm 100 \text{ }\mu\text{m}$ with respect of each other (*staggered*), to help resolve left-right ambiguity. To further aid in pattern recognition, avoid dead regions, and facilitate calibration, each layer is offset in azimuth (φ) with respect to each other. The sense wires are read out at both ends to also provide the z position measurement using the method of charge division.

The active medium for the chambers is a gas mixture of CO_2 (94.5%) and ethane (5%) with small (0.5%) admixture of H_2O (which was shown to stabilize the chamber operations in a high radiation environment) with a gas gain of 4×10^4 and typical drift velocity of about $7.3 \text{ }\mu\text{m}/\text{ns}$ under normal operating conditions of average drifting electric field of approximately $1 \text{ kV}/\text{cm}$. Unfortunately, the method for the measurement of the z coordinate does not work well with the usual observed high cell occupancies, achieving z position resolution of only about 1.5 cm . In contrast, the VTX has a good $r - \varphi$ resolution of about 60 mm and also is 90% efficient in separating two hits 0.63 mm apart.

3.3.2 The Transition Radiation Detector

The electric field associated with the moving charge of a particle traversing a medium causes polarization along its path. The effective range of this electric field or, equivalently, the spatial extent of the induced polarization are different in materials with different electromagnetic properties. As a result of this difference, the

sudden redistribution of charges in the medium associated with the changing electric field of highly relativistic particle crossing the interface between two media with different dielectric or magnetic properties gives rise to electromagnetic radiation in the X-ray range called the “transition radiation”. Transition radiation becomes useful for particle detection when the photons are emitted in the soft X-ray range (energy range of 2–20 keV) and along the particle direction at very low angles of order $1/\gamma$, with γ being the usual Lorentz factor. Therefore this method is useful for highly relativistic particles with γ larger than 10^3 . As a result, detectors based on transition radiation emission are used to provide electron/pion separation in the momentum range 0.5–100 GeV. In addition, the typically very low photon yield per each boundary crossing must be increased, which is often achieved by stacking several hundred layers of low- Z foil (radiators) in a gas.

The DØ Transition Radiation Detector (TRD), with the schematics of its section shown in Figure 3.5, surrounds the Vertex Chamber. It consists of three separate concentric layers each containing a radiator and an X-ray detector. The radiator part of each of the TRD layer has 393 foils of 18 μm thick polypropylene in the volume filled with nitrogen gas to provide inter-foil gaps between radiation interfaces of 150 μm . The X-ray detection is accomplished by a wire drift chamber mounted just after the radiator. Since electrons are the only likely inducers of detectable transition radiation at Tevatron energies, the TRD is used to identify them. Pion rejection factors of about 50 are found at 90% efficiency for electron detection.

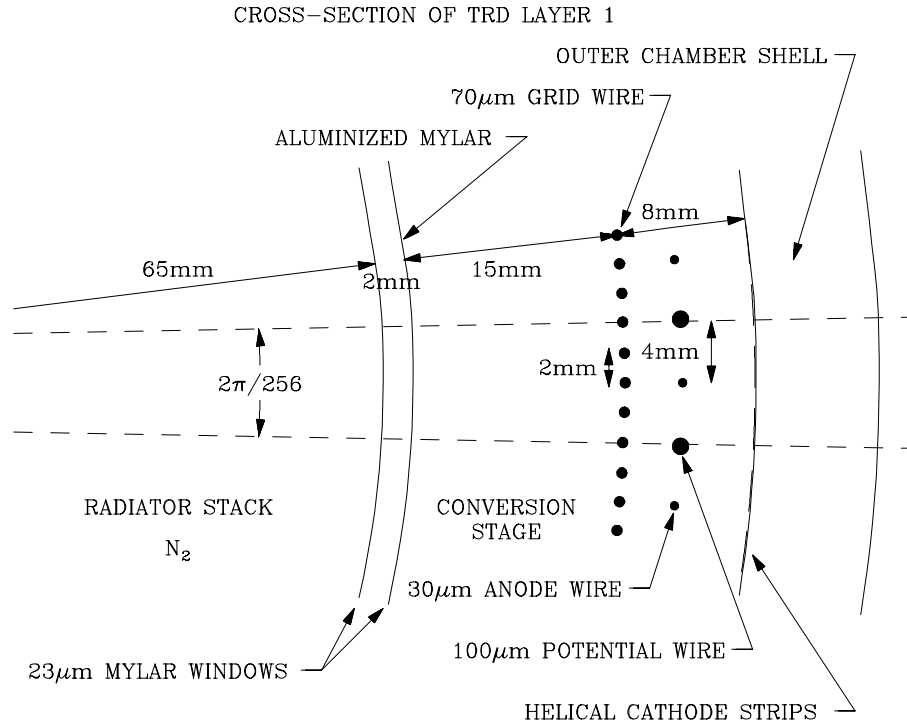


Figure 3.5: A section of the Transition Radiation Detector.

3.3.3 Central Drift Chamber

The Central Drift Chamber (CDC) is the outermost tracking device, fitting between the TRD and the Central Calorimeters with inner and outer radii of 49.5 and 74.5 cm, respectively, extending 92 cm in $\pm z$ direction, thereby providing wide angle (out to $|\eta| \sim 1.2$) coverage for charged particle tracks. The CDC is a cylindrical shell made of four concentric rings, each divided into 32 azimuthal unit cells. A segment of the CDC is shown in Figure 3.6. Each cell contains 7 gold-plated tungsten sense wires of 30 μ m in length running parallel to the beam line and are read out from one end. As in the VTX, in order to help resolve left-right ambiguity, the adjacent sense wires are staggered by 0.2 mm. In addition, the cells in different layers are also

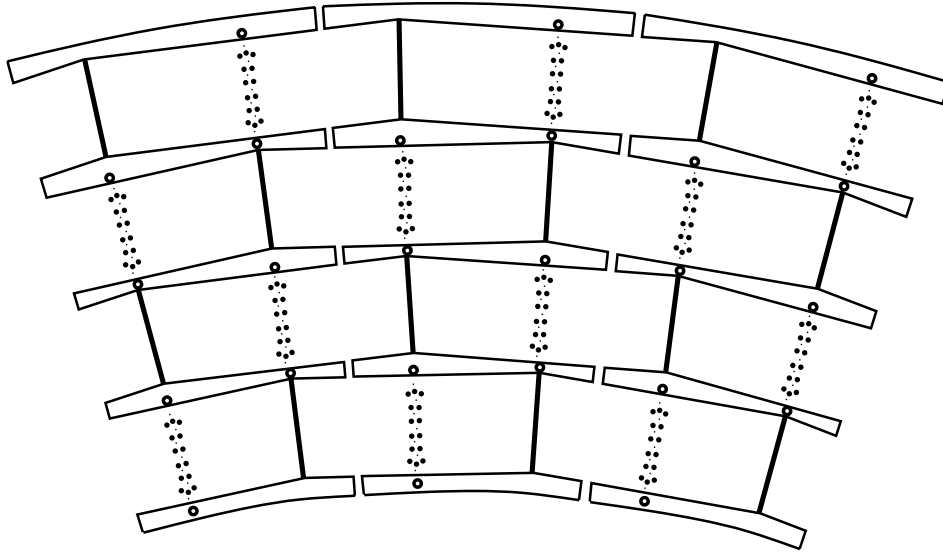


Figure 3.6: End view of a section of the Central Drift Chamber.

offset in φ by about one half of unit cell to aid in pattern recognition. To measure the z -position of the avalanche, two delay lines are embedded in the inner and outer walls of each layer next to the sense wires. The delay lines are carbon fiber rods wrapped with a winding of magnet wire. The fast gas active medium for the CDC was chosen to be argon doped with 3 and 4% of CO_2 and CH_4 , respectively, with a small admixture of H_2O (for the same reason as in the VTX). With an operational drift field of 620 V/cm the average drift velocity is about $34 \mu\text{m}/\text{ns}$. The voltages on the outer sense wires (1.58 kV) are raised with respect to the inner sense wires (1.45 kV) to induce larger delay line signals, achieving 6×10^4 and 2×10^4 gas gains, respectively. The CDC has z position resolution of about 2 mm, with $r - \varphi$ resolution between 150–250 μm (the latter understandably poorer than that of the VTX), and 90% efficiency for resolving two hits is achieved at 2 mm hit separation.

3.3.4 Forward Drift Chamber

As seen in Figure 3.3, the two Forward Drift Chambers (FDC's) cap the other central detectors. The FDC's extend up to the End Calorimeter cryostats and provide charged particle tracking coverage down to $|\eta| \sim 3.1$ ($\theta \sim 5^\circ$). Each FDC is made of three chambers: one Φ module for the measurement of azimuth (φ) sandwiched by two Θ modules for the determination of the polar angle (θ), see Figure 3.7. The Φ module is one chamber with inner and outer radii of 11 and 61.3 cm, respectively, containing 36 sectors with full coverage in azimuth. Each sector has 16 sense wires of about 50 cm in length directed radially from the beam to facilitate measurement of φ coordinate. The anode wires are placed 8 mm apart along the direction of the z axis and are staggered transversely by ± 0.2 mm.

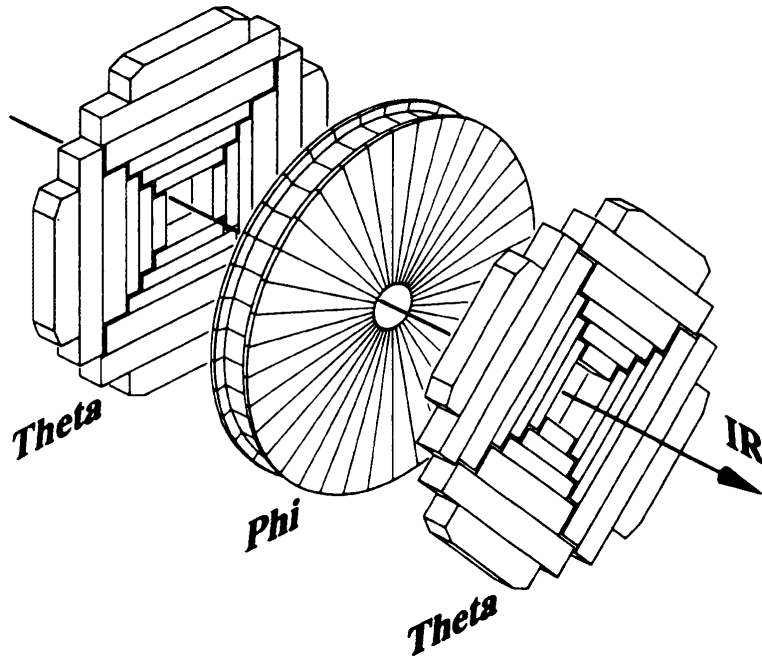


Figure 3.7: Exploded view of one of the two FDC packages illustrating the Φ module sandwiched by the two Θ modules.

The Θ chambers consist of four mechanically separated quadrants with six rectangular cells each. Each cell has eight anode wires transverse to the direction of the beam. The sense wires are separated by 8 mm, as in the Φ chamber, and are staggered. The Θ chambers also have delay lines identical in construction to those in the CDC to measure the orthogonal coordinate. Because the θ -layers are four-fold symmetric, a 45° angle between the two Θ modules maximizes the position resolution of the FDC. The FDC uses the same gas as the CDC and obtains similar resolution and efficiency values.

3.3.5 Central Detector Readout

For the first stage of signal processing, the signals from the chamber wires are led into preamplifiers mounted on the ends of the chambers themselves. From there, the signals are fed into analog pulse shaping cards located on the platform underneath the detector. Finally the signals are sent to flash analog-to-digital converters (FADC's) located in the moving counting house. There the signals are sampled and digitized at a rate of 106 MHz, starting at the beam crossing. If the event is not accepted by the Level 1 trigger, the data are overwritten by the next crossing. Otherwise, the data are compressed by eliminating the flat portions of the signal between the pulses ("zero suppression") and sent on to the Level 2 trigger.

3.4 The Calorimeter

The $D\bar{O}$ Calorimeters are the most important tool for jet detection. They provide energy measurement for electrons, photons, and jets. Other important roles of $D\bar{O}$ calorimetry are particle identification and the determination of the Missing

Transverse Energy (E_T). Calorimeters are detector subsystems relying on total absorption of the energy of the incoming particle. As a high energy particle enters a sufficiently large block of matter, all of its energy will be degraded to the level of detectable atomic ionization and excitations (and eventually heat, hence the name—“calorimeter”). As energetic particles enter and traverse the calorimeter, they initiate cascades, or showers, of particles caused by the secondary, tertiary, ... interactions along the path of the primary particle. This phenomenon is perhaps most vividly demonstrated in experiments detecting particle showers resulting from the cosmic rays entering the earth atmosphere.

Particle showers in the same material originating from electromagnetic and hadronic incoming particle are generally quite different. For simplicity, let us follow a high energy electron entering a medium. It is known that at energies above a few tens of GeV, an electron loses energy primarily via emitting a photon, or bremsstrahlung. So, the electron will bremsstrahlung radiate many energetic photons. It is also known that photons with energies well above the electron-positron pair production threshold of about 1 MeV, will predominantly undergo e^+e^- pair production. These secondary electrons and positrons will again radiate more photons, and so on. The multiplicity of particles in such a cascade will continue to grow until the average energy of the particles falls below the “critical energy”, the energy at which (in a given material) the energy loss due to the radiation equals the energy loss due to ionization. After this, the development of the particle shower will quickly cease. For a high energy electron, the mean distance in the medium, traversing which it loses all but $1/e$ (e here being a base of natural logarithm) of its energy due to bremsstrahlung, is called radiation length² and is traditionally denoted by

²Radiation length X_0 can roughly be parameterized as $X_0 \sim 180A/Z^2$ g/cm² for a material

X_0 . It is clear that X_0 sets the scale for the EM shower penetration into the medium and therefore units of X_0 are a convenient measure of the material thickness when dealing with electrons or photons.

Upon entering a dense medium, hadronic particles can also initiate particle cascades. Hadrons interact either via the electromagnetic or the strong force. In the former case, the electromagnetic part of the hadronic shower will develop in much the same way as described in the previous paragraph. Strong interactions on the other hand take place between the hadron and nuclei, exciting them. De-excitation of the nucleus can result in the production of protons and neutrons or mesons depending on the amount of excitation. The atoms whose nuclei got excited to a lesser degree, could emit photons and ionized electrons. All of these secondary particles can in turn become sources for tertiary particles (and so on) creating a hadronic shower, generally much more complex in its nature than its purely electromagnetic counterpart.

A substantial amount of the incoming hadron energy also goes (with large fluctuations) into overcoming nucleon binding energy, and is therefore lost. As a result, the calorimeter response to electrons is usually higher than to the hadrons of the same energy. Somewhat analogous of X_0 for EM showers, a nuclear interaction length³ λ , roughly corresponding to the depth at which the hadronic shower maximum would appear, sets a length scale when dealing with hadronic showers. Hence the thickness of the material with respect to such showers is usually given in terms of λ .

with atomic mass A and atomic number Z .

³Nuclear interaction length λ can very roughly be parameterized as $\lambda \sim 35A^{1/3}$ g/cm² for materials of atomic mass A .

Calorimeters are aimed at reconstructing the characteristics of the incoming particle based on the precise identification and measurement of the induced shower in the material. Because of the different intrinsic nature of electromagnetic (EM) and hadronic showers in the medium, calorimeters are often designed with a specific goal to achieve a better measurement of either type of shower.

Calorimeters can be used to measure not only the energy but also the spatial position, the direction, and, in some cases, the nature of the primary particle. Their performance, which generally improves with increasing incoming energy, is limited both by fluctuations of the elementary processes through which the original energy is dissipated and by the techniques chosen to measure the final products of the cascade process. Most often calorimeters measure the energy based on the electric charge released through ionization in the active medium. Calorimeters are sensitive to both charged and neutral particles, and the differences in its response to electrons, muons, and hadrons can be used for particle identification.

The depth necessary for full energy containment scales only logarithmically with incoming particle energy, and uncertainties in the energy measurement are governed by statistical fluctuations of the number of particles in the cascade, N , and hence the relative energy resolution improves as $1/\sqrt{N} \sim 1/\sqrt{E}$. Segmented calorimeters allow precise measurements of the position and angle of the incident particle. Fast time response of calorimeters allows operation at high particle rates, and the pattern of energy deposition can be used for rapid online event selection (triggering).

Sampling calorimeters, where several absorber and active layers are following each other have become most popular. As the particles enter the sampling

calorimeter, they interact with the array of absorber plates producing a shower of particles and losing most of their energy. A small fraction of their total energy is deposited in the gaps of active medium as its atoms are ionized. To collect liberated electrons, an electric field is applied across the gap, and as the charges drift towards and reach the anode, an electric signal is induced that can be detected and read out. This signal is then calibrated to the incoming particle energy.

As mentioned earlier, usually the calorimeter response to electrons and hadrons is different. The ratio of the electromagnetic and hadronic responses denoted as e/h is an important characteristic of the calorimeter; usually $e/h \sim 1.4$. Since such a difference in the two responses leads to degraded hadronic resolution and signal nonlinearity, it is desirable to remove this effect, i.e. achieve “compensation”. Two general methods for doing so are: accurate determination of the electromagnetic component of the hadronic shower with the idea of applying certain weighting factors for the EM fraction at the time of reconstruction, and a careful choice of the absorber material and its thickness to boost the purely hadronic component of the shower. As it is shown below, the DØ Calorimeters achieve nearly full compensation employing the second general method by choosing uranium for the absorber plates and selecting appropriate thicknesses for the plates as well as for the active regions between them.

The DØ calorimeter is a sampling design using liquid argon (LAr) as an active medium. The choice of LAr was supported by its many desirable characteristics. To name a few: LAr has unit gain; it is relatively dense (1.4 g/cm^3); It does not attach electrons easily, but has a relatively low ionization energy of about $\sim 24 \text{ eV}$; it has high electron mobility ($\sim 5 \text{ mm}/\mu\text{s}$ at 1 kV/mm field strength); the

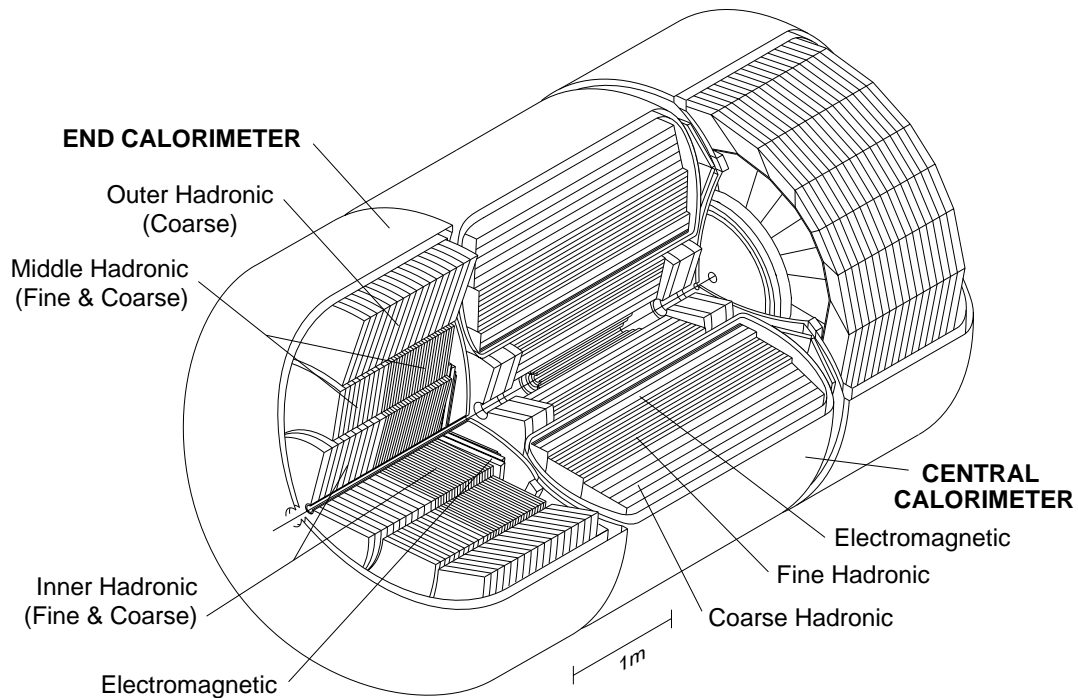


Figure 3.8: General view of DØ LAr calorimeters.

cost is relatively low; it is easy to obtain in a pure form and easy to purify; many electromagnetic impurities are frozen out in LAr, and it allows long term stable operation in a high radiation environment such as that at the Tevatron. The use of LAr obviously necessitates a good cryogenics system to maintain the operational temperature of 78 K for LAr (cooling to this temperature takes approximately 10 days), and containment vessels (cryostats) which unavoidably introduce regions of uninstrumented material. In order to have access to the Central Detectors within the calorimeter cavity, more than one vessel is necessary. Therefore, DØ calorimeters are housed in three separate double-walled stainless steel cryostats, one central and two end-caps, the latter two being mirror images of each other. A general view of the DØ LAr calorimeters is shown in Figure 3.8. The boundary between

the Central Calorimeters (CC) and the End Calorimeters (EC) is chosen to be perpendicular to the beam line. This design was shown to be superior for \cancel{E}_T reconstruction compared to one in which the EC's nest within the CC shell with a boundary roughly parallel to the beam line. Excellent containment and hermeticity are achieved with the CC providing coverage for roughly $|\eta| < 1$ and the two EC's extending it to $|\eta| \approx 4$. The number of nuclear absorption lengths (λ) is typically 7 for the CC and 9 for the EC.

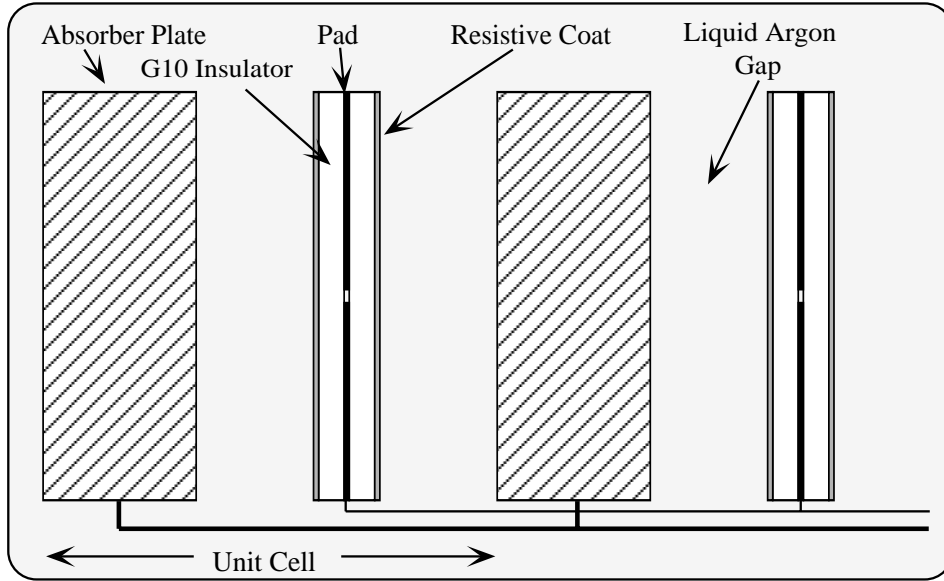


Figure 3.9: Schematic view of the DØ calorimeter unit cell.

The CC and EC are actually made of three types of modules: an electromagnetic (EM) section of modules with relatively thin uranium absorber plates, a fine hadronic (FH) section of modules with thicker uranium plates and a coarse hadronic (CH) section of modules with thick copper and stainless steel plates in the CC and EC, respectively. A schematic view of a DØ unit calorimeter cell, regardless of its position in the calorimeters and the type of calorimetry (EM or hadronic), is

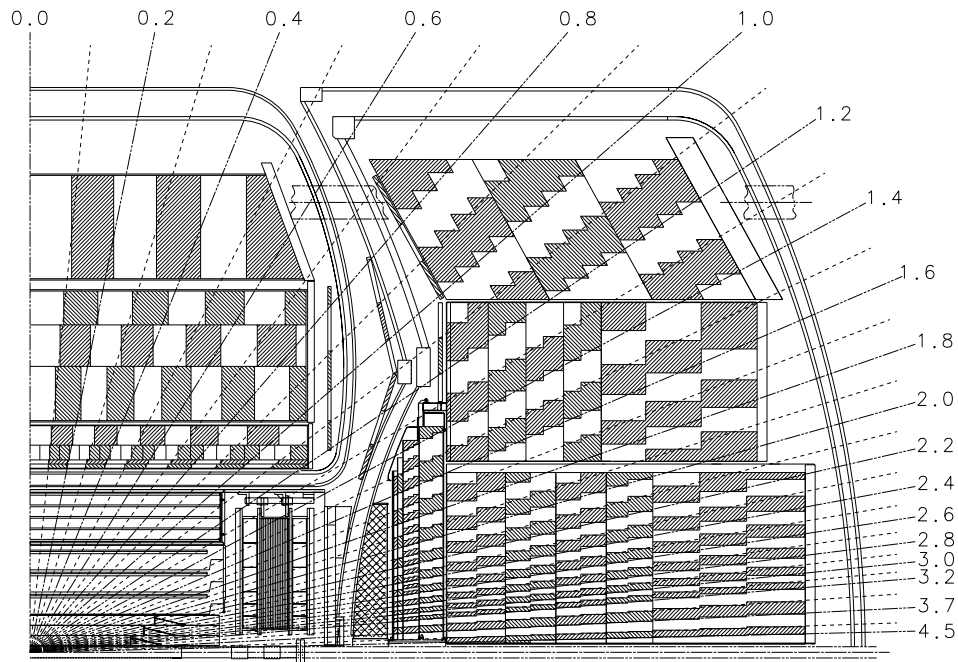


Figure 3.10: Side view of calorimeter trigger towers.

shown in Figure 3.9. It consists of a grounded metal absorber plate and a signal board plated with a coat of resistive epoxy on each surface with a copper plane on the inner side kept at $+2-2.5$ kV potential creating an electric field drift across the 2.3 mm LAr gap, resulting in a drift time for electrons across this gap of about 450 ns. While all calorimeters are immersed in LAr, different absorber materials are used in different locations. The EM modules use 3 and 4 mm thick plates of nearly pure depleted uranium in the CC and EC, respectively. The absorber plates for the FH modules are made of 6 mm thick uranium-niobium (2%) alloy, while the CH modules use even thicker (46.5 mm) plates made of copper (stainless steel) in the CC (EC).

The actual size of the readout cells is set by the typical parton jet size in

$\eta - \varphi$ space of $\Delta R = \sqrt{(\Delta\eta)^2 + (\Delta\varphi)^2} \sim 0.5$. However, the segmentation is finer than this in the transverse direction and is useful for probing jet shape, and the longitudinal (in depth) segmentation is desirable since longitudinal shower profiles can be used to distinguish electrons from hadrons. The transverse size of the readout cells are thus chosen to be in the order of characteristic transverse shower sizes in the EM and hadronic modules of about 1–2 and 10 cm respectively. Multi-layer in-depth segmentation is pseudoprojective in its nature, meaning that although cell centroids lie on the rays of constant pseudorapidity drawn from the geometrical center of the DØ Detector (corresponding to $z = 0$), the actual cell boundaries are perpendicular to the absorber plates. The cells electronically ganged along the rays of constant η form DØ calorimeter “towers” of $\Delta\eta \times \Delta\varphi$ transverse segmentation of 0.1×0.1 radians, providing excellent shower position resolution. The deviations from this segmentation in certain parts of the calorimeters are discussed in the following sections. The pseudoprojective nature of the DØ calorimeter towers is illustrated in Figure 3.10.

A side view of the DØ calorimeter modules in CC and EC is shown in Figure 3.11 along with the Massless Gaps and the Intercryostat Detectors (ICD’s), the latter are two needed to populate otherwise uninstrumented transitional region between central and end-cap cryostats. More detailed description of these different types of calorimeter modules follows.

3.4.1 The Central Calorimeter

The Central Calorimeter (CC) is composed of three concentric rings of electromagnetic (EM), fine hadronic (FH), and coarse hadronic (CH) calorimeters. The EM

ring is made of 32 azimuthal modules, while the the FH and CH rings have 16 azimuthal modules. To avoid azimuthal coincidence of intermodule gaps from different rings, the EM, FH, and CH modules are offset in φ so that no projective ray encounters more than one such gap.

The cells in the EM modules are read out in four longitudinal layers (ganged) which have the thickness of 2.0, 2.0, 6.8 and 9.8 radiation lengths (X_0) in depth. Thus the third EM layer is located where the EM shower maximum is expected to appear. Therefore, to achieve a better transverse measurement of the EM shower maximum, the third layer has finer transverse segmentation (0.05×0.05) than the usual (0.1×0.1) “granularity” in the $\eta - \varphi$ space. A full EM module

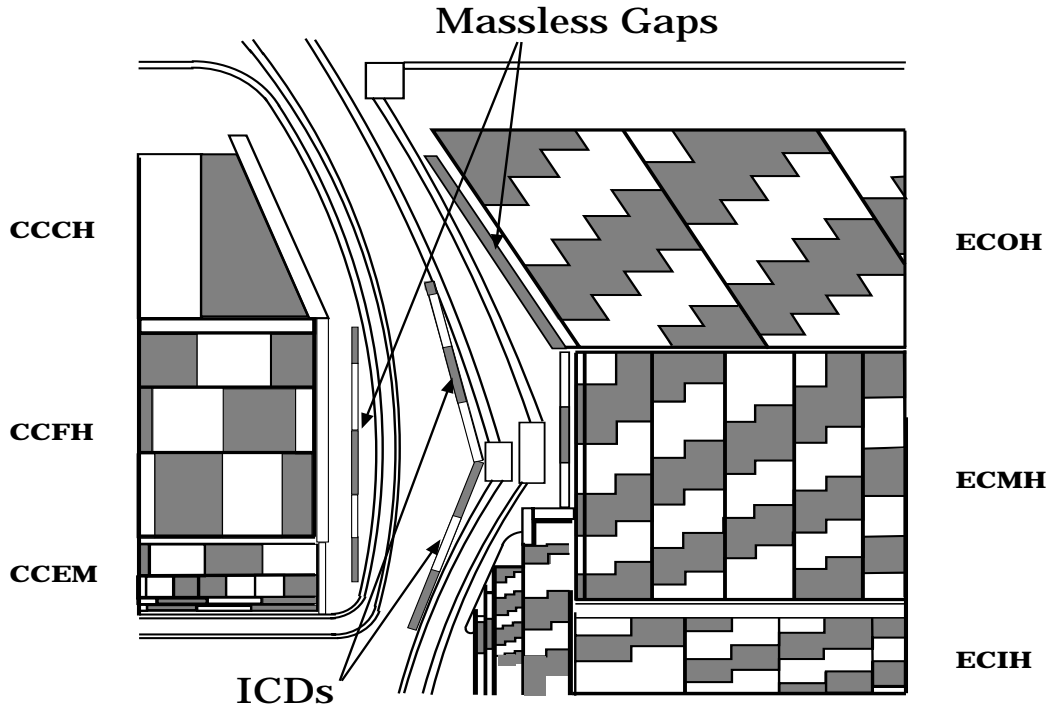


Figure 3.11: Side view of calorimeter modules, intercryostat detectors, and massless gaps.

comprises $20.5X_0$ and 0.76λ and weighs 0.6 tons, requiring about 10,000 readout channels.

The FH modules have cells longitudinally ganged in three layers of approximately 1.3 , 1.0 , and 0.9λ , with the hadronic shower maximum expected to appear in the first FH layer. It has 3500 readout channels and a full ring weighs about 8.3 tons.

The CH modules contain just one depth segment of about 3.2λ . The CH modules weigh about 7.2 tons and has 770 readout channels. The total weight of the CC modules and their support structure is 305 tons, not counting the additional 26 tons of LAr needed to fill the cryostat.

3.4.2 The End Calorimeters

The End Calorimeters (EC) are similar to the CC. There are two mirror-image EC's containing four types of modules as shown in Figure 3.11, each EC with an overall weight of about 238 tons. The single EC electromagnetic module (ECEM) is divided into four read out sections of 0.3 , 2.6 , 7.9 , and $9.3X_0$ with outer radii varying between 84 and 104 cm and inner radius of 5.7 cm. The material in front of the first ECEM layer brings its thickness to about $2X_0$, and the third layer, corresponding to the expected location of the EM shower maximum is more finely segmented transversely, in the same way as in the CC. Each ECEM module weighs about 5 tons and provides 7488 signals.

There is also only one Inner Hadronic module (ECIH) with four fine

hadronic readout sections each about 1.1λ thick, and one coarse hadronic readout segment of 4.1λ in depth. The FH absorber plates are made of uranium, while the CH plates are stainless steel. The full ECIH module weighs 28.4 tons and has 5216 readout channels.

Outside the ECEM and ECIH, there are concentric rings of 16 Middle and Outer Hadronic (ECMH and ECOH) modules. Each ECMH module of total weight of 4.3 tons and 1856 readout signals has four FH readout sections with uranium plates each about 0.9λ deep, and one 4.4λ thick CH section with stainless steel plates. The ECOH modules have three CH readout layers with stainless steel plates at about 60° with respect to the beam line (see Figure 3.11), and have the total longitudinal depth of about 4.4λ .

All EC calorimeter modules have $\eta - \varphi$ segmentation of 0.1×0.1 , except that very close to the beam line $\sim |\eta| > 3.2$, where the physical size of the cells of this size would get tiny, the transverse segmentation is increased to 0.2×0.2 in $\eta - \varphi$ space.

The variation in the thickness of the DØ calorimeters in terms of integrated nuclear interaction lengths, λ , can be read off Figure 3.12 which in addition shows the thickness of the muon system (to be discussed later).

3.4.3 Massless Gaps and Intercryostat Detector

As already mentioned, the intercryostat gap, roughly defined by $0.8 < |\eta| < 1.4$, is instrumented with the Intercryostat Detectors (ICD's) supplemented by the Massless Gaps (MG's), as seen in Figure 3.11. The ICD's are a set of scintillation

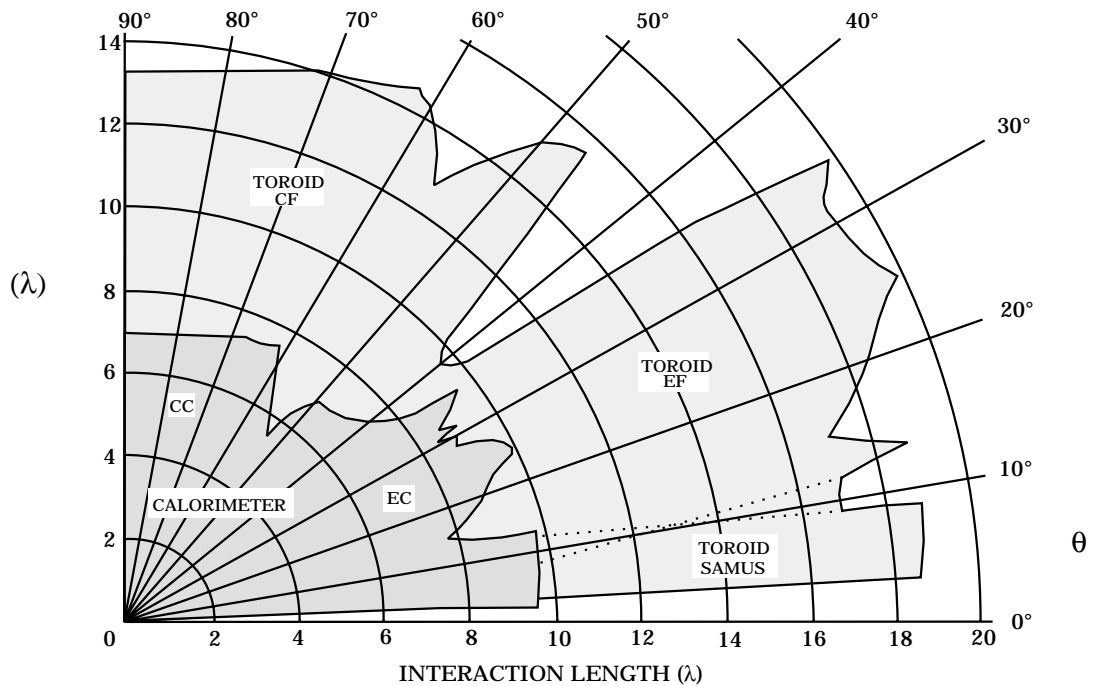


Figure 3.12: Calorimeters and muon system interaction lengths as a function of θ .

counters mounted on the front surface of the EC cryostats. Each ICD consists of 385 scintillator tiles of size 0.1×0.1 in $\eta - \varphi$, thereby matching the LAr calorimeter segmentation. The MG detectors are mounted inside the CC and EC cryostats. They are copper readout boards identical to single-cell calorimeter readout pads. They provide additional sampling of the showers leaving the CC cryostat and entering the EC cryostat. Together, the ICD's and MG's provide good approximation to the standard $D\phi$ sampling of the electromagnetic showers in more uniform sections of the calorimeter.

3.4.4 Calorimeter Readout

The signals induced on the readout pads are pulses with widths on the order of 450 ns. These signals are led out through four ports (feedthroughs) in the cryostats to charge sensitive preamplifiers mounted on top of the cryostats. From the preamplifiers, the signals are led to base line subtractor (BLS) modules located in the platform below the detector. The BLS modules perform analog shaping and split the signal into two paths.

The first path is used for triggering. The signals from all the fine hadronic cells within a tower are summed; the signals from the electromagnetic cells are similarly summed. These signals then form the input to the Level 1 calorimeter trigger.

The second path is used for the data readout. The incoming signal is sampled just before the beam crossing and again $2.2 \mu\text{s}$ later. The difference between these two samples is a DC voltage which is proportional to the total collected charge. This difference is sent to the ADC's where, if the event is accepted by the Level 1 trigger, the signals are digitized and sent on to the Level 2 trigger. In addition, the zero-suppression process eliminates the cells with no or very little energy deposited in them. This process minimizes the readout time and reduces the size of the data to be stored.

3.4.5 The Calorimeter Performance

The $D\bar{O}$ calorimeter module prototypes as well as the actual modules have been tested in many different ways using the beams of particles of known energies as well

as the cosmic rays. Among important characteristics of the calorimeter performance, the ones often quoted are their response linearity as a function of incoming energy and their energy resolution. For instance, the DØ ECEM/ECIH modules have been subjected to extensive tests with electron and pion beams in the energy range of 10–150 GeV. The response to both electrons (above 10 GeV) and pions (above 20 GeV) was found to be linear with beam energy to within 0.5%.

The sampling calorimeter fractional energy resolution σ_E/E is expected to improve as $1/\sqrt{E}$ simply because it is dominated by the statistical fluctuations in the number of sampled charged tracks, which is directly proportional to the incoming energy. However, contributions to the resolutions arising from the noise become increasingly important at low energies, and the resolution may not improve with energy as quickly as the sampling term alone would predict because of the appearance of the “constant term”, usually due to the dead material in front of the calorimeter and other calibration errors. The fractional energy resolution of the calorimeter traditionally is therefore parameterized as the sum in quadrature of these three terms:

$$\left(\frac{\sigma_E}{E}\right)^2 = \frac{N^2}{E^2} + \frac{S^2}{E} + C^2,$$

where N represents contribution from noise, S is the sampling term, and C is a constant offset term. Test beam studies show that the calorimeter energy resolution is approximately $15\%/\sqrt{E}$ for electrons and $50\%/\sqrt{E}$ for pions. The calorimeter energy resolution for jets is measured from the *in situ* collider data. The method used for jet energy resolution measurement, and its effect on the jet cross section, are discussed in chapter 9.

During muon beam tests, it had been determined that a minimum ionizing particle (MIP), crossing the central calorimeter, would liberate approximately 10^4 electrons in each gap and lose a total energy of ≈ 2 GeV. Moreover, the ratio of electron to pion response (e/π ratio) was measured in the combined ECEM and ECIH modules to fall from about 1.11 at 10 GeV to about 1.04 at 150 GeV. The equivalent e/h ratio value is about 1.08, demonstrating the nearly compensating nature of the DØ calorimeters.

3.5 The Muon Spectrometer

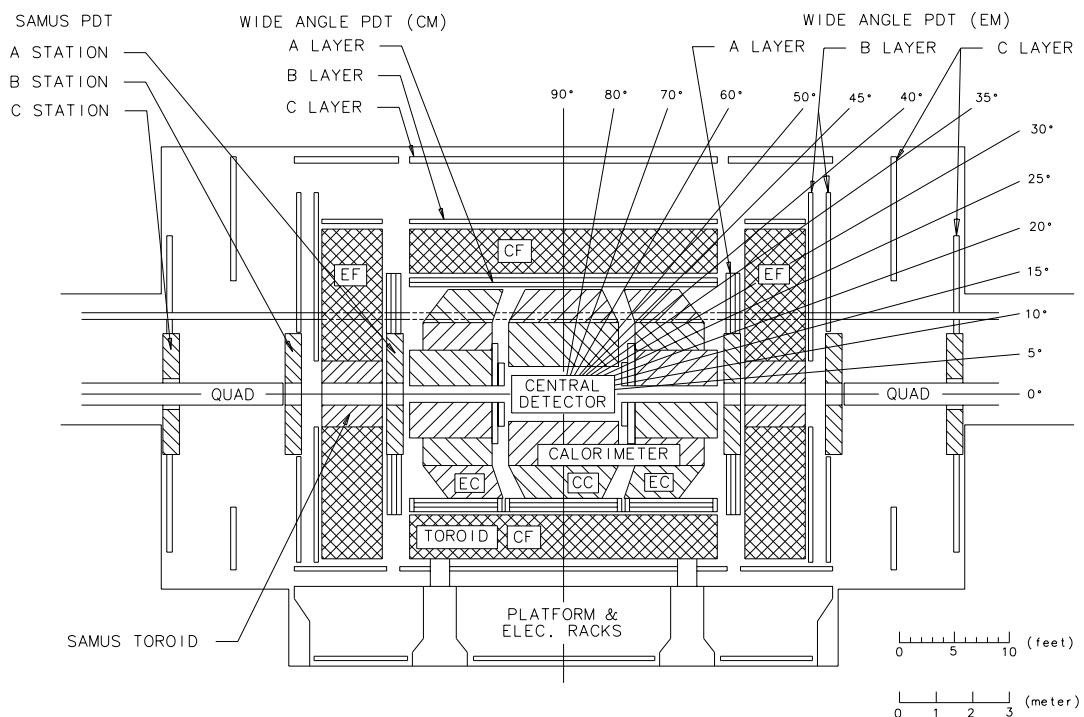


Figure 3.13: Elevation view of the DØ Detector including the muon system.

Although very similar to the electron in quantum numbers, the muon is much heavier and therefore passes through the calorimeters as a MIP particle. Therefore,

the muon spectrometer, a set of saturated iron magnets and proportional drift tube (PDT) chambers, is placed right outside the calorimeters to determine the momenta and trajectories of muons emerging from $p\bar{p}$ interactions. The muon system may also be used in jet analysis to detect cosmic ray shower contamination, and to correct for energy leakage from the back of the calorimeters (*punchthrough*), especially in cases of jets with high transverse momentum. The muon system provides wide coverage in polar angle θ , down to approximately 3° degrees from the beam line. As shown in Figure 3.13, there are two main muon subsystems, described below.

3.5.1 The Wide Angle Muon Chambers

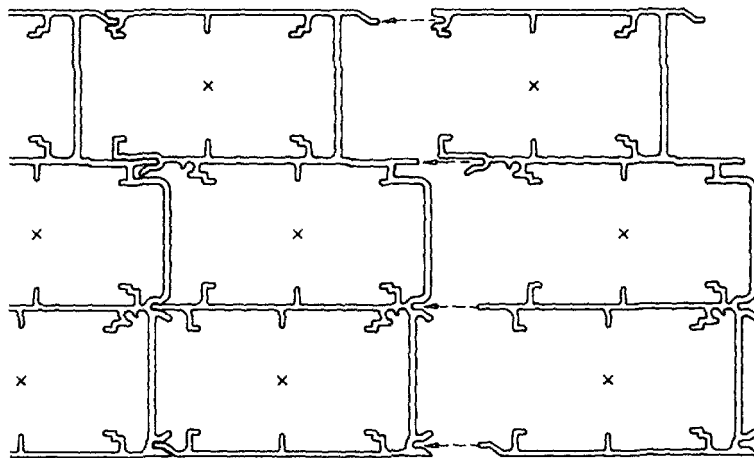


Figure 3.14: Extruded aluminum section for B and C layers. The A layer has four decks of cells instead of three.

The Wide Angle Muon System (WAMUS) measures muons within ($|\eta| < 2.5$). There are three WAMUS toroid magnets: the central (CF) toroid, covering $|\eta| < 1$, and the two end (EF) toroids, covering $1 < |\eta| < 2.5$. The CF region toroid is a meter thick square iron magnet centered on the beam line, surrounding the CC

calorimeters, weighing about 2000 tons. Twenty coils of 10 turns each carry a current of 2500 A to generate internal deflecting magnetic field of 1.9 T; the fringe field near the interaction region is about 0.01 T. The two EF toroids cap the CF magnet from both ends, completely enclosing the calorimeters. They are perforated by the MR (Main Ring), as are the calorimeters and the cryostats. The EF toroids are large iron magnets each weighing about 800 tons. A magnetic field of 2 T is created in the iron by a 2500 A current flowing in eight coils of eight turns. The magnetic field from all toroids has the same direction, bending the muons in the $r - z$ plane.

The PDT's are formed from aluminum extrusion unit cells, as shown in Figure 3.14. The copper-clad Glasteel (polyester and epoxy copolymer sheets with chopped glass fibers) cathode pads are inserted into the top and bottom of each cell and the 50 μm gold-plated tungsten anode wires are held near the center of the cell. The aluminum extrusion is grounded, while the cathode pads and the anode wires are kept at +2.3 and +4.6 kV potential, respectively. The chambers are operated with a gas mixture of $\text{Ar}(90\%)\text{CF}_4(5\%)\text{CO}_2(5\%)$ for which a typical drift velocity is about of order 6.5 cm/ μs . A total of 164 individual chambers are deployed in three layers: the *A* layer before the iron toroids, and the *B* and *C* layers after the magnets (see Figure 3.13). There are 4 decks of cells in *A* layer chambers, and 3 in *B* and *C* layer chambers. The decks of cells are staggered so as to break the left-right ambiguity (see Figure 3.14). The muon direction is measured before and after the magnets, and the momentum is obtained from the bending angle. The hit resolution is about 3 mm along the wire direction and 700 – 900 μm along the drift plane. The muon fractional p_T resolution is $\Delta p/p \approx 20\%$ due to multiple scattering at low momenta and is limited by the bend coordinate resolution at higher momenta.

3.5.2 The Small Angle Muon Chambers

The Small Angle Muon System (SAMUS) is designed to provide coverage for the higher pseudorapidity range of $2.5 < |\eta| < 3.6$. The SAMUS magnets are relatively smaller and are embedded in the WAMUS end toroids within a 2 m square hole centered on the Tevatron beam pipe. They each weigh roughly 32 tons. Two coils of 25 turns each carry current of 1000 A, generating a 2 T magnetic field in the same direction as that of the WAMUS magnets. SAMUS is composed of three stations: *A*, before the magnets, and *B* and *C* after the magnets. Each station consists of three doubled planes of cylindrical proportional drift tube chambers. They are oriented in *x*, *y* and *u* directions (*u* is at 45° with respect to *x* and *y* directions). SAMUS PDT's are stainless steel tubes which are grounded and the anode is a $50\text{ }\mu\text{m}$ gold-plated tungsten wire kept at +4.0 kV potential. The chamber gas used is $\text{CF}_4(90\%)\text{CH}_4(10\%)$ with an average drift velocity of $9.7\text{ cm}/\mu\text{s}$ and a maximum drift time of 150 ns. The hit resolution is approximately $400 - 500\text{ }\mu\text{m}$. The fractional p_T resolution is dominated by multiple scattering and is about 20% for p_T less than $10 - 15\text{ GeV}$.

3.6 The Trigger and Data Acquisition Systems

The bunches of protons and antiprotons are brought to a collision intersection in the center of the DØ detector about 300 thousand times every second corresponding to a readout rate of 300 kHz. Equivalently, and technically more precisely, the beam crossings take place every $3.5\text{ }\mu\text{s}$ at the Tevatron. Since the cross sections for the most interesting and rare physics processes are small, most of these beam

crossings result in events of limited interest. Therefore, a system is designed to quickly analyze events in real time and to select only those with an interesting signature. This system, known as the “trigger”, is an essential part of the Data Acquisition system in hadron–hadron collisions.

Triggering at DØ is done in a multi-stage process, consisting of different trigger levels, increasing in sophistication and time requirements with each higher level. The ultimate goal of the trigger is to reduce the event rate to that at which events can be written to tape (*bandwidth* of about 2 Hz), by accepting interesting events, and at the same time rejecting background events. The following description of different trigger levels puts particular emphasis on calorimeter triggering. Jet triggers will be discussed in chapter 4.

3.6.1 The Level Ø Trigger

The Level Ø trigger is the first hardware trigger stage. Its main purpose is the detection of an inelastic $p\bar{p}$ collisions. The Level Ø detector is made of two sets of scintillating hodoscopes, each mounted on the front surface of the end-cap cryostats, perpendicular to the beam line, providing full coverage for $2.2 < |\eta| < 3.9$ and partial coverage for $1.9 < |\eta| < 4.3$. It measures the difference in the time arrival of particles from the interaction point to the two hodoscopes with excellent time resolution in the order of 100 ps. Coincidences near this resolution signal the presence of inelastic collisions with nearly 100% efficiency. The precise measurement of the time of flight difference also allows the determination of the z position of the interaction vertex with about 3.5 cm resolution. By measuring the cross section for non-diffractive inelastic $p\bar{p}$ collisions and employing the time between the beam

crossings, the Level \emptyset detector also provides a very important measurement of the instantaneous luminosity, one of the major ingredients used in the determination of the integrated luminosity which sets the scale of any cross section measurement.

If a Level \emptyset trigger occurs the event is passed on to the higher trigger levels for further analysis. It significantly reduces the beam crossing rate to a much more manageable rate of about 17 kHz. It must be noted that not all the data recorded by D \emptyset is subjected to the Level \emptyset requirement. Notable exceptions are diffractive events, some of which cannot be triggered by Level \emptyset , and the events intentionally recorded without a requirement of inelastic collision (so called **ZERO BIAS** data), very useful for certain systematic studies.

3.6.2 The Level 1 Trigger

The Level 1 Trigger Framework, a two dimensional network of AND-OR logic circuits with 256 inputs and 32 outputs (also known as trigger bits), accepts information from the Level \emptyset trigger, the Level 1 Calorimeter trigger, and the Level 1 Muon trigger. Each trigger bit is pre-programmed to require a logical combination of selected AND-OR input terms. The goal of the Level 1 trigger is to filter out uninteresting events within a very short time of the beam crossing ($3.5 \mu\text{s}$). This time limitation does not allow the use of the tracking information from the Central Detectors in the Level 1 trigger decision making process.

Level \emptyset supplies the z position of the interaction vertex. The Level 1 calorimeter trigger electronically sums up analog signals in the trigger towers—regions defined by 0.2×0.2 solid angle in $\eta - \varphi$ space—and compares it to thresholds set by the user. The sums are done over all the electromagnetic and fine hadronic

layers of the calorimeter towers with the range $|\eta| < 4.0$. It thus identifies electron/photon and jet candidates and also measures the missing transverse energy. The Level 1 Muon trigger provides muon hit information. Based on this information alone, the Level 1 Trigger Framework checks if the event satisfies one or more of the 32 available trigger requirements. If it does, the event is passed on to the next trigger level, otherwise it is discarded. Level 1 further reduces the event rate to about 200 Hz.

Despite careful design of the requirements for each trigger bits, some of them still are “fired” more often than acceptable for passing to the next trigger level. These trigger bits are then *prescaled*, meaning that only one out of a fixed number of passed events will actually pass the Level 1 trigger (“divide by N”). Some of the Level 1 muon trigger bits require more complex selection criteria based on muon tracks in order to reduce the corresponding trigger rates and also provide a cleaner event sample. For this, the simple muon reconstruction available in the Level 1 is not sufficient, and the candidates are passed to an intermediate trigger level (Level 1.5) for further analysis. However, such detailed reconstruction sometimes can not be achieved within the beam crossing time, introducing a detector dead time while all systems await decision.

3.6.3 The Level 2 Trigger

The Level 2 trigger and the Data Acquisition (DAQ) systems are closely intertwined. The information from Level 1 is passed on to Level 2, which is a farm of 48 microVax VS4000-60 processors working in parallel. The interesting event candidates are further reconstructed using the information from the entire DØ detector, focusing

on the areas identified in Level 1. In Level 2, there are 128 software filters connected to the 32 trigger bits of Level 1. Similar to Level 1, the trigger bit prescale values can be set for Level 2 filter bits as well. In the case of the calorimeter filters, for instance, the data are unpacked in the region flagged by the Level 1 trigger. Level 1 towers are used as seeds for the jet filter. A jet finding algorithm sums all the trigger towers within a cone of radius 0.7 in $\eta - \varphi$ space. The events with jet-like energy clusters above various thresholds are then sent to the host computer. The Level 2 trigger reduces the event rate to about 2 Hz.

As is clear from the above discussion, the data collection efficiency depends crucially on the optimization of the entire trigger system. Trigger requirements for identifying physics events of interest are, therefore, carefully designed, tested, and implemented. Various sets of trigger requirements comprise trigger lists which are downloaded from the database during the regular data taking periods. In certain circumstances, due to high luminosities and loose trigger requirements, more events may be accepted by the triggers than can be handled by the system's bandwidth. This results in a dead time for the entire detector, the state specifically dubbed as *front-end busy* or *Level 2 disable*, depending on whether it happens in the Level 1 or the Level 2 trigger.

3.7 The Offline Data Processing

During Run 1, events were primarily written to two data streams. The ALL stream contained all events sent to the host and was directly written to tape. The EXPRESS stream contained only events from a small subset of filters which was of the most interest for rapid analysis (mostly top and W/Z triggers). EXPRESS stream

events were copied to the express line, where they were immediately reconstructed and rapidly made available for analysis. For Run 1, events were recorded at the rate of 2–3 Hz, with about 10% of the events going to the EXPRESS stream.

Each day, the raw data tapes written by the online system were collected and transported to the Feynman computing center. There, the raw data were reconstructed on a farm of Silicon Graphics machines. The product of the reconstruction was two sets of files. STA's contain the raw data of the event augmented with the results of the reconstruction, and are about 600–1000 kilobytes per event. DST's contain only the reconstruction results for high-level objects, such as electrons, muons, etc. They are about 15 kilobytes per event. Most analyses start with the DST's. STA's are usually required only when one wants to re-reconstruct an event, or to scan an event in detail with the event display.

The reconstructed events were further split into a set of offline streams. This was done on the basis of filter procedures supplied by the various physics groups, which were designed to select the events of most interest. The filtered event streams were then made available to users on the DØ file server.

CHAPTER 4

THE DATA SAMPLE AND RECONSTRUCTION

This analysis is based on Run 1B data (runs 72250–93115) collected from December 1993 through July 1995 with four inclusive jet triggers: Jet_30, Jet_50 and Jet_Max versions 8–10, and Jet_85 versions 9 and 10 only, resulting in integrated luminosities for these filters of 0.36, 4.7, 93 and 55 pb⁻¹ respectively, as derived from the Production Data Base (PDB) [46]. The data have been reconstructed using RECO version 12 [47] with the standard DØ fixed cone jet-finding algorithm [48] for jet cone sizes of 0.3, 0.5, 0.7 and 1.0. This study is limited to jets with cone size of 0.7. After the reconstruction, the data have been ntupled in a standard multi-cone DØ QCD format to facilitate easier and faster access. In what follows, we discuss in more detail jet triggers, relevant topics of general event reconstruction in DØ with RECO v. 12 (such as the jet and the event \cancel{E}_T reconstructions), and the corrections we apply to the reconstructed QCD events.

4.1 The Inclusive Jet Triggers

As discussed in chapter 3, the triggering in DØ is done in a multi-stage system consisting of three basic trigger levels. The inclusive jet triggers exist in the Level 1 and Level 2. In the hardware trigger level, the Level 1, jet triggers require a desired number of trigger towers (0.2×0.2 in $\eta - \varphi$ space) or large trigger *tiles* (4×8 in

Name	Runs	Level 1 (GeV)	Level 2 (GeV)	QCD bit
Jet_Min	all	1 jet with $E_T > 3$	1 jet with $E_T > 20$	2
Jet_30	all	1 tile with $E_T > 15$	1 jet with $E_T > 30$	40
Jet_50	≤ 77824	1 tile with $E_T > 35$		4
	$77825 \leq \text{runs} \leq 85226$	1 tile with $E_T > 25$	1 jet with $E_T > 50$	
	≥ 85227	1 tile with $E_T > 15$		
Jet_85	≤ 77824	1 tile with $E_T > 60$	1 jet with $E_T > 85$	5
	≥ 85227	1 tile with $E_T > 35$		
Jet_Max	≤ 77824	1 tile with $E_T > 60$		6
	$77825 \leq \text{runs} \leq 85226$	1 tile with $E_T > 35$	1 jet with $E_T > 115$	
	≥ 85227	1 tile with $E_T > 45$		

Table 4.1: Run 1B inclusive jet trigger configurations.

trigger towers, i.e. 0.8×1.6 in $\eta - \varphi$) to have transverse energy (E_T) above certain threshold value. If Level 1 accepts an event, it passes information onto Level 2, also providing it with a list of Level 1 trigger towers. When large trigger tiles are used in Level 1, it then provides to Level 2 the E_T weighted centroid positions of the tiles.

In the software filter level, the Level 2, jet-like clusters are reconstructed starting from the “seed” tower list from Level 1. In addition to the threshold requirement in Level 1, there is also a seed threshold requirement in Level 2. However, this is somewhat redundant as the seed threshold is always lower than the Level 1 threshold and thus does not affect Level 1 trigger. In Level 2, around each trigger seed centroid, a box of 1.4×1.4 in $\eta - \varphi$ is drawn. The E_T weighted centroid of this box is taken as a Level 2 jet center. All trigger towers not already claimed by other Level 2 jets are then summed up within a fixed cone radius of 0.7 in $\eta - \varphi$ drawn from the Level 2 jet centroid. If Level 2 jet passes a preset threshold for the designated jet filter, the corresponding trigger bit is set on, or is “fired”, and the event is accepted.

Level 2 single jet filters used in this inclusive jet cross section analysis are: Jet_30, Jet_50, Jet_85 and Jet_115, where, by convention, the number in the jet trigger name indicates Level 2 trigger E_T threshold in GeV. The highest (lowest) E_T jet trigger is often called Jet_Max (Jet_Min). In the studies of the jet energy resolutions we also use the Jet_20, or Jet_Min, trigger for determining the resolutions at the lowest E_T point, thereby better constraining a fit to the standard resolution parameterization. Table 4.1 summarizes Level 1 and Level 2 requirements for all the inclusive jet triggers used in this analysis [49].

Jet triggers are not fully (100%) efficient in all E_T and η ranges. The coarse hadronic (CH) layers, Massless Gaps (MG’s), and Intercryostat Detectors (ICD’s) are not included in Level 1 trigger towers. Moreover, there are smearing effects related to the vertex measurement in Level 0 and the jet energy resolutions. A combination of these effects may distort jet E_T in Level 1 and Level 2 in

such a way that a real jet may fall below the trigger thresholds. As a function of jet E_T , the jet triggers are inefficient below their E_T thresholds but they become nearly 100% efficient, or “turn on”, very quickly thereafter. On average, triggers turn on slightly sooner in the End Calorimeters (EC’s) compared to the Central Calorimeters (CC’s), but, on the other hand, their turn on curves are degraded in the intercryostat region (ICR). The jet trigger efficiencies have been measured in the dedicated studies [49]. The turn on E_T thresholds for the four single jet filters used in this analysis have been additionally checked by taking the ratios of the cross sections from more restrictive to less restrictive triggers as a function of E_T in the same way as in reference [46]. In the measured inclusive jet cross section, the single jet triggers are used in the E_T ranges where they are at least 99% efficient.

4.2 Jet Definition

Jet definition is non-trivial issue both theoretically and experimentally. As was discussed in chapter 2, instead of the usual particle four-momentum, a preferred set of jet kinematic variables is its transverse momentum (E_T), azimuthal angle (φ), pseudorapidity (η), and mass (m). In theoretical calculations, it is important that a jet is defined in such a way that no divergences appear in physically observable quantities. That is to say, sums over final state partons or particles belonging to a jet should be infrared safe. If a jet is composed of n objects, then the theoretically preferred definition of overall jet kinematic variables is that of the “Snowmass”

accord [50]:

$$\begin{aligned}
 \text{the sum } E_T : \quad E_T &= \sum_i E_{T,i}, \\
 \text{the } E_T \text{ weighted } \eta : \quad \eta &= \frac{\sum_i E_{T,i} \eta_i}{\sum_i E_{T,i}}, \\
 \text{the } E_T \text{ weighted } \varphi : \quad \varphi &= \frac{\sum_i E_{T,i} \varphi_i}{\sum_i E_{T,i}},
 \end{aligned} \tag{4.1}$$

with the mass of the jet set equal to zero. Furthermore, in next-to-leading order (NLO) QCD it is necessary to implement a scheme for assigning partons to jets. A convenient measure of separation in $\eta - \varphi$ space is the distance $\Delta R = \sqrt{(\Delta\eta)^2 + (\Delta\varphi)^2}$, with $\Delta\eta$ and $\Delta\varphi$ being the “distances” in the corresponding angles between the two objects. One way to define a jet then is to assign to it all the partons within some chosen distance \mathcal{R} from the jet centroid, where the jet direction can be calculated using Eqs. (4.1).

In general, such a prescription cannot be used for the experimental definition of a jet without some modifications. In DØ, historically, a scheme somewhat different from the Snowmass accord has been used. We will refer to this scheme as the DØ definition or algorithm. It was shown in dedicated studies that such a definition gave jet kinematic variables closer to those of the parent partons. Although we define, find, and reconstruct experimental jets using this standard DØ algorithm, we then apply corrections (to be discussed later on in this chapter) to obtain jets that would have been reconstructed with the Snowmass accord. Putting experimental and theoretical jets on the same footing also makes comparison to theoretical predictions more straightforward.

The primary tool for identifying and measuring jets in DØ is the LAr–Ur Calorimeters. Experimental jets used in this analysis are defined and reconstructed using the DØ fixed-cone jet finding algorithm with a cone size of 0.7 in $\eta - \varphi$ space¹. It is an iterative algorithm which starts from the calorimeter towers (see page 108) that have E_T ’s greater than 1 GeV. The $\eta - \varphi$ “granularity” of the towers is 0.1×0.1 except at highest pseudorapidities where the calorimeter segmentation is coarser, as discussed in chapter 3. Starting from the highest E_T calorimeter tower, *preclusters* of contiguous cells are formed around them out to a radius of 0.3 in $\eta - \varphi$ space. All towers falling within preclusters are removed from the original list of available towers. The E_T weighted centroid of the precluster is calculated and a cone of radius \mathcal{R} (for this analysis, $\mathcal{R} = 0.7$) is drawn from there.

A new E_T weighted center of the candidate jet is then found from *all* towers within radius \mathcal{R} . This process of finding the jet $\eta - \varphi$ centroid is repeated until a stable solution of the jet direction is found. This is usually achieved in three to four iterations. The found jet must have E_T greater than 8 GeV. If two nearby jets overlap, they are either split into two jets or merged into one. They are merged if more than 50% of the E_T of the jet with the smaller E_T is contained in the overlap region; otherwise the two jets are split into two distinct jets, the energy of each calorimeter cell in the overlap region is assigned to the nearest (in $\eta - \varphi$) jet and the jet direction is recalculated. It is worth noting that the jet E_T threshold of 8 GeV is applied *before* possible splitting or merging of jets in the event. Therefore, two jets with E_T ’s lower than 8 GeV cannot be combined to create a single jet with

¹An alternative, successive combination algorithm, called the k_T algorithm [51], is also developed in DØ and is used in some analyses. Both algorithms have their strengths and weaknesses, especially from the experimental point of view, and complement our current understanding of hadronic jets.

$E_T > 8$ GeV. Furthermore, either or both jets resulting from splitting may have E_T 's less than the threshold value of 8 GeV.

Jet kinematic variables are calculated by summing over all calorimeter towers inside a jet. For each calorimeter tower, the basic experimentally measured quantities are: energy (E_i), azimuthal (φ_i) angle and polar (θ_i) angle. Jet energy is the sum over all towers belonging to the jet:

$$E = \sum_i E_i. \quad (4.2)$$

Each tower is assumed to be massless and, consequently, $\mathbf{p}_i = p_i \hat{\mathbf{n}} \equiv E_i \hat{\mathbf{n}}$, where $\hat{\mathbf{n}}$ is the unit vector in the direction of the tower centroid from the interaction point. Because of this massless approximation we often talk of jet energy and momentum interchangeably, and even introduce the x , y , and z , components of jet energy. The three components of jet momentum or energy are thus defined in the following way:

$$\begin{aligned} E_z = p_z &= \sum_i E_{z,i} = \sum_i p_{z,i} \equiv \sum_i E_i \cos \theta_i, \\ E_x = p_x &= \sum_i E_{x,i} = \sum_i p_{x,i} \equiv \sum_i E_i \sin \theta_i \cos \varphi_i, \\ E_y = p_y &= \sum_i E_{y,i} = \sum_i p_{y,i} \equiv \sum_i E_i \sin \theta_i \sin \varphi_i. \end{aligned} \quad (4.3)$$

It should be noted that even though towers are massless, the jet defined in this way still acquires non-zero invariant mass

$$M = \sqrt{E^2 - \mathbf{p}^2}, \quad (4.4)$$

where jet energy is given by Eq. (4.2) and its three-momentum is $|\mathbf{p}| = \sqrt{p_x^2 + p_y^2 + p_z^2}$, with the components defined in Eq. (4.3).

In jet physics, we often work with the transverse energy of a jet which should clearly be distinguished from the jet transverse momentum. Jet transverse

energy (E_T) is the sum of the transverse energies of all jet-associated towers:

$$E_T = \sum_i E_{T,i} = \sum_i E_i \sin \theta_i, \quad (4.5)$$

while the jet transverse momentum (p_T) is the transverse component of its three-momentum \mathbf{p} , or:

$$p_T = \sqrt{p_x^2 + p_y^2} \equiv \sqrt{\left(\sum_i p_{x,i}\right)^2 + \left(\sum_i p_{y,i}\right)^2}, \quad (4.6)$$

which is clearly different from the jet E_T as defined in Eq. (4.5). The difference between E_T and p_T of a jet is due to its finite opening angle and can be very large for wider jets. On the other hand, with increasing Lorentz boost of a jet, it becomes more collimated and in this limit E_T and p_T become nearly equal. As long as one uses the same quantity in experimental reconstruction and theoretical calculations, the particular choice of E_T or p_T does not matter in most physical quantities. For historic reasons, we use jet E_T more often than p_T .

Finally, jet angles are found from the components of \mathbf{p} :

$$\begin{aligned} \varphi &= \tan^{-1}\left(\frac{p_y}{p_x}\right) \equiv \tan^{-1}\left(\frac{E_y}{E_x}\right), \\ \theta &= \tan^{-1}\left(\frac{p_T}{p_z}\right) \equiv \tan^{-1}\left(\frac{\sqrt{E_x^2 + E_y^2}}{E_z}\right), \end{aligned} \quad (4.7)$$

The pseudorapidity (η) is then derived from the polar angle (θ) in the massless limit:

$$\eta = \ln \left[\cot \left(\frac{\theta}{2} \right) \right]. \quad (4.8)$$

The event reconstruction for this analysis was performed with the DØ reconstruction package RECO version 12. The RECO package, along with other pattern recognition software, contains the fixed cone jet finding algorithm just described. Jets were

reconstructed for cone sizes of 0.3, 0.5, 0.7, and 1.0, but the analysis presented here is based on $\mathcal{R} = 0.7$ only. It has been shown in Monte Carlo studies that the jet reconstruction efficiency is 100% for jets with E_T 's greater than 20 GeV at all pseudorapidities [33].

4.3 Missing Transverse Energy

The RECO package also provides us with an important “global” quantity—the missing transverse energy vector ($\vec{\cancel{E}}_T$) in the event. The DØ hermetic calorimeters, with nearly full solid angle coverage, are designed to give precise measurement of $\vec{\cancel{E}}_T$. $\vec{\cancel{E}}_T$ is defined in the following way:

$$\vec{\cancel{E}}_T = \left(\underbrace{-\sum_i^{\text{cells}} E_{x,i}}_{\cancel{E}_x} ; \underbrace{-\sum_i^{\text{cells}} E_{y,i}}_{\cancel{E}_y} \right), \quad (4.9)$$

where the sums are over *all* calorimeter *cells* including the ICD's and MG's [47]. The event missing transverse energy, \cancel{E}_T , is simply the magnitude of $\vec{\cancel{E}}_T$. The azimuthal direction of $\vec{\cancel{E}}_T$ is defined as:

$$\varphi_{\cancel{E}_T} = \tan^{-1} \left(\frac{\cancel{E}_y}{\cancel{E}_x} \right). \quad (4.10)$$

In ideal calorimeters, a non-zero missing transverse energy indicates the presence of non-interacting particles in the event, such as high p_T neutrinos. Also, high p_T muons traverse the calorimeters as minimum ionizing particles (MIP), depositing only 2–3 GeV of their energy. The \cancel{E}_T measurement is also affected by the electronic and uranium noise and the calorimeter energy and position resolutions. Precise measurement of $\vec{\cancel{E}}_T$ is crucial in searches for new phenomena with signatures of nonzero missing transverse energy. In most QCD events, however, rather

small values of \cancel{E}_T are expected.

4.4 The Treatment of Hot Cells

The appearance of calorimeter cells with spurious energies and unusually high frequencies of occurrence is an undesirable, but to some degree unavoidable, effect. Such cells are commonly referred to as “hot” calorimeter cells or channels. The sources of hot cells range from electronic noise and hardware failures in the calorimeter to non-collider physics processes always present at the Tevatron. Such bad or hot cells must be identified and removed from the data samples.

4.4.1 Anomalous Isolated Deposit Algorithm (AIDA)

Despite the existing CALIB [52, 53] and CHOT [53, 54, 55] utilities, the number of hot cells observed during Run 1A was still high. Therefore, for Run 1B, DØ was forced to introduce another hot cell suppressor—AIDA.

AIDA is applied *event by event* with the purpose of removing true hot calorimeter cells (THCC). First it makes a list of *candidate* THCC’s whose transverse energies $E_T^{cand} > 10$ GeV, and orders them in E_T , starting with the highest E_T candidate cell. Then for each of these candidate cells AIDA calculates the ratio of the average transverse energy of the longitudinal neighbors (i.e. adjacent cells with lower and higher layer numbers) $\langle E_T \rangle$ to the E_T^{cand} . This ratio is expected to be close to one for cells inside a cluster of energy and small for isolated hot cells. Therefore, AIDA identifies a candidate cell as a THCC if this ratio is:

$$\frac{\langle E_T \rangle (\text{longitudinal neighbors})}{E_T^{cand}} < 0.05. \quad (4.11)$$

However, sometimes the candidate cell does not have both longitudinal neighbors *physically* present in the calorimeter. In such cases E_T of either of the neighbors that is physically present is taken instead of the average to calculate the ratio in Eq. 4.11. To summarize, $\langle E_T \rangle$ in Eq. 4.11 is generally defined as:

$$\langle E_T \rangle = \begin{cases} (E_T^{up} + E_T^{down})/2 & \text{if both neighbors are present,} \\ E_T^{up} \text{ or } E_T^{down} & \text{whichever one neighbor is present.} \end{cases} \quad (4.12)$$

AIDA was introduced offline² in version 11.03 of the full DØ RECO on April 13, 1993 [58]. It ran in CAHITS, i.e. *before* jet finding took place, scanning a complete CAEH bank. It was allowed to suppress *as many hot cells as it found* based on the above described THCC identification algorithm [47]. The THCC's found by AIDA were then all suppressed in the CAEH bank by a factor of 10^{-9} , and were recorded in the CAID bank. In other words, the cells identified as hot by the offline version of AIDA were removed not only from the \cancel{E}_T and the total scalar E_T calculations, but also were not allowed in any of the jets reconstructed thereafter by the CAJETS package.

4.4.2 Effects of AIDA on Jets

Unfortunately, the offline version of AIDA damaged many good jets by removing good, “isolated” cells which—as it turns out—result from the natural fluctuations due to hadronization, hadronic shower development, and calorimeter segmentation [53]. This effect has also been noticed and discussed in earlier studies [54, 59, 60]. It turns out that AIDA most often, about 93% of the time, removes

²For completeness we must also mention that AIDA was first introduced *online* in Level 2 during Run 1A, but online versions of it did not seem to have caused any problems [56, 57, 53].

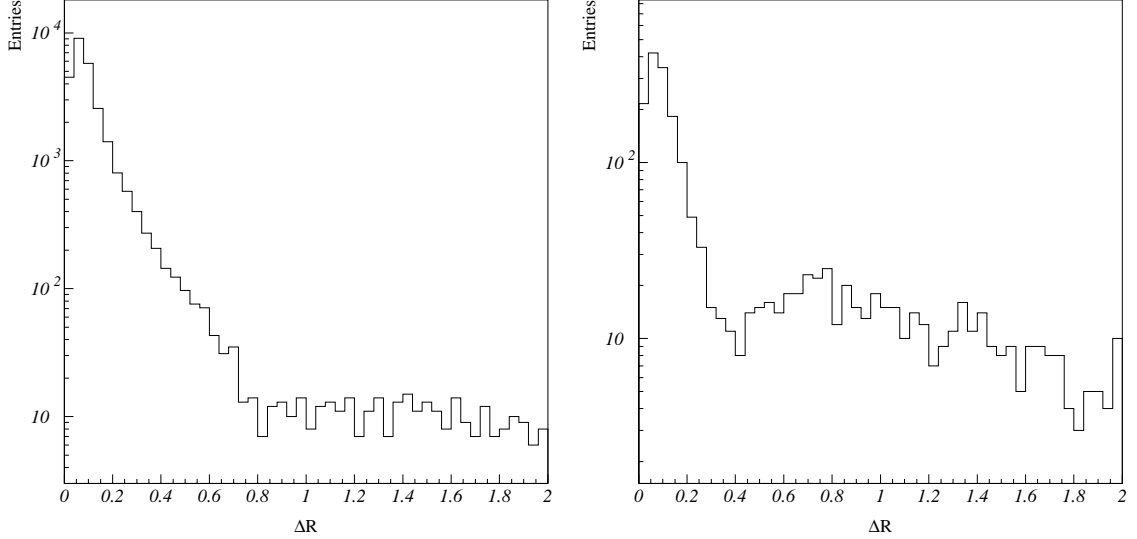


Figure 4.1: The ΔR distributions for jets with $0.0 \leq |\eta_d| < 1.0$ and E_T of 100–120 GeV (left) and with $1.5 \leq |\eta_d| < 3.0$ and E_T of 40–60 GeV (right). Overwhelming majority of AIDA cells are found in a close vicinity of the jet centroid, well within the jet cone radius of 0.7.

only one cell. It flags five or more cells in the events with a frequency of less than a tenth of a percent

Since jets in the data sample under consideration are reconstructed using the standard DØ fixed-cone algorithm, it is natural to rely on the distance in $\eta - \varphi$ space ΔR , between the AIDA cell and the jet's centroid as a good indicator of whether or not a cell might actually belong to a jet. The distributions of ΔR to the nearest jet are examined when there is only one AIDA cell present in the event for different detector pseudorapidities η_d and various jet E_T . Figure 4.1 shows the ΔR distributions for jets in the central and forward regions of the detector at E_T 's of 100–120 GeV and 40–60 GeV, respectively. These distributions show that the overwhelming majority of the AIDA cells are in fact removed from a very close vicinity of the jet centroid.

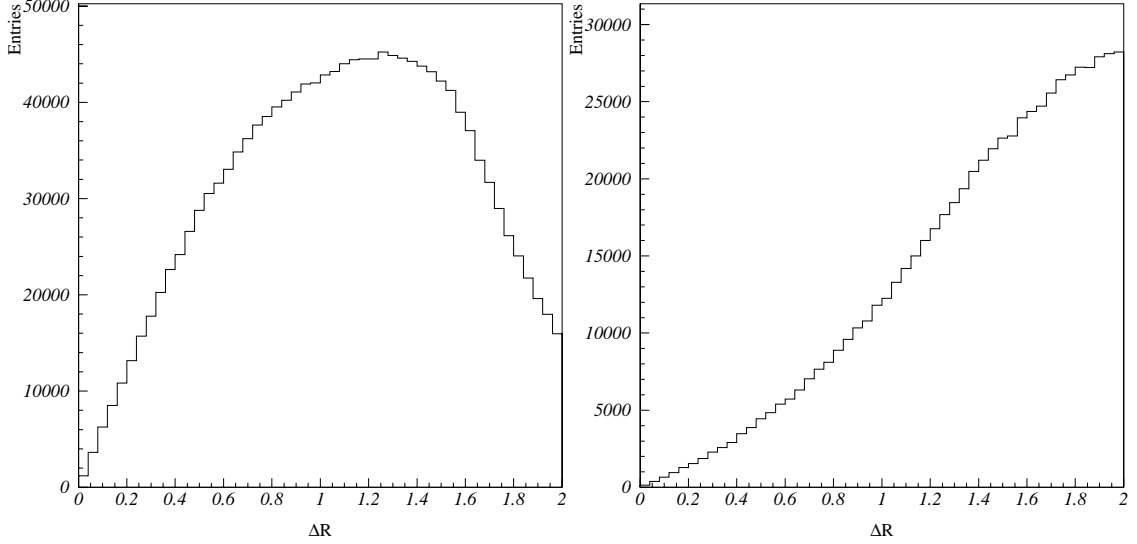


Figure 4.2: The ΔR distributions for simulated THCC's with packed integer ID's of +075701 (left) and +251517 (right).

To determine whether these AIDA cells are the THCC's or “jet-associated” cells *incorrectly* removed by AIDA, similar plots for the known THCC's must be examined. However, which cell is a THCC is not known a priori. Nevertheless, one can use the main feature of a THCC—its unusually high frequency of appearance—to obtain a good approximation of such a distribution from the data. To do this, a random direction (i.e. any calorimeter cell) is chosen in the calorimeter to “simulate” a THCC location. Then the ΔR distribution of this arbitrarily chosen, simulated THCC to the nearest jet is obtained from the data. To exclude any possible biases in the AIDA algorithm itself, only the events not flagged by AIDA are considered. Throughout this note a signed packed integer ID is used to identify a calorimeter cell which is composed of ieta, iphi and the layer number of the cell. For example, the cell with the ID of -170311 refers to the cell with ieta, iphi and layer number of -17 , 3 and 11 , respectively³. The ΔR distributions for several such

³The cells in the third electromagnetic module (EM3) are subdivided into four to achieve finer granularity of 0.05 by 0.05 in η and φ , but they are being addressed using layer numbers $3, 4, 5$

simulated THCC's are obtained. For the simulated THCC's with ID's of +075701 and +251517 these distributions are shown in Figure 4.2. One of the characteristic features of the ΔR distributions of simulated THCC's is that they approach zero very quickly as $\Delta R \rightarrow 0$. Also, all of them have a rising part, reaching maximum and then falling back to zero. The position of the maximum in ΔR is determined by the location of the THCC in the calorimeter and by the detector acceptance as observed from this particular location in the calorimeter.

Comparison of the ΔR distributions for the AIDA cells to those of the simulated THCC's shows a drastic difference suggesting that most of the cells removed by AIDA do not exhibit behavior that is characteristic of randomly firing THCC's. Thus most of AIDA cells in fact are not THCC's but rather belong to jets! However, away from the jet centroids, i.e. at high values of ΔR , the ΔR distributions of the AIDA cells do resemble those of THCC's. For example, the ΔR distribution for jets in the forward region presented in the right plot of Figure 4.1 clearly shows a rising part at about $\Delta R = 0.4$. Also, all of the ΔR distributions obtained with the AIDA cells have tails extending to high values of ΔR —another characteristic feature seen in the ΔR distributions of the simulated THCC's.

Thus the evidence forces us to conclude that most often AIDA removes good, jet-associated cells that happened to be isolated due to the fluctuations in the energy deposition pattern of a jet in the calorimeter. Sometimes, however, AIDA *correctly* identifies and removes THCC's. These conclusions have also been confirmed by visually scanning many of the events with removed AIDA cells.

Next, we want to examine the number of the cells removed by AIDA in

and 6. Unless otherwise noted, we collectively refer to them as layer number 3.

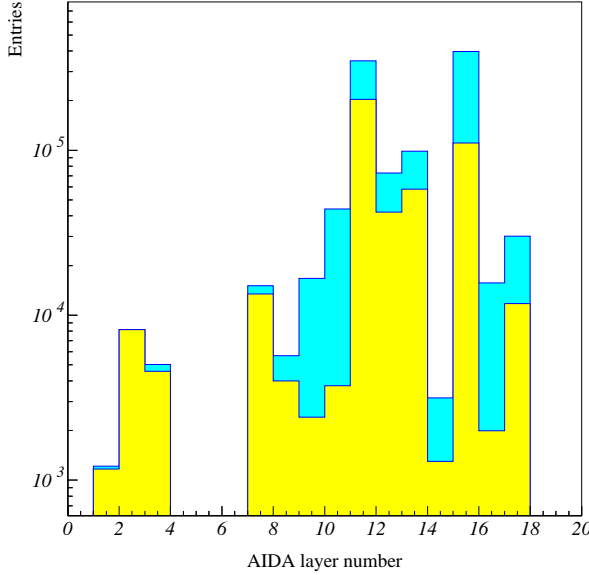


Figure 4.3: Layer number distribution of the cells removed by AIDA. The dark shaded histogram represents all AIDA cells, while the gray shaded distribution has AIDA cells nearby the Main Ring removed. Note the logarithmic scale.

different layers. To make a fair comparison, however, the cells lying very close to the Main Ring (MR) must be removed first, because the MR goes through coarse hadronic (CH) layers of the calorimeter and through the EC Massless Gap, contaminating the calorimeter cells nearby. This is achieved by ignoring cells from the close proximity of the MR (i.e. cells with azimuth of $1.0 < \varphi < 2.2$, see chapter 5). Figure 4.3 shows the layer number distribution of all AIDA cells (dark shade) and of all AIDA cells except the ones satisfying the MR azimuth cut (gray shade). Comparing these two distributions, we see that when the MR region is removed, the number of the AIDA cells in CH layers is reduced more than in fine hadronic (FH) layers, as expected. In addition, the number of AIDA cells in the two (CC and EC) MG's (represented by layer numbers 8 and 10) become almost equal to each other once the MR contamination is removed, and the number of AIDA cells in the Intercryostat Detector (layer number 9) is significantly reduced as well. The latter is due to the fact that the MR losses can easily fire cells in the Intercryostat Detector (ICD) since there is no material in the crack between the MR, the ICD

and the cryostat walls.

Figure 4.3 also shows that, after the removal of the MR contamination, the cells in layer 11 (the first fine hadronic layer, or FH1) are removed most often by AIDA. This is understood by examining how much material is present in different layers of the calorimeters and in front of them. The integrated nuclear interaction length for the FH1 is much larger than that for any of previous layers, and is almost three times larger than that of the last electromagnetic layer 7 (EM4) [53, 61]. To determine whether the candidate cell has an isolated deposition of energy, AIDA compares the cell E_T to the average E_T deposited in the longitudinal neighbors. Then, if the candidate THCC is in the FH1, one of its longitudinal neighbor cells is in succeeding hadronic layers located deeper than the FH1, while the other neighbor is necessarily located either in the ICD or in the the MG, both with vanishing values of λ , or in the last layer of the electromagnetic modules, depending on the pseudorapidity. For either of the three preceding layers, the integrated λ is about 3 times smaller than that for FH1. Therefore, on average large or even comparable energy depositions should not be expected in the preceding neighbors of the FH1. This is true even for the succeeding FH layers since the FH1 is located where the hadronic shower maximum is expected to appear. Therefore, of course, the ratio in Eq. 4.11 may be rather small even for good, jet-associated cells in the FH1, but these cells will then be *incorrectly* removed by AIDA: hence, the high frequency of the AIDA cells in the FH1.

The next most populated layer 15 (or the first coarse hadronic layer, CH1). Basically the same argument explains why AIDA cells appear in layer 15 so frequently—its lower lying longitudinal neighbors have integrated λ smaller by a

factor of 2 and the late developing hadronic showers may deposit most of their energy in this “tail-catcher” coarse hadronic layer. In addition, by visual scanning of many events, it is seen that hadronic showers in the calorimeter may naturally have highly “popcorn-like” energy deposition pattern resulting from inhomogeneities in the hadronic shower development and nuclear interactions. Still, the largest depositions of energies are most likely to appear in cells with larger values of λ , once more leading us to layers 11 and 15.

In addition, we have also looked at the Monte Carlo (MC) sample with *no* noise added that was reconstructed with AIDA “turned on”. The standard MC sample has the noise overlayed on top of the particle level generated events [62]. AIDA removed cells in the MC sample as well, where clearly there were no hot calorimeter cells present! Therefore, each and every cell that AIDA removed in the MC data is a result of natural fluctuations in the energy deposition pattern of a jet in the calorimeter and as such should not have been removed by AIDA.

These examples make it clear that the AIDA algorithm was inadequate. It can not account for the natural fluctuations in the hadronic showers, and the comparison of the energy depositions in different neighbors does not take into consideration how likely the energy is to be deposited in different layers based on the amount of material present in them as well as in front of them.

Furthermore, the AIDA package had a mistake in its code. Instead of calculating the ratio of the transverse energies: $\langle E_T \rangle$ to E_T^{cand} according to Eq. 4.11, AIDA actually calculated the ratio of the average *energy* of the longitudinal neighbors to the *transverse energy* of the candidate cell [63]. While the consequences of this mistake are negligible in the central region, AIDA removes *fewer* cells in

the forward region than it would have had the calculation been done according to Eq. 4.11. Fortunately, this means that there was less damage done to the forward jets.

4.4.3 AIDA Cell Restoration

To be able to repair the damage caused to the jets by AIDA, we first need to identify cells correctly removed by AIDA (i.e. THCC's), separate them from the cells *incorrectly* removed by AIDA, and restore the latter to jets.

The high frequency appearance of THCC's once again guides us in identifying them among the AIDA cells. Various “scatter” plots of cells removed by AIDA are examined in all layers, see for example Figure 4.4 for layer 15. The THCC's clearly stand out in scatter plots of i_{eta} vs. i_{phi} . Furthermore, scatter plots of i_{eta} vs. ΔR and i_{phi} vs. ΔR show that these cells have a specific behavior: their ΔR distributions are uniform in ΔR extending to high values of ΔR . This feature is also seen in the ΔR distributions of simulated THCC's, as noted in the previous section. Such cells then are identified in every layer and they make up a list of the *candidate* THCC's—there are in total 30 of them found among the AIDA cells.

To make sure that these are actual THCC's, as a next step, the ΔR distributions of all these THCC candidates are examined. Figure 4.5 shows the ΔR distributions of two of them with the cell ID's of -192315 and -134917 . These distributions should be compared to the ΔR distributions of the simulated THCC's in Figure 4.2. It is clear that the cell -134917 exhibits THCC-like behavior while the cell -192315 has drastically different ΔR distribution being always found very close to the jet centroid, well within the jet cone radius of 0.7. Such a signature indicates

AIDA cells in layer 15 (CH1), THCCs removed

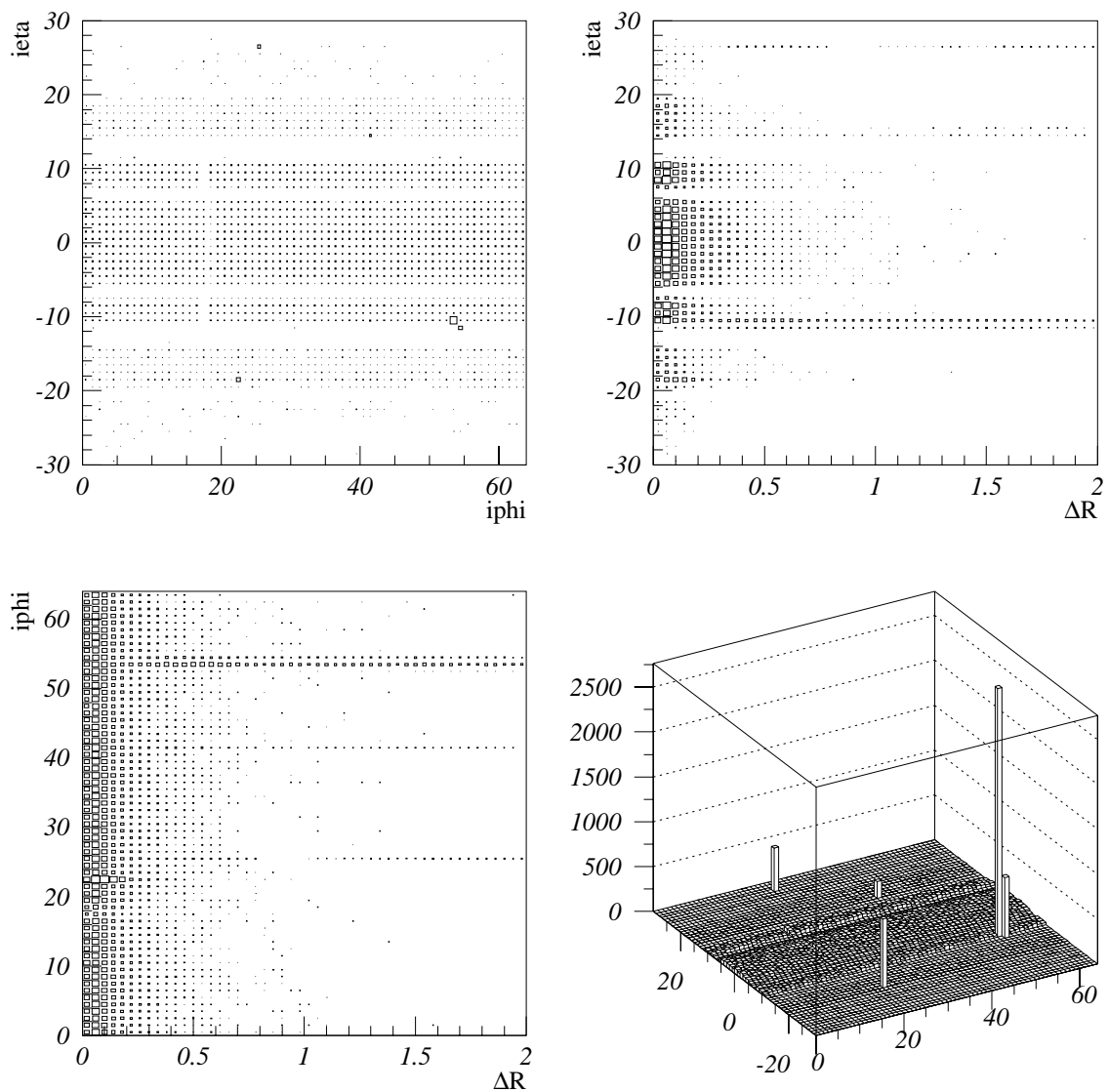


Figure 4.4: Different scatter plots of the AIDA cells in layer 15: $i\eta$ vs. $i\phi$ (top left), $i\eta$ vs. ΔR (top right), $i\phi$ vs. ΔR (bottom left), and a “lego” plot of $i\eta$ vs. $i\phi$ (bottom right). The THCC’s can clearly be identified due to their high frequency of appearance.

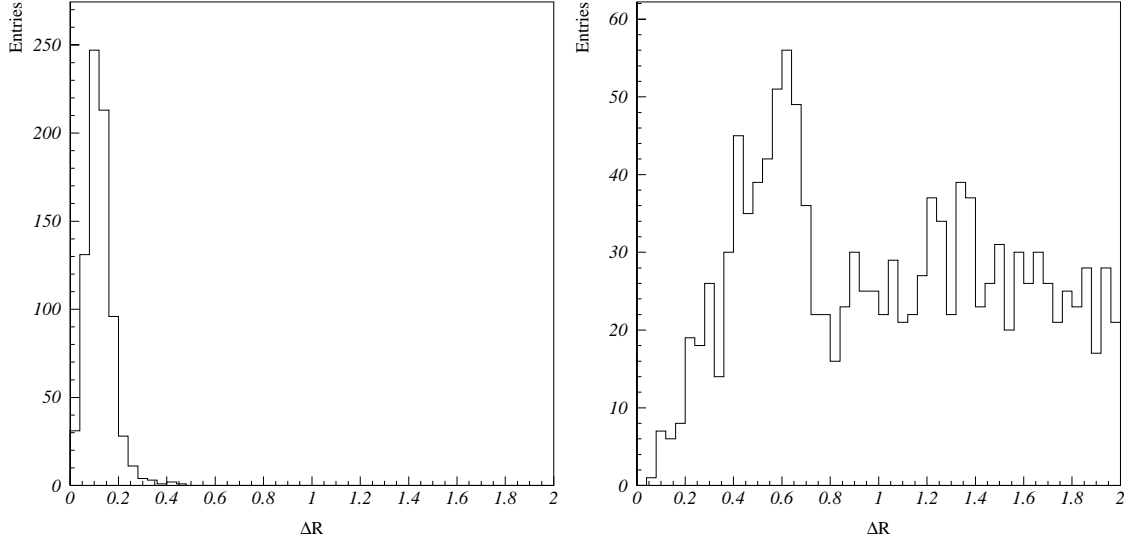


Figure 4.5: The ΔR distributions of two THCC candidates among the cell removed by AIDA with packed integer ID's of -192315 (left) and -134917 (right). Difference between the two is apparent—the cell -192315 is most likely a jet-belonging cell incorrectly removed by AIDA while the cell -134917 has the ΔR distribution very much alike of that of the THCC.

that this cell most likely is not a randomly firing THCC but rather a jet-associated cell and as such was incorrectly removed by AIDA. Therefore, such cells should be allowed to be restored to jets, while cells like -134917 should be identified as a THCC and must be removed before the restoration procedure. Having examined the ΔR distributions of all 30 THCC candidates, only 26 of them were identified as THCC's and they are listed in Table 4.2.

The only cell with relatively high frequency of occurrence remaining in these plots is the cell -192315 which despite this has not been identified as a THCC based on its ΔR distribution (see the discussion in the previous paragraph). Furthermore, removal of the THCC's significantly cleans the ΔR distributions, as can be seen by comparing the cleaned ΔR distributions in Figures 4.6 to the original ΔR distributions with THCC's presented in Figures 4.1.

Calorimeter Module	Layer Number	Packed Integer ID of THCC's
EM1	1	+075701
EM2	2	+085802, +114502
EM3	3(4, 5, 6)	−243803, −026403, +042503, +186003
EM4	7	+024807
CCMG	8	None
ICD	9	+092209, +102209, +112209, +131509
ECMG	10	+084510, +084610
FH1	11	None
FH2	12	+021412, +133012
FH3	13	−315013, −084113,
FH4	14	None
CH1	15	−125515, −115415, +154215, +272615
CH2	16	None
CH3	17	−133017, −134917, −135017, −114217

Table 4.2: THCC's found among the cells removed by AIDA.

The remaining AIDA cells can be restored if they pass two requirements. One of them is based purely on “geometrical” considerations and requires a cell to be within

$$\Delta R < 0.7 \tag{4.13}$$

of the jet's centroid in order for it to be restored to this jet. The choice of 0.7 matches the cone size of jets used in these studies, it is a reasonable choice based on the cleaned ΔR distributions everywhere in the detector (i.e. in every pseudorapidity region), and it is very “efficient” as can be seen in Figure 4.6.

Another variable is also checked before allowing the AIDA cell into the jet.

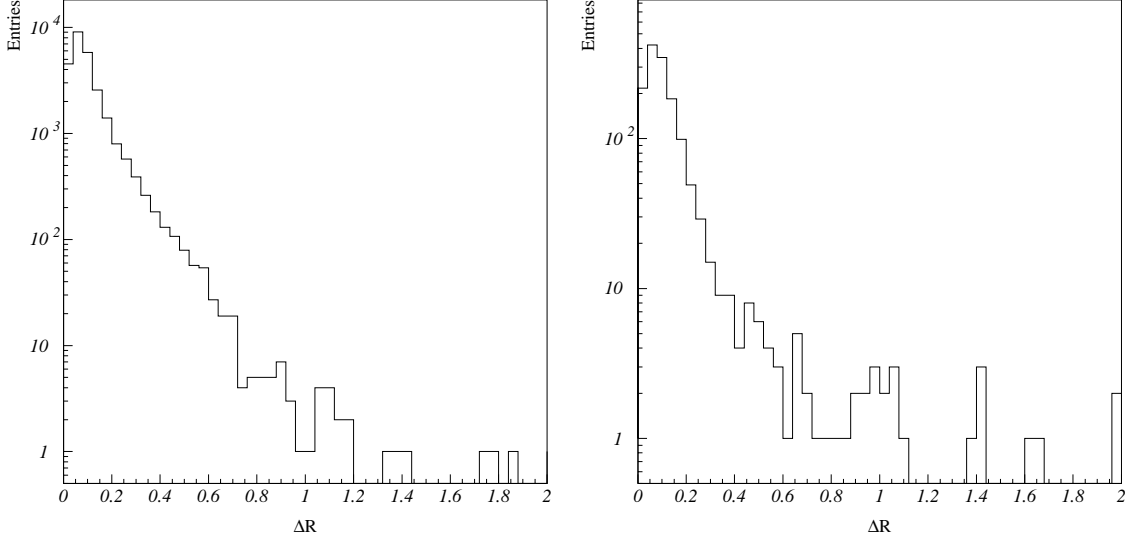


Figure 4.6: The ΔR distributions for jets with $0.0 \leq |\eta_d| < 1.0$ and E_T of 100–120 GeV (left) and with $1.5 \leq |\eta_d| < 3.0$ and E_T of 40–60 GeV (right) after the removal of the THCC’s.

It is referred to as f_{E_T} and is defined as:

$$f_{E_T} = \frac{E_T^{cell}}{E_T^{jet} + E_T^{cell}}. \quad (4.14)$$

The f_{E_T} distributions for different η_d regions and jet E_T are shown in Figure 4.7 for the events with only one AIDA cell present after the THCC’s are removed from the sample and for those jet-AIDA cell pairs that pass the $\Delta R < 0.7$ requirement. Based on these distributions, the reasonable and “efficient” choice of the f_{E_T} “cut” is 0.5 which is equivalent to requiring the candidate AIDA cell to have transverse energy less than that of the jet. Thus the second requirement is more of a kinematic cut:

$$E_T^{cell} < E_T^{jet}, \quad (4.15)$$

and it must be satisfied simultaneously with the ΔR requirement of Eq. 4.13.

If an AIDA cell is *not* a THCC and it passes the two restoration criteria as defined in Eqs. 4.13 and 4.15, it is added back to the jet. Jet kinematic variables

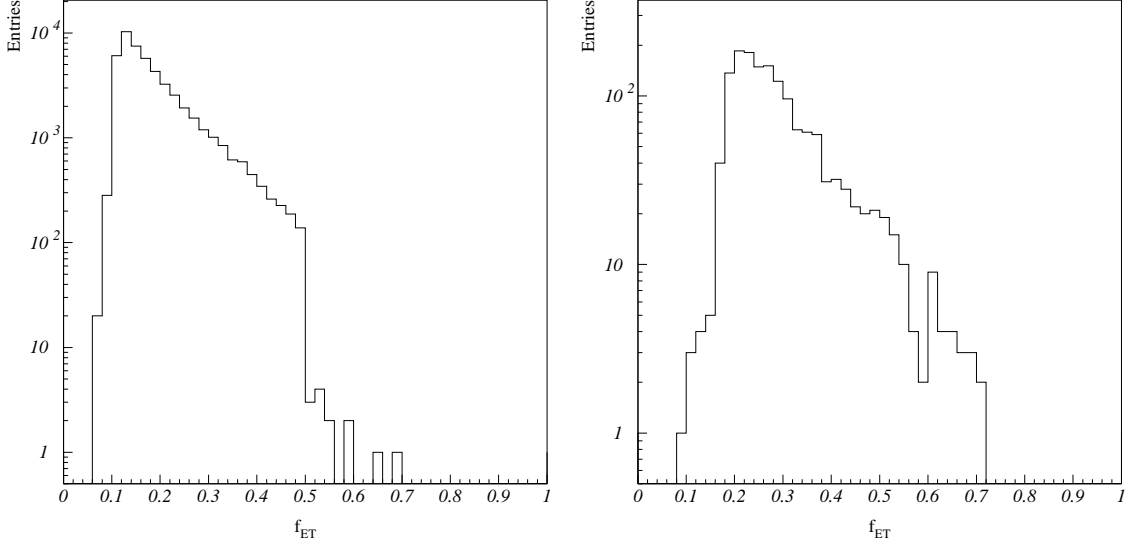


Figure 4.7: The f_{E_T} distributions for jets with $0.0 \leq |\eta_d| < 1.0$ and E_T of 80–100 GeV (left) and with $1.5 \leq |\eta_d| < 3.0$ and E_T of 40–60 GeV (right) after the removal of the THCC's.

are then re-calculated following the Snowmass accord [50] (as the corresponding calculations consistent with the DØ definitions cannot be performed from ntuple information):

$$E_T^{jet} \longrightarrow E_T^{jet} + E_T^{cell} \quad (4.16)$$

$$\eta_{jet} \longrightarrow \frac{\eta_{jet} \cdot E_T^{jet} + \eta^{cell} \cdot E_T^{cell}}{E_T^{jet} + E_T^{cell}} \quad (4.17)$$

$$\varphi_{jet} \longrightarrow \frac{\varphi_{jet} \cdot E_T^{jet} + \phi^{cell} \cdot E_T^{cell}}{E_T^{jet} + E_T^{cell}}. \quad (4.18)$$

In addition, the restored cell is vectorially subtracted from the missing transverse energy of the event:

$$\vec{E}_T \longrightarrow \vec{E}_T - \vec{E}_T^{cell}. \quad (4.19)$$

Because of the E_T weighted re-calculation of the pseudorapidity and azimuth of jet's centroid according to Eqs. 4.17 and 4.18, we sort AIDA cells in ascending order in E_T (i.e. starting with the lowest E_T cell) prior to restoration.

The reason is that if a high E_T cell gets restored to a jet first, then the re-calculation of jet’s centroid may not allow another, lower E_T cell to get restored to the same jet—it may fail the ΔR restoration criteria only because the jet’s centroid has already moved significantly due to the first cell’s high transverse energy. If we start with the lowest E_T cell, then the jet’s centroid does not move as much because of the E_T weighted scheme of its re-calculation, and this may effectively allow more cells to get restored to this jet.

Each time an AIDA cell gets restored to a jet, it is removed from the list of AIDA cells, and the corresponding original jet is replaced by the “restored” jet, whose kinematic quantities are now given by Eqs. 4.16–4.18. This means that when the next cell from the AIDA cell list is checked on the restoration criteria of Eqs. 4.13 and 4.15, the most current jet quantities will be used. The reader will notice that the re-calculation of the jet kinematic variables every time a cell gets restored to it may cause a problem when the AIDA cells appear in groups very close to each other in $\eta - \varphi$ space (for example, due to a BLS card failure) and a jet happens to be nearby. Of course, it would be a mistake to restore such cells to the jet. However, in such cases the $\Delta R < 0.7$ will most likely be passed by most of these cells and only the $E_T^{cell} < E_T^{jet}$ cut may stop a jet from “picking up” all or most of these cells. But the E_T of the jet is *increased* each time one of these cells is being restored to it according to Eq. 4.16, and thus it is going to be less and less likely for the next cell to fail the E_T requirement. This way the jet may pick up many or all of such cells, obviously creating a bad jet. Nevertheless, such events or jets are then more likely to be removed by the event or jet quality cuts (especially by the \cancel{E}_T fraction cut). On the other hand, not re-calculating the jet quantities, and in particular its E_T , may allow fewer such cells to be restored to it, making it

more feasible for such jets or events to pass the quality cuts and hence contaminate the sample.

Whether or not we sort AIDA cells prior to restoration and re-calculate jets each time a cell gets restored to it will yield the same results most of the time since, as it was shown earlier, events with $\text{NAID} = 1$ dominate. However, we have calculated the difference between the fraction of the cells being restored in each bin of NAID when sorting the cells *and* re-calculating the jet quantities each time a cell gets restored to it and without doing any of this. The result is intuitively expected: when one sorts and re-calculates, the fraction of the restored cells is higher by 0.9%, 2.2%, and 4.4% for the events with NAID of 2, 3, and 4, respectively. (As NAID increases, this difference becomes even larger. However, the fraction of events with $\text{NAID} \geq 5$ is less than a tenth of a percent and therefore the overall effect is negligible.) Therefore, our choice is to sort cells in ascending order in E_T and to recalculate the jet quantities each time a cell gets restored to a jet.

To summarize, this is how the AIDA cell restoration algorithm (ACRA) works:

- (1) If the DØ J.E.S. correction has been applied to jets, un-correct them.
- (2) Remove the THCC's from the AIDA cell list.
- (3) Sort the remaining AIDA cells in ascending order in E_T and start with the first cell (i.e. lowest E_T cell) in this list.
- (4) For the AIDA cell under consideration, calculate ΔR with respect to every jet in the event, using the most current, updated jet quantities.

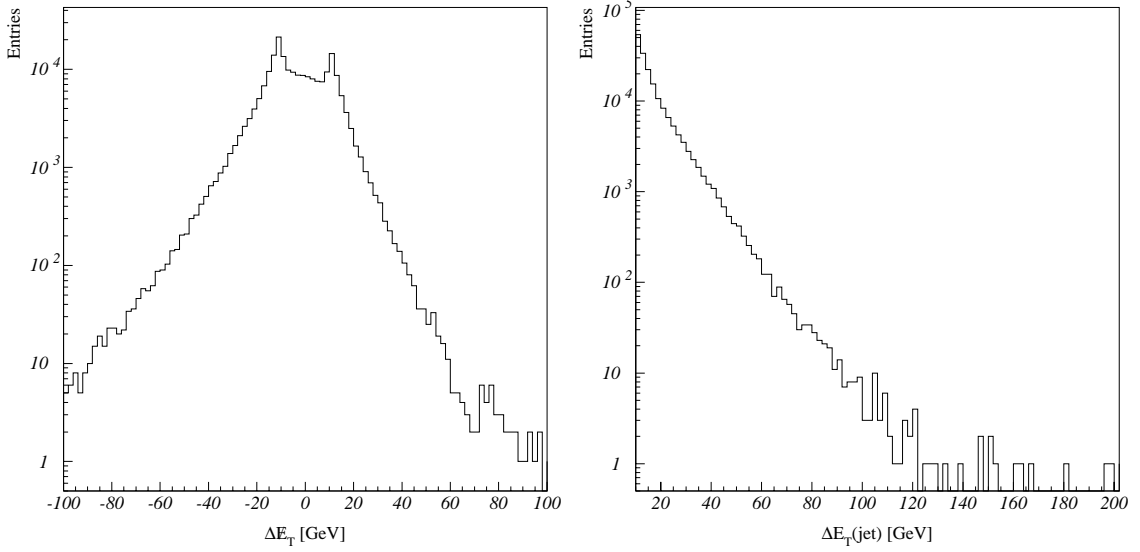


Figure 4.8: The distributions of change of the missing E_T of the event (left) and the jet E_T (right) due to ACRA. Note the logarithmic scales.

- (5) Beginning with the *nearest* jet, check if this cell passes the ΔR and the E_T requirements of Eqs. 4.13 and 4.15.
- (6) If so, add this cell to the jet, i.e. re-calculate the jet quantities according to Eqs. 4.16–4.18 and the \cancel{E}_T of the event according to Eq. 4.19. Remove this cell from the AIDA cell list and go to the next cell (i.e. step 4 above).
- (7) If this cell does not pass the restoration criteria, go to the next nearest jet in the event. Once all the jets are checked, go to the next AIDA cell (step 4 above) until all AIDA cells are examined.
- (8) Apply the J.E.S. correction to all jets in the event if they had been un-corrected for performing this restoration procedure.

Figure 4.8 shows distributions of the change in the \cancel{E}_T of the event and the jet E_T due to restoration. The \cancel{E}_T of the event decreases 64% of the time after

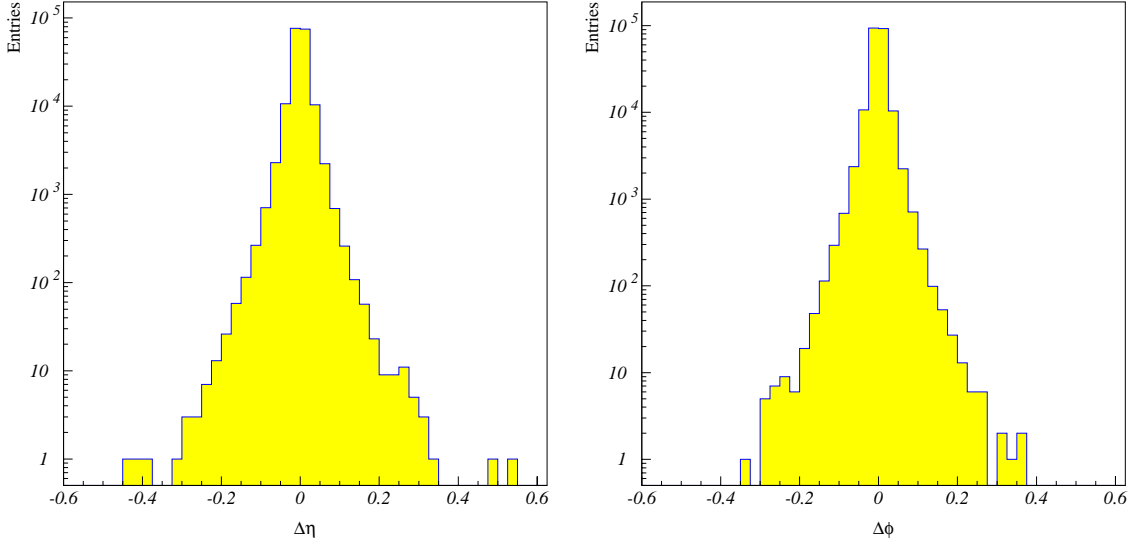


Figure 4.9: The distributions of change of the pseudorapidity η (left) and azimuth φ of a jet due to ACRA. Note the logarithmic scales.

applying the ACRA. One may expect the \cancel{E}_T of the event to always decrease if the restoration algorithm works properly. However, due to finite detector resolution and possible miscalibration, the \cancel{E}_T can either decrease or increase—only in case of an ideal detector one may expect the \cancel{E}_T to always decrease. The possibly symmetric background in this plot due to the finite detector resolution is very hard to estimate in order to give some reliable numerical measure of this effect. On the other hand, the change in the jet E_T is 20 GeV or greater 24% of the time, and 40 GeV or greater 3% of the time.

Finally, Figure 4.9 shows distributions of the change in the pseudorapidity η and the azimuth φ of a jet due to the ACRA. The shapes are rather symmetric indicating no bias in either direction. In addition, the absolute magnitude of the change is rather small—both $\Delta\eta$ and $\Delta\varphi$ distributions having an *rms* of about 0.02.

4.5 The $\vec{\mathcal{H}}_T$ Correction

Due to the high instantaneous luminosity in Run 1B, the tracking system often finds more than one vertex for the primary interaction point, and it may make a mistake in determining which of the vertices in fact corresponds to the primary interaction. For events with two vertices present the QCD group has developed a so called misvertexing (or $\vec{\mathcal{H}}_T$) correction [46]. It calculates the vector sum of transverse energies of all jets in the event with respect to both vertices. This global event quantity is referred to as $\vec{\mathcal{H}}_T$.

The magnitude of $\vec{\mathcal{H}}_T$ for the two vertices is compared, and the vertex with the *minimum* value of corresponding \mathcal{H}_T is retained to be the true vertex of the primary interaction. If the true vertex determined by this method is different from the primary vertex as given by the tracking system, all jet kinematic variables are recalculated with respect to this new true vertex using simple geometric conversions. Also, in such cases $\vec{\mathcal{H}}_T$ is taken to be the new missing transverse energy of the event because the event $\vec{\cancel{E}}_T$ as given by RECO is defined as a vector sum of all calorimeter *cell* transverse energies with respect to the primary vertex and it cannot be recalculated from ntuple information. Moreover, there is a strong correlation between the $\vec{\cancel{E}}_T$ of the event and the \mathcal{H}_T as illustrated in Figure 4.10, justifying the replacement of the $\vec{\cancel{E}}_T$ with the \mathcal{H}_T in cases when the $\vec{\mathcal{H}}_T$ algorithm picks the second vertex as primary.

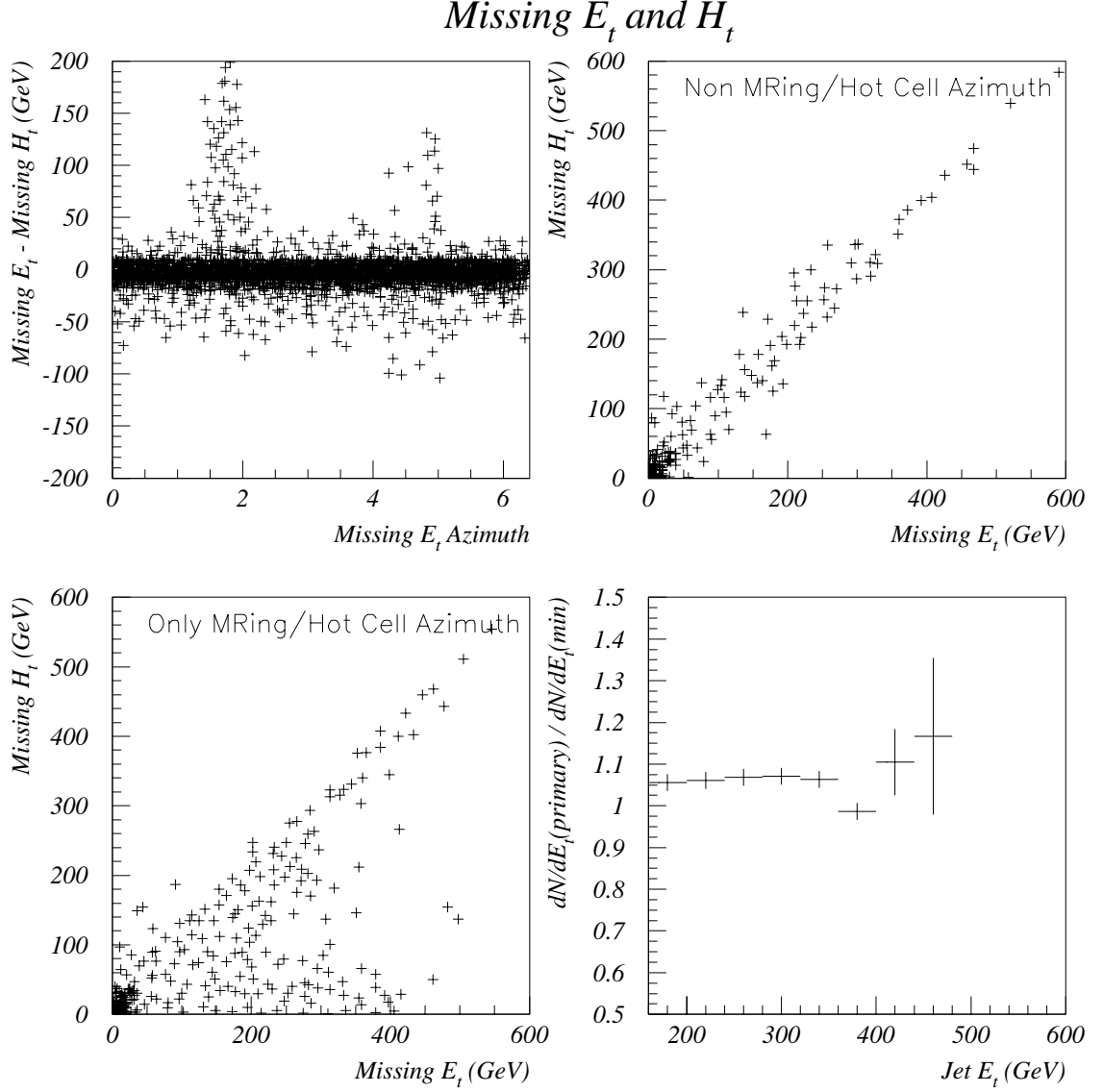


Figure 4.10: Correlation between the event \cancel{E}_T and the \mathcal{H}_T . The sample with the MR and hot cells removed clearly shows that the two quantities are highly correlated (top right). Choosing the correct vertex lowers the cross section by about 5% on average (bottom right).

4.6 The Total η Bias Correction

The angular position of jets reconstructed in DØ is usually given by their azimuth φ and pseudorapidity η (or, equivalently, polar angle θ). The cross sections in

this analysis are averaged over φ and thus the only relevant measure of jet's angular position is η . It has been observed in full MC simulations that reconstructed calorimeter jets are biased towards central rapidities compared to their particle level counterparts [64]. The detailed analysis of this effect is described in this section.

In addition, at DØ, we compare the measured jet cross sections to the partonic level theoretical predictions (usually, with JETRAD), which use the Snowmass accord as a default for combining partons into jets. The standard DØ jet finding and reconstruction algorithm is different from the Snowmass accord in calculating jet angles, as can be seen by comparing Eqs. (4.1) to Eqs. (4.7). The effects of DØ versus Snowmass definitions have been addressed in the past as well [65].

Jet reconstruction and differences in algorithms may introduce biases in some jet quantities. The relevant jet quantities have to be checked against such biases and, if necessary, corrections must be derived. The jet cross sections that we measure correspond to *particle* level cross sections, i.e. prior to jets entering the calorimeters. Therefore, our goal is to derive the corrections to take a DØ Calorimeter Jet (call it DØCJ) to the corresponding jet that would have been measured by the Snowmass algorithm at the particle level, or a Snowmass Particle Jet (SNPJ). All possible biases arising due to the reconstruction and algorithm differences are pictorially shown in Figure 4.11 by the arrows. One can think of a “true” jet to be a SNPJ (Snowmass Particle Jet) in the upper left corner of the rectangle. Then the possible biases may distort the corresponding jet quantities via the two possible routes to its reconstructed value as measured with the standard DØ algorithm—the bottom right corner of the rectangle, or DØCJ. It is this net or combined change in a given jet quantity that is of interest. We refer to this combined bias as a *total*

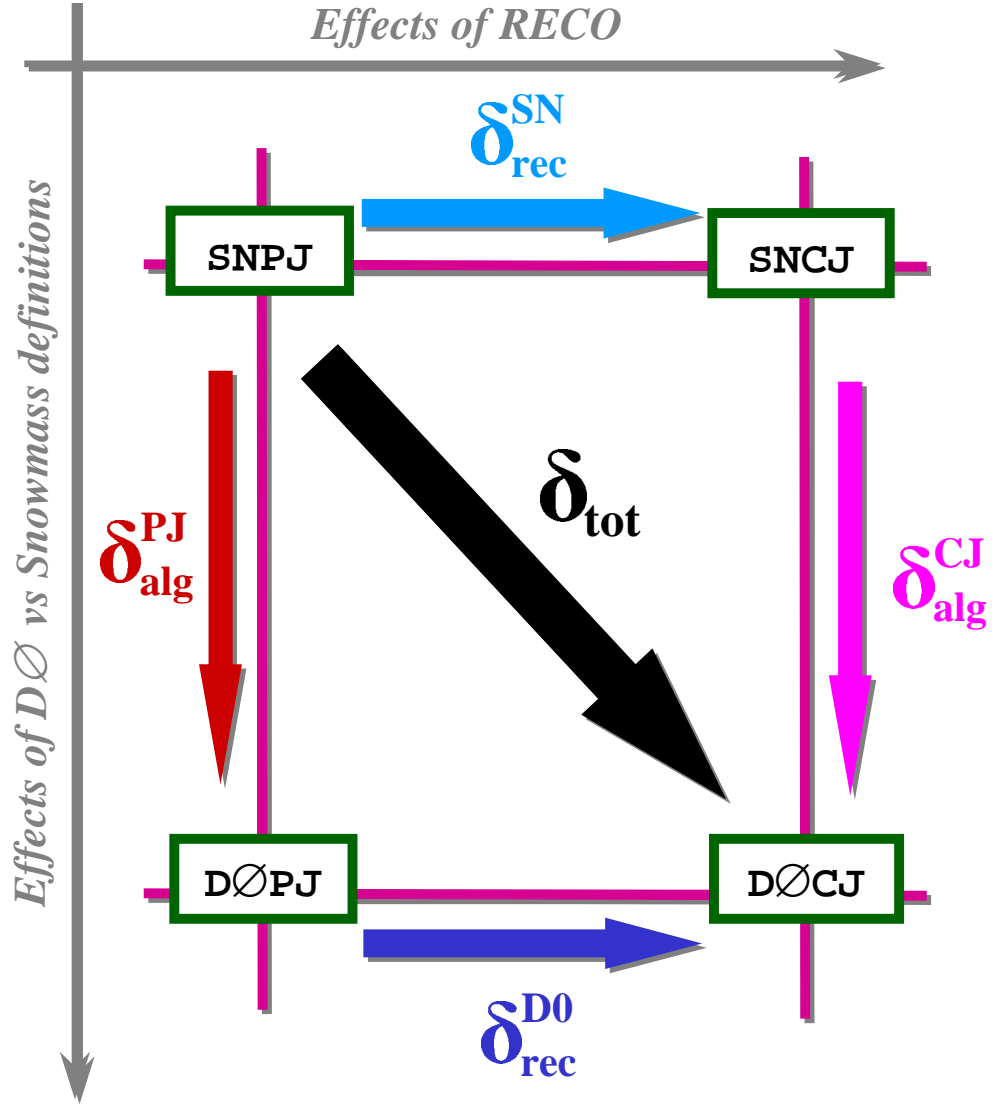


Figure 4.11: Possible biases in any jet quantity due to reconstruction and algorithm differences.

bias, δ_{tot} , which can be thought of as a “direct sum” of the two biases due to the two different effects considered. For example: $\delta_{\text{tot}} \sim \delta_{\text{alg}}^{\text{PJ}} \oplus \delta_{\text{rec}}^{\text{DØ}}$, as the corresponding “vector” sum triangle rule would indicate in Figure 4.11.

To address this concern, we analyzed a HERWIG+SHOWERLIB’ed MC [66] sample which has *both*, particle and calorimeter jets reconstructed with *both* DØ

and Snowmass algorithms. That is to say, the four, generally different, jets as shown in the four corners of the rectangle in Figure 4.11 are all available. Our eventual goal is to derive a correction, if necessary, for the *total bias* that would take the DØCJ to the corresponding particle jet SNPJ.

However, it is interesting as well as necessary for completeness to examine the two biases of different origin (i.e. reconstruction versus definition) separately as well. In addition, although we suspect the biases in both cases to appear only in jet pseudorapidity as a function of η itself, other jet quantities (such as azimuth, E_T , etc.) must also be checked for possible biases, and the dependence of possible biases on jet quantities other than pseudorapidity must be examined as well.

First of all, the four different jets in the MC sample are matched up according to their separation in $\eta - \varphi$ space where the distance ΔR is defined in the usual way, $\Delta R = \sqrt{(\Delta\eta)^2 + (\Delta\varphi)^2}$. The reference jet is always the DØCJ. Jets are matched as follows. Consider two types of jets, X and Y, and let there be N_X jets of type X, and N_Y jets of type Y. A matrix of dimension $(N_X \times N_Y)$ is built, with the elements being the distances in $\eta - \varphi$ space $\Delta R(I_X, I_Y)$, $I_X = \overline{1, N_X}$, and $I_Y = \overline{1, N_Y}$, between *all* possible pairs of jets of type X and Y. The smallest distance $\Delta R(I_X, I_Y)$ is found in the matrix, the corresponding jets I_X and I_Y are paired/matched, and the corresponding I_X -th row and I_Y -th column of the matrix are “erased”, or ignored from any further consideration. Then, in the remaining elements of the matrix (that is, ignoring all columns and rows of previously identified pairs), the procedure for finding the smallest distance R is repeated until all possible pairs—which cannot be more than $\min(N_X, N_Y)$ —are found.

Next, the average difference of the jet quantity suspected for bias is studied

as a function of various jet quantities to get a general understanding of the biases and their magnitudes. For instance, one can study a bias in jet η between SNCJ and SNPJ. We first examine average biases of the matched jets, without any cut on ΔR . However, it turns out that a loose ΔR cut is necessary. The reason is that not all particle level jets may have the corresponding calorimeter jets reconstructed due to the differences in E_T thresholds, energy resolutions, etc. This may lead to badly mismatched jets with unexpectedly large values of ΔR , contributing to the background at large values of the distributions of ΔR . They can be removed by a rather loose cut of $\Delta R < 0.7$, the radius of the algorithm cone itself. One should be careful when applying such a cut not to bias the measurement of the bias itself. Various other cut values have been checked and no measurable biases have been observed as long as the cut value is in the order of the jet cone radius, hence our choice of the cut value of 0.7 [67]. To reiterate, the cut $\Delta R < 0.7$ is very efficient in removing mismatched jet background and at the same does not bias the measurement.

We consider all jets above E_T of 10 GeV in this study. Having studied biases in jet η and φ , we see that the biggest effect is on jet η , as expected [67]. Figure 4.12 shows all four, plus the *total*, biases in jet η as a function of $\eta^{\text{D}\emptyset\text{CJ}}$ for *all* jet energies. The top squares and upward triangles show the effect on jet η due to the algorithm differences alone. They respectively correspond to $\delta_{\text{alg}}^{\text{CJ}}$ and $\delta_{\text{alg}}^{\text{PJ}}$ in Figure 4.11. The bias is calculated with respect to the reference jet which is the jet at the origin of the corresponding bias “vector” in Figure 4.11; for example, $\delta_{\text{alg}}^{\text{PJ}}[\eta] = \eta^{\text{D}\emptyset\text{PJ}} - \eta^{\text{SNPJ}}$. However, the bias is always plotted against quantities of the jet D \emptyset CJ, which serves as an overall reference point in these studies. It is seen that the bias due to definition differences is larger in the calorimeter jets (triangles)

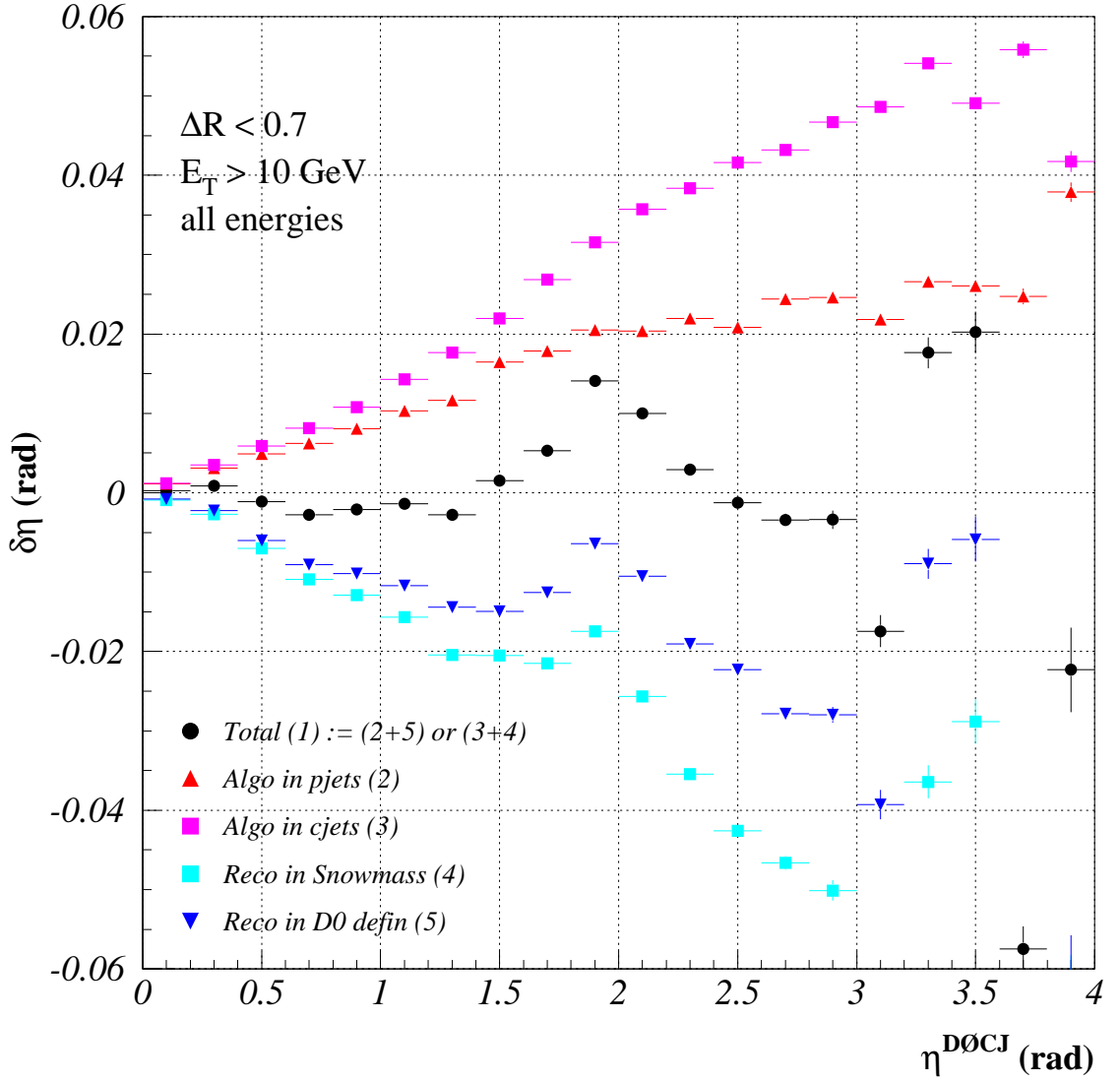


Figure 4.12: Biases in jet η due to differences in jet angle definitions (top squares and upward triangles) and due to the reconstruction (bottom squares and downward triangles). Filled circles show the *total* η bias.

compared to the particle jets (squares) which is a consequence of additional smearing effects that the calorimeters introduce. The notable feature of this bias is that it plateaus at $\eta^{\text{DØCJ}} \approx 2.0$ in case of particle jets. The plateau is less prominent and seems to appear at higher η 's in case of the calorimeter jets.

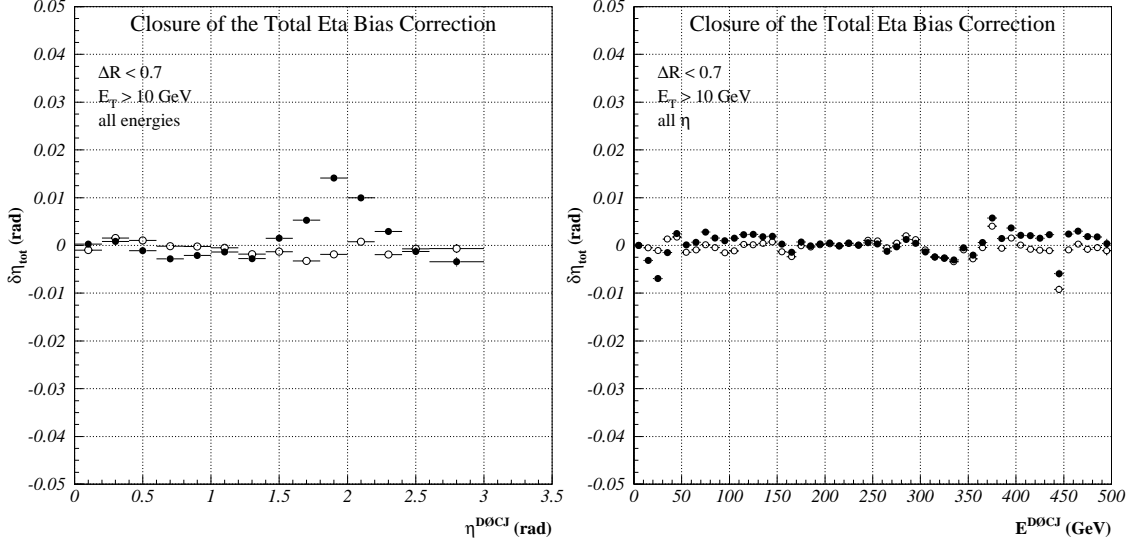


Figure 4.13: Closure of the parameterization of the *total* η bias correction as a function of DØ jet η for all energies (left) and as a function of energy for all pseudorapidities (right).

The bottom squares and downward triangles in Figure 4.12 indicate the biases in jet η due to reconstruction alone with the Snowmass and DØ algorithms, respectively $\delta_{\text{rec}}^{\text{SN}}$ and $\delta_{\text{rec}}^{\text{DØ}}$ of Figures 4.11. It is seen that the bias in case of the DØ definitions is smaller (triangles). The dip in the $\eta^{\text{DØCJ}}$ region of 0.5–1.8 is due to the degraded response in the intercryostat region as a result of which jets are pulled towards more central pseudorapidities. The increase of the effect above $\eta = 3$ is attributed to the fact that jets start to lose a significant part of their energy through the beam pipe, which also results in pulling jet centroids to lower η 's.

It is evident that the biases due to algorithm differences and to reconstruction go in opposite directions, nearly canceling each other. Filled circles show the net or the *total* η bias indicating a maximum bias of about 0.15 radians for jet η 's below 3.0.

The total η bias is also studied as a function of jet energy which is an

unbiased quantity—definitions of jet angles do not affect it. Slight dependence on jet energy is observed. Therefore, we fitted the total η bias as a function of $\eta^{\text{D}\emptyset\text{CJ}}$ in 6 energy bins from 20 to 500 GeV to 3-rd to 4-th degree polynomials in combination with a Gaussian as necessary. The details can be found in reference [67] which also lists the routine that provides the total η bias correction as a function of the $\text{D}\emptyset\text{CJ}$ η and energy. The closure plot showing the total η bias before (filled circles) and after (open circles) application of the correction derived in such a way is presented in the left plot of Figure 4.13 as a function of $\eta^{\text{D}\emptyset\text{CJ}}$ for all energies. The right plot in the same Figure shows the total η bias correction closure as a function of jet energy for *all* pseudorapidities. The closure is excellent. An uncertainty on jet η of ± 0.005 rad is assumed and the cross sections are rederived with this uncertainty applied to jet η . The total η bias error is on the order of 2–4% and decreases with decreasing jet pseudorapidity.

We also check possible biases in jet azimuth. There is a slight φ -bias present which presumably is an artifact of the Monte Carlo sample. It most likely has to do with the φ misalignment of the calorimeters in the MC, or the bias in the single particle shower MC generator. In any case, since the majority of physics analyses are not going to be affected by a bias in an absolute jet azimuth, and because its magnitude is small (about 0.01 rad at most), we do not concentrate on this issue.

Finally, we note that although there is a bias in jet η , there is none in jet E_T . The reconstruction η bias moves jet centroid so insignificantly (compared to the calorimeter tower segmentation of 0.1×0.1 in $\eta - \varphi$) that it does not cause wrong calorimeter towers to get assigned to a jet. According to the $\text{D}\emptyset$ jet definition, jet E_T is a sum of the E_T 's of individual towers inside the fixed algorithm cone and

therefore, in the process of reconstruction, jet E_T can only get biased if wrong towers are assigned to a jet. Since this does not happen we conclude that no recalculation of jet E_T is required when correcting for jet η . The situation would have been different if jet p_T were actually used. It would be affected because the bias in the jet centroid is *independent* of its magnitude. We also remark that jet E_T 's are defined in the same way in DØ and in the Snowmass accord eliminating the second possible E_T bias source as well. To summarize, we apply the total η bias correction to jet η but do not recalculate jet E_T . The total η bias correction is applied after all other reconstruction as well as jet energy scale corrections.

CHAPTER 5

DATA SELECTION AND ASSOCIATED EFFICIENCIES

While observed jets at DØ are most often produced as a result of hard $p\bar{p}$ collisions, there are numerous processes that can cause appearance of so called “fake” jets in the calorimeters—the primary tools for jet energy measurement. These processes include cosmic ray bremsstrahlung, losses of protons from the main ring, beam-gas interactions, and some hardware malfunctions such as the appearance of a hot channel due to a high voltage discharge in a calorimeter cell or failure of baseline subtractors (BLS), etc. All of these will occasionally deposit large amounts of “fake” energy in the calorimeter, and may either become a source of “fake” jets, or get reconstructed as part of good jets that happened to be nearby this “fake” deposition of energy, thus damaging these jets.

In addition to various utilities that have been designed to remove hot cells due to electronic failures, the DØ QCD group has developed a number of cuts to be applied event-by-event (event quality cuts) or jet-by-jet (jet quality cuts) in order to remove “fake” jets from the data samples. Naturally, however, these cuts sometimes remove good jets which have just fluctuated outside the range set by the quality cuts. Therefore, it is necessary to determine the good event and good jet efficiencies associated with the quality cuts to compensate for the removal of these good events and jets.

In order to establish such quality cuts and their efficiencies *independent* of the version of the DØ jet energy scale (JES) correction, this portion of the analysis is done *without* the JES correction. Also, the data from the four jet filters (Jet_30, Jet_50, Jet_85, Jet_Max) are combined to increase the statistics of the sample. This method has been checked against possible trigger biases on the quality cut efficiencies and none have been observed [68, 69].

After applying ACRA, the data sample naturally gets divided into two classes of events: Restored (events with at least one restored cell present) and Normal (events with no restored cell). Furthermore, jets from the Restored event sample can be subdivided between two types of jets: Restored (jets with at least one restored cell) and Normal (jets without restored cells, i.e. as given by RECO). Of course, all jets from the Normal event sample are Normal jets as well. This classification has been adopted and is used throughout this section since the different samples may require different treatment. It should be noted that the fraction of Restored jets ranges from about 5% for low E_T jets up to about 10% for high E_T jets [46, 53].

Provided with AIDA cell layer information in the most current version of the Run 1B QCD ntuples, ACRA can re-calculate most of the event and jet quantities if restoration takes place in the event. Among these quantities are the \cancel{E}_T of the event and all jet kinematic variables. One of the jet quantities that can not be re-calculated by ACRA is the hot cell fraction of a jet—defined as a ratio of transverse energies of the second most energetic calorimeter cell to the most energetic cell in the jet¹—because the cell information is not available in the QCD ntuples.

¹The original definition of the HCF at DØ is actually inverse of this but for the purposes of this analysis this definition is used.

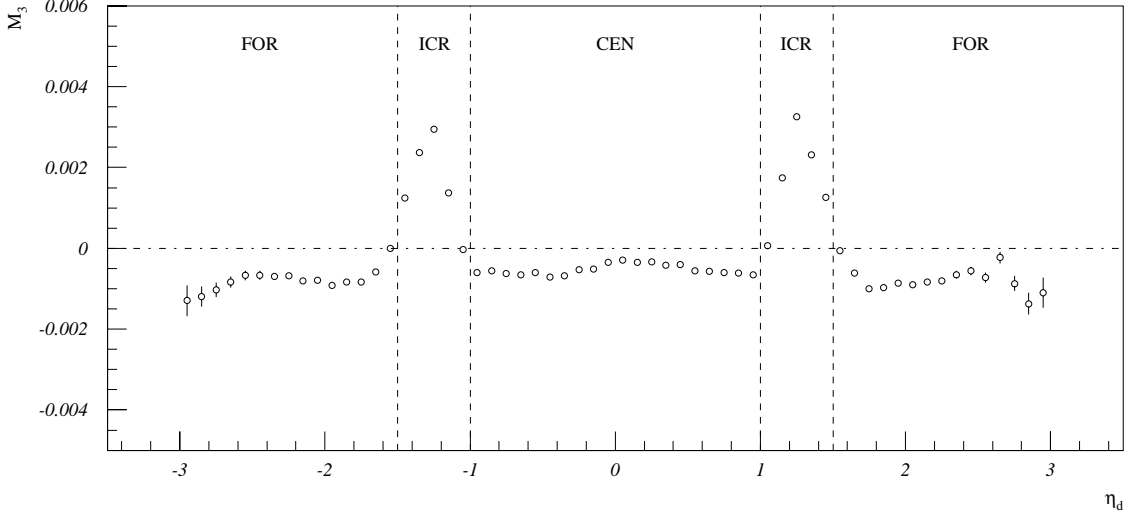


Figure 5.1: The third moment about the mean \mathcal{M}_3 of the EMF distributions of Normal jets as a function of jet η_d for jet E_T of 40–60 GeV. Only the vertex cut $|Z| < 50$ cm has been applied.

Efficiencies of jet quality cuts are expected to be functions of jet transverse energy E_T and detector pseudorapidity η_d . Therefore the final combined data sample is binned in E_T and η_d . The choice of a particular E_T binning is driven purely by statistics and is somewhat arbitrary but, for consistency, the efficiencies for different cuts are calculated in the *same* E_T bins.

The binning in η_d is planned so as to best isolate non-uniformities in the calorimeter coverage as a function of η_d . These include differences between the central and the forward calorimeters as well as poorly instrumented detector regions such as intercryostat region (ICR) with intercryostat detectors and massless gaps. Therefore the choice of a particular η_d binning is guided by the DØ detector geometry. In addition, the electromagnetic fraction of a jet’s transverse energy (EMF) is sensitive to the ICR since this region has non-uniform electromagnetic coverage. Therefore the EMF is used to better identify the boundaries of this region.

For low and high values of η_d , the EMF distributions resemble (visually) a Gaussian distribution while in the ICR they are strongly shifted and skewed towards lower values of EMF [69]. Such behavior of distributions is statistically well described by odd moments of distributions about the mean. The lowest order odd moment of interest is the third moment \mathcal{M}_3 , or “skew”. For a normalized, continuous distribution $f(x)$ of a random variable x the third moment about its mean $\langle x \rangle$ is generally defined as:

$$\mathcal{M}_3 = \int_{-\infty}^{\infty} (x - \langle x \rangle)^3 f(x) dx. \quad (5.1)$$

It must be noted that \mathcal{M}_3 as well as all higher order odd moments are exactly zero for a Gaussian distribution. Third moments of the EMF distributions of Normal jets are then calculated in fine η_d bins of 0.1 (equal to detector granularity) and are plotted against η_d in Figure 5.1 for jets with E_T of 40–60 GeV. Similar plots for Normal jets of higher E_T are presented in [69]. Error bars on these plots correspond to standard statistical errors equal to the square root of the variance of the third moment. The variance itself is given by [70]:

$$\text{Var}(\mathcal{M}_3) = \mathcal{M}_6 - \mathcal{M}_3^2 - 6\mathcal{M}_4\mathcal{M}_2 + 9\mathcal{M}_2^3, \quad (5.2)$$

where \mathcal{M}_n denotes the n -th moment of the distribution about its mean.

The ICR is clearly identified in Figure 5.1 as a region with $\mathcal{M}_3 > 0$ (everywhere else \mathcal{M}_3 being negative) suggesting $1.0 < |\eta_d| < 1.5$ to represent the boundaries of the ICR. The plot also shows the statistically significant deviation of the EMF distributions from a Gaussian distribution (characterized by $\mathcal{M}_3 = 0$) even in the central and the forward regions of the detector. Therefore the following three η_d bins are considered in this study:

$0.0 \leq \eta_d < 1.0$	Central Region (CEN)
$1.0 \leq \eta_d < 1.5$	Intercryostat Region (ICR)
$1.5 \leq \eta_d < 3.0$	Forward Region (FOR)

This binning also follows the detector geometry and is very close to the choices of the η_d binning made in earlier studies [71, 72, 73].

5.1 Determination of Jet Quality Cuts

For the determination of jet quality cut values the studies are limited to the Normal jet sample. We present limited number of illustrative plots and the reader is referred to [69] for a complete set of plots as well as more detailed discussions where applicable.

5.1.1 Electromagnetic Fraction Cut

The electromagnetic fraction of a jet (EMF) is defined as a fraction of its transverse energy deposited in electromagnetic modules of the calorimeters. By definition then the EMF is sensitive to large depositions of fake energy by a noisy cell located in either the electromagnetic or the hadronic layers of the calorimeters. In the former case, the fake energy will produce an excess at the high end of the EMF distribution while in the latter case noise will mostly appear at low values of the EMF distribution. The cuts on the EMF are therefore designed to remove such noise.

Typical distributions of the EMF with different event cuts applied beforehand are shown in Figure 5.2 for the CEN region and jet E_T of 100–120 GeV. The

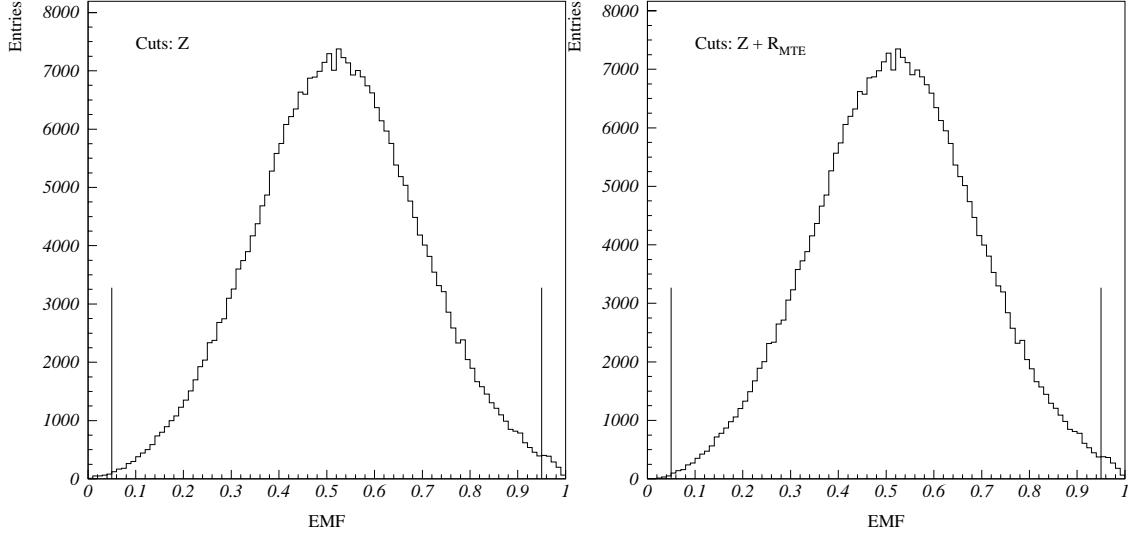


Figure 5.2: The EMF distributions of Normal jets in the CEN region for jet E_T of 100–120 GeV with only the Z cut applied (left) and with the Z and the R_{MTE} cuts applied (right). Vertical lines indicate the low and the high EMF cuts.

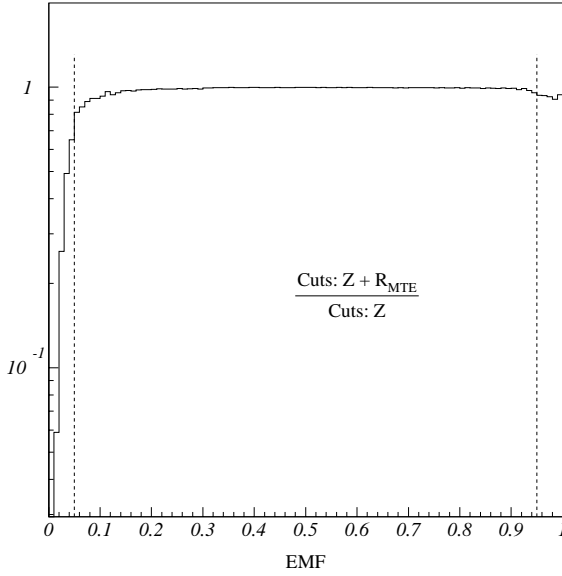


Figure 5.3: The ratio of the EMF distributions with and without the R_{MTE} cut (in addition to the standard Z cut) from Figure 5.2. Vertical lines indicate the low and the high EMF cuts.

EMF distributions with only Z cut are compared to the EMF distributions with the missing transverse energy fraction (R_{MTE}) cut applied in addition to the Z cut. The R_{MTE} cut is very powerful in removing noise and therefore the sample is considered to be clean after applying the R_{MTE} cut. The ratio of the EMF distributions with

and without the R_{MTE} cut (in addition to the standard Z cut) is shown in Figure 5.3 for the CEN region. The ratio plots prove that the R_{MTE} cut cleans up the sample and show that the noise in EMF distributions appears approximately below 0.05 and approximately above 0.95.

Note: The goal is to establish the jet quality cuts *independently* from the event cuts to make good jet selection possible even when the R_{MTE} cut is not desirable to use. The ratio plots in the CEN and FOR regions then suggest 0.05 and 0.95 to be a good choice for the EMF cut values since they will remove most of the noise and will be reasonably efficient.

However, as discussed in section 2.5, in the ICR the EMF distributions are shifted and skewed towards lower values due to the lack of electromagnetic modules in this poorly instrumented region of the DØ detector and the low EMF cut of 0.05 should not be applied in this region. Therefore, good jets are selected with:

$$\begin{aligned} 0.00 < \text{EMF} < 0.95 & \quad \text{in the ICR} \\ 0.05 < \text{EMF} < 0.95 & \quad \text{elsewhere} \end{aligned} \tag{5.3}$$

5.1.2 Coarse Hadronic Fraction Cut

The coarse hadronic fraction of a jet (CHF) is defined as a fraction of its transverse energy deposited in the coarse hadronic layers of the calorimeters. The CHF cut is studied after applying the EMF cut. This cut is mostly designed to remove jet-like objects appearing due to the Main Ring (MR) losses in the calorimeter. Along with the MR objects it is also intended to remove jets with noisy cells in the coarse hadronic layers of the calorimeters.

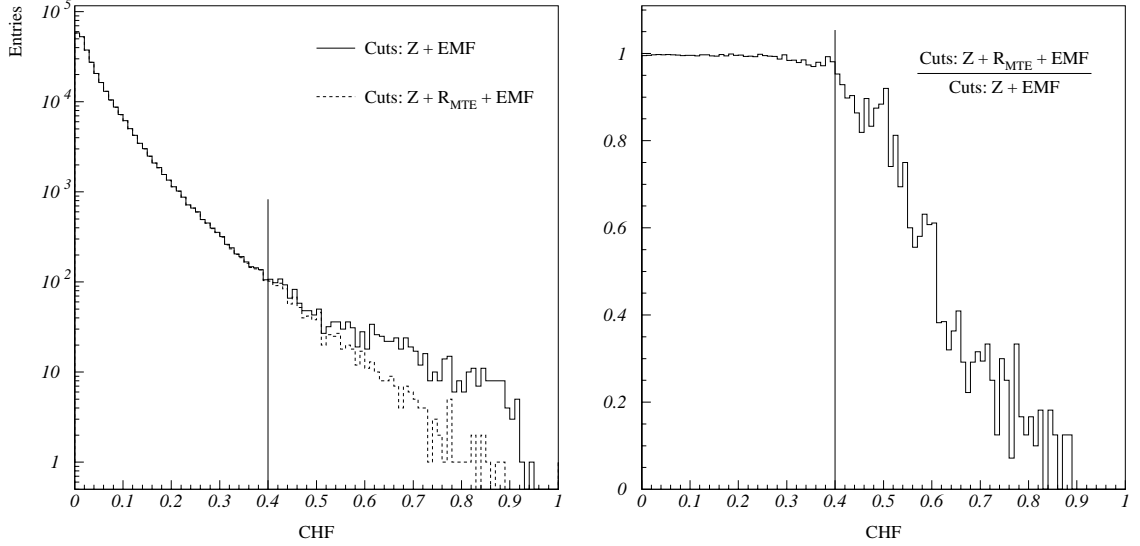


Figure 5.4: The CHF distributions of Normal jets in the CEN region for jet E_T of 100–120 GeV with and without the R_{MTE} cut superimposed on top of each other (left). The ratio of these two distributions is also shown (right). Vertical line indicates the CHF cut.

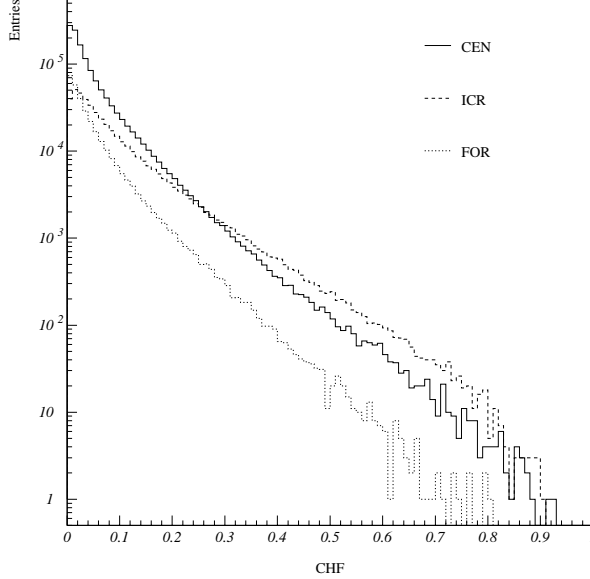


Figure 5.5: The CHF distributions of Normal jets with E_T of 60–100 GeV in the CEN, ICR and FOR regions superimposed. The Z , R_{MTE} and the EMF cuts have been applied.

Following an approach similar to that used for the EMF cut determination, the CHF distributions after the Z and the EMF cuts only are compared to the CHF distributions with the R_{MTE} cut applied in addition to further clean up the sample.

Typical CHF distributions with these two sets of cuts superimposed are shown in Figure 5.4 for the CEN region and jet E_T of 100–120 GeV. It is clear that the noise removed by the R_{MTE} cut mostly appears above CHF of about 0.4. The ratio of these distributions also clearly demonstrates this effect, suggesting the cut value for CHF to be 0.4.

In the ICR, however, CHF distributions are shifted to higher values, see for example Figure 5.5. This is due to the fact that in the ICR there is no or very little material in front of the coarse hadronic layers. Thus it is not surprising that in the ICR larger fraction of jet’s energy is contained in the coarse hadronic layers compared to the CEN or the FOR regions. The 0.4 cut would be inefficient in the ICR, and thus has been moved to a higher value of 0.6 in the ICR only.

In summary, after applying the EMF cuts, good jets are further selected with:

$$\begin{aligned} \text{CHF} &< 0.6 && \text{in the ICR} \\ \text{CHF} &< 0.4 && \text{elsewhere} \end{aligned} \tag{5.4}$$

5.1.3 Hot Cell Fraction Cut

The hot cell fraction of a jet (HCF) is defined as a ratio of transverse energies associated with the second most energetic calorimeter cell to the most energetic cell in the jet. Sometimes RECO finds jets with unusually low values of HCF which means that most of their energy comes from one calorimeter cell. In a good jet, energy is expected to be distributed over many calorimeter cells due to longitudinal as well as lateral development of particle showers in the calorimeters. It is therefore

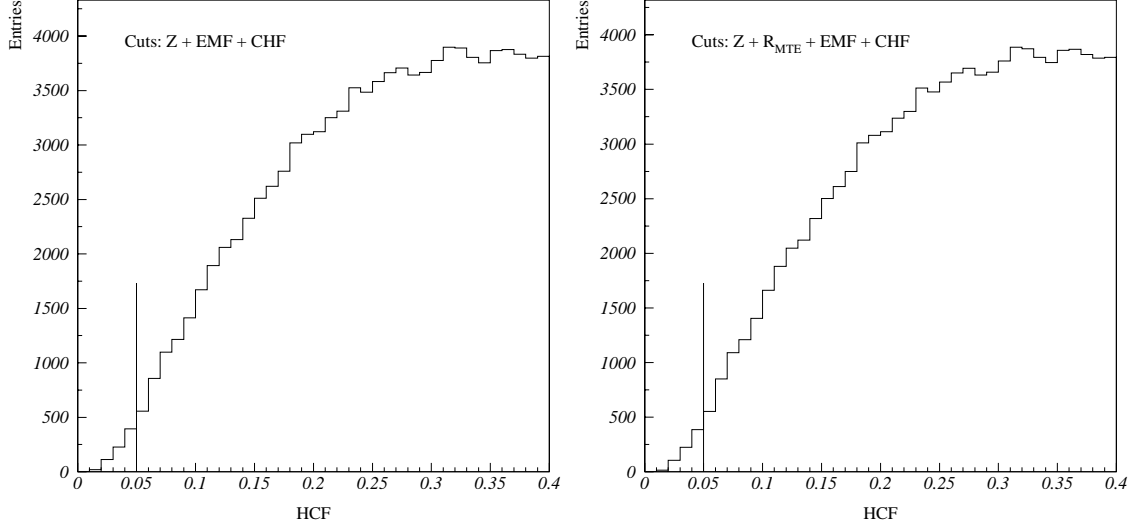


Figure 5.6: The HCF distributions of Normal jets in the CEN region for jet E_T of 100–120 GeV with (right) and without (left) the R_{MTE} cut. Vertical line indicates the HCF cut.

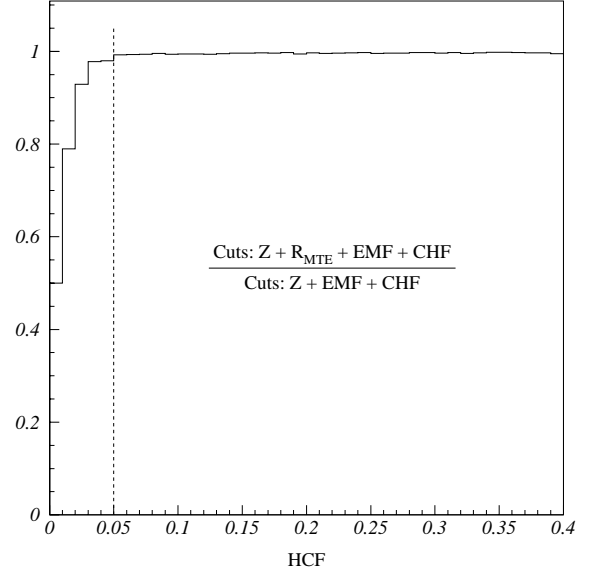


Figure 5.7: The ratio of the HCF distributions with and without the R_{MTE} cut from Figure 5.6. Vertical line indicates the HCF cut.

probable that jets with very low values of HCF are “fake” jets reconstructed from a single electronically noisy cell. The HCF cut thus aims at removing these unphysical jets and is applied after the EMF and the CHF cuts.

Typical HCF distributions after all other cuts have been applied and with

and without the R_{MTE} cut are shown in Figure 5.6 for the CEN region and jet E_T of 100–120 GeV. The distribution with an additional R_{MTE} cut is cleaner, as can be seen from the ratio plot of HCF distributions with and without the R_{MTE} cut in Figure 5.7. Similar plots for the ICR and the FOR region are presented in [69]. The ratio plots then suggest to cut the HCF at 0.05, and therefore after the EMF and the CHF cuts, good jets are selected with

$$\text{HCF} > 0.05 \tag{5.5}$$

everywhere in the calorimeter.

5.2 Determination of Event Quality Cuts

Events are selected by applying cuts on the missing transverse energy and on the position of the reconstructed primary vertex.

5.2.1 Determination of the R_{MTE} Cut

The missing transverse energy fraction of the event is defined as:

$$R_{MTE} = \frac{\cancel{E}_T}{E_T^{lj}}, \tag{5.6}$$

where \cancel{E}_T is the missing transverse energy of the event and E_T^{lj} is the transverse energy of the *leading jet* in the event. The leading jet is also required to be *good*, i.e. to pass jet quality cuts. Detailed studies show that, for cut value determination purposes, this allows combining events and jets independently of whether or not ACRA has been applied to them, and, for the corresponding efficiency calculation purposes, provides us with clean enough subsample [69]. Also, the distributions

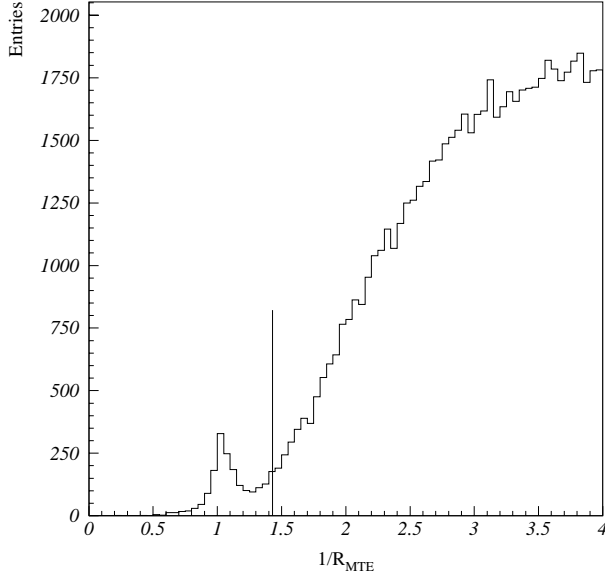


Figure 5.8: The $1/R_{MTE}$ distribution in the CEN region for leading jet E_T of 60–80 GeV. Only the vertex cut $|Z| < 50$ cm has been applied. Vertical line indicates the R_{MTE} cut.

for $1/R_{MTE}$ show the noise more clearly and are more convenient to use for these studies.

A typical $1/R_{MTE}$ distribution is shown in Figure 5.8 for the CEN region and leading jet E_T of 60–80 GeV. The $1/R_{MTE}$ distributions clearly show the noise peak at about $R_{MTE} = 1$. Events in this peak as well as ones with $1/R_{MTE} < 1$ have very large \cancel{E}_T . Possible sources may be cosmic rays, the Main Ring losses as well as electronic malfunctions, like BLS failure, etc. The R_{MTE} cut is thus introduced to remove such backgrounds. As can be seen from the plots, a good event must satisfy the cut of $R_{MTE} < 0.7$ or equivalently:

$$1/R_{MTE} > 1.43. \quad (5.7)$$

This cut value is accepted for all rapidities and transverse energies of the leading jet of the event (also see discussion on page 186).

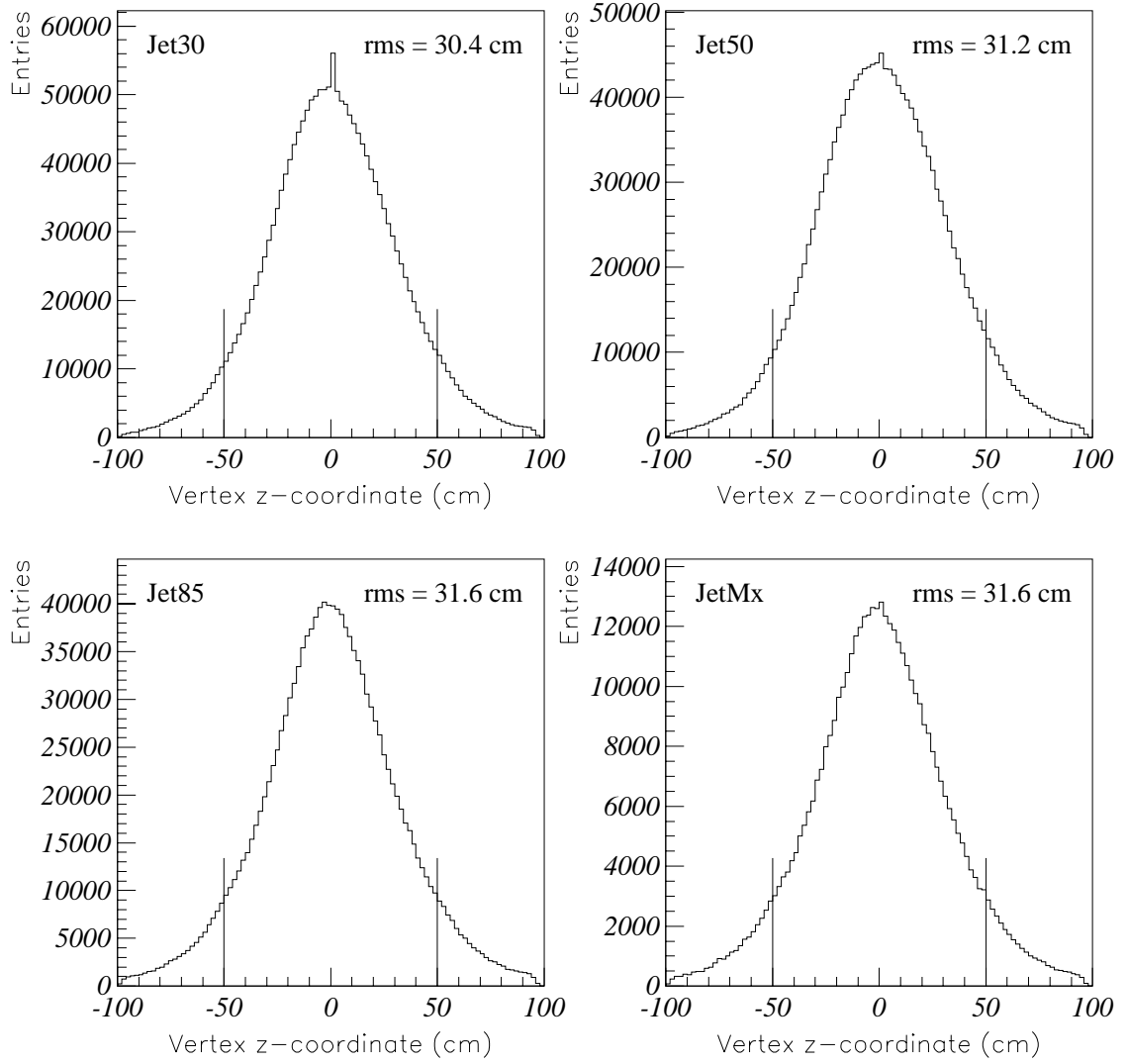


Figure 5.9: The vertex distributions for four jet triggers during Run 1B are centered at about $Z = 0$ cm and have a characteristic rms of about 30 cm.

5.2.2 Determination of the Vertex Cut

The distribution of the z-coordinate of the primary interaction vertex during Run 1B for each of the jet triggers used in this analysis and after the $\vec{\mathcal{H}}_T$ revertexing is applied as needed, are shown in Figure 5.9. The plots exhibit the random, close-to-Gaussian nature of the spread in the Z-vertex position which is due to non-zero length of the colliding beam particle bunches at the Tevatron. The distributions are centered at zero and have a typical *rms* of about 30 cm. Frequently, however, the vertex can be found quite far away from the center of the detector. Such events may contribute jets with degraded resolution because they may shower in less well instrumented regions of the DØ detector such as ICR. In addition, due to the pseudo-projective nature of the DØ detector, jet pseudorapidity (and hence its transverse energy) is less precisely measured the further from the detector's center the vertex is found. For these reasons, the vertex is required to be within 50 cm of the detector's center, i.e. $|Z| < 50$ cm.

5.3 The Methodology for Cut Efficiency Calculation

The most important step in cut efficiency determination is to obtain a *true* distribution of the cut variable, i.e. a distribution containing only good jets or events. Once such a *true* distribution is known, the efficiency of the corresponding cut is calculated in a straightforward way as:

$$\varepsilon = \frac{N_{surv}}{N_{tot}} \quad \text{with} \quad N_{tot} = N_{surv} + N_{fail}, \quad (5.8)$$

where N_{surv} and N_{fail} respectively are the number of *good* entries surviving and failing the cuts in the *true* distribution of the cut variable under consideration. By

definition then the variable N_{surv} follows a binomial distribution with a variance of $\sqrt{N_{tot} \cdot \varepsilon \cdot (1 - \varepsilon)}$. Therefore the standard statistical error on the efficiency is given by:

$$\Delta\varepsilon = \frac{\text{Var}(N_{surv})}{N_{tot}} = \sqrt{\frac{\varepsilon \cdot (1 - \varepsilon)}{N_{tot}}}. \quad (5.9)$$

There is also a systematic error involved in the determination of the cut efficiency using the procedure described above. It originates from the method used for obtaining the *true* distribution of the variable and from the possible noise contamination in such a distribution. This systematic error becomes significant at higher E_T due to larger statistical fluctuations that make it harder to determine the *true* distribution of the variable.

5.4 The Efficiency of Jet Quality Cuts

For the determination of EMF and CHF cut efficiencies, Normal and Restored jets are combined. The HCF cut is however applied only to Normal jets since the ACRA can not re-calculate the HCF of the Restored jet. Therefore the HCF cut efficiency is determined for Normal jets only.

5.4.1 Electromagnetic Fraction Cut Efficiencies

To obtain a *true* EMF distribution from the data, the Z and the R_{MTE} cuts are applied to clean up the sample. EMF distributions with the same event cuts are also obtained from the Monte Carlo (MC) sample. The MC sample is the one used for $D\bar{O}$ jet energy resolution studies and is described in detail elsewhere [62]. The MC EMF distributions show that jet's EMF may extend all the way down to

Figure 5.10: The fits to the low (left) and the high (right) ends of the EMF distribution in the CEN region for jet E_T of 100–120 GeV. Normal and Restored jets are combined. Vertical lines indicate the low and the high EMF cuts.

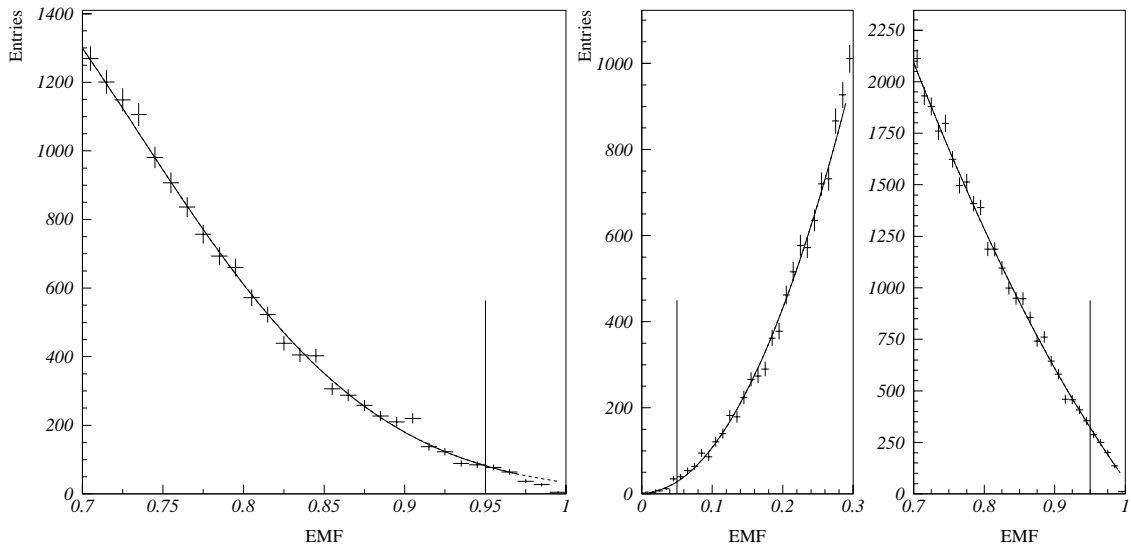
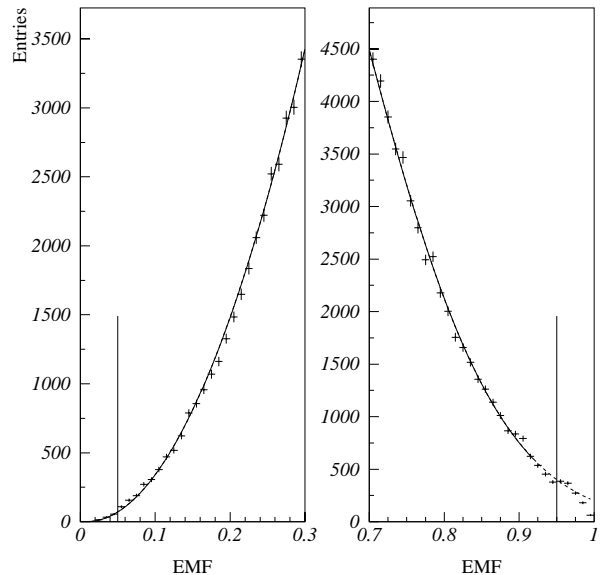


Figure 5.11: The fits to the EMF distributions. The left plot shows the fit to the high end of the EMF distribution in the ICR for jet E_T of 50–60 GeV. The right plots shows fits to the low and the high ends of the EMF distributions in the FOR region for jet E_T of 80–100 GeV. Normal and Restored jets are combined. Vertical lines indicate the EMF cuts.

EMF = 0 and all the way up to EMF = 1, being higher at EMF = 1 [69]. The same behavior is observed in the EMF distributions obtained from the data sample. Therefore it is believed that after both event cuts are applied, the remaining jets in

the EMF distributions are all good. Then N_{fail} is just the number of jets outside the EMF cuts and N_{surv} is the number of jets enclosed within the cut boundaries. The nominal efficiency and the statistical error are then calculated according to Eqs. 5.8 and 5.9.

To calculate the systematic uncertainty the two ends of the cleaned EMF distributions are fitted to either a second order polynomial or a Gaussian, whichever describes the distributions better judging by the χ^2 of the fits. The fits are performed in the region between the cuts and are then extrapolated all the way to 0 and 1 for low and high ends of the EMF distributions. See Figure 5.10 for the CEN region and Figure 5.11 for the ICR and the FOR regions.

Then the fitted function is assumed to be a *true* distribution of the EMF and N_{surv} is therefore equal to the integral of the fitted model with limits of integration set at the cut values, while N_{fail} is calculated as the integral of the fitted functions outside the cut values. The corresponding efficiency is calculated using Eq. 5.8 and the difference between this and the nominal value of the efficiency is assigned a systematic uncertainty.

5.4.2 Coarse Hadronic Fraction Cut Efficiencies

The coarse hadronic layers are located very deep in the calorimeters. There are two reasons not to rely on the CHF distributions obtained from the Monte Carlo. One is that the hadronic shower model in GEANT (GHEISHA) does not accurately simulate the rare longitudinal fluctuations in the shower tails. Second, in order to increase the speed of the MC, DØ uses a “Shower Library” to store a selection of hadronic showers [47]. Simulated jets, following fragmentation, are constructed from this

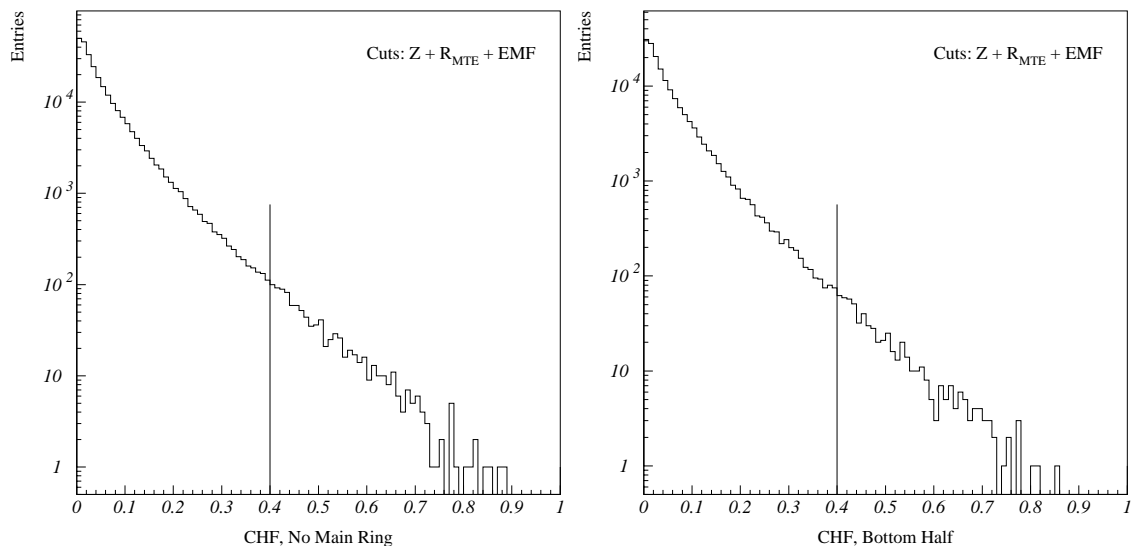


Figure 5.12: The CHF distributions in the CEN region for jet E_T of 100–120 GeV excluding the Main Ring region (left) and for the bottom half of the calorimeter only (right). Normal and Restored jets are combined. Vertical line indicates the CHF cut.

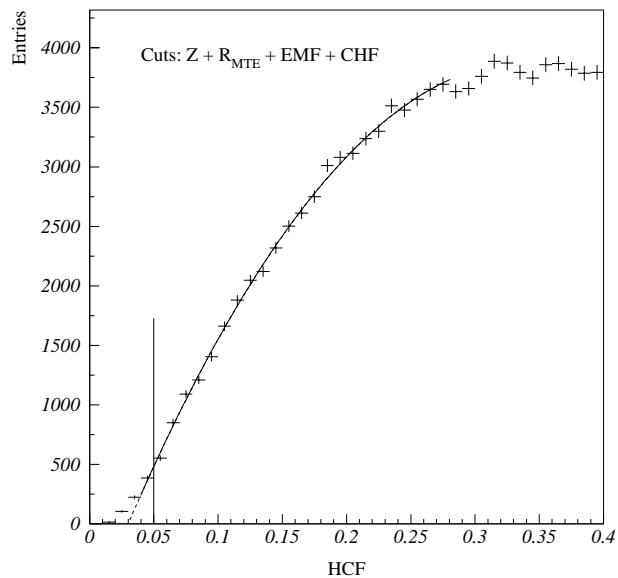


Figure 5.13: The fit to the HCF distribution in the CEN region for jet E_T of 100–120 GeV. Normal jets only. Vertical line indicates the HCF cut.

library of particle showers. The limited number of showers in this library further worsens the representation of rare longitudinal fluctuations deep in the calorimeter.

As mentioned earlier, the CHF cut is designed to remove mostly the MR

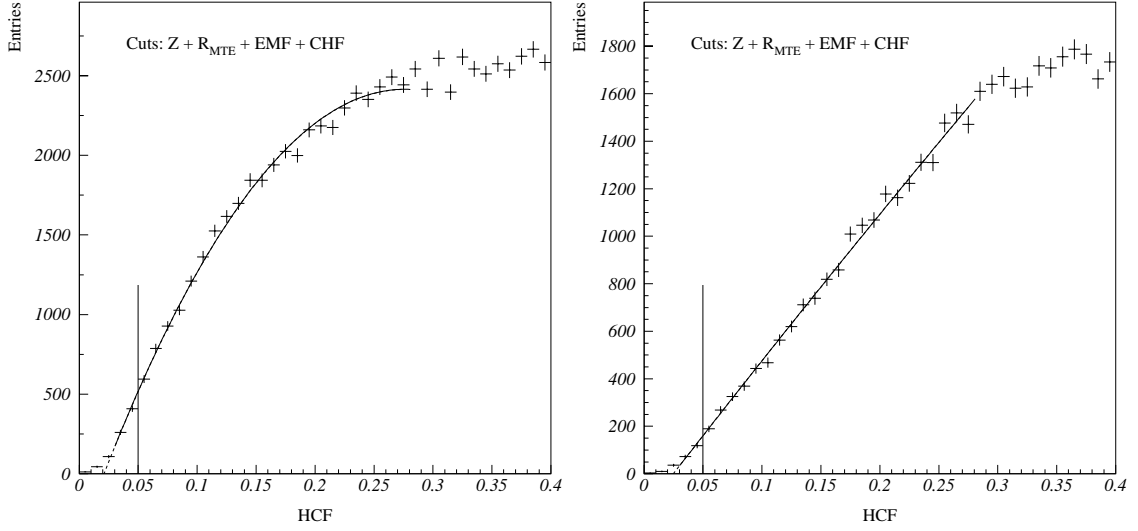


Figure 5.14: The fits to the HCF distributions in the ICR for jet E_T of 60–80 GeV (left) and in the FOR region for jet E_T of 80–100 GeV. Normal jets only. Vertical line indicates the HCF cut.

jets. To obtain a *true* distribution then the MR region ($1.0 < \phi < 2.2$) is excluded and all the event and the EMF cuts are applied beforehand. Then the CHF cut efficiency is calculated from the resulting clean CHF distribution according to Eq. 5.8, where now N_{surv} is the number of jets with $\text{CHF} < 0.4$ and N_{fail} is the number of jets with $\text{CHF} \geq 0.4$.

To estimate systematic error, the CHF efficiency is calculated in the same way but for the lower half of the calorimeter only, i.e. for $3.14 < \phi < 6.28$. Figure 5.12 shows the CHF distributions used for the CHF cut efficiency calculations in the CEN region. The mean of the two values of efficiencies obtained this way is taken to be a nominal CHF efficiency ε_{CHF} and the difference between the mean and the two efficiencies is assigned to the systematic uncertainty.

5.4.3 Hot Cell Fraction Cut Efficiencies

To obtain a clean HCF distribution all event cuts as well as EMF and CHF cuts are applied beforehand. Then, to a good approximation, the resulting distributions are *true* HCF distributions (which is also confirmed using the MC sample). Therefore the nominal HCF efficiencies ε_{HCF} and the statistical errors are calculated using Eqs. 5.8 and 5.9, where N_{surv} is the number of jets with $HCF > 0.05$ and N_{fail} is the number of jets with $HCF \leq 0.05$.

To estimate systematic uncertainty on ε_{HCF} , the HCF distribution is fitted to a second order polynomial starting at about the cut value of 0.05 (see Figure 5.13 for the CEN region and Figure 5.14 for the ICR and the FOR regions.). The fitted function is then extrapolated below the cut and the systematic efficiency is evaluated using Eq. 5.8 where now N_{surv} is the integral of the fitted function above the cut and N_{fail} is the integral of the function below the cut. The difference between this efficiency and the nominal efficiency is assigned to the systematic error.

5.4.4 Global Jet Quality Cut Efficiencies

The above described procedures for each jet quality cut are repeated in every E_T and η_d bin. The statistical and systematic errors are added in quadrature to yield combined (total) errors on the efficiencies. The tabulated efficiencies and their uncertainties for each jet cut and in every pseudorapidity region are listed in reference [69].

Since jet quality cuts are applied in succession, as a final step, the efficiencies for EMF, CHF, and HCF cuts are multiplied in each E_T bin to give a

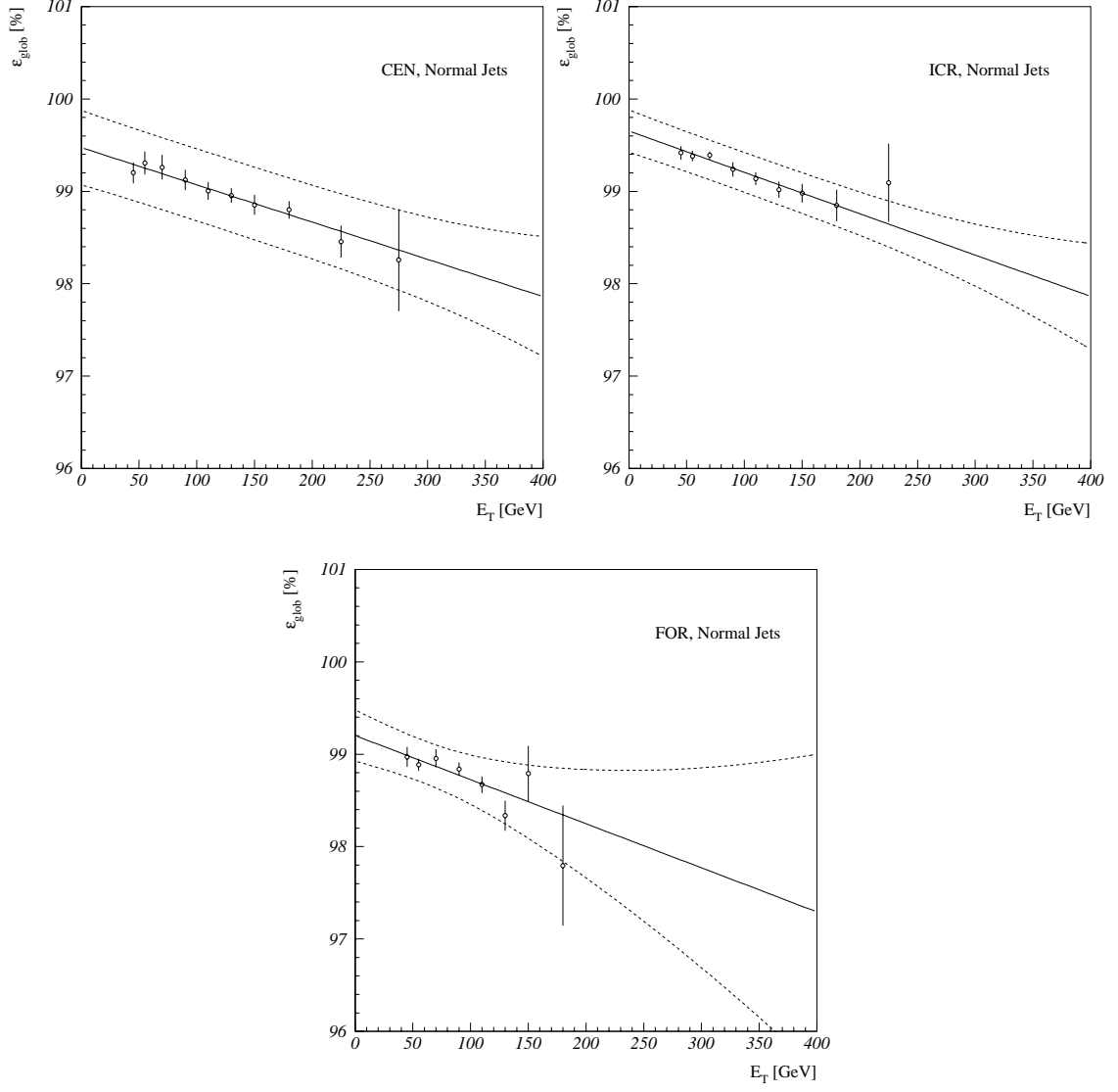


Figure 5.15: ε_{glob} as a function of un-corrected jet E_T in three η_d regions for Normal jets. Error bars shown are combined statistical and systematic uncertainties. The error band on the fitted model is also indicated.

combined global jet quality cut efficiency ε_{glob} for Normal jets. To obtain ε_{glob} for Restored jets, only EMF and CHF efficiencies are combined because, as mentioned earlier too, the HCF cut is not applied to Restored jets. The uncertainties in the global efficiencies are calculated by adding total uncertainties of individual jet cut efficiencies in quadrature.

The global jet efficiencies are then fit to a straight line

$$\varepsilon_{glob} = p_1 + p_2 \cdot E_T \quad (5.10)$$

in each η_d bin and the obtained parameterization is presented in Table 5.1 for all η_d regions. The global jet quality cut efficiencies along with the final fitted models and associated error bands are presented in Figure 5.15 for Normal jets. The global efficiencies for Restored jets are rather similar in shape but generally slightly higher, as expected, and for completeness are presented in reference [69]. The error band on the fitted function has three contributions:

$$\Delta\varepsilon_{glob} = \sqrt{\Delta_1^2 + \Delta_2^2 + \Delta_3^2}, \quad (5.11)$$

where Δ_1 represents the error propagation of the fitted function value as derived from the errors in the parameters Δp_1 and Δp_2 and their covariance $Cov(p_1, p_2)$:

$$\Delta_1 = \sqrt{(\Delta p_1)^2 + 2 \cdot Cov(p_1, p_2) \cdot E_T + (\Delta p_2 \cdot E_T)^2}, \quad (5.12)$$

Δ_2 is a systematic error to account for the uncertainty due to the particular choice of the fitted model and is estimated as a difference between the nominal linear fit and the fit to the second order polynomial. Finally, Δ_3 is the largest of the systematic errors in the global efficiency data points. The difference between the Normal and the Restored jet quality cut efficiencies is within 0.5%.

$\varepsilon_{glob} = p_1 + p_2 \cdot E_T$				
η_d region	Normal Jets		Restored Jets	
	$p_1 \pm \Delta p_1$ [%]	$p_2 \pm \Delta p_2$ [%/GeV]	$p_1 \pm \Delta p_1$ [%]	$p_2 \pm \Delta p_2$ [%/GeV]
CEN	99.47 ± 0.08	-0.004 ± 0.001	99.60 ± 0.06	-0.003 ± 0.001
ICR	99.65 ± 0.06	-0.004 ± 0.001	99.96 ± 0.04	-0.004 ± 0.001
FOR	99.20 ± 0.07	-0.005 ± 0.001	99.41 ± 0.08	-0.005 ± 0.001

Table 5.1: Parameterization of the global jet quality cut efficiencies for Normal and Restored jets and for all η_d regions.

5.5 The Efficiency of Event Quality Cuts

In this section, we describe the methods used for the determination of missing transverse energy fraction cut and vertex acceptance cut efficiencies.

5.5.1 Missing Transverse Energy Fraction Cut Efficiencies

$\varepsilon_{MTE} = p_1$	
η_d region	$p_1 \pm \Delta p_1$ [%]
CEN	99.98 ± 0.02
ICR	99.97 ± 0.02
FOR	99.97 ± 0.03

Table 5.2: Parameterization of the R_{MTE} cut efficiencies in three η_d regions.

The $1/R_{MTE}$ distributions clearly show a noise peak at about $R_{MTE} = 1$. In the past a double Gaussian model has been used to obtain a true distribution—the first Gaussian describing the noise peak and the second Gaussian describing the rising edge of the signal distribution. It is however hard, if not impossible, to imagine good

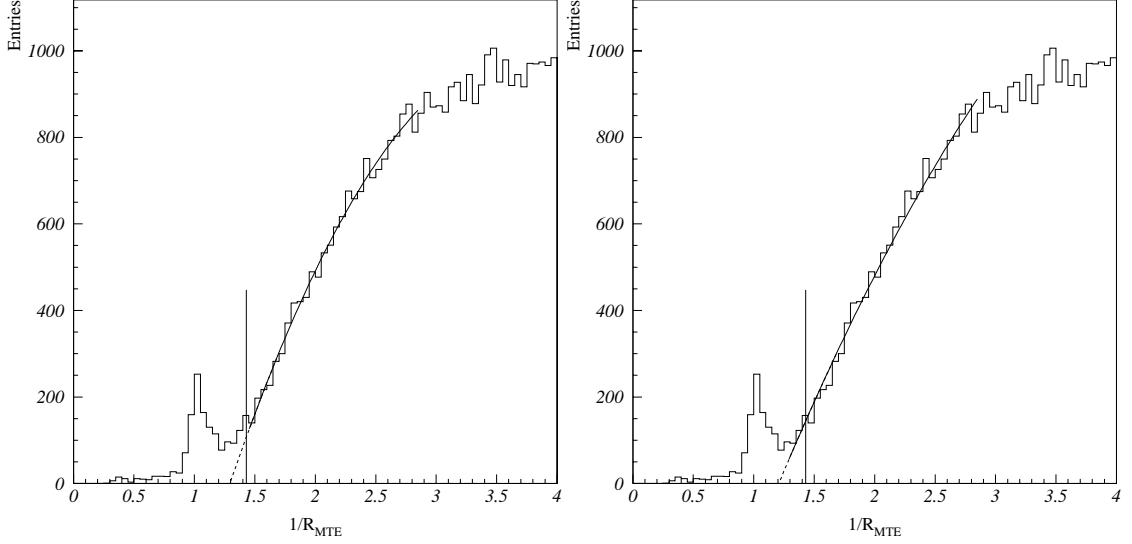


Figure 5.16: The nominal (left) and the systematic (right) fits to the $1/R_{MTE}$ distribution in the CEN region for leading jet E_T of 100–120 GeV. Vertical line indicates the R_{MTE} cut.

QCD events that have $1/R_{MTE} \leq 1$. Therefore the double Gaussian method may underestimate cut efficiency [68]. For this reason, instead of two Gaussians, a second order polynomial is fit to the $1/R_{MTE}$ distributions starting from $1/R_{MTE} \geq 1.43$. This fitted function is assumed to represent a *true* distribution of $1/R_{MTE}$ and the nominal efficiency and the corresponding statistical error are calculated according to Eqs. 5.8 and 5.9, where now N_{fail} is the integral of the fitted polynomial up to a cut value, and N_{surv} is the integral of this function above the cut value.

To estimate systematic uncertainty, the fit starts from the abscissa intercept point of the nominal fitted model and the systematic efficiency is evaluated in the same way as the nominal efficiency. (See Figure 5.16 for the CEN region.) Then the difference between the nominal and the systematic efficiencies is assigned as systematic error.

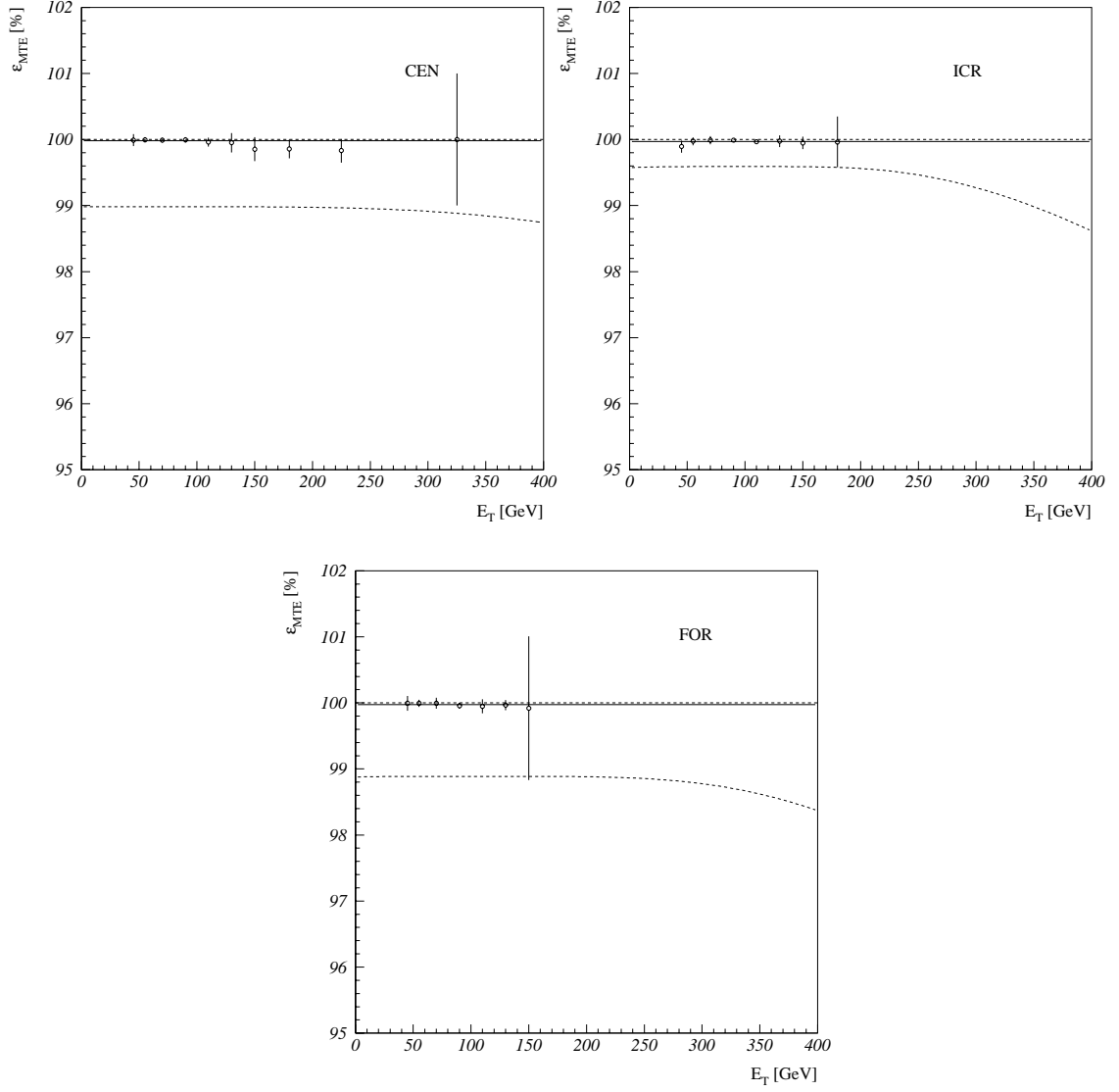


Figure 5.17: ε_{MTE} as a function of un-corrected leading jet E_T in three η_d regions. Error bars shown are combined statistical and systematic uncertainties. The error band on the fitted model is also indicated. The upper error band is truncated at 100%.

This procedure is repeated in each E_T and η_d bin, the statistical and systematic errors are added in quadrature, and the final results are tabulated in reference [69]. Finally, the ε_{MTE} is fit in every η_d region to a constant and this parameterization is presented in Table 5.2. The fitted models along with the estimated error bands are shown in Figure 5.17 for all η_d regions. The error band is obtained in a similar way as for the global jet quality cut efficiency parameterization except in this case $\Delta_1 = \Delta p_1$ and the upper error band is truncated at 100%.

Event Scanning and Modified R_{MTE} Cut

In addition to the systematic studies of the data sample quality, many events (especially at highest E_T 's) were also visually scanned using DØ event display software. The detailed analysis of the events with leading jet in the central pseudorapidity region demonstrated that unacceptable level of contamination was passing the R_{MTE} cut of 0.7 [46]. Therefore, for pseudorapidities up to $|\eta| = 0.7$, the R_{MTE} cut was modified: \cancel{E}_T had to be less than the larger of 30 GeV or $0.3E_T^{lj}$. The efficiency associated with this modified R_{MTE} cut was determined as a function of E_T^{lj} to be 0.982 for $E_T^{lj} > 150$ GeV, and $1.031 - 0.663 \times 10^{-3} E_T^{lj} (1.0 - E_T^{lj}/300.0)$ for $E_T^{lj} \leq 150$ GeV. This cut and efficiency were used in the cross section analysis for events with leading jet in the central region ($|\eta| < 0.7$).

5.5.2 The Z-vertex Cut Efficiency

Application of the Z-vertex cut generally improves the quality of the data. However, in contrast with the rest of the quality cuts discussed, by its nature this cut is more of an acceptance cut rather than a cut intended to directly remove background

contamination. Therefore all events in the vertex distribution are assumed to be “good” events and the efficiency of this cut ε_z is calculated according to Eq. 5.8, where N_{surv} and N_{fail} are simply the number of events passing and failing $|Z| < 50$ cm, respectively. The error is considered to be purely statistical and is estimated using the binomial formula of Eq. 5.9. The results for each jet trigger are summarized in Table 5.3.

Jet Trigger	$\varepsilon_z[\%]$
Jet_30	89.55 ± 0.02
Jet_50	88.84 ± 0.02
Jet_85	88.15 ± 0.03
Jet_Max	88.11 ± 0.05

Table 5.3: ε_z for each jet trigger.

CHAPTER 6

JET ENERGY SCALE

One of the primary purposes for using calorimeters in high energy physics experiments in general, and in DØ in particular, is to accurately measure the energy of incoming objects of interest *prior* to their interaction with the detector. The jet energy measured by the DØ calorimeters is generally distorted by response effects, uranium noise, spectator interactions, reconstruction, and finite resolution. In DØ, the correction that *on average* restores measured jet energy to the final state particle level jet energy (i.e. prior to jet entering the calorimeters) is commonly referred to as the jet energy scale (JES) correction. The linearity, hermeticity, and compensating nature of the DØ calorimeters allow separation of jet energy resolution effects from the scale correction.

The determination of the jet energy scale (JES) in DØ Run 1 has not, however, been a trivial exercise. The lack of a central magnetic field and the unavailability of test beam data at low energies and for a large sample of calorimeter modules do not allow an *in-situ* calibration of jets from particles. Monte Carlo (MC) simulations of the calorimeters do not mimic the jet energy response and resolution to within uncertainties needed by many physics analyses. The jet energy calibration is, therefore, not derived from the MC tuned to the data, but mostly from collider data alone, employing various methods and techniques. In this chapter, we will first

discuss methods for determining the DØ JES and its subcomponents [74], followed by the description of a novel and independent closure test of the entire JES and of its results [75].

6.1 Determination of the DØ JES

Given the measured jet energy (E_{jet}^{meas}), the corresponding particle level energy (E_{jet}^{ptcl}) is given by the following relation with \mathcal{R} being the jet algorithm cone radius, η —the pseudorapidity, \mathcal{L} —the instantaneous luminosity, and E —the jet energy:

$$E_{jet}^{ptcl} = \frac{E_{jet}^{meas} - E_O(\mathcal{R}, \eta, \mathcal{L})}{R_{jet}(\mathcal{R}, \eta, E) \cdot S(\mathcal{R}, \eta, E)}, \quad (6.1)$$

where $E_O(\mathcal{R}, \eta, \mathcal{L})$ is the so called offset energy due to underlying event and noise, $R_{jet}(\mathcal{R}, \eta, E)$ is the calorimeter response, and $S(\mathcal{R}, \eta, E)$ is fraction of the jet calorimeter shower contained inside the fixed cone size of the jet. The offset correction is derived from studies of energy deposition patterns in minimum bias events, the response subcorrection is measured using the missing E_T projection method, and out-of-cone and in-cone showering effects are determined from collider data and HERWIG particle level MC samples. In what follows, we discuss in more detail each subcomponent of the DØ JES.

6.1.1 The Offset Correction

The DØ JES Offset correction removes the portion of the measured jet energy that does not belong to the hard scattered jet. It is given as the energy *density* in $\eta - \varphi$ space, D_O . This allows the use of D_O for obtaining the Offset energy E_O contribution to a fixed-cone jet of arbitrary size, \mathcal{R} , by multiplying the Offset

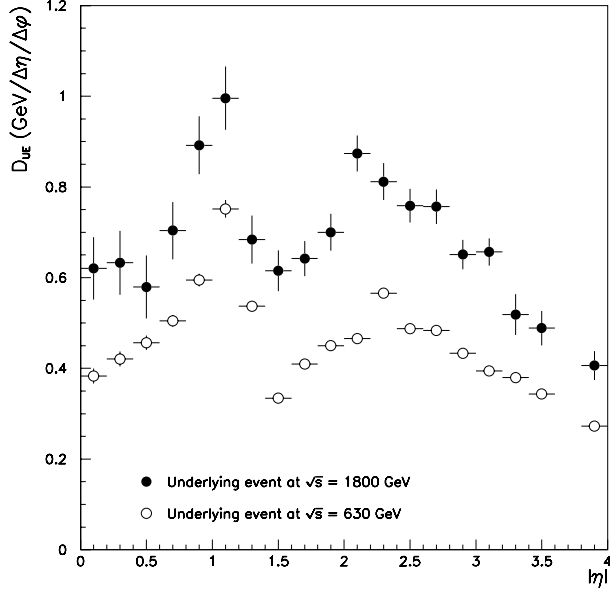


Figure 6.1: The transverse energy density of physics underlying event D_{ue} as a function of pseudorapidity at $\sqrt{s} = 1800$ (smaller sample) and 630 GeV (larger sample).

energy density by the “area” of a jet in the $\eta - \varphi$ space, $\pi\mathcal{R}^2$. Several phenomena of distinct origin and characteristics contribute to the Offset energy. It can be split into two pieces: $D_O = D_{ue} + D_\Theta$, where the D_{ue} represents energy due to physics underlying event, while the term D_Θ absorbs all effects of noise, pileup and extra interactions.

The portion of jet energy due to the underlying event (UE) arises from the spectator parton interactions in inelastic $p\bar{p}$ collisions. Depending on the physics analysis, this contribution may or may not be desirable to remove. In the analysis presented here, we are interested in high E_T QCD behavior. Therefore, for the determination of jet cross sections, we remove the energy due to the UE. D_{ue} is measured as the energy density in the **MINIMUM BIAS (MB)** events, the data sample collected with a requirement of inelastic collision in the beam crossing. In general, the transverse energy activity in the **MB** events is so low that there are no hard jets reconstructed—they do not make it past the 8 GeV jet E_T threshold. Furthermore, in order have no more than one inelastic collision in the events, the **MB** data sample

is subject to the requirement of low luminosity of about $0.1 \times 10^{30} \text{ cm}^{-2}\text{s}^{-1}$.

However, in addition to the UE, the MB events still have contributions from noise and pileup. To remove their contribution, the corresponding energy density is measured in low luminosity ZERO BIAS events (ZB, see page 120). The difference in the energy densities from low luminosity MB and ZB events thus gives a good estimate of the underlying event density D_{ue} . It is measured as a function of pseudorapidity and is shown in Figure 6.1 for the two center-of-mass (CM) energies. The UE energy density appears to be fairly flat in η . The peak in the range $0.7 \leq |\eta| \leq 1.2$ is attributed to the miscalibration of the intercryostat detectors. Associated with the soft interactions in a single $p\bar{p}$ collision, the underlying event is independent of luminosity and of the number of $p\bar{p}$ interactions. It however increases with increasing $p\bar{p}$ CM energy as this latter is accompanied by the growth in the particle multiplicity as well as in the average energy per particle in the final state. The UE energy density for the JES Offset correction is taken directly from the histogram in Figure 6.1, where the D_{ue} values for η 's between the bin centers are obtained using linear interpolation.

The second term in the JES Offset correction, D_{Θ} is measured from a ZB sample to account for noise, pileup, and extra interactions. The initial electronic calibration of calorimeter cells shifts the average empty cell energy to zero. In DØ, the cells which have a measured electronic signal within two standard deviations (σ) from zero are not read out—to save significant processing time and disk storage space. This mechanism is referred to as *zero suppression*. However, in addition to random electronic noise, in DØ calorimeter cells, there is additional contribution from radioactive decays of uranium. The uranium noise, unlike electronic, is not

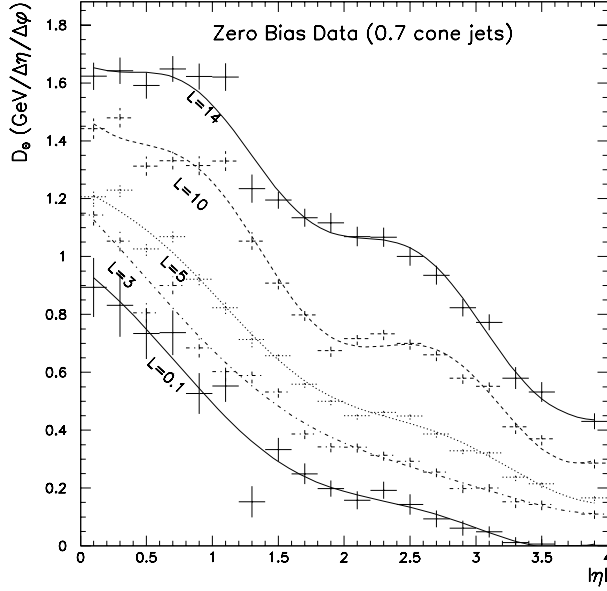


Figure 6.2: The contribution to the JES Offset from uranium noise, pileup, and additional $p\bar{p}$ interactions is measured as a transverse energy density, D_Θ , shown here as a function of pseudorapidity for different luminosities in units of $10^{30} \text{ cm}^{-2}\text{s}^{-1}$.

Gaussian or even symmetric. Because of zero suppression, the asymmetric tails of the total noise, *outside* a 2σ window centered on zero, on average create a net positive energy in a cell. The magnitude of this contribution depends on the number of zero suppressed cells in a given event. Therefore, D_Θ from the ZB data must be extrapolated to a value consistent with average occupancies for jet data. The rather limited number of jets in non-zero suppressed MB data introduces a large uncertainty of $\pm 0.25 \text{ GeV}$ in the measured value of D_Θ . Figure 6.2 shows D_Θ as a function of pseudorapidity at different luminosities. The measurement is fitted to an eight-parameter functional form which introduces additional statistical and systematic errors due to the fit [74].

The uncertainty due to the entire Offset correction is the dominant source of error at lowest jet E_T 's, but is negligible at high E_T 's. The systematic uncertainties related to this analysis method are considered to be correlated in E_T , while the statistical uncertainties are uncorrelated as a function of pseudorapidity.

6.1.2 The Response Correction

The electronic signal measured in the calorimeter cells is mapped onto energy using calibration from single particle test beam data of individual modules assuming ideal instrumentation and linear response¹. However, the response to low energy particles is non-linear. Furthermore, dead material in front of the calorimeters (such as the cryostat walls, for example) distorts the response. And when many particles are put together in a jet, calorimeter module-to-module non-uniformities also affect the signal. The net effect is that the jet response is below unity.

The jet response in $D\bar{O}$ is measured from the photon-jet data using the missing E_T projection method. The idea is to employ conservation of energy in the transverse plane along with the better understood purely electromagnetic response to photons (in most η regions) in order to derive the hadronic response to the jet. In an ideal calorimeter, the total missing transverse energy in photon-jet events would be zero, $\vec{\cancel{E}}_T = 0$. A good estimator of the total $\vec{\cancel{E}}_T$ is the vector sum of the transverse energies of the photon and the recoil hadronic system. However, in real calorimeters, the response to both purely electromagnetic and recoil objects is different from unity. Therefore, the *measured* photon and recoil transverse momenta may not balance perfectly, even on average:

$$R_{em}\vec{E}_T^\gamma + R_{recoil}\vec{E}_T^{recoil} = -\vec{\cancel{E}}_T, \quad (6.2)$$

where R_{em} (R_{recoil}) is the calorimeter response to electromagnetic (recoil) object. The energy scale of $D\bar{O}$ calorimeters for electromagnetically interacting particles is determined [76] from $Z \rightarrow e^+e^-$, J/ψ , and π^0 data samples. After electromagnetic

¹The sampling fractions remained as measured in the test beams. However, the gain constants in electromagnetic sections of calorimeters were later adjusted based on the precision measurement of the Z mass.

calibration and the recalculation of the event $\vec{\cancel{E}}_T$, Eq. (6.2) can be rewritten in the following form: $\vec{E}_T^\gamma + R_{recoil}\vec{E}_T^{recoil} = -\vec{\cancel{E}}_T$, or:

$$1 + R_{recoil} \frac{\hat{n}_T^\gamma \cdot \vec{E}_T^{recoil}}{E_T^\gamma} = -\frac{\hat{n}_T^\gamma \cdot \vec{\cancel{E}}_T}{E_T^\gamma}, \quad (6.3)$$

with \hat{n}_T^γ a unit vector in the direction of the photon.

In the presence of offset and showering losses, in the photon-jet data, R_{recoil} is the energy response to the calorimeter jet, R_{jet} . Since the transverse momenta of the photon and recoil should balance at the particle level ($\hat{n}_T^\gamma \cdot \vec{E}_T^{recoil} = -\vec{E}_T^\gamma$), Eq. (6.3) can be rewritten for R_{jet} as:

$$R_{jet} = 1 + \frac{\hat{n}_T^\gamma \cdot \vec{\cancel{E}}_T}{E_T^\gamma}. \quad (6.4)$$

The second term on the right hand side of Eq. (6.4) is the fraction of the $\vec{\cancel{E}}_T$ projected onto the direction of the photon, hence the name of the method—the missing E_T projection fraction, or MPF.

Jet response R_{jet} is expected to be energy dependent. However, studying R_{jet} as a function of jet energy in the MPF method poses a problem. The photon and jet energy resolutions introduce smearing bias in the measurement. Since the electromagnetic energy resolution is much better in $D\bar{O}$ than hadronic resolution, the dominant effect is from the jet energy resolution. In addition, steeply falling prompt photon cross section, trigger and reconstruction thresholds, as well as event topology, all contribute biases which must be removed. Most of these biases and smearing effects are removed by introducing a better jet energy estimator, the quantity $E' = E_T^\gamma \cosh \eta$. It is composed of two relatively well measured quantities: photon transverse momentum E_T^γ and jet pseudorapidity η . The response is studied as a function of E' , and then mapped onto jet energy by determining average

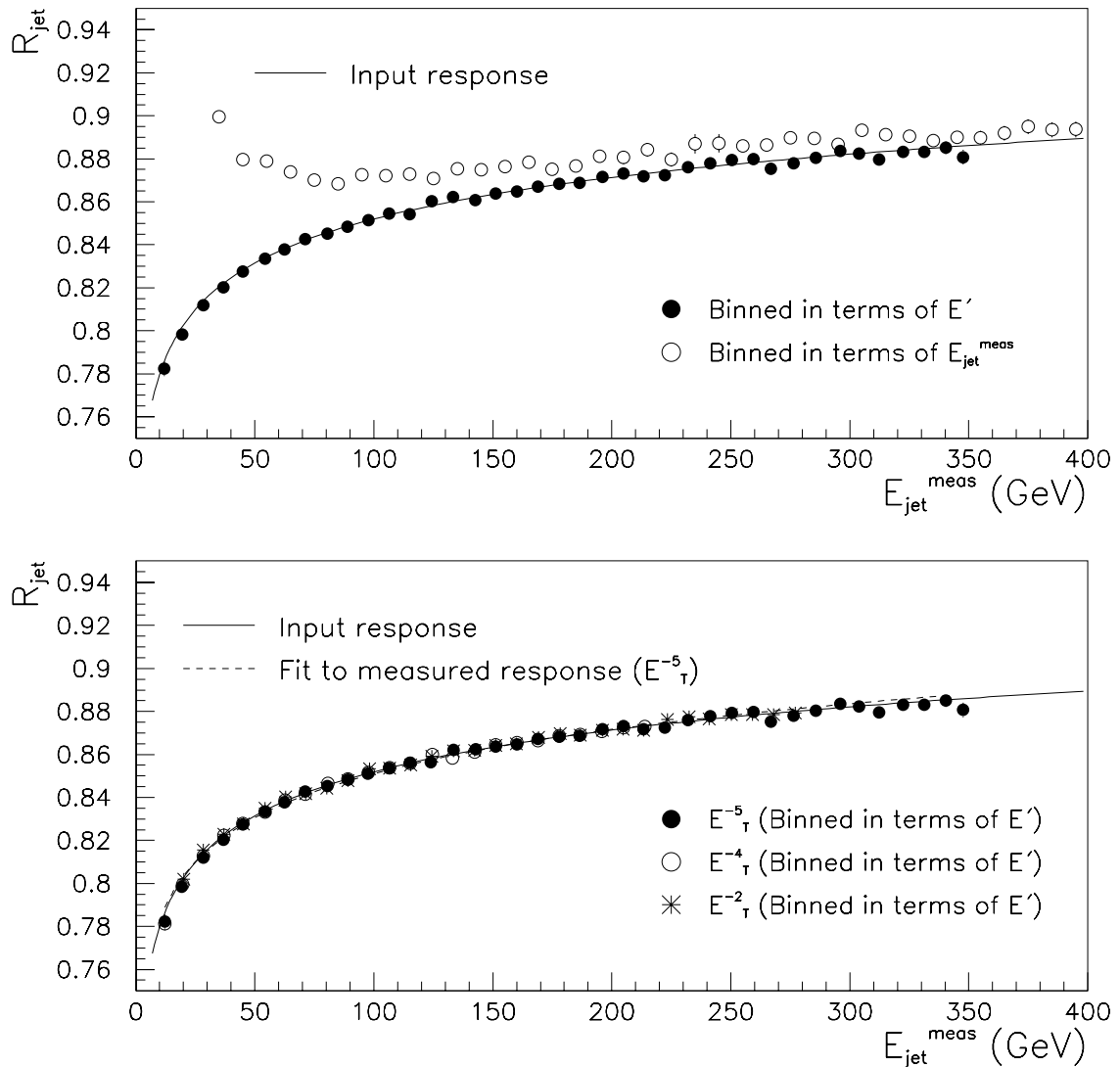


Figure 6.3: Parametric simulation of the R_{jet} measurement. A fit to R_{jet} “measured” from the simulated data, when binned in terms of E' to remove resolution effects, agrees very well with the input response (top). The agreement between the fit and the input function is also excellent given different reasonable assumptions for the E_T dependence of the γ cross section, such as E_T^{-5} , E_T^{-4} , and E_T^{-2} (bottom).

measured jet energy in bins of E' .

This method is tested using parametric MC simulation where photon–jet data are generated with a given E_T dependence. The photon and jet energies are

scaled by the response measured in the data. They are also smeared according to the corresponding fractional energy resolution parameterizations. The response is then measured from this simulated sample using the MPF method. The top plot in Figure 6.3 shows the input response (solid line) along with the extracted R_{jet} binned in terms of the jet energy (open circles) and in terms of jet energy estimator E' (filled circles). It is seen that the resolution bias, present if binned in terms of E_{jet} , is removed when binned in terms of E' . The bottom plot shows excellent agreement between the fits to R_{jet} versus E' and the input response function under various reasonable assumptions on the E_T dependence of the photon cross section, such as E_T^{-5} , E_T^{-4} , and E_T^{-2} .

In order to achieve jet energy calibration at high pseudorapidities, R_{jet} is studied as a function of η . First, the CC's and EC's are put on the same footing by applying a cryostat factor F_{cry} measured as $F_{cry} \equiv R_{jet}^{CC}/R_{jet}^{EC} = 0.977 \pm 0.005$. It is obtained from a fit to the ratio of the measured R_{jet} versus E' dependences in the CC/EC *overlap* region. F_{cry} is a constant as a function of E' as is expected since the CC's and EC's are designed and constructed with the same technology. The uncertainty due to the cryostat factor is assumed to be correlated as a function of E_T and η .

The intercryostat region (ICR), on the other hand, requires extra care. The dependence of R_{jet} on η is expected to be a smooth function arising via the R_{jet} dependence on energy $R_{jet} \sim \ln E$, where $E = E_T \cosh \eta$. Therefore, to make calorimeters uniform in η , jet response as a function of η is fit to a functional form: $R_{jet} = a + b \ln[\cosh \eta]$, where R_{jet} is measured from both photon-jet and jet-jet data. In the former case, the photon is kept central and in the latter case one of the

leading jets is required to be central, i.e. $|\eta| < 0.5$. The residuals from the fit are then fit in the ICR in bins of detector η of 0.1 rad as a function of the central jet E_T , giving the correction factor F_η . The ICR correction is performed after the cryostat factor correction and before the energy dependent correction of the response. In the ICR, the η dependent correction contributes about 1% error, which is larger above $\eta = 2.5$. This error is assumed to be uncorrelated as a function of E_T and η .

The energy dependence of R_{jet} is measured after the Offset (to remove the energy not associated with the hard parton scattering) and the η dependent (to make the calorimeters uniform as a function of pseudorapidity) corrections. The fact that F_{cry} is independent of E' allows complementing the hadronic response measurement in the CC's by the data points from the EC's which—because forward jets have higher energies than the central jets with the same E_T —thereby extends the jet energy reach from about 150 GeV to nearly 300 GeV (after $E' \rightarrow E_{jet}$ mapping), as is seen in Figure 6.4 for 0.7 cone-jets.

Motivated by the logarithmic dependence of the electromagnetic fraction of the hadronic shower energy, $\langle f_{em} \rangle$, on the incoming energy E , i.e. $\langle f_{em} \rangle \sim \ln E$, R_{jet} is parameterized by the functional form:

$$R_{jet} = a + b \ln E + c(\ln E)^2. \quad (6.5)$$

The fit of R_{jet} to this function is shown in Figure 6.4 along with the data points. The top plot in Figure 6.4 is presented in the semi-logarithmic scale on the x -axis, while the bottom plot is in the linear scale. Along with a nominal value of the fit, shown is the uncertainty band corresponding to the 68% confidence region in the correlated fit parameter space. The errors due to the fit are the dominant sources of uncertainties in the measurement of R_{jet} , contributing an error of about

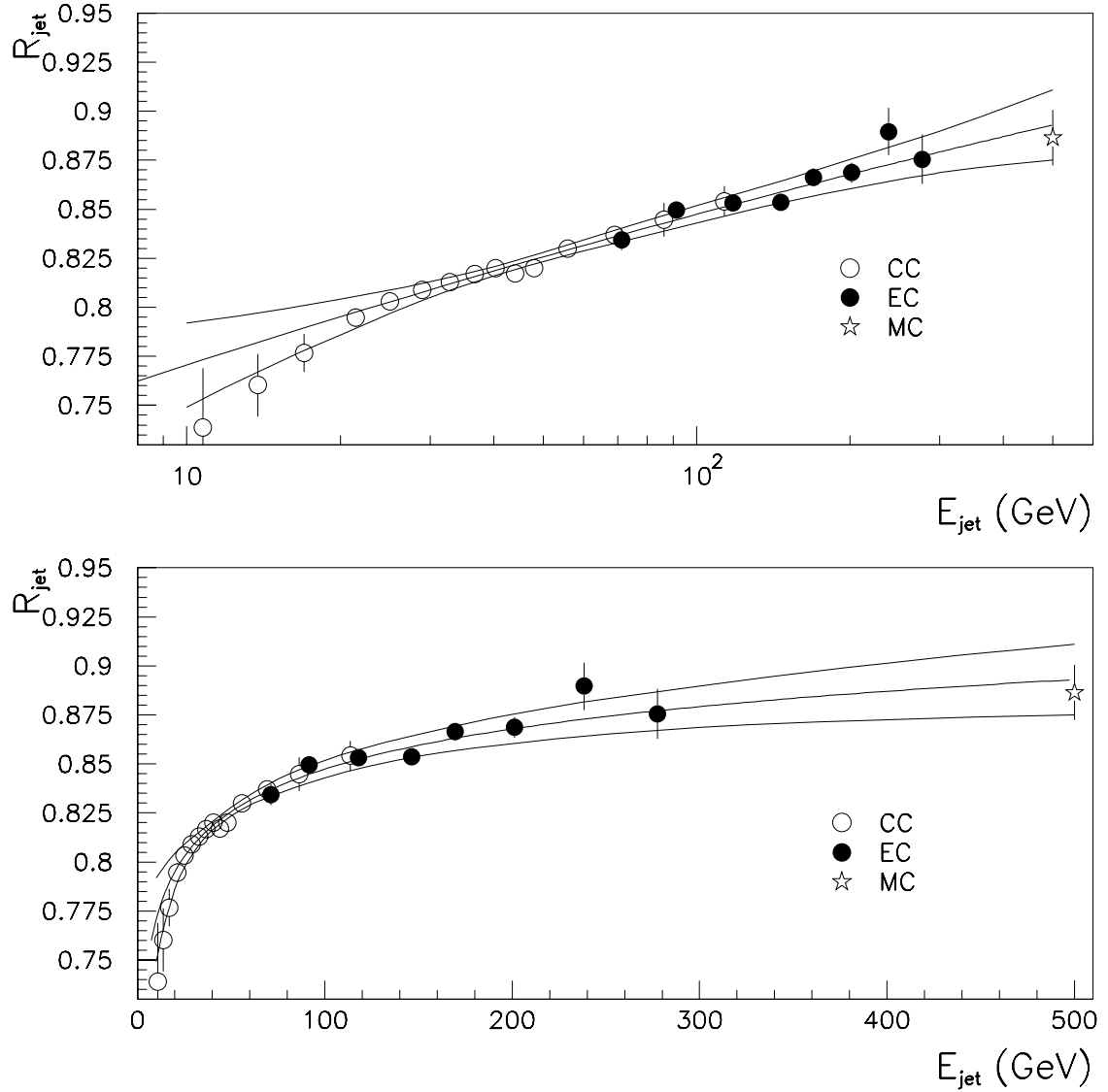


Figure 6.4: R_{jet} versus jet energy on a semi-logarithmic (top) and linear (bottom) energy scales for the 0.7 cone jet algorithm. The outer band corresponds to the uncertainty in R_{jet} equivalent to the 68% confidence region (a volume defined by the $\chi^2 \leq \chi^2_{min} + 3.5$ surface) in the correlated three (fit) parameter space.

1.5/0.5/1.6% for 20/100/450 GeV jet energies. There is also an additional $\sim 0.5\%$ error from the W background in the photon sample. Most of the events in the γ -jet data are not two body processes. This topology bias in the R_{jet} measurement is compensated by another bias due to contamination from highly electromagnetic

jets faking photons.

The uncertainties introduced by the fit of R_{jet} as a function of energy are strongly correlated in energy. The standard correlation coefficients between the responses measured at each of the 11 uncorrected² energy levels are obtained by independently fluctuating the fitted parameters many times within the volume constrained by $\chi^2 \leq \chi^2_{\min} + 3.5$, corresponding to the 68% confidence volume in the three parameter space. The hadronic response correlation matrix for 0.7 cone size jets can be found in reference [74]. The uncertainty associated with the hadronic response is not important at low E_T 's but becomes dominant at high E_T 's.

6.1.3 The Showering Correction

The showering correction arises from the fact that the particle showers originating from jets entering the calorimeters may deposit a fraction of the “jet-associated” energy outside the calorimeter level algorithm cone. By jet-associated energy we mean the energy that would have been contained within the algorithm cone at the *particle level*, i.e. prior to jet entering the calorimeters. In addition, upon entering the calorimeters, particles from the outside of the algorithm cone in the particle level, develop calorimeter showers which may spill additional energy into the calorimeter cone-jet. The combination of these effects must be measured and, if necessary, the corresponding correction must be applied to measured jets.

The showering correction used in this analysis is entirely derived [77] from the Monte Carlo (MC) sample generated by HERWIG and put through full detector

²In this context, uncorrected energy means energy not corrected for response. The low- E_T bias, offset, and η -dependent corrections have already been applied.

simulation based on GEANT [78]. In the MC, measured jet energy can be defined as $E_{jet}^{meas} = \sum_{R_{cell} < 0.7} E_{cell}$, where the sum is over all calorimeter cells within the radius of 0.7 of the jet centroid. On the other hand, the *true* energy of the jet is given by $E_{jet}^{true} = \sum_{R_{part} < 0.7} E_{cell}$, where the sum runs over all calorimeter cells that receive energy from the particles from inside the *particle* level algorithm cone, $R_{part} < 0.7$. The showering correction S of Eq. (6.1) is then defined as the ratio $S = E_{jet}^{meas} / E_{jet}^{true}$.

It turns out that the response correction derived from the MPF method partially accounts for showering effects as well. There is a bias in the MPF method because it is based on the transverse momentum balance in γ -jet data and, as such, is better suited to correct jet momentum rather than jet energy. The particle showers in the calorimeter develop laterally as well as longitudinally, causing the jet widening and resulting in a larger decrease in jet momentum than in jet energy. This loss in jet momentum compensates a fraction of the true showering loss. Therefore, in order to use the MPF-derived response to calibrate jet energy, only the *residual* showering correction must be measured.

This MPF bias can very well be modeled by introducing a variable called *jet limit* which is the distance in $\eta - \varphi$ space, larger than the algorithm cone size, within which the total energy of the particle level jet would be contained in the calorimeter. It is obtained by examining energy flow profiles of jets as a function of a distance from the jet centroid. Jet limit is estimated as the maximum distance from the jet center up to which the jet-associated energy extends. It is a function of pseudorapidity and increases with η . The size of the jet limit varies from 1.0 in the central η region to 1.8 at η 's above 3.0.

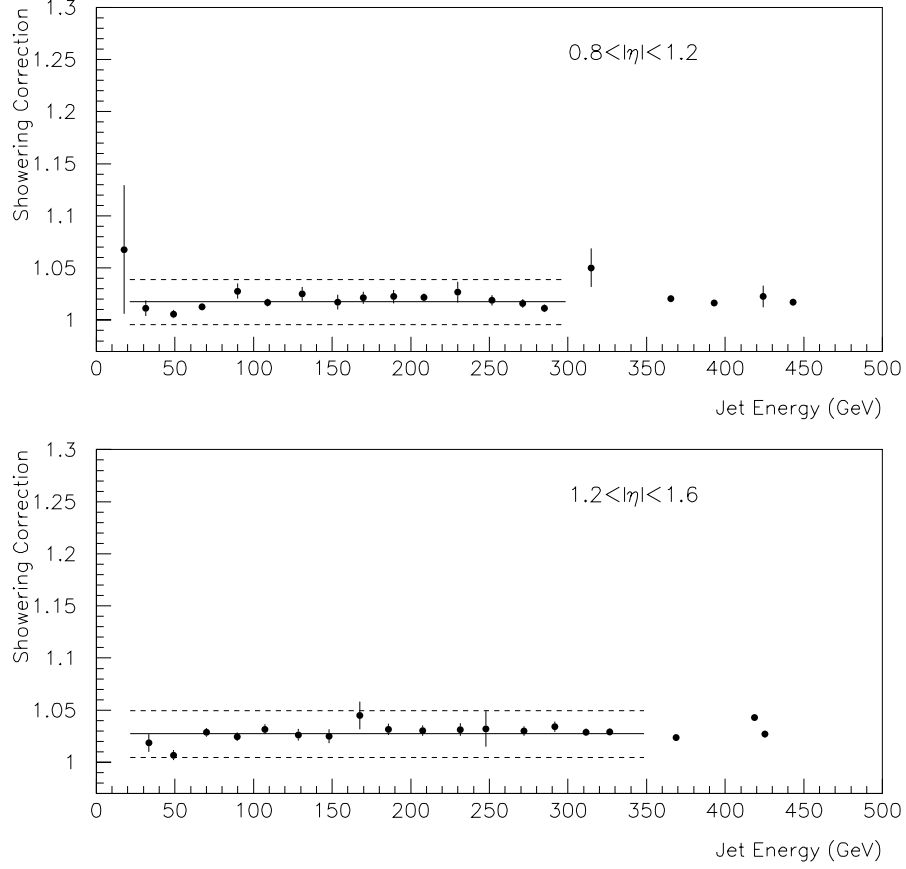


Figure 6.5: The parameterization of the showering correction (actually, S^{-1}) as a function of the response corrected jet energy in two intermediate pseudorapidity regions. The dashed lines indicate 1σ total uncertainty band.

With the jet limit, the definition of the true jet energy is modified to:

$$E_{jet}^{true} = \sum_{\left\{ \begin{array}{l} R_{part} < 0.7 \\ R_{cell} < jet \text{ limit} \end{array} \right\}} E_{cell} . \quad (6.6)$$

It is this definition of the true energy that is used in this MC based derivation of the *residual* showering correction $S = E_{jet}^{meas}/E_{jet}^{true}$. The showering correction derived in this way can therefore be applied to the hadronic response corrected jets.

The showering correction as a function of jet energy is studied in eight pseudorapidity intervals of 0.5 units in width from $\eta = 0$ up to $|\eta| = 3.5$. The

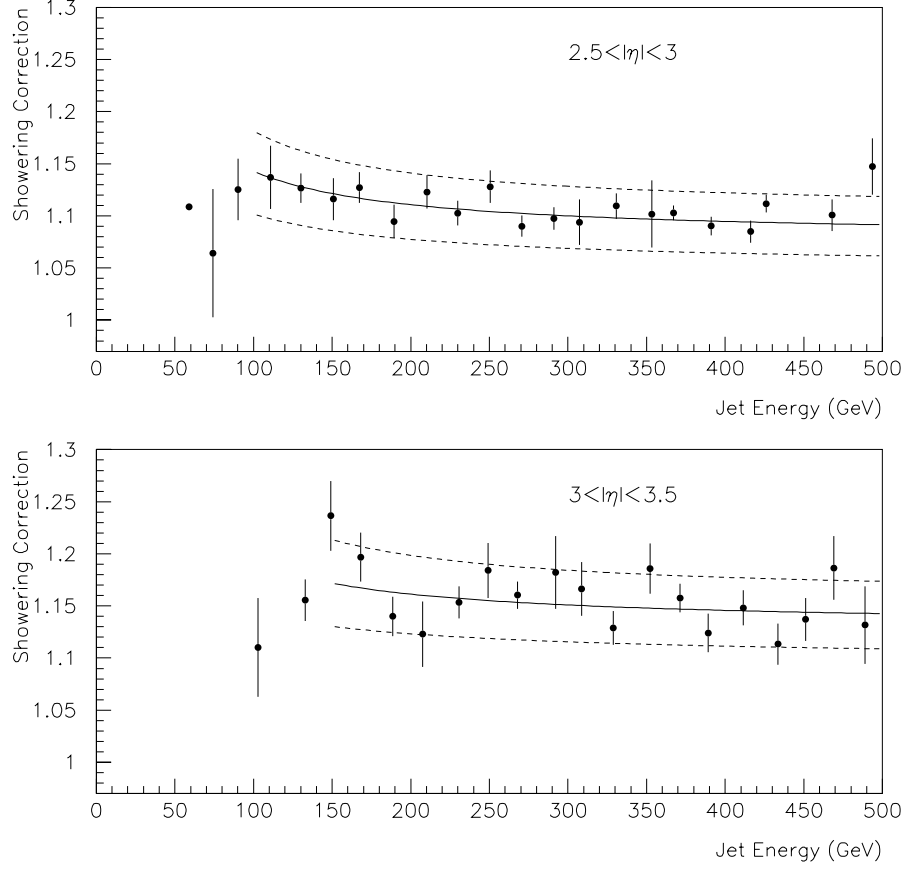


Figure 6.6: The parameterization of the showering correction (actually, S^{-1}) as a function of the response corrected jet energy in two forward-most pseudorapidity intervals considered. The dashed lines indicate 1σ total uncertainty band.

correction is fitted to a flat line in the regions $|\eta| \leq 2.5$ and to a functional form $a/E_{jet} + b$ in the forward-most η bins. To obtain a smooth parameterization as a function of η , however, an interpolation between η bins is necessary. This is somewhat complicated by the fact that the showering correction exhibits no energy dependence for $|\eta| \leq 2.5$, but becomes energy dependent at higher η 's, as can be seen in Figure 6.6. To account for this behavior, the following functional form is chosen to fit the showering correction spanning all pseudorapidities:

$$S^{-1} = 1.0088 + A(E)\eta^2 + B(E)\eta^4. \quad (6.7)$$

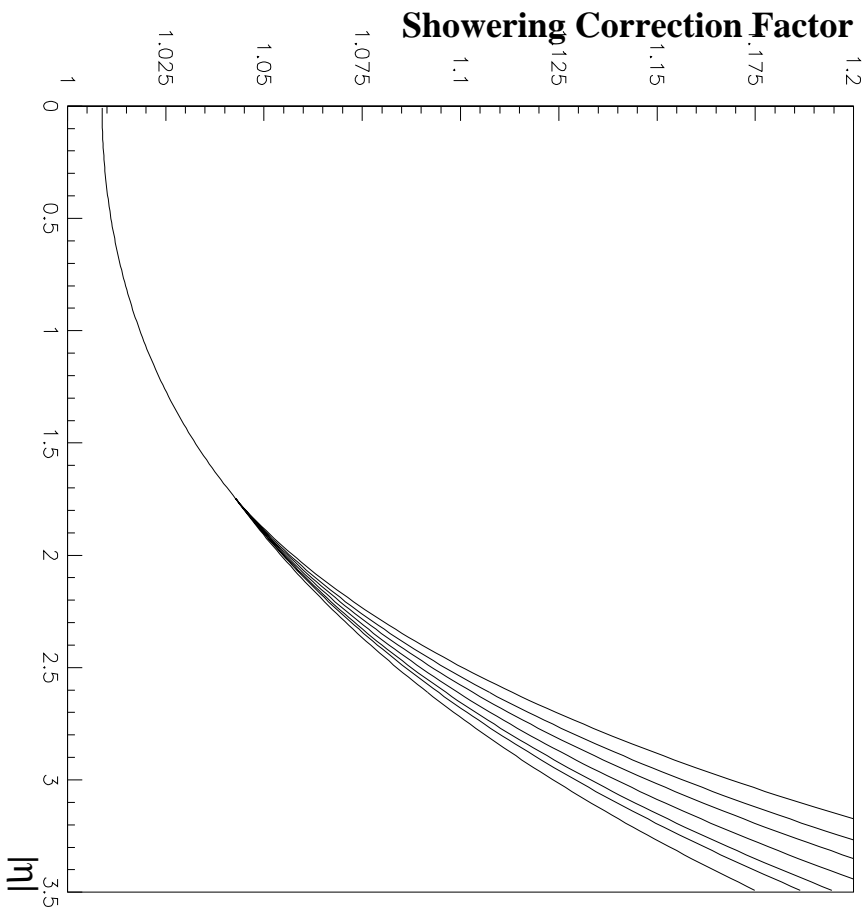


Figure 6.7: The parameterization of the showering correction (actually, S^{-1}) as a function of jet pseudorapidity for different jet energies of 100, 130, 160, 200, 250, 300, and 600 GeV, from top to bottom. For all energies, the correction for $|\eta| \leq 1.75$ corresponds to the fit for jet mid-energy considered, 160 GeV. The energy dependence is allowed for $|\eta| > 1.75$. No discontinuities are present at $|\eta| = 1.75$.

The showering correction as a function of η is fit to this even-power polynomial for several jet energies, and then the fit parameters A and B themselves are fit as a function of energy. The energy dependence of the fit parameters results in a small spread in the showering correction as a function of η below approximately $|\eta|$ of 1.75, where *no* energy dependence should appear. To remove this feature, the fitted function for $E = 160$ GeV, corresponding to the middle of the range spanned by different energies, is chosen for the showering correction for *all* energies

and pseudorapidities smaller than 1.75. For higher pseudorapidities, the energy dependence is allowed and no discontinuity is observed around $|\eta| = 1.75$. The final correction, S^{-1} , as a function of pseudorapidity for several jet energies is shown in Figure 6.7.

The sources of uncertainty are: error in the fit parameters, error due to the disagreement between showering effects in the data and in the MC samples (2% for all η regions), and error associated with the actual value of the jet limit variable. This latter error is measured by varying the jet limit above and below its nominal value and remeasuring the showering correction in each case. Deviations from the showering correction corresponding to the nominal value of jet limit are then assigned to the systematic uncertainty. Illustrations of the measured showering correction (actually the inverse of S) in the four pseudorapidity regions are shown in Figures 6.5 and 6.6. The uncertainty band includes the three sources of error added in quadrature. The uncertainties in the cross sections due to jet limit are considered to be anticorrelated in E_T within a given $|\eta|$ region and fully correlated in η for similar energies. Statistical (fit) and MC closure errors are completely uncorrelated both in E_T and η .

The showering correction described here is implemented in the most recent version of the DØ jet energy scale, CAFIX 5.2. This is the *only* difference between CAFIX 5.2 and its predecessor JES version, CAFIX 5.1. The detailed description of the showering correction implemented in CAFIX 5.1 is contained in reference [74] and discussion of the differences between the old and new showering corrections is presented in [77].

6.2 Independent Closure Test of the JES

In the course of this analysis, we also developed a method for testing the entire DØ JES based on transverse momentum balance in photon–jet and jet–jet data. The detailed discussion of this Closure test is presented elsewhere [75]. Here we will concentrate on the key issues of the method and will discuss the final results of the test for the two most recent versions of the DØ JES, CAFIX 5.1 and CAFIX 5.2.

6.2.1 The Method

Suppose that in a collider event along with a reconstructed jet, whose energy calibration we would like to examine, there is a calorimeter object present whose energy is well measured. Then the transverse momentum³ balance between this well-measured energy cluster and the jet can be directly employed to test the energy calibration of the latter. Since the energy scale for electromagnetic (EM) objects (such as electrons and photons) showering entirely in the EM sections of the DØ calorimeters is very accurately determined from the Z , J/ψ , and π^0 data samples [76], the large p_T direct photon production at the Tevatron in the events with exactly one photon and one jet would be an example of such events, with the photon in the role of a well-calibrated calorimeter object.

In real life, however, it is hardly possible to obtain such ideal reconstructed events—usually there are more objects present in the calorimeters as a result of next-to-leading or even higher order processes. While we still would like to select events with two *leading* (i.e. highest E_T) objects, one of which is well calibrated, in

³All calorimeter objects are considered to be massless, hence throughout we use transverse *momentum* (\vec{p}_T) and transverse *energy* (\vec{E}_T) interchangeably.

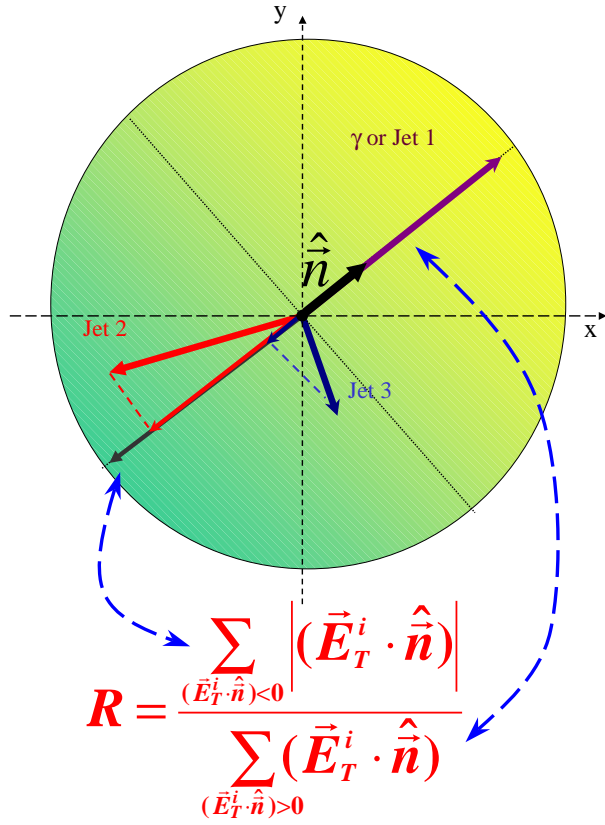


Figure 6.8: The illustration of the JES Closure method. In the x - y transverse plane, we calculate the ratio \mathbf{R} of the *total* E_T projection from the halfplane *not* containing a well-calibrated calorimeter object (with Jet 2 and/or Jet 3 in the picture) to that from the other halfplane (γ or Jet 1 in the picture for the photon-jet and jet-jet data, respectively).

order to significantly improve statistics and make the test of the E_T balance more precise, we generalize to include the lower E_T clusters in the following way. In the *transverse* plane we introduce a unit vector \hat{n} in the direction of the well-measured energy deposit. The line perpendicular to \hat{n} divides the transverse plane into two halfplanes and all objects in the event can be classified as belonging to either of them. For each of the halfplanes we calculate the total E_T projection of all objects in that halfplane onto the direction \hat{n} . Finally we calculate the ratio \mathbf{R} of the total E_T projection from the halfplane *not* containing a well-calibrated calorimeter object

to that from the other halfplane. Mathematically \mathbf{R} can be written as:

$$\mathbf{R} = \frac{\sum_{(\vec{E}_T^i \cdot \hat{\vec{n}}) < 0} |(\vec{E}_T^i \cdot \hat{\vec{n}})|}{\sum_{(\vec{E}_T^i \cdot \hat{\vec{n}}) > 0} (\vec{E}_T^i \cdot \hat{\vec{n}})}, \quad (6.8)$$

where $(\vec{E}_T^i \cdot \hat{\vec{n}})$ is a scalar product of the two vectors. One would like to study \mathbf{R} as a function of the energy and the pseudorapidity of the reconstructed jet under consideration. The closeness of such a ratio \mathbf{R} to unity is a measure of the correctness of the jet energy scale.

As mentioned earlier, the photon-jet (γ -jet) data provides us with a very good sample for testing the JES for relatively low E_T jets using \mathbf{R} in Eq. (6.8). Unfortunately, we quickly run out of statistics in the γ -jet sample as we go to forward regions of the detector because the γ -jet cross section at the Tevatron is smaller by three orders of magnitude than that of dijet production, and because it also falls rather steeply with both E_T and pseudorapidity. Therefore, we use the γ -jet data to test the JES primarily in the central region, where the jet-jet data do not help. Once we establish that the jets in the central region are well calibrated, we then move to the jet-jet data sample, where we request that one of the two leading jets be central and the other one be forward. In the jet-jet data we then test the JES of the forward jet against that of the central jet (that is, the central jet now plays the role of a well-calibrated energy cluster for the purpose of constructing Eq. (6.8)) with increased statistics for the energy and the pseudorapidity coverage of interest. The γ -jet data is also used in the forward regions to verify the jet-jet results in the kinematic range where both samples overlap.

We note that the generalized \mathbf{R} which includes all reconstructed calorimeter objects for estimating the E_T balance in the event is, by definition, sensitive to the

unclustered energy (UCE) of the event, which results from the RECO E_T thresholds for reconstructing calorimeter objects, the most notable of which is the E_T threshold of 8 GeV in the standard DØ cone jet finder (see page 129). Therefore, the effect of the UCE must be estimated and removed prior to interpreting \mathbf{R} of Eq. (6.8) as a measure of the E_T balance in the event.

In addition, depending on the physics of the event, \mathbf{R} may test the E_T balance at either *parton* or *particle* level. In the γ -jet data, the photon energy is fully contained and the photon should directly balance the final state hard parton. Thus the E_T balance between the leading photon and jet tests the JES at the parton level whereas in the jet-jet sample the E_T balance between the two leading jets is the test at the particle level. There is a possible loss of energy when going from parton to particle level jets due to the clustering algorithms applied for the jet finding at each level. However, the purpose of the DØ JES is to correct calorimeter jets to only *particle* level jets. Therefore, when drawing conclusions from the E_T balance studies in the γ -jet data regarding the JES, one needs to examine and take into consideration parton to particle energy difference for the jets.

Finally, studying \mathbf{R} as a function of energy is challenging too. This is because binning the distributions of \mathbf{R} in terms of the energy of the forward jet may bias the ratio due to the combined effect of the finite jet energy resolutions in the calorimeters and the steeply falling jet production cross section. Consider the jet-jet sample with the central and the forward leading jets and suppose we bin \mathbf{R} in terms of the forward jet energy. Then, in a given energy bin, we will have more of the lower *particle* level energy jets which have fluctuated high due to the energy smearing than the higher *particle* level energy jets which have fluctuated low.

However, we have made no constraint on the energy of the corresponding central jet in the event—the jet energy smearing is completely uncorrelated from jet to jet. As a result, the ratio \mathbf{R} of Eq. (6.8) will be biased towards the higher values. Therefore one needs to find an unbiased estimator of the forward jet energy and use it instead.

6.2.2 Systematics

JES Closure for Central Pseudorapidities

In case of γ -jet data, with jets corrected using CAFIX 5.1, we studied the ratio $\mathbf{R}_{\gamma j}$ as a function of $E' = E_T^\gamma \cdot \cosh(\eta_{jet})$ since it has been demonstrated (in a slightly different context, see page 196) that E' is an unbiased estimator of the jet energy as it is constructed from two relatively well measured quantities: photon transverse momentum E_T^γ and leading jet pseudorapidity η_{jet} . An attempt was made to determine the effects of unclustered energy (UCE) on $\mathbf{R}_{\gamma j}$. Unfortunately, due to limited statistics we were not able to extract the UCE correction in the γ -jet data, although the jet-jet results, discussed later, suggest it probably is different from zero and without such correction $\mathbf{R}_{\gamma j}$ would appear slightly lower than unity for low energies. As mentioned earlier, the E_T balance test in case of γ -jet data is a test at the parton level rather than at the particle level. In order to estimate possible losses in the jet momentum when going from parton to particle 0.7 cone jets, we performed a dedicated MC study. We generated a HERWIG MC sample and ran the DØPJET algorithm⁴ to find parton and particle jets. In order to avoid any effects of the UCE in the MC, we set the E_T threshold in the DØPJET algorithm

⁴DØPJET algorithm [79] is identical to the standard DØ jet reconstruction scheme except its input is MC partons or particles instead of calorimeter towers.

to a rather low value of 2 GeV. The particle jets were matched up with the *closest* parton jets in $\eta - \varphi$ space. Our HERWIG MC simulations suggest that particle level 0.7 cone-size jets have on average 1–2% less E_T than the corresponding parton level jets. The effect decreases with increasing E_T , or increasing pseudorapidity, of the jets [75].

Based on the results of the E_T balance study in the γ -jet data, presented in Figures 6.9 and 6.10 with open circles, we conclude that CAFIX 5.1 is correct to within 1–2% up to the pseudorapidity of 2.0 and the E_T 's covered. While the $2.0 \leq |\eta| < 2.5$ region might be somewhat unclear, the $2.5 \leq |\eta| < 3.0$ region suggests that the jets lack some energy at these high pseudorapidities. It is clear that CAFIX 5.1 works rather well in the central ($|\eta| < 0.4$) region. As was discussed earlier, the most recent DØ jet energy scale, CAFIX 5.2, has a new showering correction implemented. CAFIX 5.2 is nearly identical to CAFIX 5.1 at low η 's but corrects the lack of energy in jets at higher pseudorapidities. Therefore, γ -jet studies are not repeated with CAFIX 5.2. The results of jet-jet studies for the two most recent DØ jet energy scale versions are discussed in the following section, confirming the expectation that CAFIX 5.2 is a better JES for forward jets.

JES Closure Extension to High Pseudorapidities

To extend the limited E_T coverage (up to about 120 GeV) and to improve statistics available in the γ -jet data, we next turn to the dijet events where we require *either* of the leading jets be central, while the other one be forward. Having established that the JES for central jets is correct, we now can test the JES of the other, more forward jet.

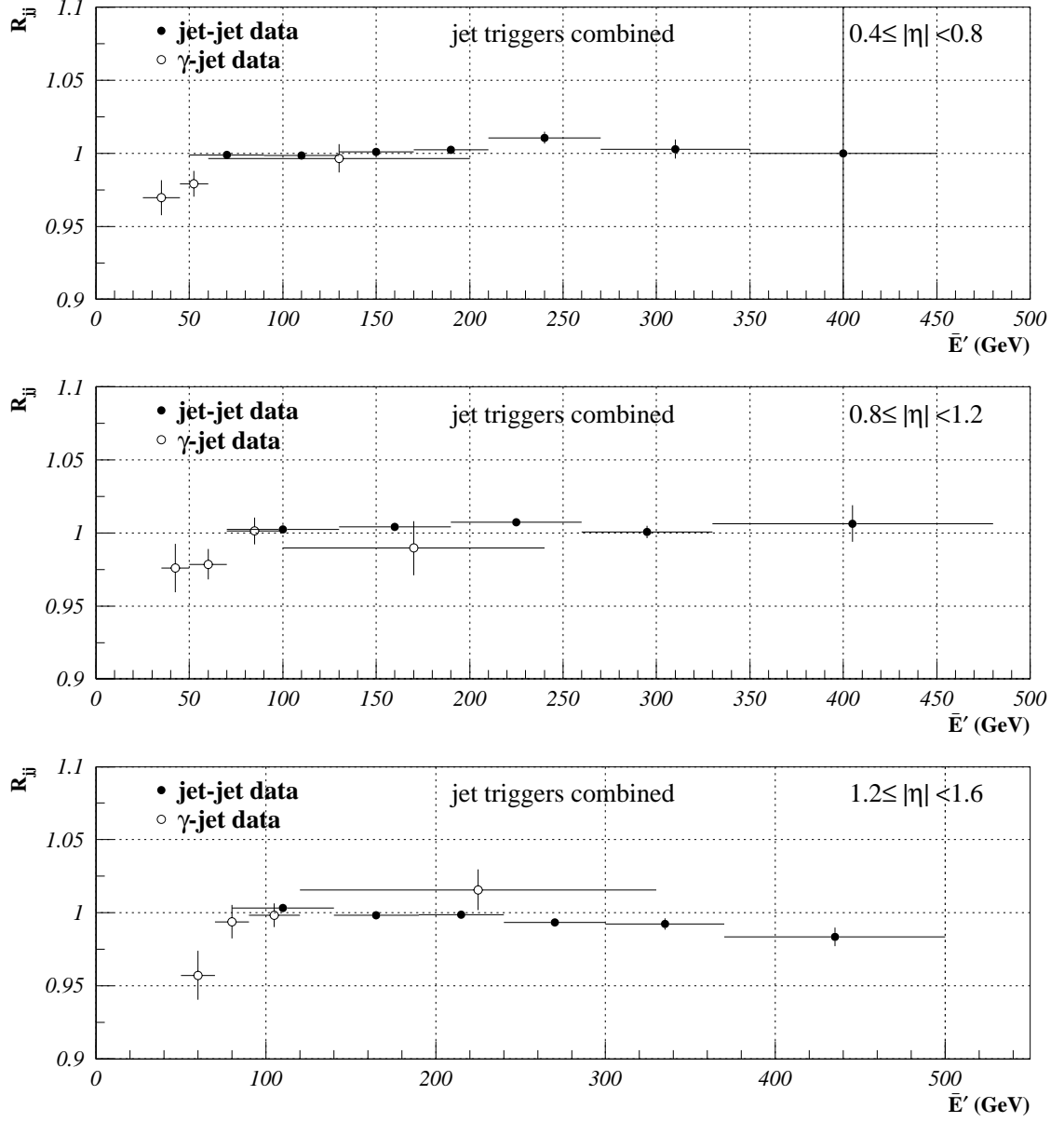


Figure 6.9: R_{jj} as a function of \bar{E}' is shown in three pseudorapidity regions. Data points from γ -jet data are overlaid for the purpose of qualitative comparison—note that the jet-jet data here are not corrected for the UCE. In both data samples, jet energy scale correction used is CAFIX 5.1.

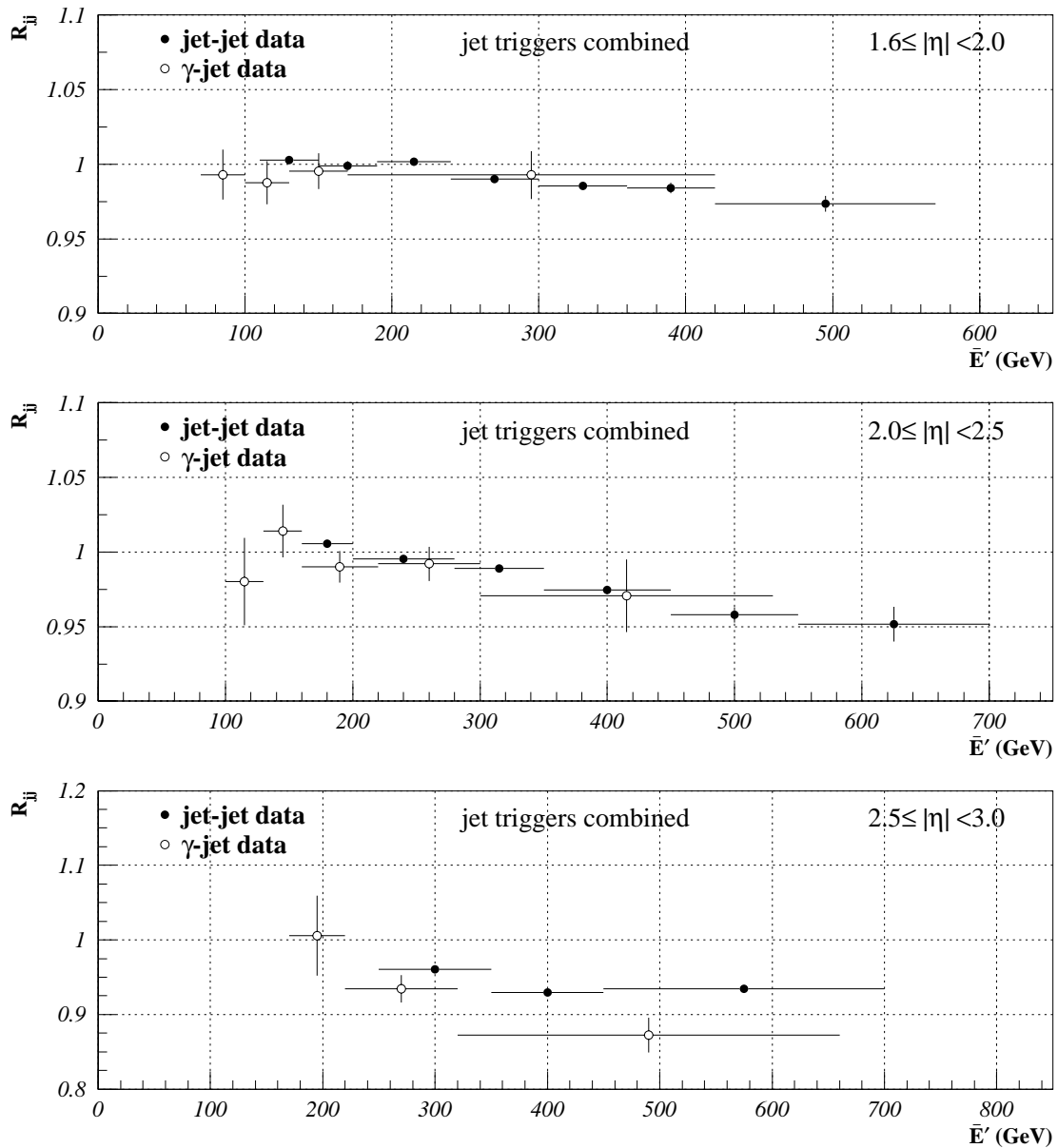


Figure 6.10: R_{jj} as a function of \bar{E}' is shown in three pseudorapidity regions. Data points from γ -jet data are overlayed for the purpose of qualitative comparison—note that the jet-jet data here are not corrected for the UCE. In both data samples, jet energy scale correction used is CAFIX 5.1.

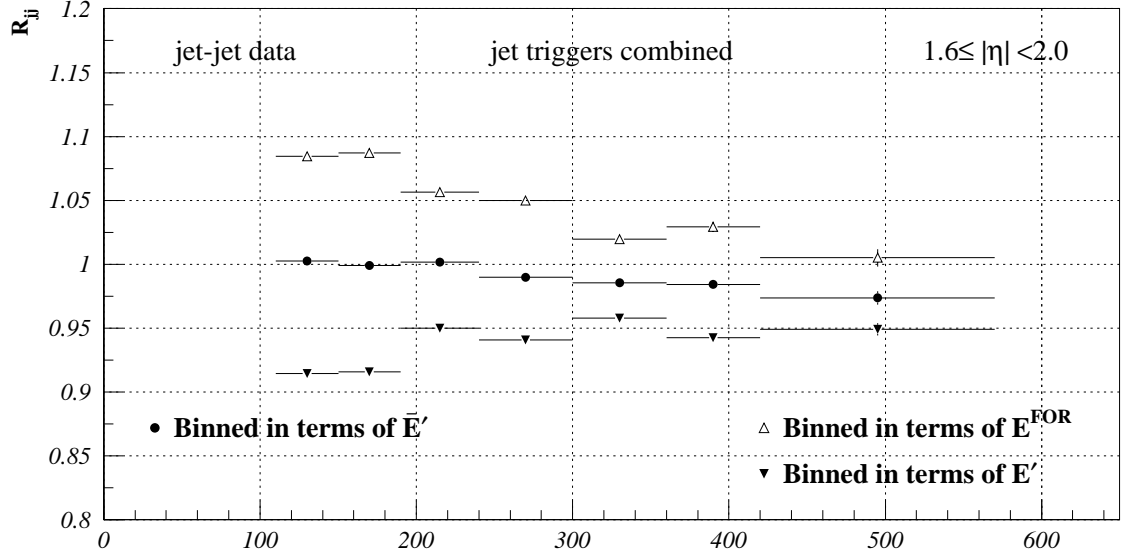


Figure 6.11: Illustration of the jet E_T resolution bias on \mathbf{R}_{jj} from jet–jet data: when binned in terms of E^{FOR} (E'), \mathbf{R}_{jj} is biased high (low), but is unbiased when binned in terms of \bar{E}' .

For jet–jet data samples, we have determined that a different variable, \bar{E}' , defined as:

$$\bar{E}' = \frac{1}{2}(E_T^{CEN} + E_T^{FOR}) \cdot \cosh(\eta_{jet}^{FOR}) \quad (6.9)$$

is the most unbiased estimator of the forward jet energy. Figure 6.11 shows the ratio \mathbf{R}_{jj} when the forward jet pseudorapidity is $1.6 \leq |\eta| < 2.0$ binned in terms of the three candidates for the forward jet energy estimator: E' —now defined as $E' = E_T^{CEN} \cdot \cosh(\eta_{jet}^{FOR})$ in an analogy with the corresponding quantity in case of γ –jet data, E^{FOR} —energy of the forward jet, and \bar{E}' of Eq. 6.9. Comparing this to the γ –jet data in the same pseudorapidity region (open circles in the top plot in Figure 6.10), one concludes that binning in terms of \bar{E}' indeed provides the most unbiased determination of \mathbf{R}_{jj} . Binning in terms of E^{FOR} biases \mathbf{R}_{jj} high, as is expected. In addition, it is clear that binning in terms of E' for jet–jet data biases \mathbf{R}_{jj} low, and therefore E' must be discarded as candidate for an unbiased estimator

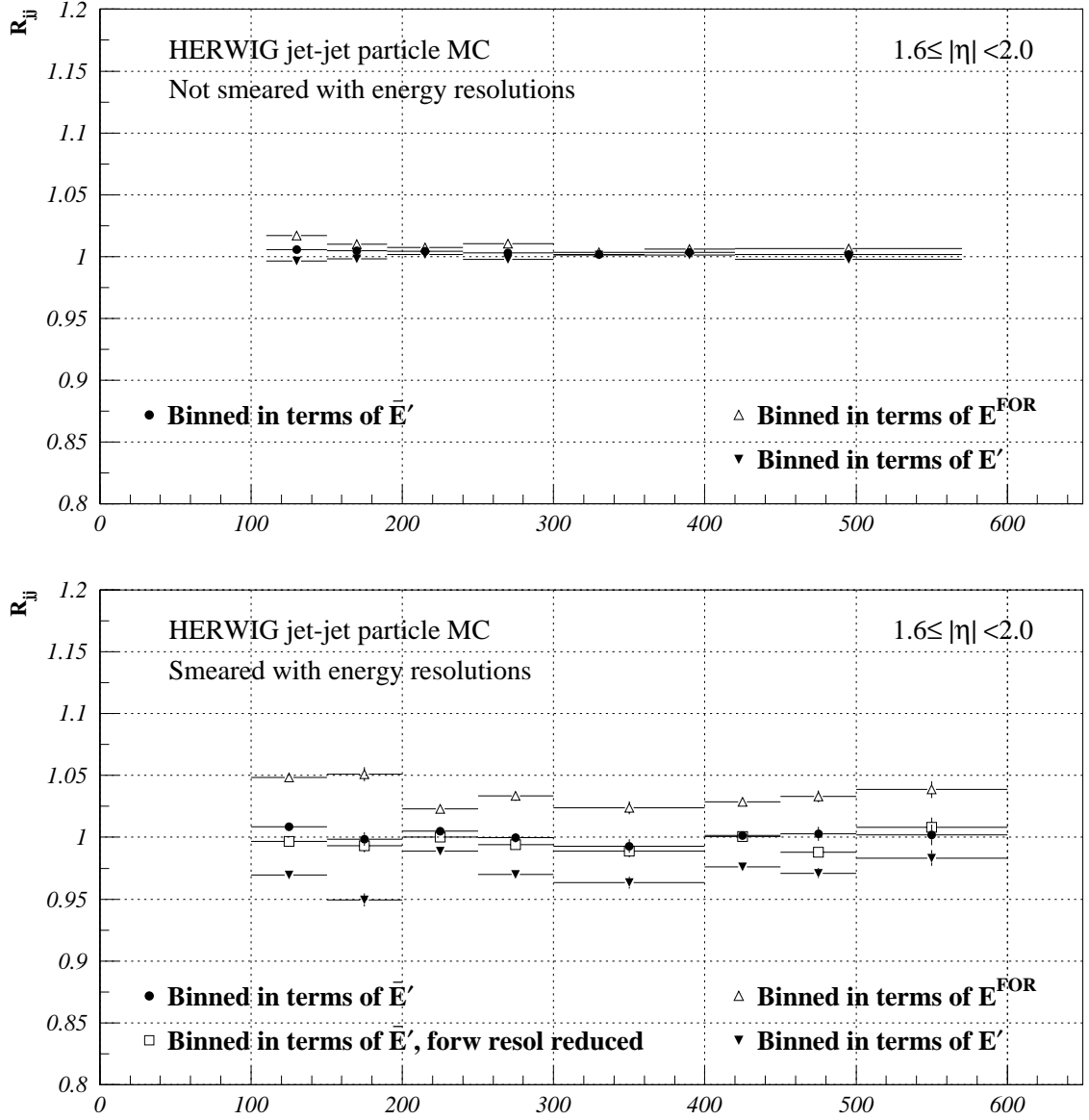


Figure 6.12: The HERWIG particle level MC shows no resolution bias (top plot). However, as soon as the MC particle jets are smeared by the jet energy resolutions (bottom plot), bias appears when binned in either E^{FOR} or E' but binned in \bar{E}' remains unbiased. Even when the forward energy resolutions are artificially lowered by additional 20%, binning in \bar{E}' stays unbiased (open squares in the bottom plot).

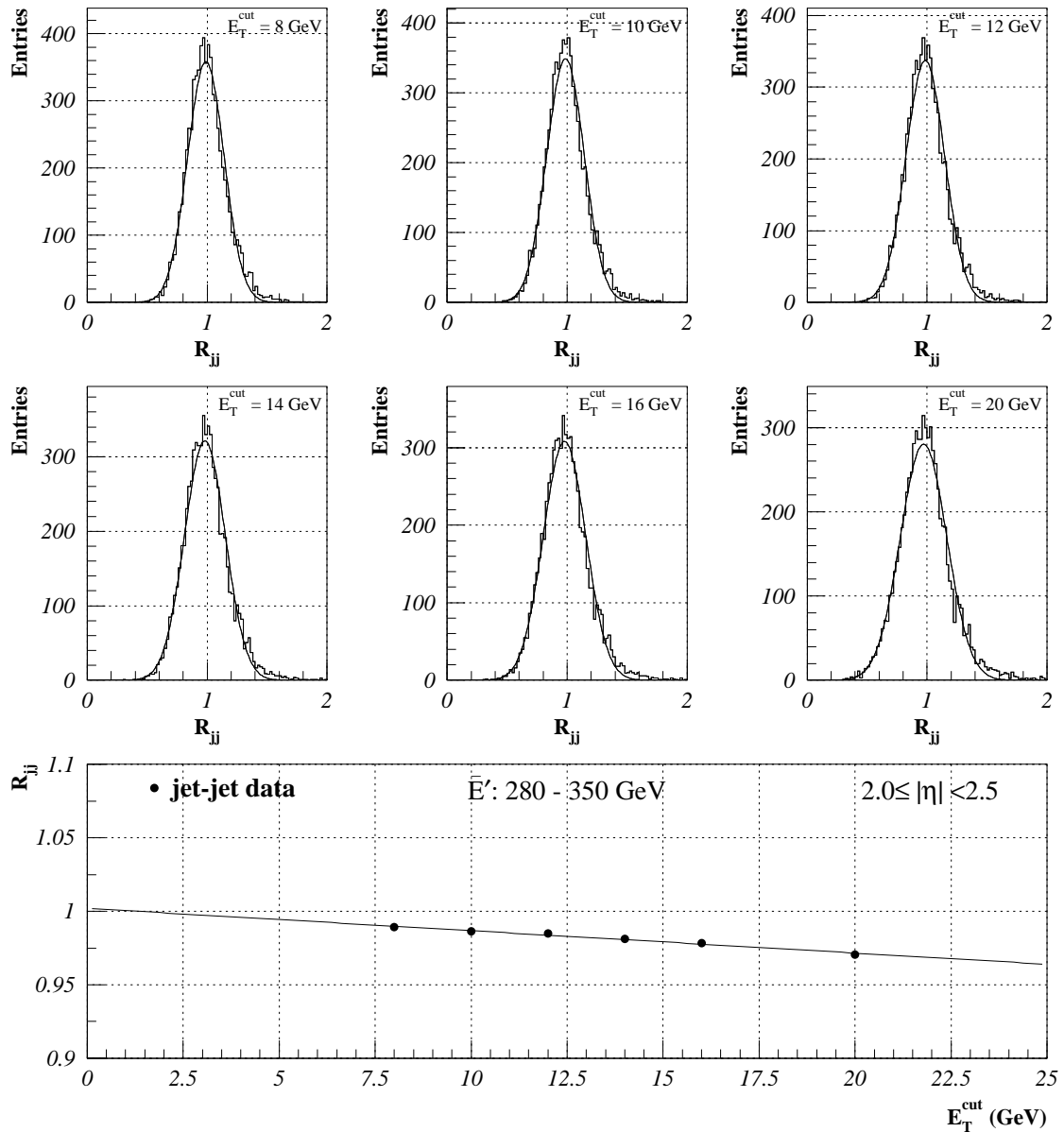


Figure 6.13: Illustration of the derivation of the unclustered energy correction in jet-jet data.

of the forward jet energy. To the extent that jet energy resolutions are the same in the Central and End Calorimeters, low E' bias is exactly the inverse of the high bias seen when binned in terms of E^{FOR} .

For further checks of these conclusions, a dedicated HERWIG particle level MC sample was generated. Once again, in order to avoid any possible effects of the UCE in the MC, we set the jet E_T threshold to 2 GeV in the DOPJET algorithm. In the particle level MC there is no energy smearing except for a rather small *effective* particle level “energy resolution” arising from fluctuations in out-of-cone particle emission. This effect has been well understood in the course of jet energy resolution studies, and in that context is often referred to as “Particle Level (Dijet) Imbalance” [80]. Therefore, one would expect that the results of binning in either of the three variables would not be different. The top plot in Figure 6.12 confirms this expectation. It also suggests that at the particle level, *without* the UCE, jets balance to within 0.5%, implying that the UCE-corrected \mathbf{R}_{jj} from jet–jet data is a good measure of jet E_T balance at the *particle* level, and as such can be used to test the entire JES.

In addition, we smear MC particle level jets by the energy resolution (see chapter 9, for example) and check if this indeed introduces a bias similar to what is observed in the jet–jet data. In the bottom plot of Figure 6.12, \mathbf{R}_{jj} is shown as a function of the three variables E^{FOR} , E' , and \bar{E}' from the MC, where now particle level jets are smeared by the jet energy resolutions from [80]. Confirming our hypothesis, the bias appears in \mathbf{R}_{jj} when it is binned in terms of either E^{FOR} or E' , while if binned in terms of \bar{E}' the ratios remain unbiased.

We stress that, as it can be seen from Figures 6.11 and 6.12, the binning in terms of \bar{E}' actually removes the E_T resolution bias to within 1% rather than just averaging the two biases seen when binned in terms of E^{FOR} and E' . The absence of bias in \bar{E}' might be affected by the large differences between the central and forward

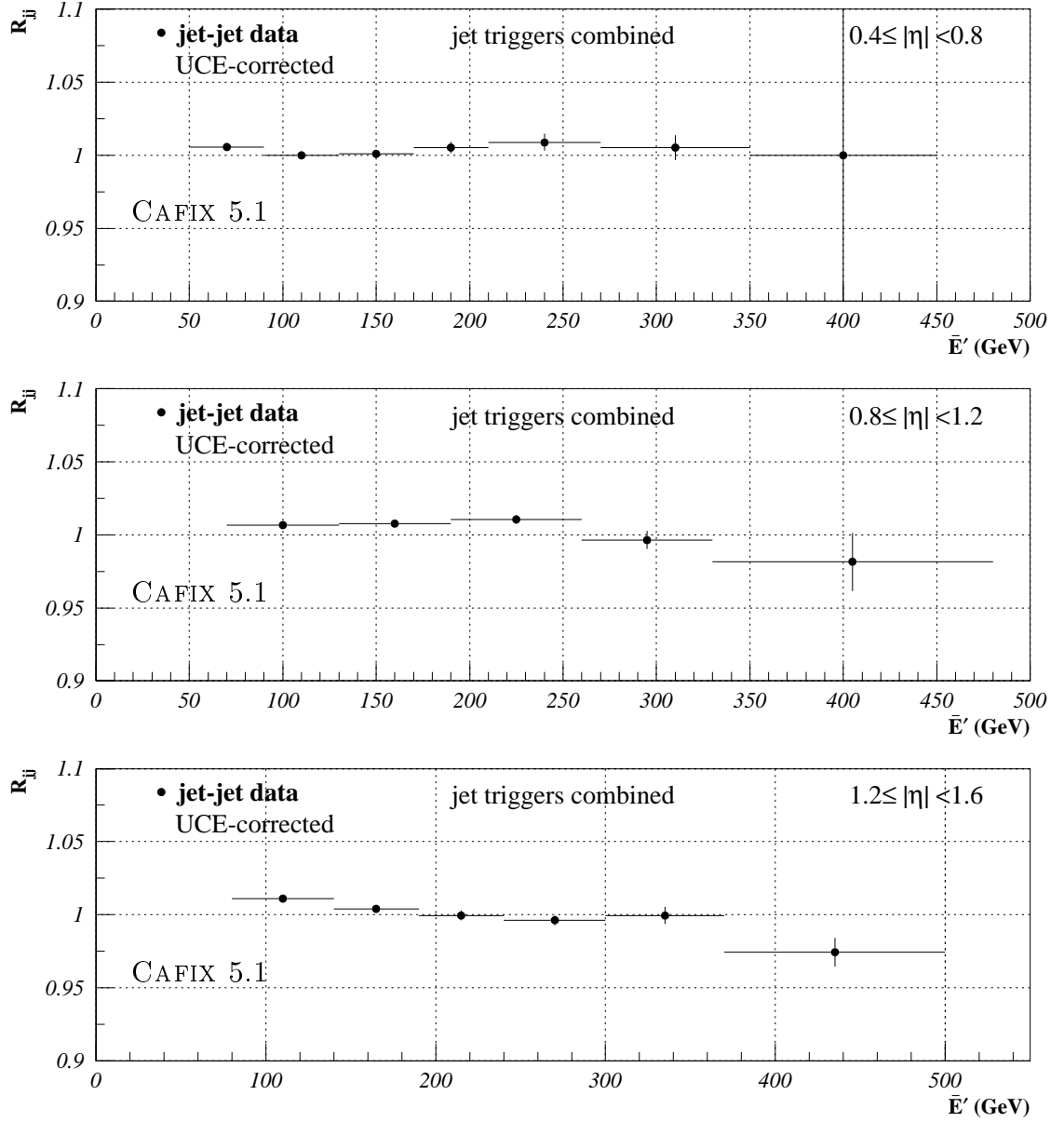


Figure 6.14: R_{jj} as a function of \bar{E}' is shown in three pseudorapidity regions after the unclustered energy correction is applied.

jet energy resolutions. Based on the available resolutions, we rather conservatively estimate the difference between the central and forward resolutions to be 20%. We once again smear the MC particle level jets, but now forward jets are smeared by 20% smaller resolution than what is measured in [80], and central jets are smeared

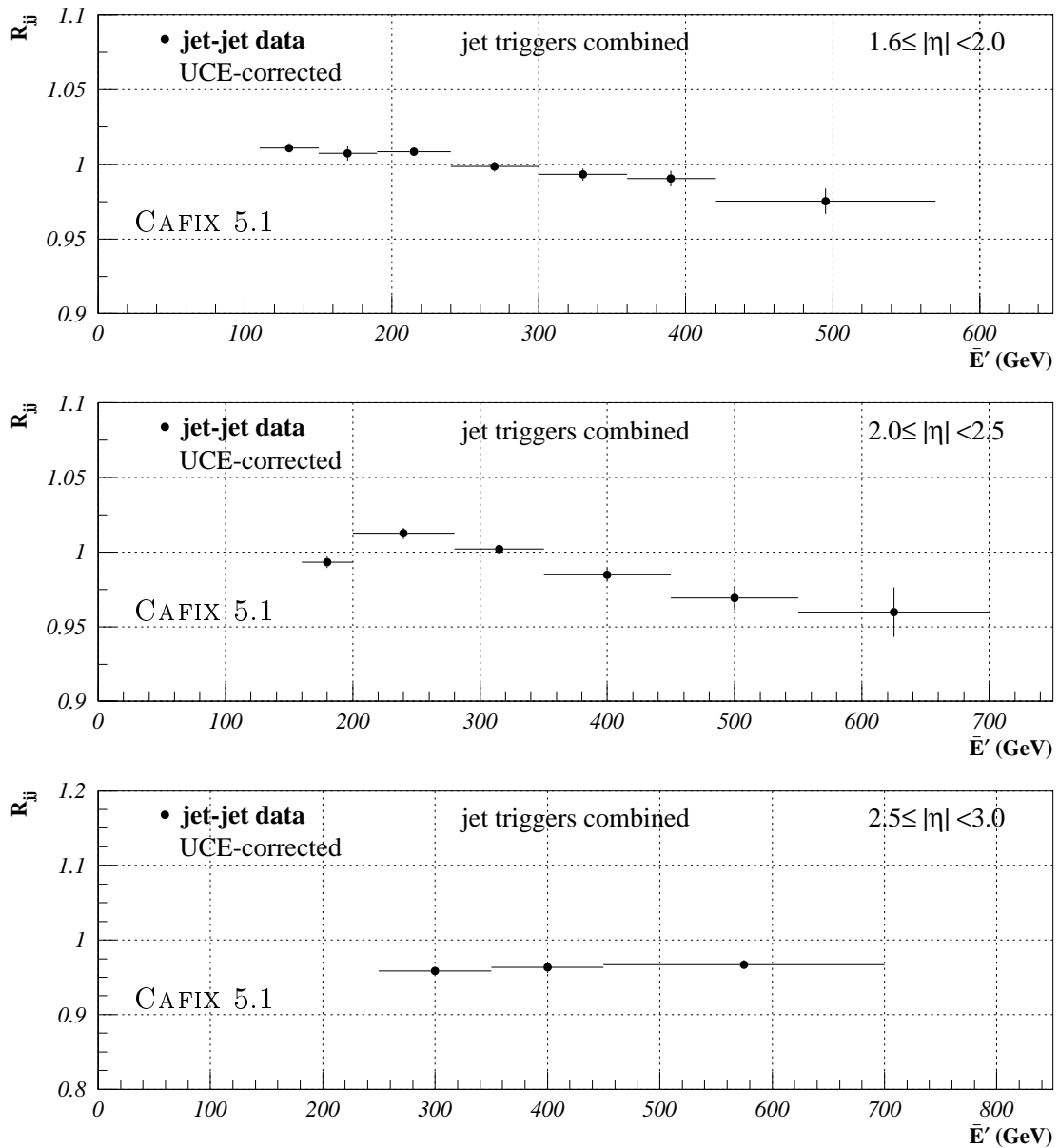


Figure 6.15: R_{jj} as a function of \bar{E}' is shown in three pseudorapidity regions after the unclustered energy correction is applied.

by the actual measured central resolution. Open squares in the bottom plot of Figure 6.12 show the resulting R_{jj} as a function of \bar{E}' . Once again, no significant bias is observed. Based on these tests, we conclude that, in the case of jet-jet data, the best estimator of the forward jet energy is \bar{E}' which is free of E_T resolution bias

to within about 1%.

Having convinced ourselves that \mathbf{R}_{jj} as a function of \bar{E}' is an unbiased and sensitive measure [75] of the correctness of the JES, we next compare results from jet–jet data to those obtained earlier from γ –jet data. Filled circles in Figures 6.9 and 6.10 show the results from jet–jet data overlayed with previously discussed γ –jet data. (For the purpose of these plots, in both data samples, jets are corrected with CAFIX 5.1). While one needs to be careful when directly comparing the results of the E_T balance from γ –jet and jet–jet data (because in the former it is a test at the parton level and in the latter—at the particle level), the agreement between the two is excellent.

Finally we study the effects of the UCE on \mathbf{R}_{jj} . We apply 8 (default), 10, 12, 14, 16, and 20 GeV cuts (E_T^{cut}) on the *uncorrected* E_T of non-leading jets and examine \mathbf{R}_{jj} as a function of E_T^{cut} . Increasing the value of E_T^{cut} results in an obvious trend of decrease of the ratio \mathbf{R}_{jj} , see for example Figure 6.13. In order to correct for the effect of the UCE, we fit a straight line to the ratios as a function of E_T^{cut} , and extrapolate the fitted function down to $E_T^{cut} = 0$ GeV. This extrapolated value of the fitted line is then taken as a UCE–corrected value for \mathbf{R}_{jj} . The UCE correction is derived and applied in every pseudorapidity region.

6.2.3 The Results for CAFIX 5.1 and CAFIX 5.2

The \mathbf{R}_{jj} as a function of \bar{E}' *after* the UCE correction for CAFIX 5.1 is finally shown in Figures 6.14 and 6.15. In the central and intercryostat pseudorapidity regions \mathbf{R}_{jj} is consistent with unity to within about 1–1.5%, ignoring the last data points in $0.8 \leq |\eta| < 1.2$ and $1.2 \leq |\eta| < 1.6$ which have larger statistical errors and have

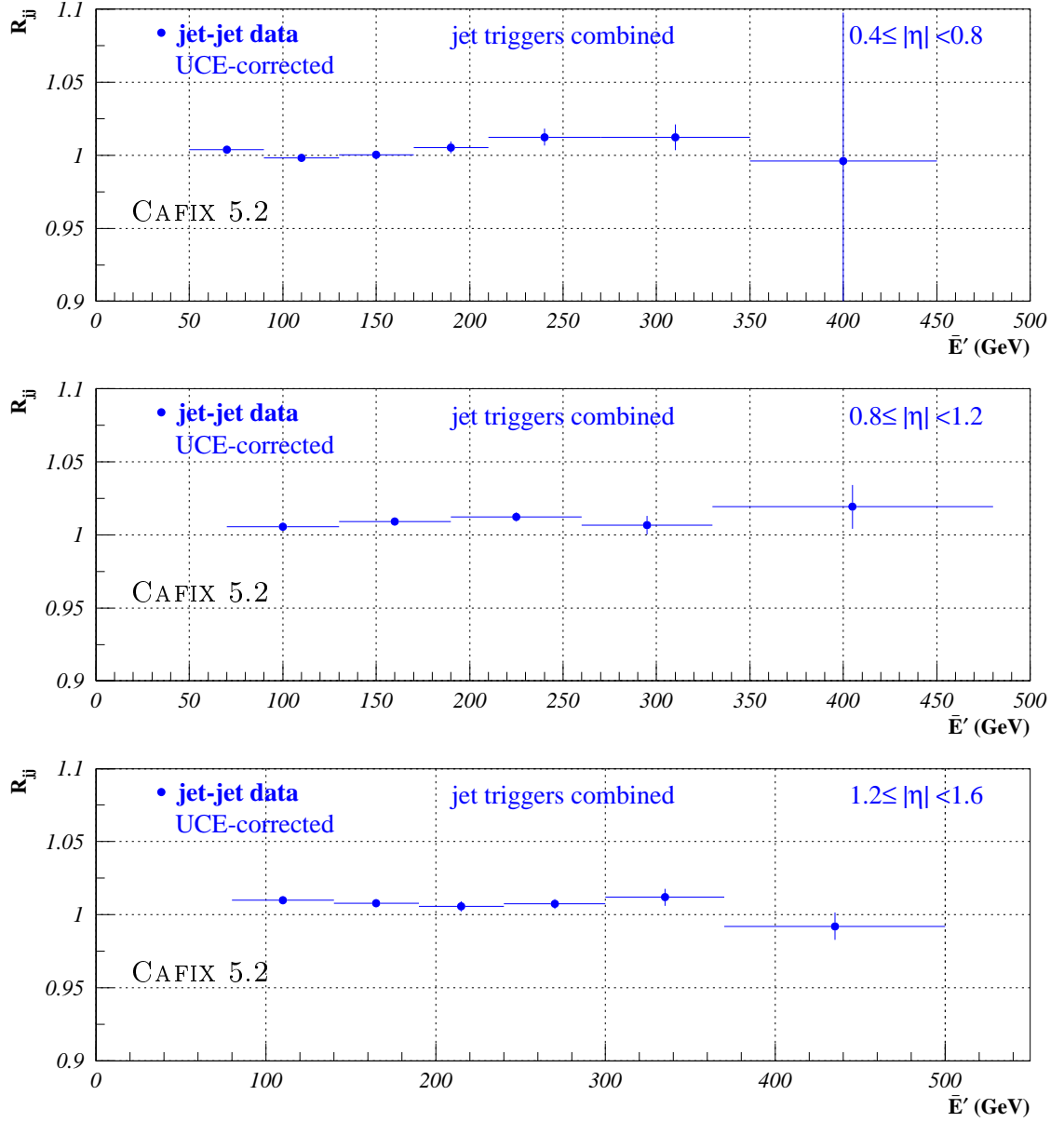


Figure 6.16: R_{jj} as a function of \bar{E}' is shown in three pseudorapidity regions after the unclustered energy correction is applied.

fluctuated by about 2.5% below unity. However, in the forward pseudorapidity regions (i.e. $|\eta| > 1.6$) we start to see some deficit in the forward jet energy. In $1.6 \leq |\eta| < 2.0$, the R_{jj} is consistent with unity to within about 1.5% up to the energies of 400 GeV, and drops below unity by about 2.5% near 500 GeV in energy.

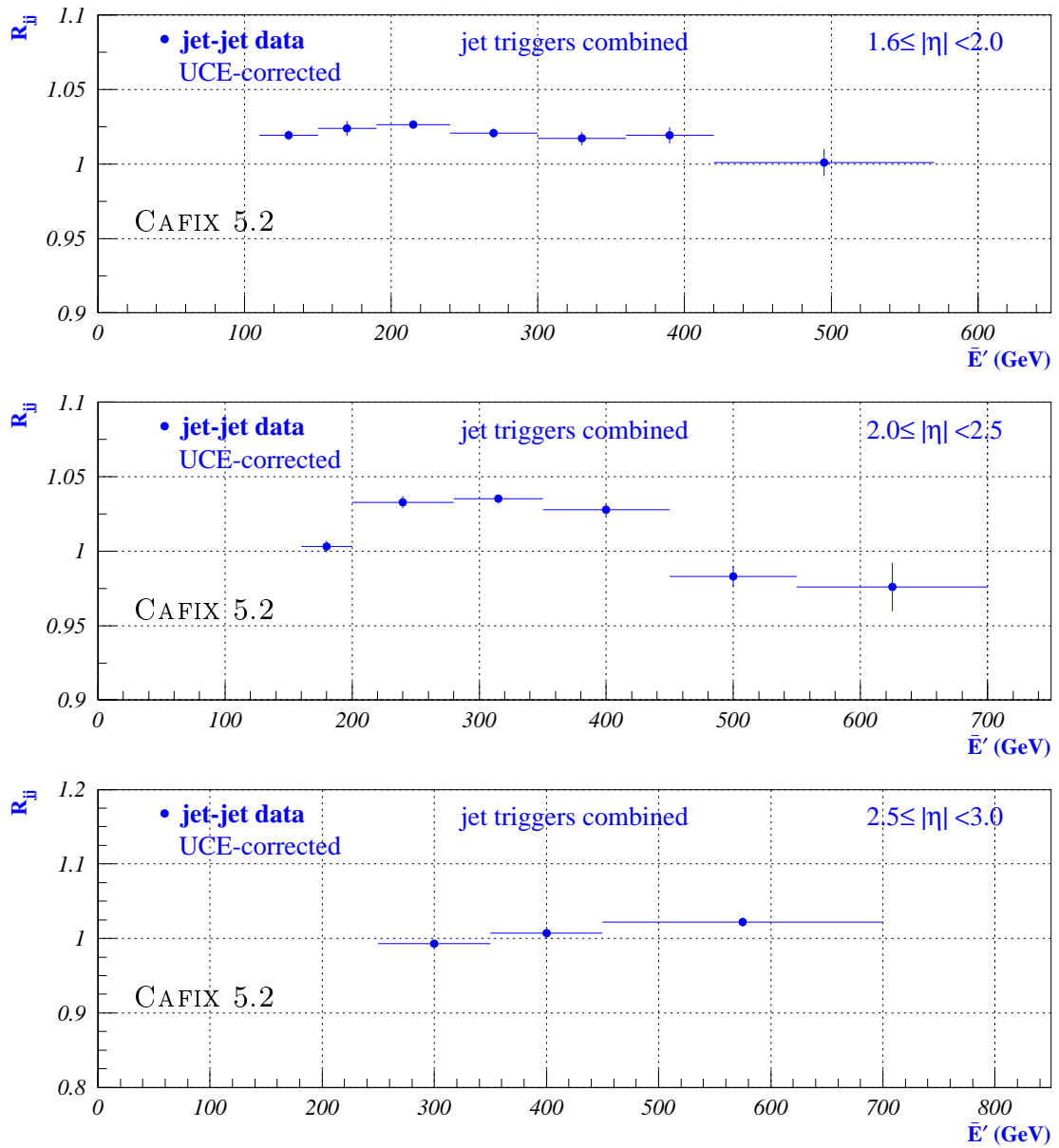


Figure 6.17: R_{jj} as a function of \bar{E}' is shown in three pseudorapidity regions after the unclustered energy correction is applied.

In $2.0 \leq |\eta| < 2.5$, deviations from unity are within 2% at and below 400 GeV and drop below unity by as much as 3–4% for energies above 400 GeV. Finally, in $2.5 \leq |\eta| < 3.0$ we see deficiency of about 4–5% in the forward jet energy.

To reiterate, CAFIX 5.1 is verified to be correct to within its uncertainty band in the range it is investigated. Our results suggest, however, that CAFIX 5.1 systematically undercorrects jets at high pseudorapidities. The difference between the nominal ratio and unity in $1.6 \leq |\eta| < 2.0$ ($2.0 \leq |\eta| < 2.5$) pseudorapidity region grows from about 1.5% (2%) at and below 400 GeV of energy up to about 2.5% (4%) above 400 GeV; in $2.5 \leq |\eta| < 3.0$, the deviation from unity is about 4–5% throughout the energy range covered.

Finally, the results of the JES Closure test for the most recent version of the DØ jet energy scale, CAFIX 5.2, are presented in Figures 6.16 and 6.17. At low rapidities, CAFIX 5.2 closes as well as CAFIX 5.1, perhaps overcorrecting central jets slightly, by about 0.5%, but well within the uncertainties of the JES and the test itself. It seems to overcorrect within 2–3.5% in the pseudorapidity region $1.6 \leq |\eta| \leq 2.5$ but, again, the closure is within the systematic errors. However, CAFIX 5.2 significantly improves the forward jet calibration at $|\eta| \geq 2.5$ compared to its predecessor, CAFIX 5.1. To summarize, closure of the current DØ JES scale, CAFIX 5.2 is good within the systematic uncertainties associated with both the JES and the closure method. It does as well as CAFIX 5.1 at low η 's and improves the jet calibration at highest pseudorapidities. As this jet cross section analysis extends to $|\eta| = 3.0$, we shall use CAFIX 5.2 JES version to obtain final physics results. A more detailed discussion of the JES errors as they pertain to the cross section measurements is deferred until later chapters.

CHAPTER 7

LUMINOSITY STUDIES

For cross section analyses, the precise measurement of integrated luminosity L becomes of primary importance, setting the normalization of the measurement. It is obtained by summing up measured (primarily by Level 0 hodoscopes) instantaneous luminosities \mathcal{L} over a specified period of time, and for Run 1B can be denoted as:

$$L = \int^{Run\ 1B} \mathcal{L} dt . \quad (7.1)$$

Without going into details on how \mathcal{L} is measured at DØ, we note that the resulting integrated luminosity is corrected for Level 0 detector acceptance, beam contamination, and events with multiple interactions, and is measured for each trigger to account for individual prescales and dead times. The integrated luminosities for the four jet triggers used in this analysis as taken from the Production Data Base, PDB, are listed in the beginning of chapter 4 (page 124). However, it turns out that additional corrections are required and we discuss them next.

7.1 Luminosity Matching

There are discrepancies observed among trigger versions 8 and versions 9 and 10, and luminosities for triggers Jet_30 and Jet_50 are generally poorly determined [46]. To correct for these effects, we begin by taking luminosities for triggers Jet_85 and

Jet_Max, versions 9 and 10, from the PDB. Jet E_T spectrum derived from Jet_Max trigger version 8 shows a 10% mismatch relative to that derived from versions 9 and 10 only of the same trigger. The luminosity of version 8 Jet_Max has been adjusted so that the dijet mass spectrum for version 8 matches that for versions 9 and 10. This adjustment is also applied to Jet_85. Thus, the 54703 and 91884 nb^{-1} luminosities for Jet_85 and Jet_Max, respectively, are 0.7% below the uncorrected PDB values. This difference is added linearly to the recommended 5.4% error on the PDB value resulting in a total error of 6.1%.

PDB luminosities of Jet_30 and Jet_50 are accurate only to 10% because the efficiency for the one-interaction requirement at Level \emptyset has an unmeasured dependence on luminosity. The correct luminosity has been determined by matching the jet E_T spectrum from Jet_50 to that from Jet_85 above the 99% efficiency threshold of about 130 GeV of E_T of the latter, more restrictive trigger. This introduces a 1.0% statistical error. Finally, the E_T spectrum from Jet_30 is matched to that from corrected Jet_50 above the 99% efficiency threshold (about 90 GeV of E_T) of the more restrictive Jet_50 trigger with a 1.4% statistical error. The matching error for Jet_30 is then given by 1.1% and 1.4% added in quadrature, or 1.7%. These errors are added to the 6.1% error on Jet_85. The final Jet_30 and Jet_50 luminosities are then 339.0 and 4612.6 nb^{-1} with errors of 7.8% and 7.1%, respectively.

7.2 Luminosity Dependence of the Cross Sections

The probability of multiple interactions in a bunch crossing increases with higher instantaneous luminosity. Multiple interactions at high luminosities may affect event

reconstruction in three ways. First, there might be a pile-up—luminosity dependent residual energy in the calorimeters from the previous bunch crossing. Second, there might be extra energy coming from multiple interactions within a given bunch crossing. This excess energy obviously is not related to the hard primary interaction we intend to study. Lastly, due to multiple interactions within a bunch crossing, the vertex of the primary interaction might be mismeasured by the tracking system. This may result in mismeasurement of kinematic variables of the objects of interest in the calorimeters. By “luminosity dependence” we generally mean the combined effect of all the above on the cross section measurement. It must be noted, however, that offset subtraction of the $D\bar{O}$ jet energy scale (JES) [74] and $\vec{\mathcal{H}}_T$ based revertexing [46, 53] correct for effects of pile-up and extra interactions, and misvertexing, respectively. In this study [81] we look for any *residual* effects these phenomena may have on the differential cross section of single inclusive jet production at $D\bar{O}$. Obviously the physical origin of all these effects lies in the number of multiple (or extra) interactions increasing with luminosity.

Any such luminosity dependence may affect either the shape or the normalization (or both) of the observed cross sections at higher luminosities. We investigate the two possible effects separately, and henceforth refer to them as “shape” and “normalization” studies, respectively.

7.2.1 Shape Studies

The probability of multiple interactions at instantaneous luminosities¹ (\mathcal{L}) of less than 5 is at most 18%, while for $\mathcal{L} > 10$, this probability is at least 46%. Therefore

¹Unless otherwise noted, throughout this note we use dimensionless instantaneous luminosity, which must be scaled by a factor of $10^{30} \text{ cm}^{-2}\text{s}^{-1}$ to obtain a proper value of \mathcal{L} .

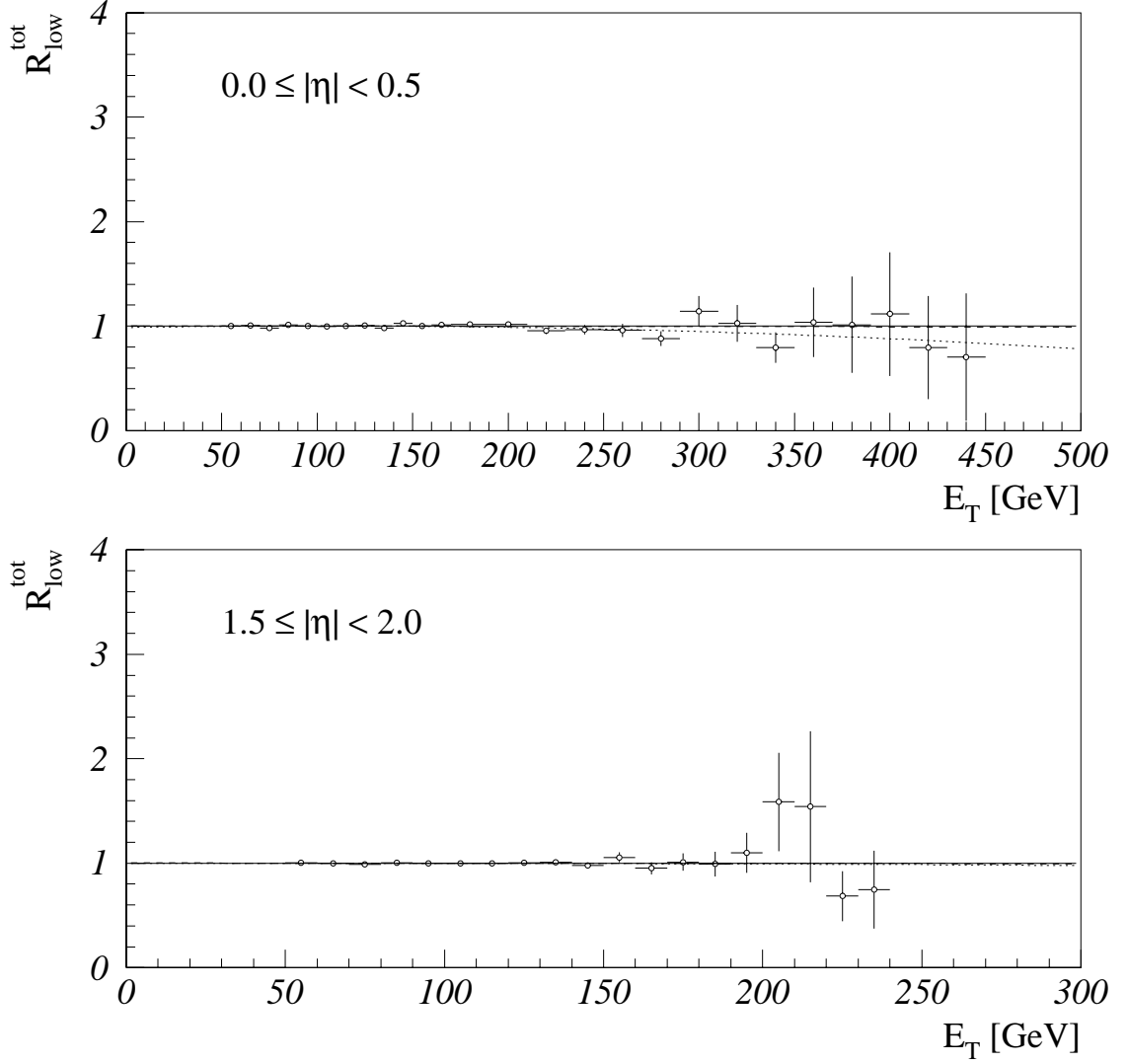


Figure 7.1: R_{low}^{tot} is fit to three models: P0 (solid line), P1 (dashed line), and P2 (dotted line). Shown here are fits in $|\eta| < 0.5$ and $1.5 \leq |\eta| < 2.0$ pseudorapidity regions.

we choose to consider various luminosity subsamples resulting from placing cuts at instantaneous luminosities of 5 and 10, as described in Table 7.1. We study ratios of the jet E_T spectra measured from these different subsamples as a function of jet E_T in different η regions. We refer to different E_T ratios using the notation: R_{den}^{num} , where the superscript refers to the subsample in the numerator, and the subscript,

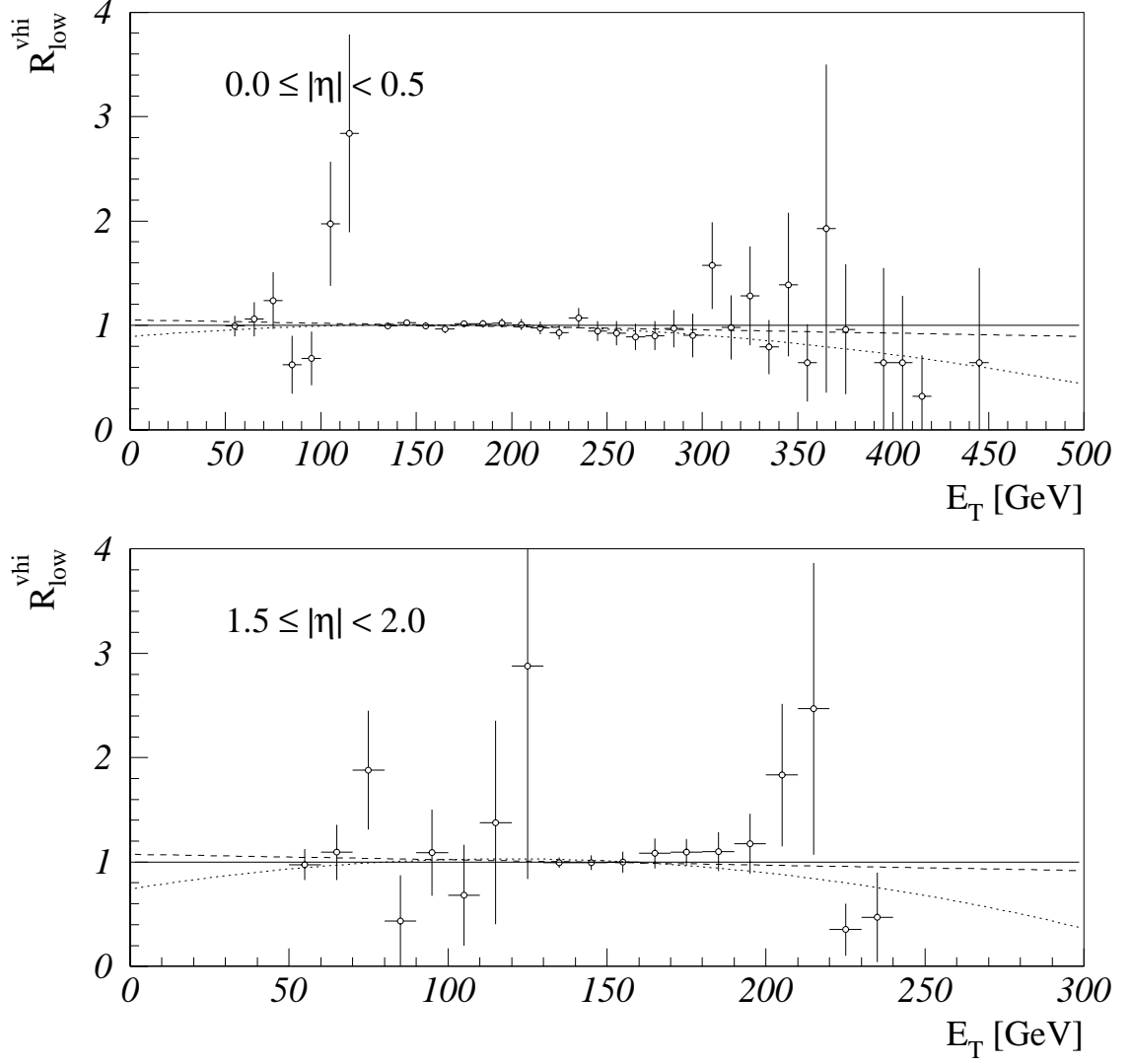


Figure 7.2: R_{low}^{vhi} is fit to three models: P0 (solid line), P1 (dashed line), and P2 (dotted line). Shown here are fits in $|\eta| < 0.5$ and $1.5 \leq |\eta| < 2.0$ pseudorapidity regions.

\mathcal{L} range	$\mathcal{L} < 5$	$5 \leq \mathcal{L} < 10$	$\mathcal{L} \geq 10$	$\mathcal{L} \geq 5$	any
Subsample	<i>low</i>	<i>med</i>	<i>vhi</i>	<i>hig</i>	<i>tot</i>

Table 7.1: Subsamples with different \mathcal{L} cuts.

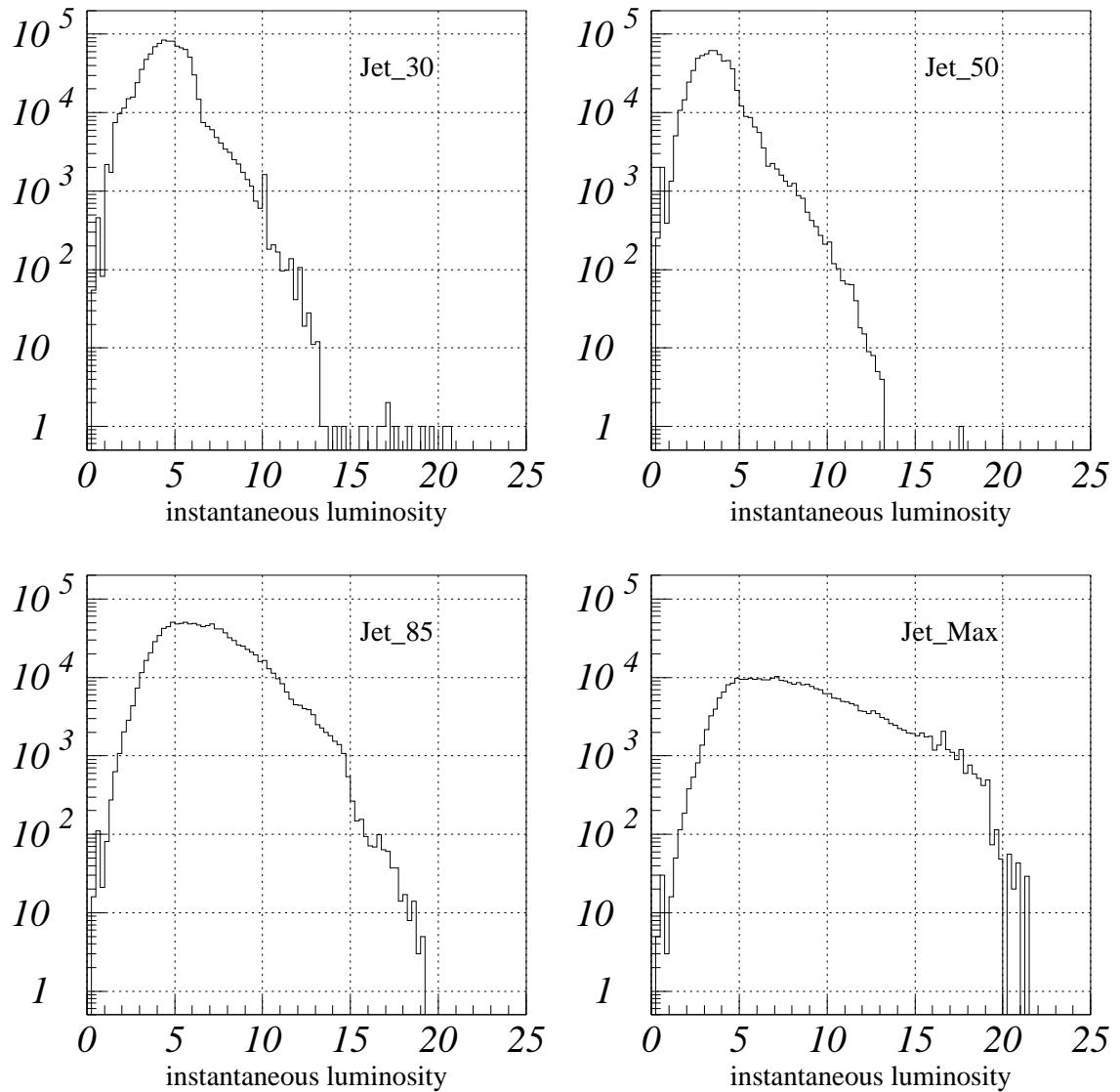


Figure 7.3: Distributions of the instantaneous luminosity for each jet trigger. Note that plotted is dimensionless luminosity, which must be scaled by a factor of $10^{30} \text{ cm}^{-2}\text{s}^{-1}$ to obtain a proper value of \mathcal{L} .

to the subsample in the denominator. For example, R_{tot}^{low} means the ratio of the E_T distributions (or cross sections, in the following section) from the *low* and *tot* subsamples.

In order to maximize statistics over the full E_T range available, and to

consider jet triggers where they are above 99% efficient, following reference [46], the E_T spectra (and hence the ratios) from 50 to 90 GeV are taken from Jet_30, 90 to 130 GeV from Jet_50, 130 to 170 GeV from Jet_85, and above 170 GeV from Jet_Max data. If one measures the ratios of *cross sections* (as opposed to E_T spectra) from different luminosity subsamples, one expects all the ratios to be close to 1 in the absence of any luminosity dependence affecting the *normalization*. However, luminosity cuts for the shape studies are applied event by event, and we are unable to calculate the integrated luminosities for such subsamples—the PDB provides us only with run by run² integrated luminosities. For this reason, an absolute normalization of the various luminosity subsample ratios from different jet triggers is a reflection of what fraction of the particular trigger data is taken from a luminosity interval under consideration. Since in this section we address only the question of shape dependence of the cross section on luminosity, it is sufficient to artificially normalize the ratios from different jet triggers to any constant number, which we naturally choose to be 1. In order to normalize the ratios to 1, for each trigger, we fit the ratios in the E_T region of interest to a constant and rescale the ratios by the inverse of this constant. As a result of this procedure, in every η region we end up with the ratios of E_T spectra over the full E_T range available, and we can test them on shape differences.

We consider the *low* sample to yield the best representation of a “truly” luminosity *independent* cross section. Then, in the case of any measurable luminosity dependence, the ratio R_{low}^{tot} indicates the overall effect on the *entire* data sample used for the cross section determination. In calculating such ratios special care is taken for proper estimation of statistical errors since the denominator is a

²more precisely, partition by partition.

subsample of the numerator. R_{low}^{tot} in various η regions are fitted to three different models: a constant (P0), a straight line (P1), and a second order polynomial (P2). See Figure 7.1 for η regions $|\eta| < 0.5$ and $1.5 \leq |\eta| < 2.0$ (for the other rapidity regions see reference [81]). The parameters of the three fitted models along with usual χ^2 values and confidence levels (CL) of the fits in all η regions are summarized in Table 7.2. We see that based on CL it is hard to generally exclude any of the fitted models. However, except for $|\eta| < 0.5$, the CL for the P0 fit is always slightly higher. Also statistical error on the fitted parameter of a constant (p_0) is rather small in all three models, being *at most* 0.5%, 1.6%, and 3.6% in P0, P1, and P2 models respectively. Contrary to this, uncertainties on the slope and quadratic correction (p_1 and p_2 respectively) are extremely large in the fitted models P1 and P2: in case of P1 model, the uncertainties on the slope are more than 100% in every η region, while in case of P2 model, uncertainties on p_1 and p_2 are always more than 50%, and very often more than 100%. Based on these observations, the fit to P0 appears to be the best candidate for describing the R_{low}^{tot} in every η region. We thus conclude that the ratios do not indicate any significant luminosity dependence affecting the shape of the cross section.

Going one step further, we also examine the ratios R_{low}^{vhi} that would be affected most by any luminosity dependence since they correspond to the extreme values of luminosity. See Figure 7.2 for illustration in the two pseudorapidity regions. The scattered points below E_T of 130 GeV are due to the fact that very little *vhi* data have been taken for Jet_30 and Jet_50 triggers, as can be seen in Figure 7.3 from the instantaneous luminosity, \mathcal{L} , profiles of different jet triggers for the period of Run 1B. The regions of reasonably good statistics, however, are still compatible with the hypothesis of no shape dependence, as can be seen directly, and

by repeating the exercise of comparing parameters for the three fitted models [81].

For completeness and as consistency checks we also examine other ratios of interest, such as R_{low}^{high} , R_{low}^{med} , R_{med}^{vhi} , and R_{high}^{vhi} . As expected, these ratios too do not provide any grounds for suspecting luminosity dependence affecting the shape of the cross section [81].

Furthermore, we study the ratios when the JES correction is not applied, when no $\vec{\mathcal{H}}_T$ correction is applied, and when the events flagged by AIDA are excluded from the sample. Not applying the JES scale worsens the ratios the most, “turning off” the $\vec{\mathcal{H}}_T$ correction has lesser effect, and excluding AIDA-flagged events has virtually no effect [81]. Based on these studies, our conclusion is that after applying all the standard corrections to the data there is no measurable residual luminosity dependence affecting the shape of the inclusive jet cross sections at all pseudorapidities up to $|\eta| = 3.0$.

7.2.2 Normalization Studies

In order to address the question of whether there is any constant offset in the luminosity calculation, one needs to subdivide the total sample based on luminosity cuts applied *run by run*. We consider the same cuts as in Table 7.1 but this time we require every event in the run to satisfy the \mathcal{L} cut in order for this run to make it into one of the subsamples. Obviously such cuts are more restrictive, and therefore one generally ends up with lower statistics—the reason why we preferred the shape studies to be carried out as described in the previous section: sacrificing the knowledge of the exact luminosity for the subsamples in order to gain the statistical power for investigating possible shape dependence.

η	Fit	χ^2	ndf	CL [%]	$p_0 \pm \Delta p_0$	$p_1 \pm \Delta p_1$ [$10^{-3}/\text{GeV}$]	$p_2 \pm \Delta p_2$ [$10^{-6}/\text{GeV}^2$]
1	P0	43.6	36	18.0	1.000 ± 0.002		
	P1	43.4	35	15.6	1.002 ± 0.005	-0.023 ± 0.053	
	P2	40.0	34	22.2	0.986 ± 0.010	0.291 ± 0.178	-1.400 ± 0.756
2	P0	34.5	31	30.4	1.000 ± 0.002		
	P1	34.2	30	27.3	1.003 ± 0.006	-0.033 ± 0.059	
	P2	34.2	29	23.2	1.004 ± 0.012	-0.038 ± 0.228	0.024 ± 1.033
3	P0	23.5	28	70.8	1.000 ± 0.002		
	P1	22.8	27	69.4	0.994 ± 0.007	0.061 ± 0.075	
	P2	22.8	26	64.4	0.997 ± 0.016	0.002 ± 0.322	0.297 ± 1.581
4	P0	8.3	18	97.5	1.000 ± 0.003		
	P1	8.2	17	96.2	1.002 ± 0.010	-0.022 ± 0.114	
	P2	8.2	16	94.2	0.999 ± 0.028	0.005 ± 0.646	-0.395 ± 3.555
5	P0	13.8	12	31.6	1.000 ± 0.005		
	P1	13.3	11	27.7	1.011 ± 0.016	-0.147 ± 0.207	
	P2	12.6	10	25.0	0.949 ± 0.034	1.521 ± 0.872	-10.280 ± 5.454

Table 7.2: Summary of fit parameters, χ^2 values, degrees of freedom (ndf), and confidence levels (CL). Pseudorapidity regions are numbered in ascending order according to increasing η , i.e. region 1 corresponds to the central-most ($|\eta| < 0.5$) interval, while region 5 is forward-most ($2.0 \leq |\eta| < 3.0$) interval.

As discussed earlier in this section, during Run 1B the luminosities for the entire Jet_30 and Jet_50 trigger data and for the Jet_Max trigger version 8 are poorly determined. Therefore, all jet triggers are being matched against the Jet_85 trigger. For this reason, we check the normalization effects for the Jet_85 trigger data only. The integrated luminosities for different subsamples of this trigger are calculated using PDB [82], and are summarized in Table 7.3. Since earlier we establish no shape dependence of the cross section on luminosity, we now fit *cross section* ratios

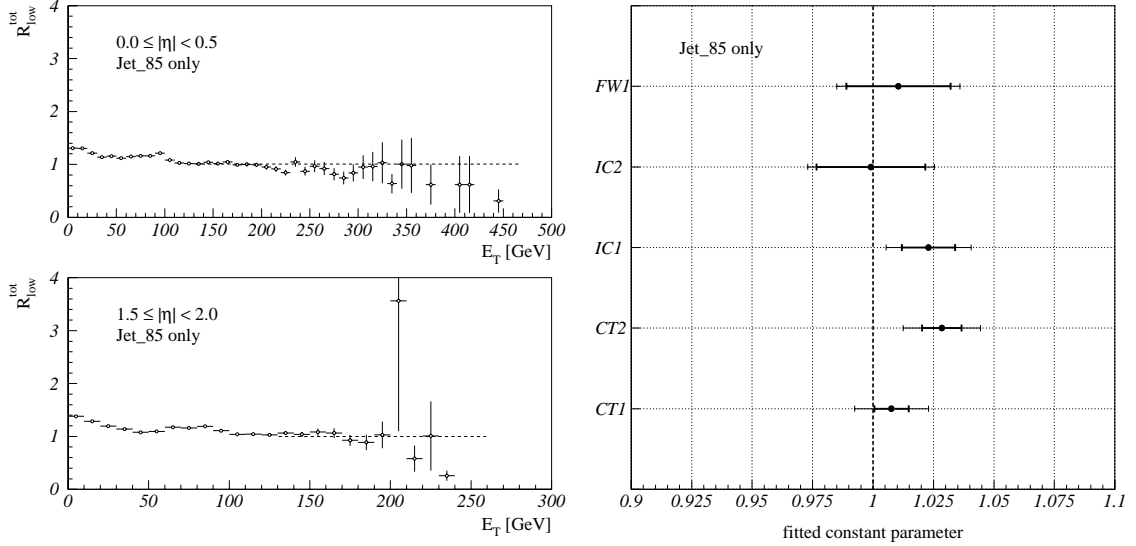


Figure 7.4: Plots on the left show R_{low}^{tot} obtained from the Jet_85 data only. The ratios are fitted (dashed line) to a constant (model P0) in the E_T range of interest. Shown here are fits in $|\eta| < 0.5$ and $1.5 \leq |\eta| < 2.0$ pseudorapidity regions. The plot on the right shows the fitted constants and their uncertainties (inner error bars represent statistical errors due to the fit alone, while outer error bars have systematic uncertainty added in quadrature). For all five η regions there is fairly good agreement with 1.

Subsample	<i>low</i>	<i>med</i>	<i>vhi</i>	<i>hig</i>	<i>tot</i>
$\int \mathcal{L} dt [\text{nb}^{-1}]$	7968	22831	2055	32121	51441

Table 7.3: Integrated luminosities for different subsamples of Jet_85 data.

R_{low}^{tot} from Jet_85 in the E_T region of interest only to a constant. See plots on the left in Figure 7.4 for rapidity regions $|\eta| < 0.5$ and $1.5 \leq |\eta| < 2.0$ (plots for all η regions considered can be found in reference [81]). The values of the fitted constants are shown on the right plot of Figure 7.4 for all five η regions. The inner error bars represent statistical errors from the fit, while the outer error bars include (in quadrature) the systematic uncertainty on the luminosity determination due to a Level 0 hardware inefficiency [83]. The systematic error of 0.95% is estimated

based on Figure 5 of reference [83] for the *low* and *high* luminosity subsamples [84]. This error is considered to be uncorrelated and independent in the *low* and *high* subsamples, thus resulting in a systematic uncertainty on the cross section ratios of 1.34%. It is this systematic uncertainty that is added in quadrature with statistical errors due to the fit. In three η regions we see a 1σ agreement between the fitted constant and expected value of 1; in $1.0 \leq |\eta| < 1.5$ the agreement is within 1.5σ and in $0.5 \leq |\eta| < 1.0$ within 2σ . Given this reasonable agreement with 1, we conclude that there is no statistically significant normalization offset in the cross sections as a function of luminosity.

To summarize, we have checked for residual luminosity dependence effects in the differential single inclusive jet cross sections at all rapidities up to $|\eta| = 3.0$. We find no significant effects in the shape or normalization of the cross sections.

CHAPTER 8

THE OBSERVED INCLUSIVE JET CROSS SECTIONS

The double differential jet cross section with respect to the jet pseudorapidity η and transverse momentum E_T is conventionally denoted by $d^2\sigma/(dE_T d\eta)$. The experimental measure of this cross section for single inclusive jet production (i.e. for the reaction $p\bar{p} \rightarrow jet + X$) in each E_T and η bin is given by:

$$\left\langle \frac{d^2\sigma}{dE_T d\eta} \right\rangle (p\bar{p} \rightarrow jet + X) = \frac{N}{\Delta E_T \cdot \Delta \eta \cdot \varepsilon_{tot} \cdot \int^{Run\ 1B} \mathcal{L} dt}, \quad (8.1)$$

where N is the number of accepted jets in a given $\Delta E_T \Delta \eta$ bin, ε_{tot} represents the total efficiency in this bin due to all the quality and acceptance cuts applied (i.e. is given by $\varepsilon_{tot} = \varepsilon_{glob} \cdot \varepsilon_{MTE} \cdot \varepsilon_Z$), and the brackets on the left hand side of Eq. (8.1) indicate that it actually is a measure of the *average* cross section in a given bin. Since measuring the jet cross section is a counting experiment, the number of jets in a bin, N , obeys a Poisson distribution. N is generally much smaller than the overall total number of jets in the cross section. Therefore, the statistical error on the cross section in a given bin is expressed by:

$$\frac{\sqrt{N}}{\Delta E_T \cdot \Delta \eta \cdot \varepsilon_{tot} \cdot \int^{Run\ 1B} \mathcal{L} dt}. \quad (8.2)$$

The cross sections are measured from the data collected by each of the four inclusive jet triggers: Jet_30, Jet_50, Jet_85, and Jet_Max. Then the cross sections from the different triggers are combined in such a way that a more restrictive trigger

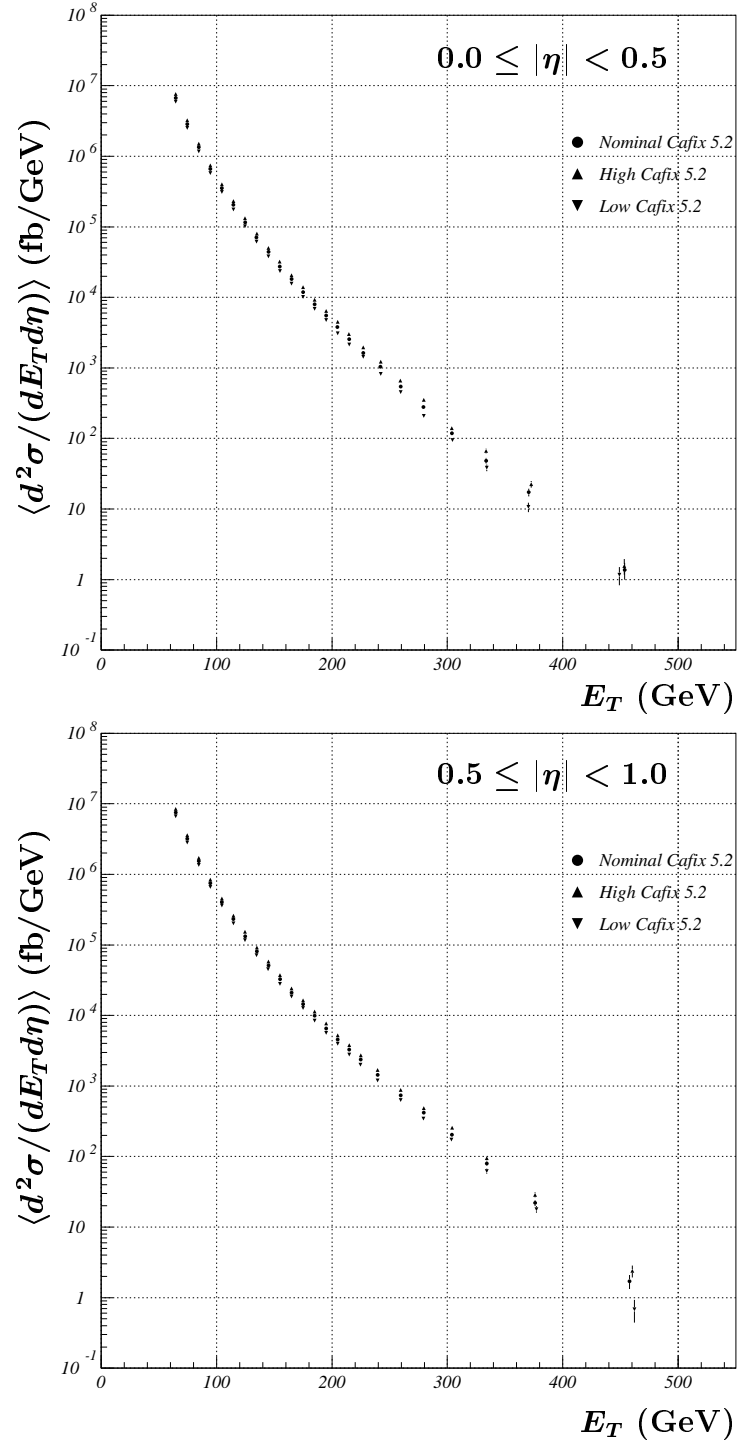


Figure 8.1: Observed inclusive jet cross sections in the two central pseudorapidity regions with the nominal, high, and low jet energy scale (CAFIX 5.2) corrections.

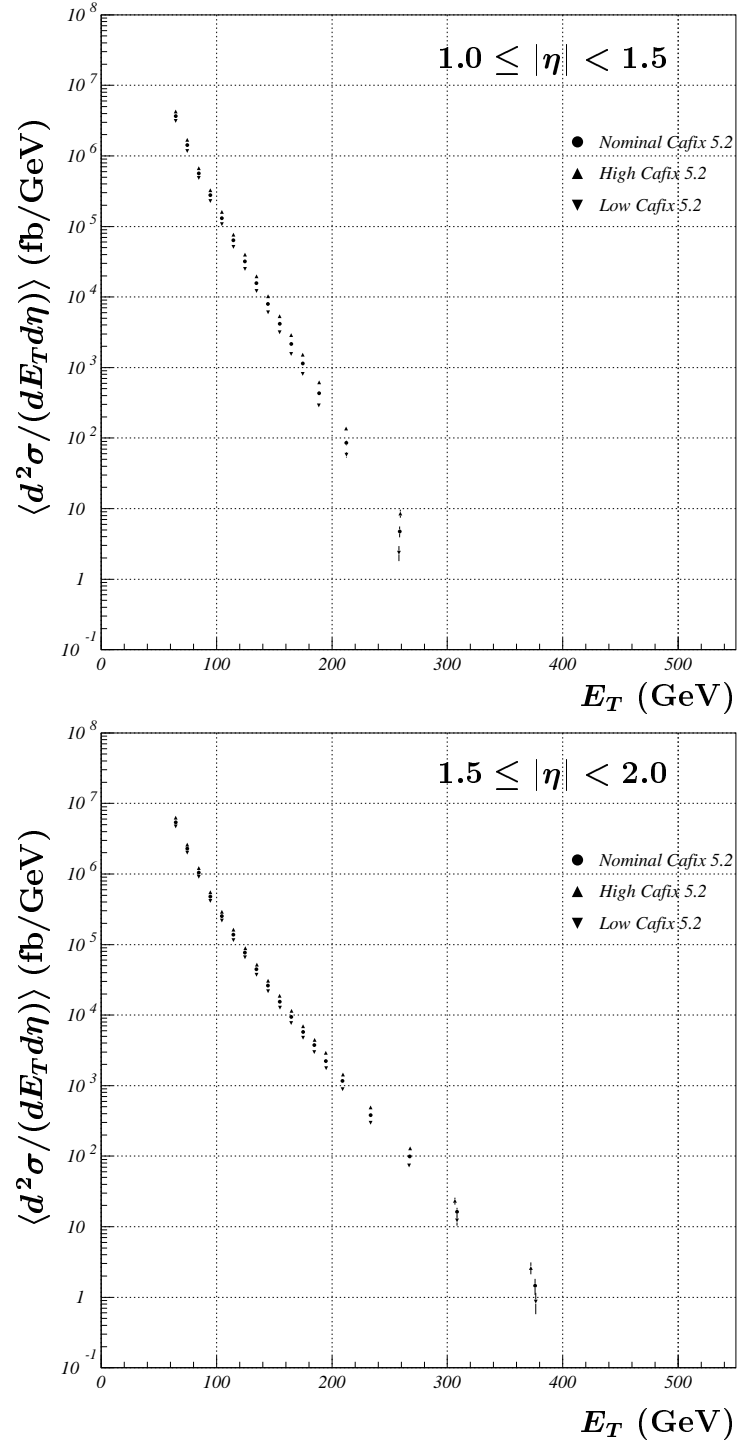


Figure 8.2: Observed inclusive jet cross sections in the two intermediate pseudo-rapidity regions with the nominal, high, and low jet energy scale (CAFIX 5.2) corrections.

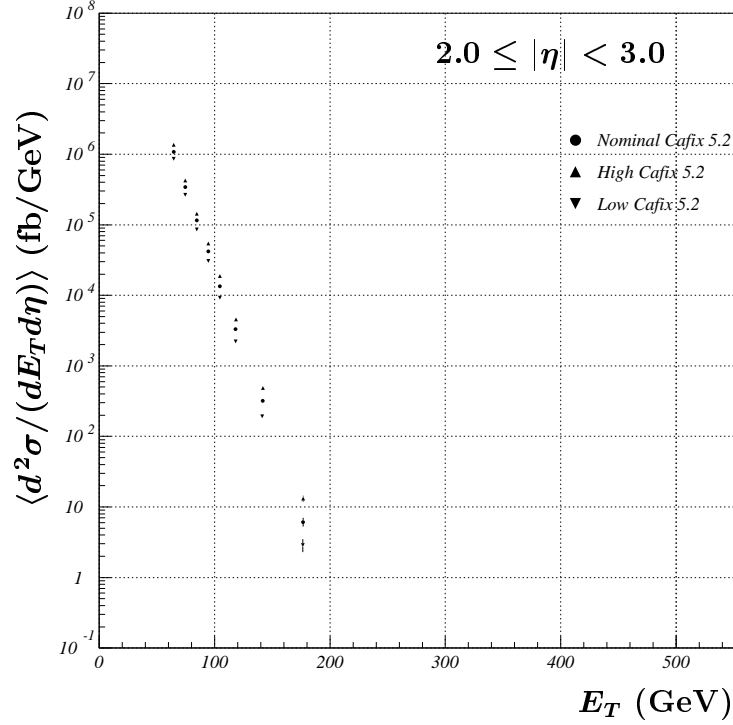


Figure 8.3: Observed inclusive jet cross section in the forward-most pseudorapidity region with the nominal, high, and low jet energy scale (CAFIX 5.2) corrections.

is taken as soon as it becomes at least 99% efficient, replacing the previous, less restrictive jet trigger. In this particular measurement, this means taking Jet_30 data from 60 to 90 GeV of jet E_T , Jet_50 data from 90 to 130 GeV, Jet_85 data from 130 to 170 GeV, and Jet_Max data above 170 GeV. The reconstructed jets are further corrected for the effects discussed in chapter 4 and are subjected to the data selection criteria as described in chapter 5. Next the jet energy scale correction is applied on a jet by jet basis according to the most recent version of the DØ JES, CAFIX 5.2. Finally, data are binned in E_T and η .

The observed cross sections in the five pseudorapidity regions considered (up to $|\eta| = 3.0$) are presented in Figures 8.1–8.3. Filled circles show the cross sections corresponding to the nominal value of the DØ JES correction (CAFIX

5.2). The upward (downward) pointing triangles represent cross sections obtained by fluctuating *all* CAFIX 5.2 subcomponent uncertainties up (down) by exactly one standard deviation. The bin widths in E_T range from 10 GeV at lowest E_T 's to as high as 150 GeV at the highest E_T point in the central region ($|\eta| < 0.5$). The choice of the particular binning in E_T is almost entirely driven by the statistics and is therefore somewhat arbitrary.

The observed jet cross sections (Figures 8.1–8.3) are distorted by the effects of the finite resolutions of the detector. The following chapter is devoted to the detailed discussion of these effects followed by the description of the method for removing the effects of resolution smearing from the observed jet cross sections.

CHAPTER 9

JET ENERGY RESOLUTIONS AND UNFOLDING

The observed jet energy scale corrected jet cross sections presented in Figures 8.1–8.3 are still distorted by the finite resolution of the detector. The single inclusive jet cross sections, $\langle d^2\sigma/(dE_T d\eta) \rangle$, are measured as a function of jet $E_T = E \sin \theta$ in five intervals of pseudorapidity η . Therefore, the effects on the cross sections of finite calorimeter resolution on jet energy measurement, as well as the effects of finite resolution on jet pseudorapidity (or, equivalently, polar angle θ) measurement, must be addressed. Distortions due to such effects should be evaluated and removed in order to produce the physics measurement, i.e. the measurement as it would appear in a detector with perfect resolution.

Consider a hypothetical sample of monoenergetic jets of energy E_0 entering the calorimeters. Their energies measured in the detector will generally be different from the incoming energy because of the intrinsic fluctuations in induced particle showers as well as in energy detection processes. In linear and hermetic calorimeters of nearly compensating nature, such as the DØ calorimeters, the measured energy of monoenergetic jets would be “smeared” around the true value by a Gaussian of some finite width. The left plot in Figure 9.1 illustrates this. We also note that in arbitrary (i.e. not necessarily hermetic or linear) calorimeters, the smearing would not be of a Gaussian nature and would have large asymmetric tails. Consequently,

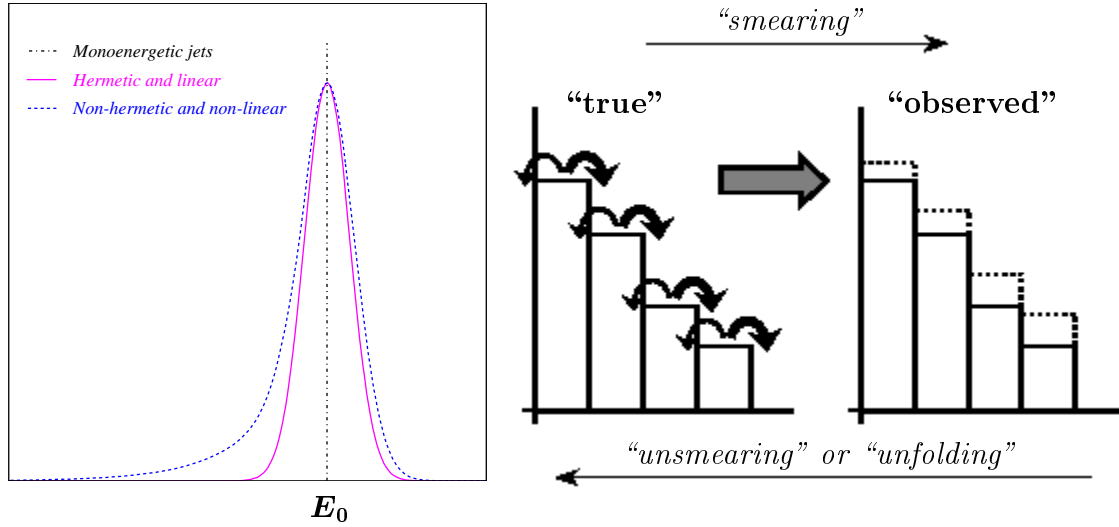


Figure 9.1: Finite energy resolution of the detector distorts the measured energy of monoenergetic jets of energy E_0 (left). In contrast with non-hermetic and non-linear calorimeters, such smearing is Gaussian when calorimeters are nearly hermetic and linear, such as the DØ calorimeters. Even though the energy smearing is Gaussian in DØ, it still distorts the steeply falling energy spectra for various cross section measurements by “smearing them up”. A cartoonist’s view of the effect on the hypothetical cross section is indicated in the plot on the right.

the Gaussian smearing of sampled energy in the calorimeters is an attractive feature, for it allows the separation of the issues of energy scale and resolutions. It is this property of the DØ calorimeters that allows consideration of jet energy scale independent of jet energy resolutions, as was also discussed in chapter 6.

However, even though jet energy is smeared randomly, it still affects the jet energy or E_T spectrum measured. It is seen in Figures 8.1–8.3 that the jet cross section is characterized by its steep fall as a function of E_T —the cross sections span six to seven orders of magnitude from the lowest to the highest E_T ’s considered. Because of the steeply falling cross sections, there are always many more jets at lower energies than at higher energies. Gaussian smearing will then result in more jets migrating to higher energies than visa versa. It is this net relocation of jets to higher

energies that “smears up” the cross section. This is illustratively depicted in the cartoon in Figure 9.1 for the hypothetical “true” energy spectrum: the “observed” distribution, indicated by the dashed line, is higher than the true spectrum.

The fact that the Gaussian smearing of a steeply falling distribution results in a “higher” spectrum can also be easily checked analytically by taking a convolution of a steeply falling function with a Gaussian of a finite width. The result of the convolution will be a function higher than the original function at any given point. On the other hand, a flat distribution will obviously be completely unaffected by a Gaussian smear.

The smearing in measured energy affects jet E_T directly via $E_T = E \sin \theta$. Therefore, we conclude that the measured cross sections of Figures 8.1–8.3 are smeared up compared to the true cross sections we intend to measure. The effect of finite resolution in η will also distort the cross sections in a similar manner. However, it will additionally introduce jet migration from one pseudorapidity bin into another, making it more difficult to predict the net effect. There are two major sources contributing to possible error in the measurement of η or θ : the angular granularity of the detector and the mismeasurement of the interaction vertex with respect to which angles are calculated. Studies of η bias, as well as other Monte Carlo investigations [33], indicate that jet η resolution due to detector segmentation is negligible.

We first discuss the method for measuring jet energy resolutions. Next, we address the issue of the effect of the finite vertex resolution on the cross sections. Finally, we describe the method used to unfold the effects of resolutions in the jet cross sections in order to obtain true distributions.

9.1 Determination of Jet Energy Resolutions

We first consider how a fractional E_T or energy resolution of a jet can be determined in case of perfectly measured angles. In terms of directly measured quantities: energy E and polar angle θ (or, equivalently, pseudorapidity η), jet E_T is given by $E_T = E \sin \theta$. Therefore, if the uncertainty on the angle measurement is sufficiently small, we can rather safely approximate the *fractional* jet E_T resolution with the fractional energy resolution $\sigma_{E_T}/E_T \approx \sigma_E/E$.

In dijet events, consider the E_T asymmetry between the jets defined as:

$$A = \frac{E_T^1 - E_T^2}{E_T^1 + E_T^2} , \quad (9.1)$$

where E_T^1 and E_T^2 are measured transverse energies of the two jets. In a carefully selected dijet event, in the absence of any resolution effects, the two jets will have exactly equal transverse momenta. Therefore it is clear that the deviation from zero of the width of the asymmetry variable in real life might be a measure of the finite detector resolution. In fact, assuming $E_T^1 = E_T^2 \equiv E_T$ and $\sigma_{E_T^1} = \sigma_{E_T^2} \equiv \sigma_{E_T}$, the root mean square width (*rms*) of the asymmetry variable, σ_A , is related to the fractional E_T resolution rather simply:

$$\frac{\sigma_{E_T}}{E_T} = \sqrt{2}\sigma_A , \quad (9.2)$$

suggesting the measurement of the σ_A as a method for extracting the fractional E_T resolutions.

Next, we consider a more complicated case which results when the polar angle is mismeasured due to the nonzero vertex position resolution σ_z [85]. For CC (Central Calorimeter) showers we assume that in $r - \varphi$ “space” the shower

occurs at a distance equal to the inner radius of the more finely segmented 3-rd electromagnetic layer of CC, $R_{cal} = 91.6$ cm. Similarly, for EC (End Calorimeter) showers we assume that the z -position of showers is equal to the length of the calorimeters, $Z_{cal} = 178.9$ cm. Under these assumptions, it follows directly from the jet E_T definition that in CC:

$$\left(\frac{\sigma_{E_T}}{E_T}\right)^2 = \left(\frac{\sigma_E}{E}\right)^2 + \frac{1}{4} \left(\frac{\sigma_Z}{R_{cal}}\right)^2 \sin^2 2\theta, \quad (9.3)$$

while in EC:

$$\left(\frac{\sigma_{E_T}}{E_T}\right)^2 = \left(\frac{\sigma_E}{E}\right)^2 + \left(\frac{\sigma_Z}{Z_{cal}}\right)^2 \cos^4 \theta. \quad (9.4)$$

It also turns out that, generally speaking, the width of the asymmetry variable σ_A cannot be directly related to either fractional E_T or E resolutions of a jet. Fortunately, however, in the special case of events with dijets on the Same Side (SS), $\eta_1 \cdot \eta_2 > 0$, a relation similar to that in Eq. (9.2) holds, but for the fractional *energy* resolutions:

$$(\sigma_A^{SS})^2 = \frac{1}{2} \left(\frac{\sigma_E}{E}\right)^2. \quad (9.5)$$

In the case where two jets are in the Opposite Side (OS), $\eta_1 \cdot \eta_2 < 0$, topology, one obtains the following relations in the CC:

$$(\sigma_A^{OS})^2 = \frac{1}{2} \left(\frac{\sigma_E}{E}\right)^2 + \frac{1}{4} \left(\frac{\sigma_Z}{R_{cal}}\right)^2 \sin^2 2\theta, \quad (9.6)$$

and in the EC:

$$(\sigma_A^{OS})^2 = \frac{1}{2} \left(\frac{\sigma_E}{E}\right)^2 + \left(\frac{\sigma_Z}{Z_{cal}}\right)^2 \cos^4 \theta. \quad (9.7)$$

It then follows from these relations that the jet energy resolution can be measured from the width of the asymmetry variable distribution in the case of SS dijet events only. Also, the fractional E_T resolution is given by:

$$\left(\frac{\sigma_{E_T}}{E_T}\right)^2 = (\sigma_A^{SS})^2 + (\sigma_A^{OS})^2. \quad (9.8)$$

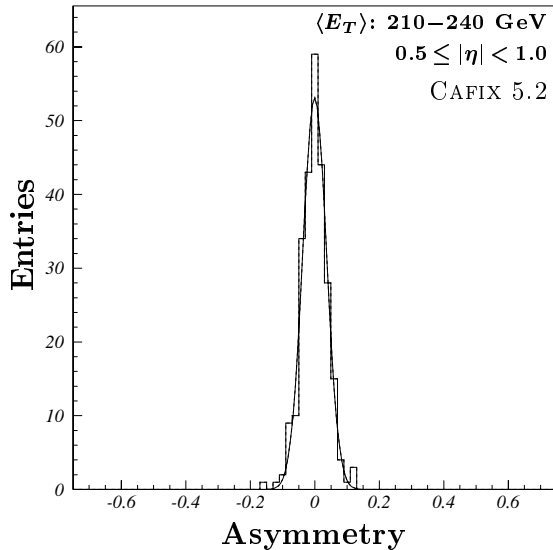


Figure 9.2: The illustration of the dijet asymmetry distribution along with a Gaussian fit.

Moreover, the difference between the $(\sigma_A^{os})^2$ and $(\sigma_A^{ss})^2$ can be employed to extract the “effective” vertex resolution (EVR), σ_z , entirely from the data. This method yields [66] a conservative estimate of the EVR of $\sigma_z \leq 7.5$ cm in *all* pseudorapidity regions up to $|\eta| = 3.0$. The investigation of the effects of the EVR on the single inclusive jet cross sections are discussed in the following section. The width of the asymmetry variable from the dijet events has been measured separately for SS and OS events in every rapidity interval up to $|\eta| = 3.0$. We will however concentrate on the SS dijet topology, for it is the σ_A^{ss} that is directly related to the fractional energy resolutions via Eq. (9.5).

Determination of the width of the asymmetry variable is performed in several steps [62, 66, 80]. Dijet events are carefully selected by requiring them to pass all jet and event quality cuts. The two leading jets are required to be in the same $|\eta|$ slice and back-to-back in azimuth to within 5° . The asymmetrized distributions of quantity A are considered in various E_T bins of the average transverse energy of dijets, $\langle E_T \rangle$, and are fitted to Gaussians as illustrated in Figure 9.2.

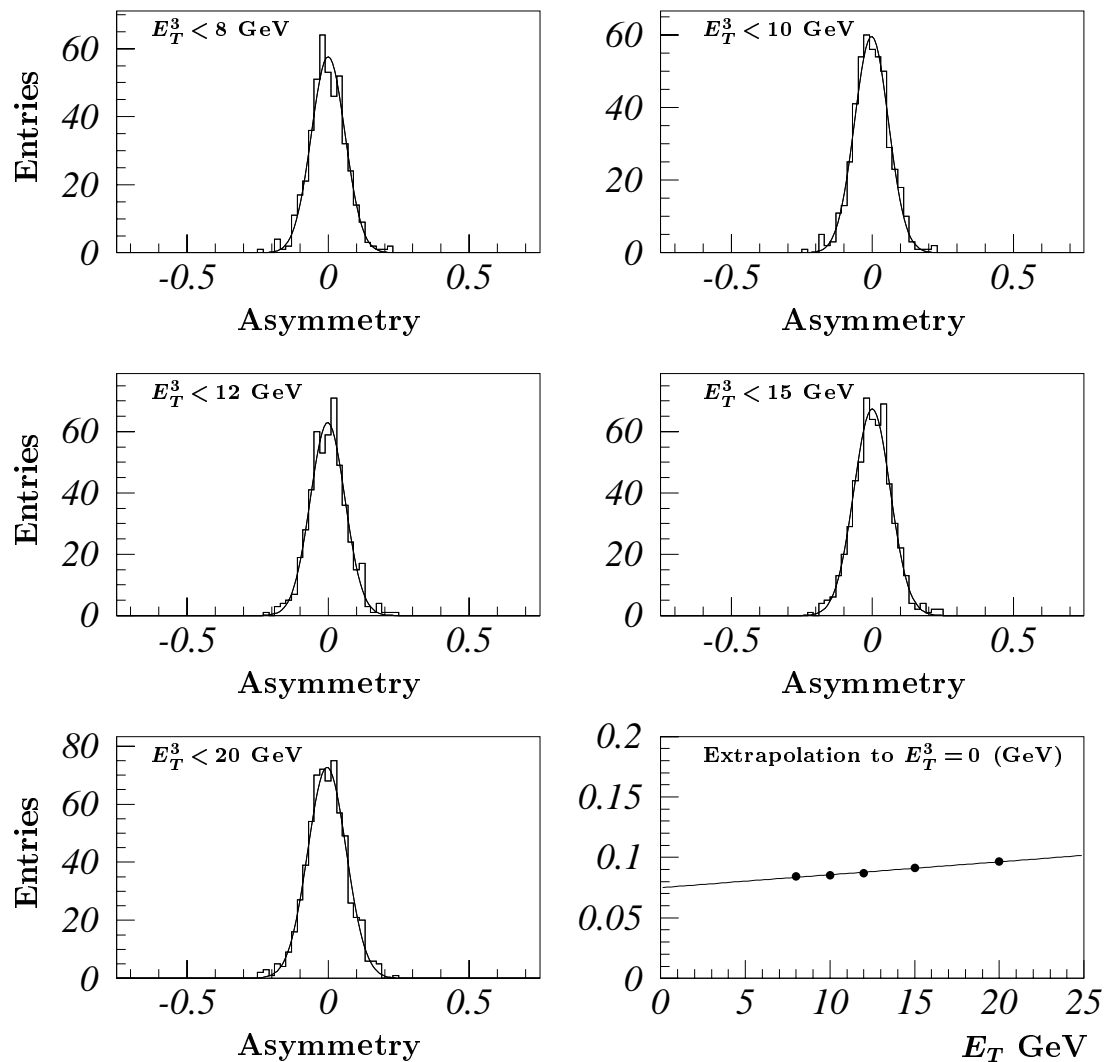


Figure 9.3: Illustration of the third jet E_T cut extrapolation for $1.5 \leq |\eta| < 2.0$ and $95 \leq \langle E_T \rangle < 150$ GeV bin with CAFIX 5.2.

Two effects distort the width of the Gaussian estimated in this way. The first of them is known as a soft radiation bias. Although dijet pair selection requirements remove events with more than two reconstructed jets, it is the unclustered soft radiation in the event that may still prevent the two leading jets from perfectly balancing in the transverse plane. To deal with this effect, σ_A is calculated with increasingly restrictive cuts on the E_T of the third jet in the event. The results

are then extrapolated to the ideal case in which the third jet E_T is equal to zero. The extrapolated value of σ_A corresponding to $E_T^3 = 0$ GeV is taken as a true measure of the width of the asymmetry variable. The illustration of this procedure for one particular η - E_T bin is shown in Figure 9.3 with the asymmetry distributions for the five soft-third-jet E_T cut values considered; the extrapolated value of σ_A is determined as the y -intercept of the fitted line in the bottom right plot.

This procedure is repeated in every η - E_T bin. The ratio of the σ_A at $E_T^3 = 0$ GeV to that at $E_T^3 = 8$ GeV gives a multiplicative correction which, when applied to the σ_A measured at $E_T^3 = 8$ GeV (the standard jet E_T threshold in the DØ jet finder), would yield the true value of σ_A in a given η - E_T bin. To account for bin-to-bin fluctuations, the correction factors as a function of the dijet average $\langle E_T \rangle$ are fit to a smooth analytic function $K(E_T) = 1 - e^{-a_0 - a_1 E_T}$ in every pseudorapidity region considered. It is this fitted value of the soft radiation correction that is actually applied to the measured σ_A (at $E_T^3 = 8$ GeV) to obtain its true value.

The second effect is commonly referred to as a particle level imbalance (PLI). It reflects the fact that, even at the particle level, dijets may not exactly balance in the transverse plane due to the nonzero energy carried away by partons or particles emitted outside the particle level algorithm cone. To estimate and remove this effect, the width of the asymmetry variable is measured from a dedicated HERWIG Monte Carlo sample with exactly the same requirements as in the data. The PLI is then subtracted in quadrature from the calorimeter level asymmetry measured in the dijet Collider data. In this manner, the method is sensitive only to the detector jet energy resolution. The final, PLI subtracted resolutions are fit

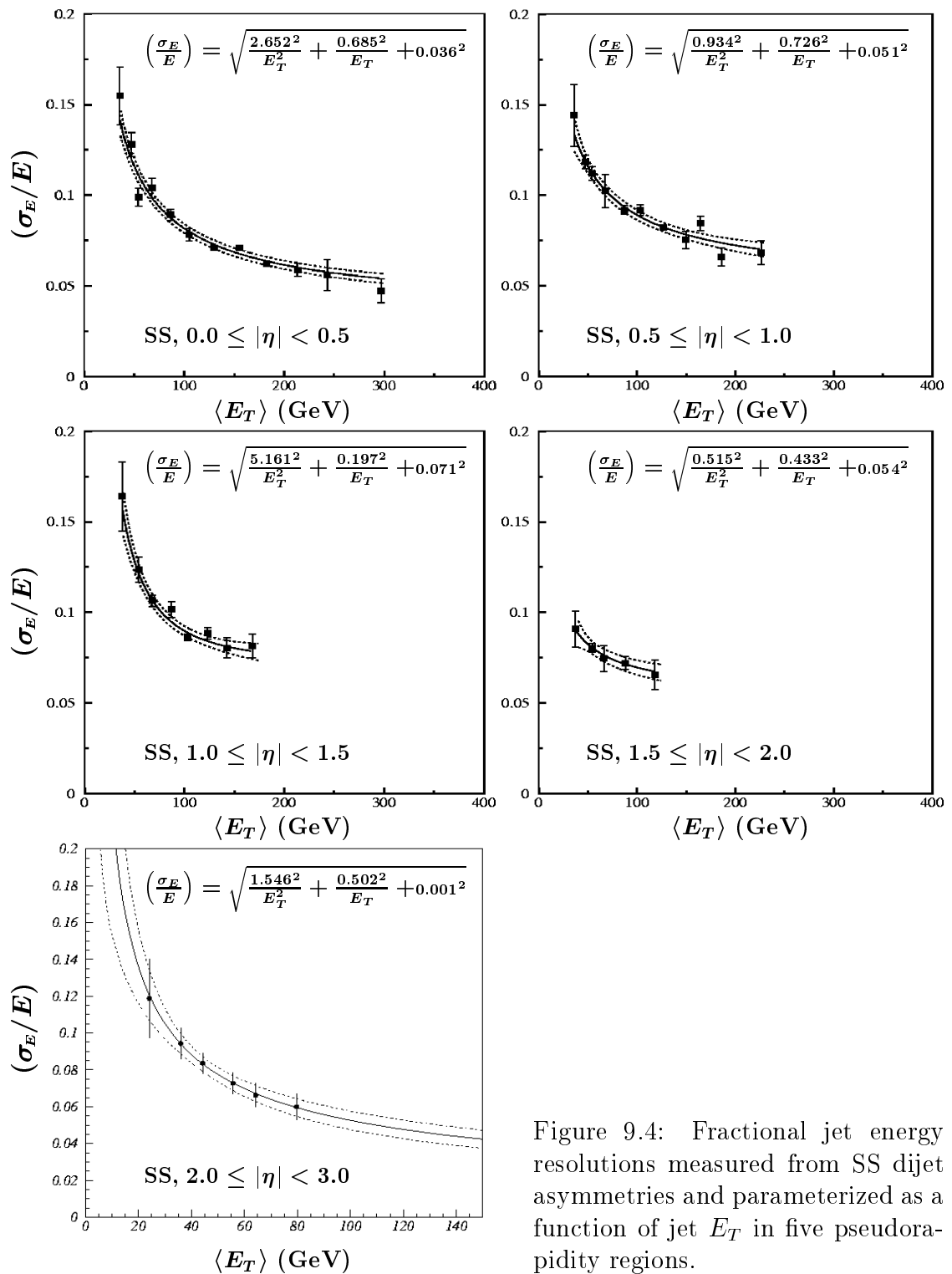


Figure 9.4: Fractional jet energy resolutions measured from SS dijet asymmetries and parameterized as a function of jet E_T in five pseudorapidity regions.

to the standard (see page 114) resolution parameterization:

$$\frac{\sigma_E}{E} = \sqrt{\frac{N^2}{E^2} + \frac{S^2}{E} + C^2}. \quad (9.9)$$

Figure 9.4 shows jet fractional energy resolutions as a function of dijet average E_T in five pseudorapidity regions, up to $|\eta| = 3.0$, as measured from the widths of the corresponding dijet E_T asymmetry variable, corrected for the soft radiation bias and with the PLI subtracted in quadrature. The error bars are statistical, while the error bands show the systematic uncertainties due to the method. An additional uncertainty, originating from imperfect closure of the method as measured in the MC, is added at the time of the unfolding (to be discussed at the end of this chapter).

9.2 Effects of Nonzero Vertex Resolution

The widths of the asymmetry variable as measured in the SS and OS dijet topologies are different. According to Eq. (9.8), this is attributed to nonzero “effective” vertex resolution (EVR), σ_z . Based on the measurement of σ_z from the data [66], a conservative estimate for the upper limit of σ_z is taken to be $\sigma_z \leq 7.5$ cm for all pseudorapidity regions up to $|\eta| = 3.0$. It is clear that the nonzero EVR affects jet cross sections not only by causing jet migration in E_T within a given pseudorapidity interval (much like the effect of the finite energy resolution), but also by introducing jet bin-to-bin migration in η , causing jets to move from E_T spectra in one η interval to that in other η regions, and visa versa. The net effect of the EVR on the cross sections is thus harder to predict and it is studied in a dedicated JETRAD Monte Carlo.

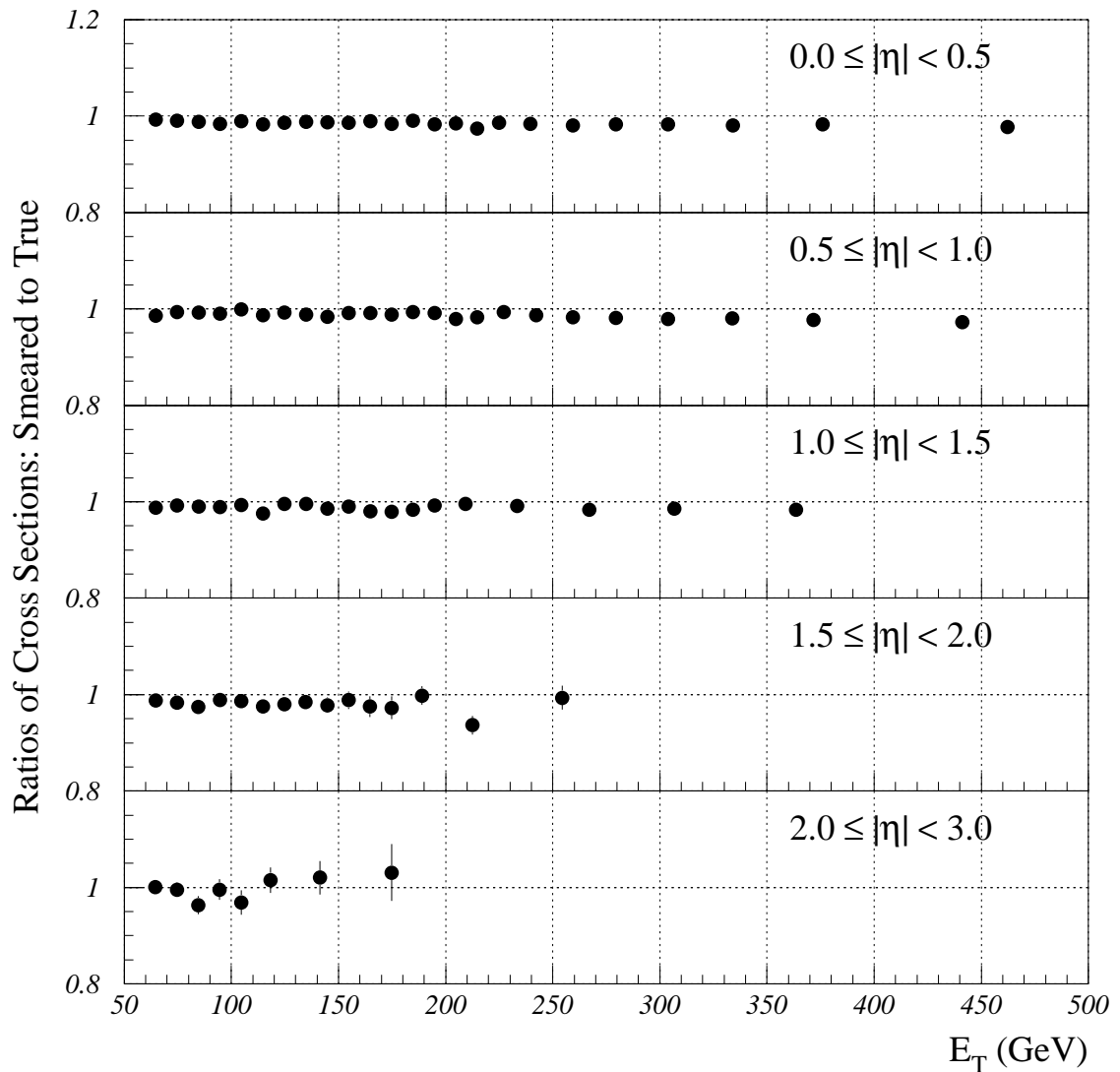


Figure 9.5: The ratios of the JETRAD cross sections smeared by the effective vertex resolution of 7.5 cm and the true cross sections. Effect of nonzero σ_z is in the order of 1–2% in all pseudorapidity regions. Therefore, no correction due to this effect is applied to the data.

JETRAD is used to generate two sets of jet cross sections in the *same* E_T and η bins as in the data. The first set corresponds to the “true” cross sections. The second set has the interaction vertex z -coordinate smeared by a Gaussian of

the width $\sigma_z = 7.5$ —a conservative estimate of EVR over the full dynamic range—and jet η and E_T are recalculated using simple geometrical conversions. Bin-by-bin ratios of the two sets of cross sections, smeared to true, are shown in Figure 9.5 for all five pseudorapidity regions. The net effect in the cross section is small (of order 1–2%), throughout all η ’s. Similar results have been observed in an analogous study for the dijet triple differential cross section [66]. The jet migration in E_T due to the EVR is nearly fully compensated by the migration in η . We note that the two effects are quite large when considered separately by recalculating *either* (but not both) jet E_T or η after the Gaussian σ_z smear of the vertex z -coordinate. Because of the smallness of the net effect of the EVR on the single inclusive jet cross sections, no correction is applied to the data.

9.3 Unfolding of the Cross Sections

The effects of finite calorimeter energy resolution and nonzero effective vertex resolution (EVR) distort the observed single inclusive jet cross sections. Since the effects of the EVR are negligible, as discussed in the previous section, the only remaining effect is the smearing upward of the jet cross sections due to the energy resolution. This effect is removed from the cross sections by a method developed in DØ and often referred to as the “unsmearing” or “unfolding” procedure [33, 46]. We describe the method and its application in the case of single inclusive jet cross sections, along with the derived corrections and associated uncertainties.

We accept as a hypothesis that the “true” inclusive jet cross section in every pseudorapidity region can be approximated analytically by an ansatz function of

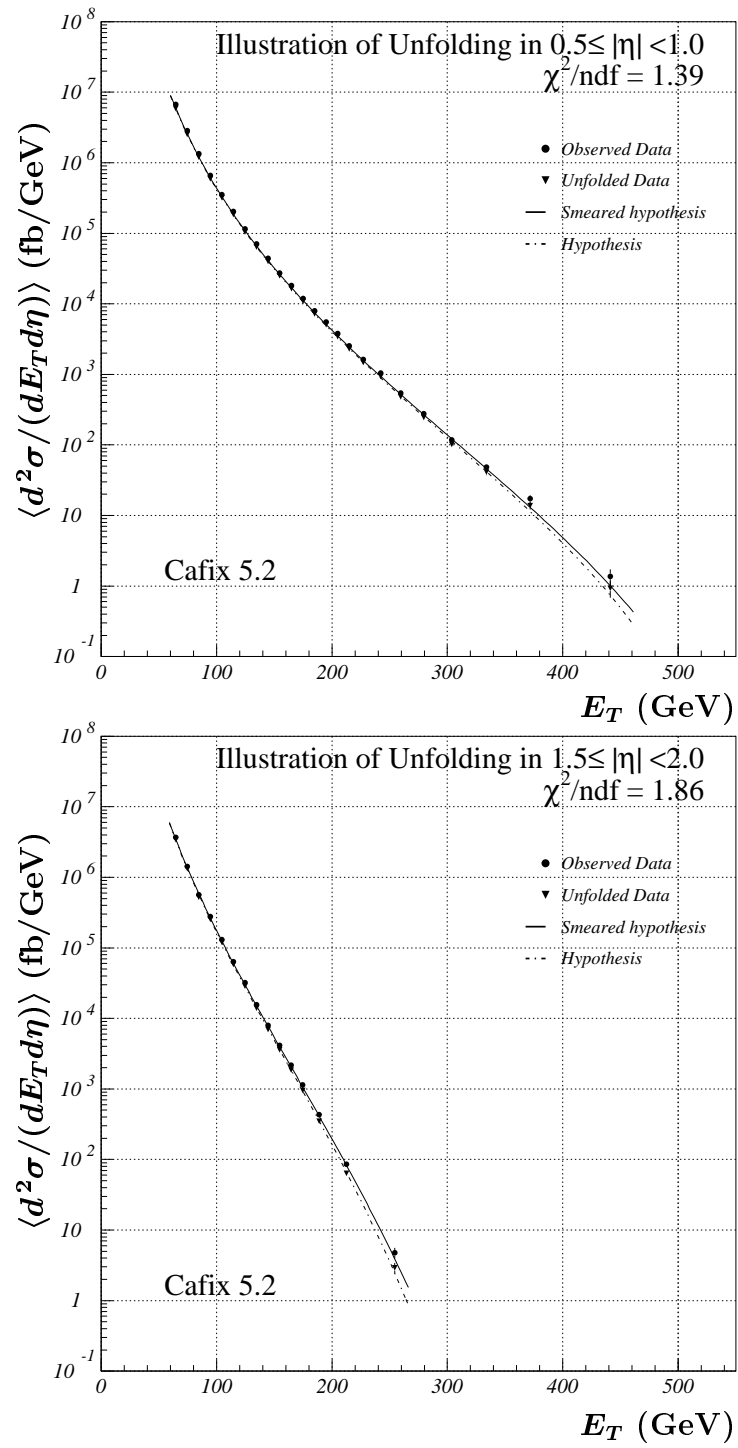


Figure 9.6: The illustration of the jet cross section unfolding method on the example of the two pseudorapidity regions.

the following form:

$$F(E_T; \alpha, \beta, \gamma, \delta) = e^\alpha E_T^\beta \left(1 + \gamma \frac{2E_T}{\sqrt{s}}\right)^\delta, \quad (9.10)$$

where α, β, γ , and δ are free parameters. At each given E_T point, the ansatz function of Eq. (9.10) is then smeared by a Gaussian of width equal to the jet energy resolution $\sigma_E(E_T)$ at that E_T . This procedure mathematically is described as a convolution of the two functions:

$$f(E_T; \alpha, \beta, \gamma, \delta) = \int dE'_T F(E'_T; \alpha, \beta, \gamma, \delta) \frac{1}{\sqrt{2\pi}\sigma_E(E'_T)} e^{-\frac{1}{2}\left(\frac{E_T - E'_T}{\sigma_E(E'_T)}\right)^2} \quad (9.11)$$

resulting in a “smeared hypothesis”, $f(E_T; \alpha, \beta, \gamma, \delta)$, which should describe the *observed* data well, if all our assumptions are correct. The standard χ^2 merit function is built between the numerically evaluated smeared hypothesis of Eq. (9.11) and the data, which is then fed into MINUIT package [86] for a multiparameter minimization, thereby fixing the free parameters α, β, γ and δ . This procedure is illustrated in Figure 9.6 on the example of the two pseudorapidity regions. The convolution of the original hypothesis (dashed line) with the Gaussian yields the smeared cross section (solid line) which is fitted to the data (filled circles) until a satisfactory value of the χ^2 per degree of freedom is achieved.

Finally, the unfolding correction is obtained in each of the pseudorapidity regions by taking the E_T bin-by-bin ratios of the original hypothesis (dashed lines in Figure 9.6) to the smeared ansatz (solid lines):

$$R_{unf}(E_T) = \frac{F(E_T; \alpha, \beta, \gamma, \delta)}{f(E_T; \alpha, \beta, \gamma, \delta)}. \quad (9.12)$$

Figure 9.7 shows the unfolding correction factors R_{unf} as a function of jet E_T for each of the five pseudorapidity intervals. The unfolding correction becomes especially large at the highest E_T ’s. This is due to the fact that jet cross sections become

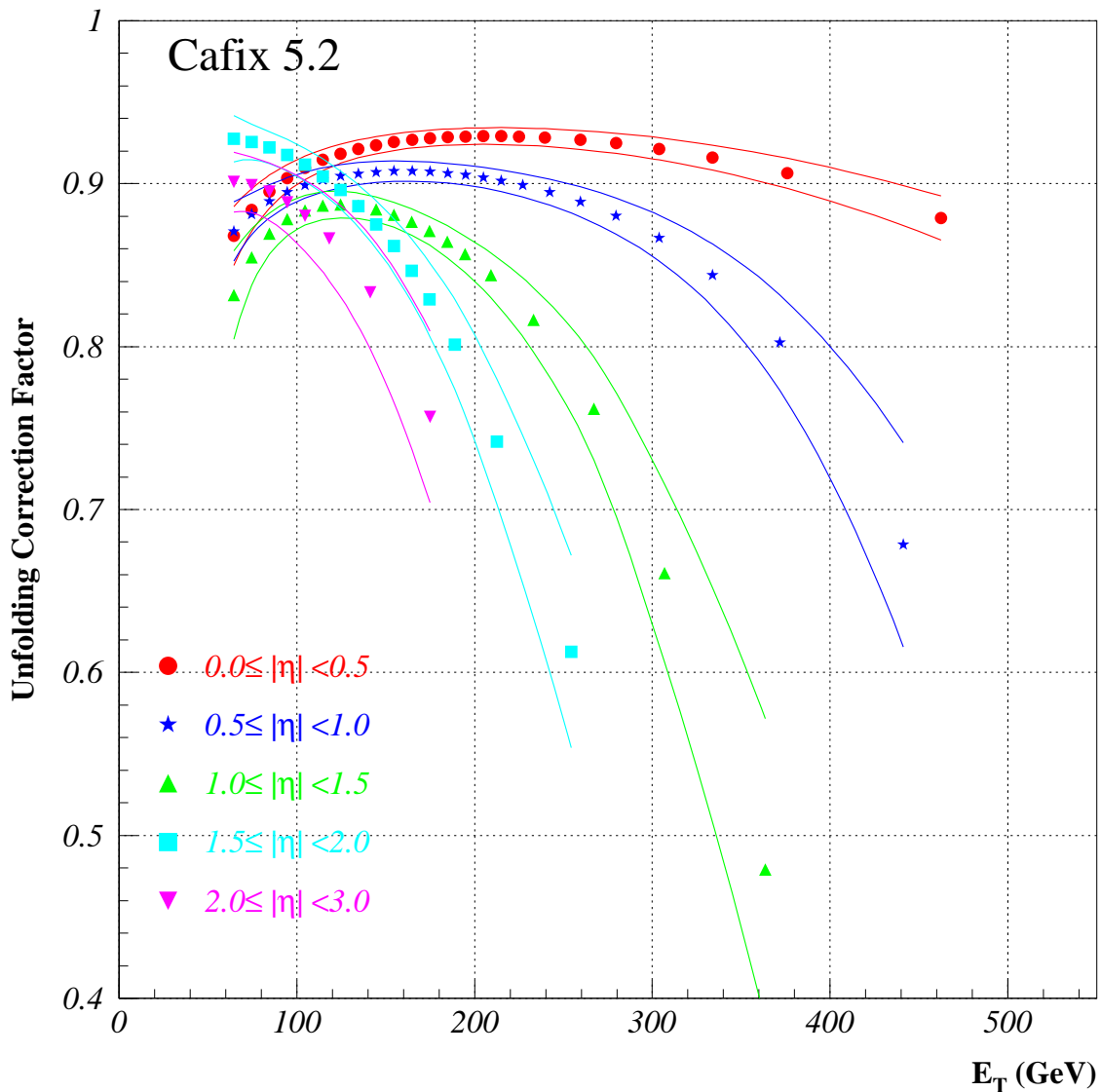


Figure 9.7: Derived unfolding correction factors in all pseudorapidity regions along with the total uncertainty bands. The correction becomes large at the highest E_T 's because of the increase in the slope of the cross sections as they approach the kinematic limit in a given η interval. On the other hand, the increase in R_{unf} at lowest E_T 's is attributed to the degraded energy resolutions.

increasingly steeply falling as they start to approach the kinematic limits at highest E_T 's. Therefore, even though the fractional jet energy resolutions improve with increasing E_T , the amount of the distortion in the cross sections due the finite resolution smearing still increases dramatically. On the other hand, at lowest E_T 's, jet

energy resolutions are poor, once again causing increase in the size of the unfolding correction. The existence of an extremum in R_{unf} as a function of E_T thus is a result of the interplay between the varying degree of the steepness of the cross section as a function of E_T and the E_T dependence of the jet energy resolutions. The final jet cross sections, unfolded for the detector resolution effects, are obtained by scaling each data point in every E_T bin by the corresponding unfolding correction factor. Figure 9.6 shows both observed (filled circles) and unfolded data (filled triangles) for visual comparison.

To estimate the statistical errors on the unfolding correction due to resolution and ansatz fits, we start from the general error propagation formula:

$$(\Delta R_{unf}(E_T))^2 = \frac{\partial^2 R_{unf}}{\partial p_i \partial p_j} \text{Cov}(p_i, p_j) , \quad (9.13)$$

where a sum over the repeated indices is understood. The indices run over the ansatz parameters α, β, γ and δ , and the resolution fit parameters N, S , and C , used in the parameterizations of (σ_E/E) as a function of jet E_T . The correlations between the ansatz and the resolution parameters are assumed to be zero. On the other hand, the correlations among the ansatz parameters and among the resolution parameters are obtained from the corresponding fits. The partial derivatives $\partial R_{unf}/\partial p_i$ are calculated numerically (of course, $\partial R_{unf}/\partial \alpha = 0$).

The systematic error due to the the resolution closure is also included, amending the usual resolution parameterizations by closure parameterization $d_1 + d_2/E_T^2$. The parameters d_1 and d_2 are then treated in exactly the same way as resolutions parameters N, S , and C , except that they are nominally zero with the errors of 0.0024 and 14.3, respectively [87].

CHAPTER 10

RESULTS AND CONCLUSIONS

The final single inclusive jet cross sections are obtained from the observed cross sections of Figures 8.1–8.3, discussed in chapter 8, by rescaling them bin-by-bin according to the unfolding correction factors of Figure 9.7, presented in the previous chapter. Figure 10.1 shows the final, unfolded cross sections as a function of jet E_T in five pseudorapidity regions considered along with the statistical errors only. The cross sections based on the integrated luminosity of 92 pb^{-1} of the Run 1B data sample are presented for the nominal values of the DØ jet energy scale correction, CAFIX 5.2. The numerical values of the cross sections, along with both statistical and systematic uncertainties, as well as the E_T bin ranges and the best estimates of the bin centroids are summarized in Tables 10.1–10.5.

The notable feature of the jet cross sections is their steeply falling nature. They span six to seven orders of magnitude from the lowest to the highest E_T 's. The cross sections are measured up to $|\eta| = 3.0$, significantly extending previously available inclusive jet cross section measurements by the DØ and CDF experiments of up to $|\eta| = 0.7$. We will next discuss the experimental errors associated with the measurement as well as the theoretical uncertainties in the pQCD predictions of the rapidity dependence of the single inclusive jet cross sections, followed by the comparisons to various theoretical predictions and concluding remarks.

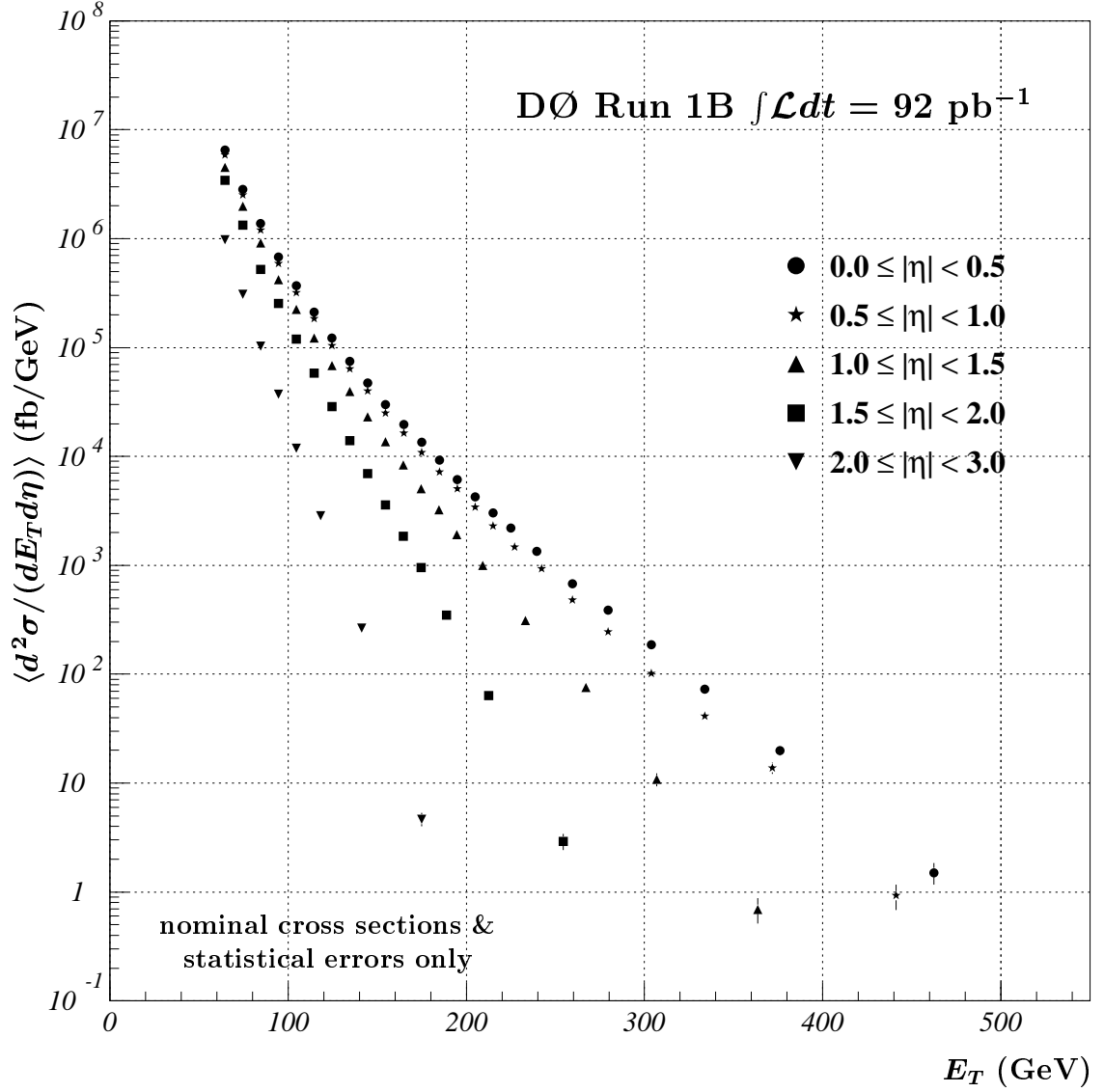


Figure 10.1: Final, unfolded single inclusive jet cross sections corresponding to the nominal jet energy scale correction (CAFIX 5.2) from all five pseudorapidity regions considered (up to $|\eta| = 3.0$) with statistical errors only.

Bin Range (GeV)	Plotted E_T (GeV)	Cross Sec. \pm Stat. (fb/GeV)	Observed Events	Systematic Uncer.(%)
60–70	64.6	$(6.52 \pm 0.04) \times 10^6$	22627	–14.1, +14.8
70–80	74.6	$(2.84 \pm 0.03) \times 10^6$	9642	–14.1, +14.7
80–90	84.7	$(1.37 \pm 0.02) \times 10^6$	4594	–14.1, +14.7
90–100	94.7	$(6.78 \pm 0.04) \times 10^5$	30208	–13.7, +14.4
100–110	104.7	$(3.69 \pm 0.03) \times 10^5$	16311	–13.8, +14.5
110–120	114.7	$(2.12 \pm 0.02) \times 10^5$	9288	–13.8, +14.6
120–130	124.8	$(1.22 \pm 0.02) \times 10^5$	5316	–13.9, +14.7
130–140	134.8	$(7.50 \pm 0.04) \times 10^4$	38318	–13.6, +14.4
140–150	144.8	$(4.74 \pm 0.03) \times 10^4$	24161	–13.7, +14.7
150–160	154.8	$(2.99 \pm 0.02) \times 10^4$	15206	–13.9, +14.9
160–170	164.8	$(1.96 \pm 0.02) \times 10^4$	9951	–14.0, +15.2
170–180	174.8	$(1.34 \pm 0.01) \times 10^4$	11416	–14.2, +15.5
180–190	184.8	$(9.21 \pm 0.10) \times 10^3$	7819	–14.5, +15.8
190–200	194.8	$(6.11 \pm 0.08) \times 10^3$	5282	–14.7, +16.2
200–210	204.8	$(4.24 \pm 0.07) \times 10^3$	3595	–15.0, +16.6
210–220	214.8	$(3.04 \pm 0.06) \times 10^3$	2574	–15.3, +17.0
220–230	224.8	$(2.21 \pm 0.05) \times 10^3$	1869	–15.6, +17.5
230–250	239.4	$(1.34 \pm 0.03) \times 10^3$	2265	–16.1, +18.2
250–270	259.4	$(6.77 \pm 0.20) \times 10^2$	1148	–16.8, +19.4
270–290	279.5	$(3.88 \pm 0.15) \times 10^2$	659	–17.7, +20.7
290–320	303.9	$(1.87 \pm 0.09) \times 10^2$	478	–18.8, +22.4
320–350	333.9	$(7.29 \pm 0.53) \times 10^1$	187	–20.4, +24.9
350–410	375.9	$(1.99 \pm 0.20) \times 10^1$	103	–23.0, +28.8
410–560	462.3	$(1.50 \pm 0.34) \times 10^0$	20	–29.5, +38.9

Table 10.1: Single inclusive jet cross section in $|\eta| < 0.5$.

Bin Range (GeV)	Plotted E_T (GeV)	Cross Sec. \pm Stat. (fb/GeV)	Observed Events	Systematic Uncer.(%)
60–70	64.6	$(5.88 \pm 0.04) \times 10^6$	20344	–14.3, +15.0
70–80	74.6	$(2.53 \pm 0.03) \times 10^6$	8650	–14.3, +15.0
80–90	84.7	$(1.19 \pm 0.02) \times 10^6$	4035	–14.4, +15.1
90–100	94.7	$(5.91 \pm 0.04) \times 10^5$	26704	–14.1, +14.8
100–110	104.7	$(3.19 \pm 0.03) \times 10^5$	14334	–14.3, +15.0
110–120	114.7	$(1.84 \pm 0.02) \times 10^5$	8218	–14.4, +15.2
120–130	124.8	$(1.04 \pm 0.02) \times 10^5$	4639	–14.6, +15.4
130–140	134.8	$(6.39 \pm 0.03) \times 10^4$	33447	–14.3, +15.2
140–150	144.8	$(4.00 \pm 0.03) \times 10^4$	20898	–14.5, +15.5
150–160	154.8	$(2.49 \pm 0.02) \times 10^4$	12991	–14.7, +15.9
160–170	164.8	$(1.64 \pm 0.02) \times 10^4$	8566	–15.0, +16.2
170–180	174.8	$(1.08 \pm 0.01) \times 10^4$	9505	–15.2, +16.6
180–190	184.8	$(7.20 \pm 0.09) \times 10^3$	6316	–15.5, +17.1
190–200	194.8	$(5.02 \pm 0.08) \times 10^3$	4409	–15.8, +17.5
200–210	204.8	$(3.42 \pm 0.06) \times 10^3$	3008	–16.1, +18.0
210–220	214.8	$(2.29 \pm 0.05) \times 10^3$	2014	–16.4, +18.6
220–235	227.2	$(1.46 \pm 0.03) \times 10^3$	1938	–16.8, +19.3
235–250	242.2	$(9.33 \pm 0.26) \times 10^2$	1241	–17.3, +20.3
250–270	259.4	$(4.82 \pm 0.16) \times 10^2$	859	–17.9, +21.4
270–290	279.4	$(2.45 \pm 0.12) \times 10^2$	440	–18.7, +23.0
290–320	203.8	$(1.02 \pm 0.06) \times 10^2$	279	–19.8, +25.0
320–350	333.8	$(4.10 \pm 0.38) \times 10^1$	115	–21.3, +27.8
350–400	371.6	$(1.38 \pm 0.17) \times 10^1$	68	–23.4, +31.9
400–530	441.1	$(0.93 \pm 0.25) \times 10^0$	14	–28.8, +41.5

Table 10.2: Single inclusive jet cross section in $0.5 \leq |\eta| < 1.0$.

Bin Range (GeV)	Plotted E_T (GeV)	Cross Sec. \pm Stat. (fb/GeV)	Observed Events	Systematic Uncer.(%)
60–70	64.6	$(4.53 \pm 0.04) \times 10^6$	16442	$-15.7, +16.7$
70–80	74.6	$(1.97 \pm 0.02) \times 10^6$	6967	$-15.6, +16.6$
80–90	84.7	$(9.10 \pm 0.16) \times 10^5$	3157	$-15.8, +16.8$
90–100	94.7	$(4.19 \pm 0.03) \times 10^5$	3157	$-15.7, +16.6$
100–110	104.7	$(2.24 \pm 0.02) \times 10^5$	10274	$-16.0, +17.0$
110–120	114.7	$(1.22 \pm 0.02) \times 10^5$	5601	$-16.4, +17.4$
120–130	124.7	$(6.80 \pm 0.12) \times 10^4$	3108	$-16.8, +17.9$
130–140	134.8	$(3.96 \pm 0.03) \times 10^4$	21307	$-16.9, +18.2$
140–150	144.8	$(2.32 \pm 0.02) \times 10^4$	12510	$-17.5, +18.9$
150–160	154.8	$(1.37 \pm 0.02) \times 10^4$	7409	$-18.2, +19.7$
160–170	164.8	$(8.34 \pm 0.12) \times 10^3$	4537	$-18.9, +20.6$
170–180	174.8	$(5.05 \pm 0.07) \times 10^3$	4636	$-19.7, +21.6$
180–190	184.8	$(3.23 \pm 0.06) \times 10^3$	2985	$-20.5, +22.7$
190–200	194.8	$(1.91 \pm 0.05) \times 10^3$	1782	$-21.4, +23.9$
200–220	209.2	$(9.93 \pm 0.23) \times 10^2$	1882	$-22.9, +25.8$
220–250	233.3	$(3.12 \pm 0.10) \times 10^2$	917	$-25.7, +29.4$
250–290	267.0	$(7.57 \pm 0.43) \times 10^1$	317	$-30.3, +35.5$
290–330	306.8	$(1.08 \pm 0.15) \times 10^1$	52	$-37.2, +44.4$
330–460	363.5	$(0.69 \pm 0.18) \times 10^0$	15	$-50.9, +61.4$

Table 10.3: Single inclusive jet cross section in $1.0 \leq |\eta| < 1.5$.

10.1 Experimental and Theoretical Uncertainties

The experimental uncertainties due to the data selection efficiencies, the luminosity determination including the trigger matching, the measurement of resolutions and unfolding corrections, and the jet energy scale correction are discussed in previous chapters. They are presented in Figures 10.2–10.4 for all pseudorapidity regions

Bin Range (GeV)	Plotted E_T (GeV)	Cross Sec. \pm Stat. (fb/GeV)	Observed Events	Systematic Uncer.(%)
60–70	64.6	$(3.42 \pm 0.03) \times 10^6$	11081	$-16.6, +18.2$
70–80	74.6	$(1.33 \pm 0.02) \times 10^6$	4306	$-17.3, +18.7$
80–90	84.6	$(5.20 \pm 0.13) \times 10^5$	1693	$-18.0, +19.5$
90–100	94.7	$(2.54 \pm 0.02) \times 10^5$	11224	$-18.6, +20.2$
100–110	104.7	$(1.20 \pm 0.02) \times 10^5$	5324	$-19.6, +21.4$
110–120	114.7	$(5.80 \pm 0.11) \times 10^4$	2591	$-20.7, +22.9$
120–130	124.7	$(2.87 \pm 0.08) \times 10^4$	1293	$-21.9, +24.6$
130–140	134.7	$(1.39 \pm 0.02) \times 10^4$	7456	$-23.0, +26.3$
140–150	144.7	$(6.95 \pm 0.11) \times 10^3$	3775	$-24.5, +28.6$
150–160	154.7	$(3.57 \pm 0.08) \times 10^3$	1967	$-26.2, +31.0$
160–170	164.7	$(1.84 \pm 0.06) \times 10^3$	1033	$-28.0, +33.8$
170–180	174.7	$(9.50 \pm 0.31) \times 10^2$	913	$-30.0, +36.8$
180–200	188.9	$(3.48 \pm 0.13) \times 10^2$	692	$-33.0, +41.4$
200–230	212.5	$(6.34 \pm 0.44) \times 10^1$	204	$-38.6, +50.3$
230–320	254.5	$(2.91 \pm 0.50) \times 10^0$	34	$-50.7, +69.8$

Table 10.4: Single inclusive jet cross section in $1.5 \leq |\eta| < 2.0$.

along with the *total* uncertainties calculated as the quadrature sum of all errors. The plots show the fractional errors in percentage as a function of jet E_T in the same bins in which the cross sections are measured. Note that the jet energy scale (JES) error dominates everywhere. Uncertainties due to the JES are determined as the difference in the cross sections derived with the nominal and with the high and low energy scale corrections. The deviations from the nominal cross sections are fit to a second order polynomial to smooth bin-to-bin fluctuations. The errors due to data selection are negligible, and uncertainties due to the luminosity determination are the next largest after the JES errors except at highest E_T 's where the errors

Bin Range (GeV)	Plotted E_T (GeV)	Cross Sec. \pm Stat. (fb/GeV)	Observed Events	Systematic Uncer.(%)
60–70	64.5	$(9.79 \pm 0.12) \times 10^5$	6531	$-22.0, +26.3$
70–80	74.5	$(3.07 \pm 0.07) \times 10^5$	2051	$-23.8, +26.9$
80–90	84.5	$(1.03 \pm 0.04) \times 10^5$	692	$-25.8, +28.5$
90–100	94.6	$(3.71 \pm 0.06) \times 10^4$	3375	$-27.9, +30.9$
100–110	104.6	$(1.19 \pm 0.04) \times 10^4$	1096	$-30.3, +34.5$
110–130	118.3	$(2.87 \pm 0.12) \times 10^3$	535	$-34.0, +41.1$
130–160	141.3	$(2.64 \pm 0.09) \times 10^2$	903	$-40.9, +56.3$
160–210	174.9	$(4.65 \pm 0.66) \times 10^1$	49	$-53.1, +88.2$

Table 10.5: Single inclusive jet cross section in $2.0 \leq |\eta| < 3.0$.

due to the resolutions and unfolding procedure become comparable to or even larger than those due to luminosity measurement.

Uncertainties in the current version of the DØ JES, CAFIX 5.2, are in the order of 2–5% in the dynamical range of this analysis, increasing as a function of both jet E_T and η . It is the steeply falling cross sections that “translate” such relatively small uncertainties into very large errors ranging from approximately 14% at lowest E_T ’s to as high as about 40–90% at highest E_T ’s and pseudorapidities. Since the statistics at highest E_T ’s are limited, the method of taking the differences between the cross sections corresponding to the nominal, low, and high CAFIX 5.2, and fitting them to a polynomial introduces additional uncertainties. Therefore, recently a new method has been devised which also gives a full covariance matrix associated with the jet energy scale correction [46, 66, 87].

As discussed in chapter 6, the JES response correction is obtained from a fit to many data points as a function of jet energy. It is the dominant source of

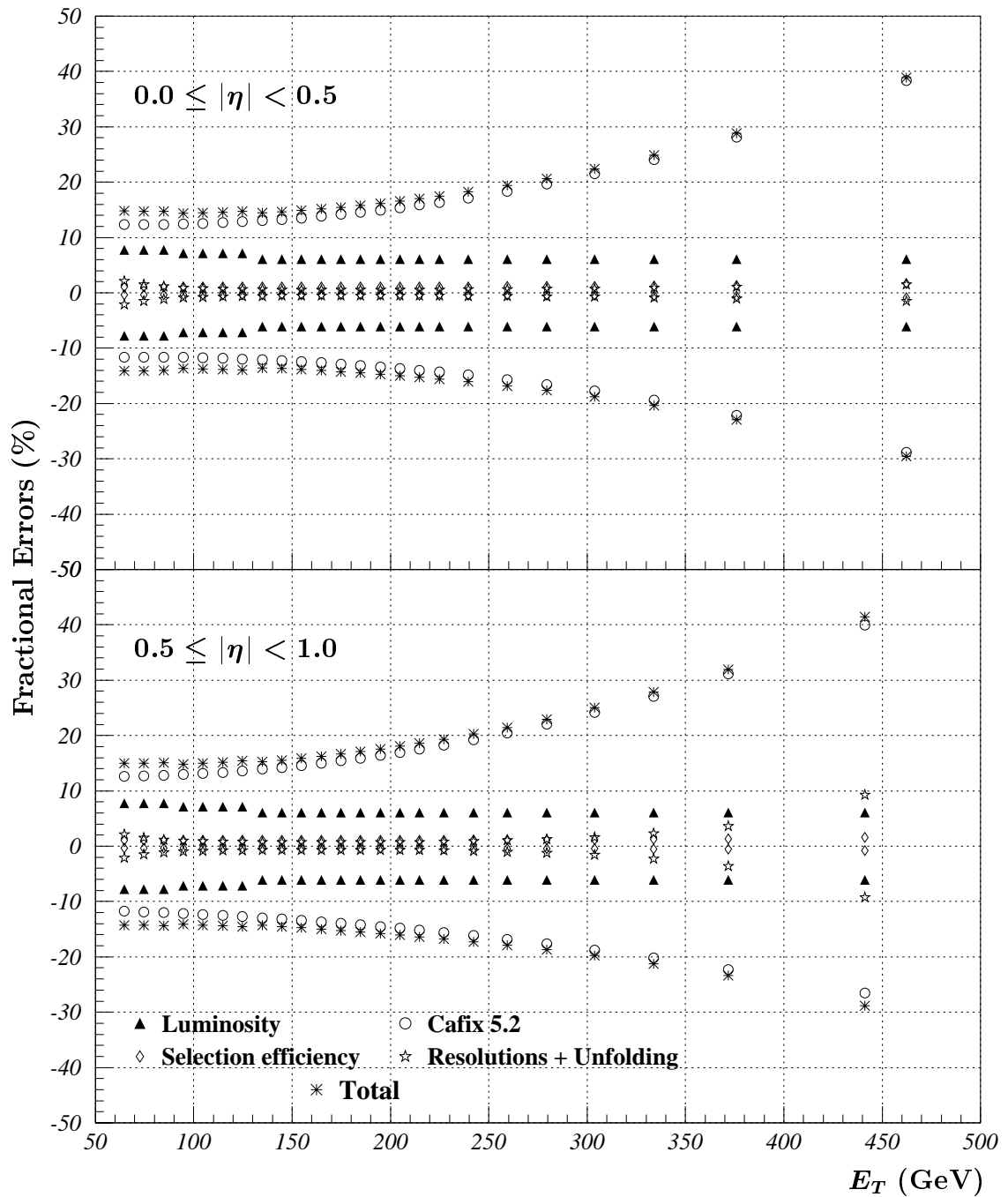


Figure 10.2: Fractional experimental uncertainties on the cross sections in the two central pseudorapidity regions. Errors originating from the different sources are distinguished. The jet energy scale error dominates the total uncertainty in the cross sections.

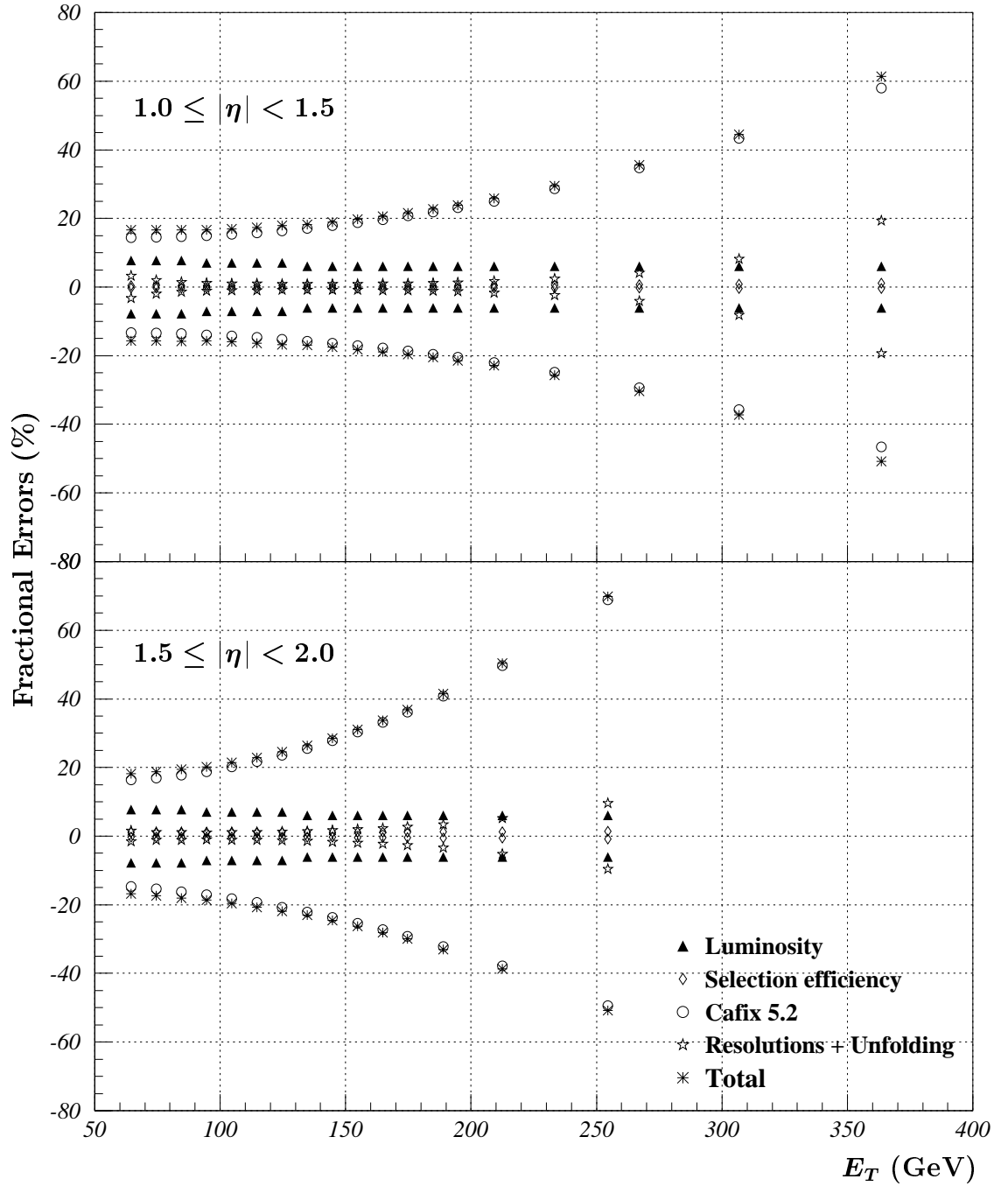


Figure 10.3: Fractional experimental uncertainties on the cross sections in the two intermediate pseudorapidity regions. Errors originating from the different sources are distinguished. The jet energy scale error dominates the total uncertainty in the cross sections.

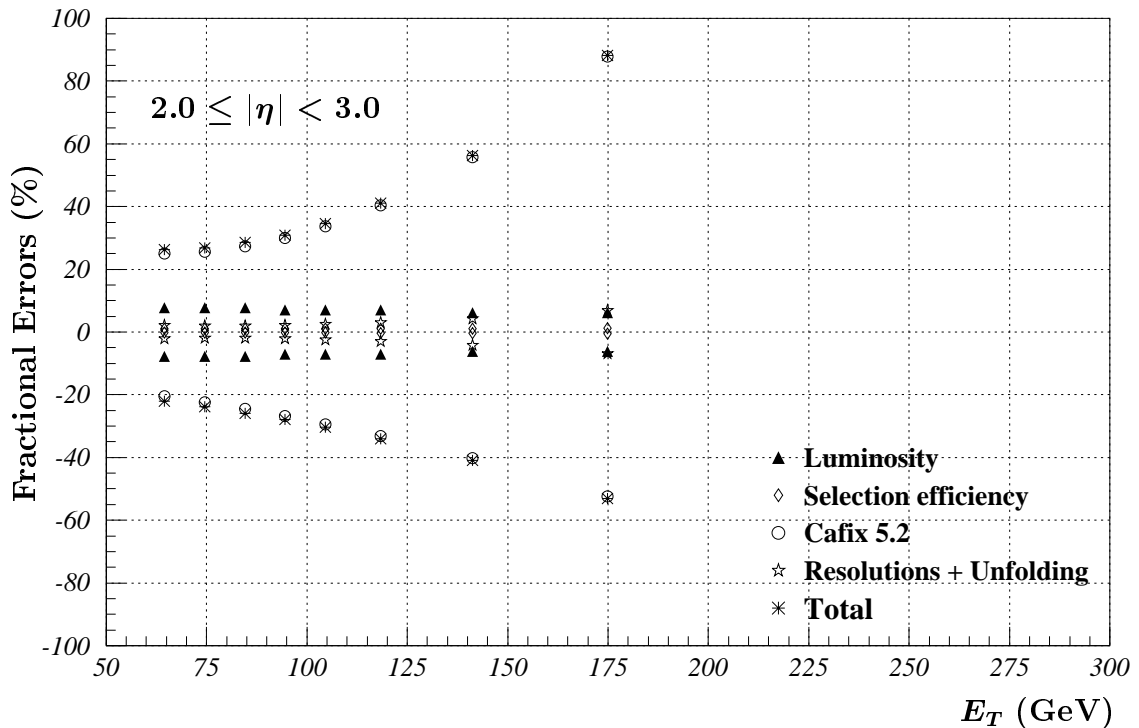


Figure 10.4: Fractional experimental uncertainties on the cross section in the forward-most pseudorapidity region. Errors originating from the different sources are distinguished. The jet energy scale error dominates the total uncertainty in the cross section.

experimental uncertainty at highest E_T 's. The correlation matrix of the response correction has been derived for the 11 values of partially corrected jet energies (see the discussion on page 199). The errors due to the rest of the subcomponents of the JES can be classified as completely correlated or uncorrelated across E_T and/or η . Thus the full error matrix of the JES correction can be obtained including the information of the error correlation of its subcomponents.

In order to improve the statistics in poorly populated bins in the data, a toy Monte Carlo (MC) jet sample is generated. In MC, Every η - E_T bin is evenly populated by a fixed, large number of jets. A dijet event is generated in a given bin by randomly selecting Bjorken x values of the hard scattered partons thereby

setting the scale of the collision ($\sqrt{\hat{s}} = \sqrt{x_1 x_2 s}$). All necessary kinematic variables of partons are calculated given the η bin that is being considered. These partons are called jets for the purposes of the rest of the discussion of this MC study. The energies of jets are smeared according to the measured resolution functions presented in chapter 9. One jet is selected at random and the procedure of generation and smearing is repeated until it falls in a desired E_T bin.

This true jet, call it the “primary” jet, is uncorrected to a best guess “measured” E_T value. Next the vertex z -coordinate, instantaneous luminosity of the event, and the value of the multiple interaction tool are sampled at random from the distributions of the corresponding variables obtained in the Collider data. All these event variables are input parameters to the jet energy scale correction, CAFIX 5.2. The generated, uncorrected jet E_T is then corrected according to CAFIX 5.2 and, if this JES-corrected E_T does not match the original MC jet E_T , the process is repeated until the convergence is achieved. Using the pre-JES (for the interpolation of the response fit correlation matrix, JES-partially corrected) value of jet E_T , the JES is asked to provide errors on its subcomponents.

To obtain the intercorrelation of the JES errors, one needs another jet which will sweep all η - E_T bins. Therefore, at the same time, other dijet events are generated and randomly selected jets from these events are forced to sweep all η - E_T bins. They undergo the smearing and JES-uncorrection procedure in exactly the same manner as the primary jet. Thus, for any given η - E_T bin there is a primary jet and as many “secondary” jets as there are the η - E_T bins.

At this point, the JES is asked to provide errors corresponding to the primary and secondary jets and also the correlation coefficients of the response correction (as the response correlation matrix is evaluated only at 11 energy points, a two dimensional interpolation of the matrix is required to obtain the correlation parameters at an arbitrary energy point). Different subcomponents of CAFIX 5.2 are classified according to their degree of correlation in E_T and η . The total JES error is split into three components: completely correlated, completely uncorrelated and partially correlated errors. Thus, the three corresponding error matrices are built and all η - E_T bins are filled by sweeping them with the secondary jet. The number of primary jets in a given sample is large enough to remove any statistical fluctuations. Then the next primary jet is generated in a different η - E_T bin and the entire process is repeated. This way, all bins are filled with corresponding values of the JES errors also taking into account their bin-to-bin correlations.

The E_T dependence of the jet cross sections as measured in the data is used to transform the uncertainties in jet energy scale into the errors in the cross section via the usual error propagation. After enough statistics are accumulated, one obtains three error matrices for the three degrees of correlations. When put together, they yield the full error matrix, or the covariance matrix of the JES in the same bins as the cross sections.

The remaining subcomponents of the total cross section error (such as due to data selection, luminosity, etc.) are also classified according to their degree of correlation and are put in the corresponding three error matrices. The toy MC is however run only for the JES correction, as it is the dominant source of the uncertainty and because the partial correlations are determined most accurately for

the JES response correction. Uncertainties due to data selection, luminosity, resolutions and unfolding are added together with the JES error matrix giving the full error matrix associated with the experimental measurement. Knowing the direct or “induced” correlations among the errors in different η - E_T bins of the total cross section errors is very important for carrying out precise comparison tests with the corresponding theoretical predictions. These final comparisons are presented in the following section but before turning to them we discuss the theoretical calculations of jet cross sections used for these comparisons along with the associated uncertainties.

Next-to-leading order (NLO) predictions for the inclusive cross section have been published in reference [88] and provided through the NLO program JETRAD by Giele, Glover, and Kosower [89]. The two predictions agree within a few percent. Whereas the prediction by Ellis *et al.* is analytic, JETRAD generates “events” with final state partons. Cross sections can be obtained by histogramming jets from a large number of events as a function of E_T and η . All predictions have been generated with the JETRAD program ported to the DØ environment.

A NLO QCD calculation requires specifying several “parameters”. First, the parton distribution function (PDF) must be selected. The many PDF’s available can result in 5–10% variations in the inclusive jet cross sections. Truncation of the QCD NLO predictions at order α_s^3 additionally introduces some residual dependence on the renormalization (μ_R) and factorization (μ_F) scales at which the calculations are done. The two scales are usually set equal to each other, $\mu_R = \mu_F = \mu$. The dependence is of the order 5–15% for small η depending on E_T . Typical μ scale choices include $c \cdot E_T$ or $c \cdot E_T^{max}$, where c varies from 0.25 to 2 and E_T^{max} represents

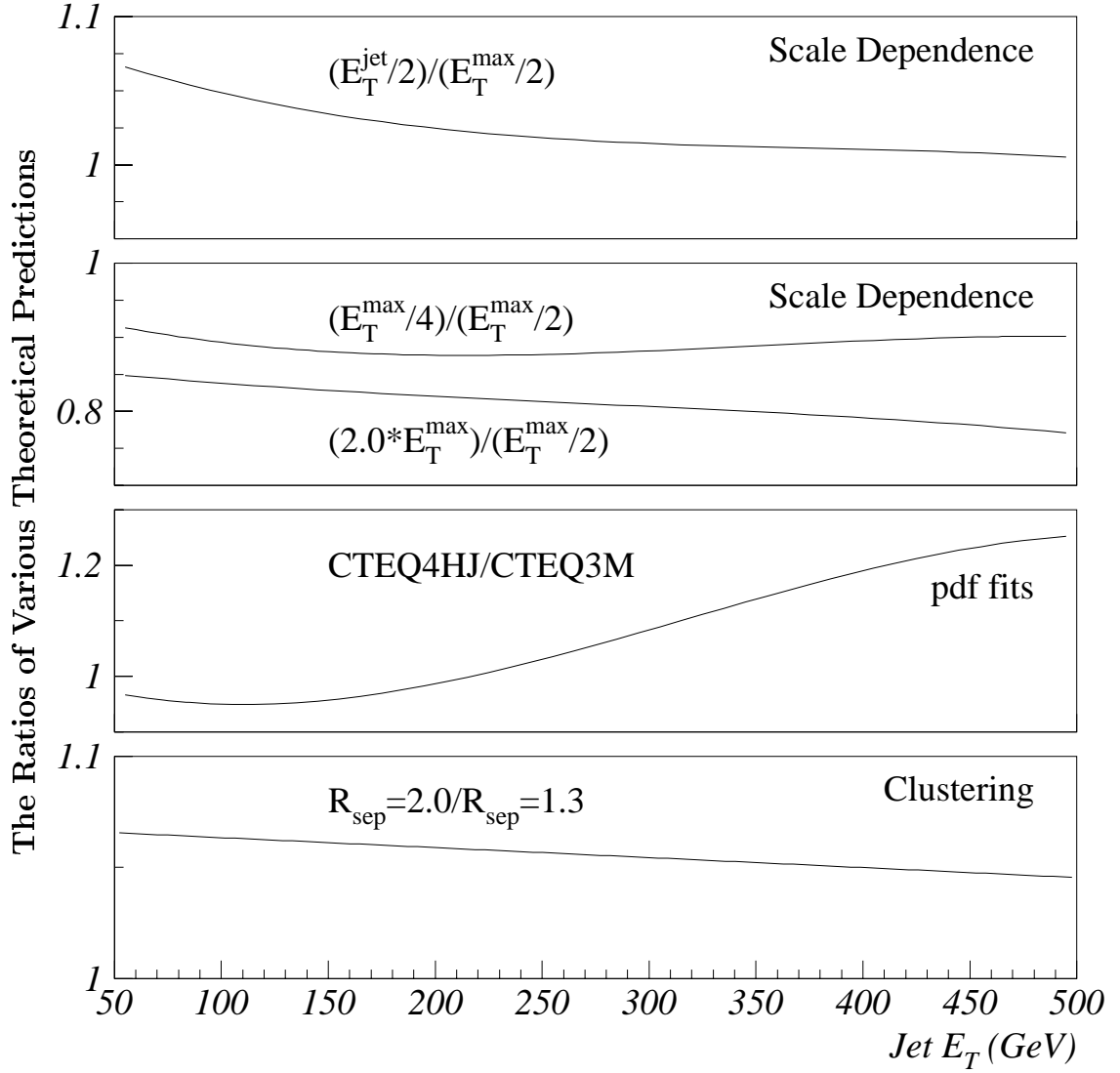


Figure 10.5: The illustration of the uncertainties in the theoretical pQCD predictions calculated with JETRAD for the central pseudorapidity region ($|\eta| < 0.5$). The uncertainties become larger at higher η 's. They are generally in the order of the systematic experimental uncertainties.

the leading jet E_T in the event.

In addition to the PDF and renormalization scale, each NLO prediction must incorporate a NLO jet finding algorithm. At NLO, the clustering algorithm must include a parameter indicating the proximity of partons to be clustered in η - φ space. We choose the algorithm which requires the final state partons to be within one cone width (\mathcal{R}) of their summed E_T vector direction and within 1.3 cone widths of one another (i.e. $\mathcal{R}_{sep} = 1.3$). In other words, only final state partons within $\mathcal{R}_{sep} = 1.3$ of each other are to be clustered into final state “jets”. An extensive study of this parameter can be found in the reference [90].

In summary, the NLO calculation with JETRAD provides theoretical predictions for the inclusive jet cross section. The NLO calculation is sensitive to the choice of PDF, renormalization and factorization scale μ , and clustering algorithm. Overall the theoretical inclusive jet prediction carries about 15% normalization uncertainty and about 15% shape uncertainty as jet E_T is varied from 50 to 450 GeV in the central ($|\eta| < 0.5$) pseudorapidity region. Figure 10.5 shows some of the dependences in the theoretical predictions as the ratios of the cross sections generated with the different input parameters for the central pseudorapidity region. The theoretical uncertainties increase with increasing η and are generally of the same order as the systematic experimental uncertainties.

10.2 Data and Theory Comparison

In this section we discuss the comparison of our results to NLO QCD predictions for the inclusive jet cross sections. Figures 10.6–10.8 present linear differences between

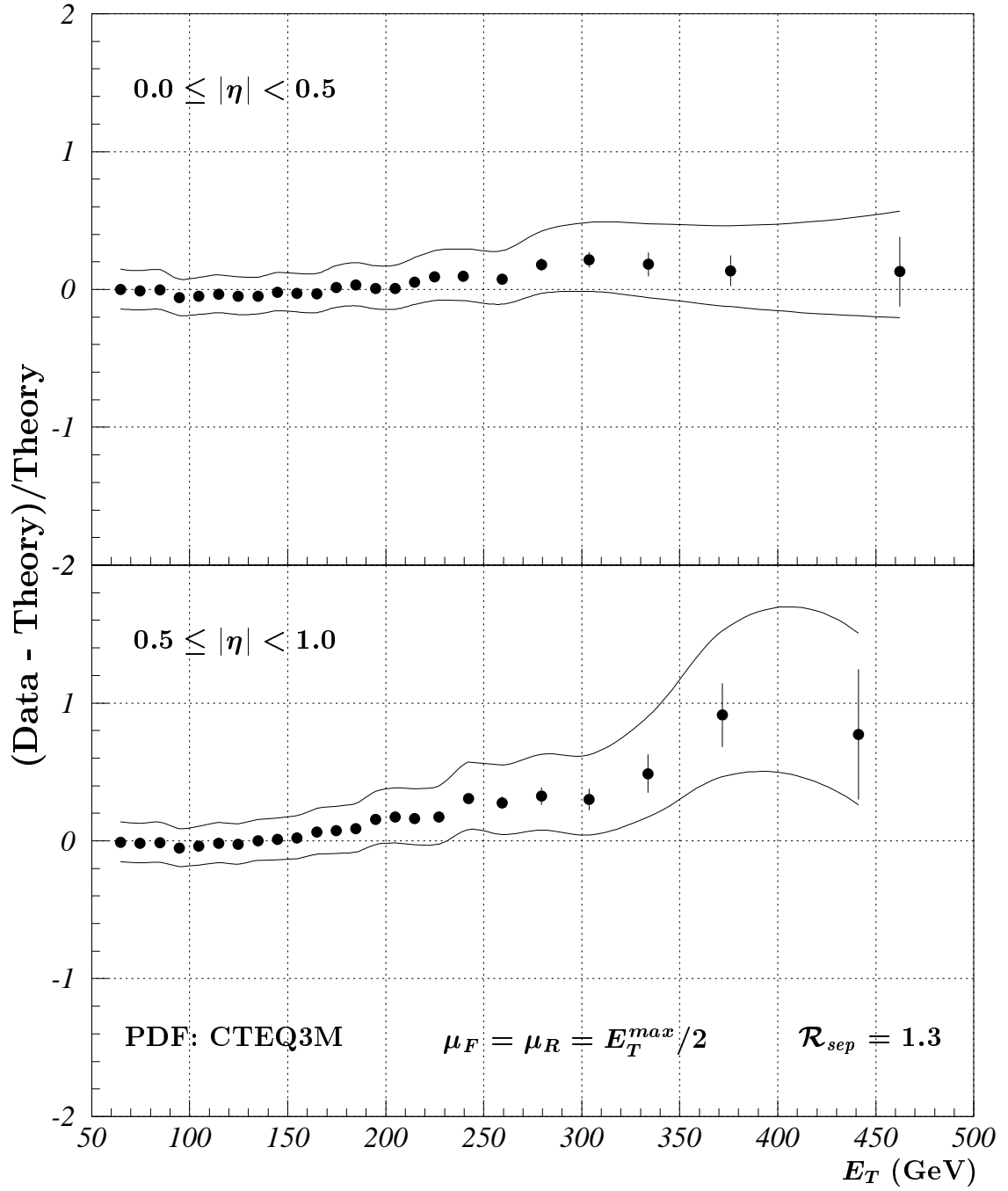


Figure 10.6: The comparison between the DØ single inclusive jet production cross sections, $\langle d^2\sigma/(dE_T d\eta) \rangle$, as a function of jet E_T in the two central pseudorapidity regions and the α_s^3 QCD predictions calculated by JETRAD with the CTEQ3M PDF and the input parameters $\mu_R = \mu_F = E_T^{max}/2$ and $\mathcal{R}_{sep} = 1.3$.

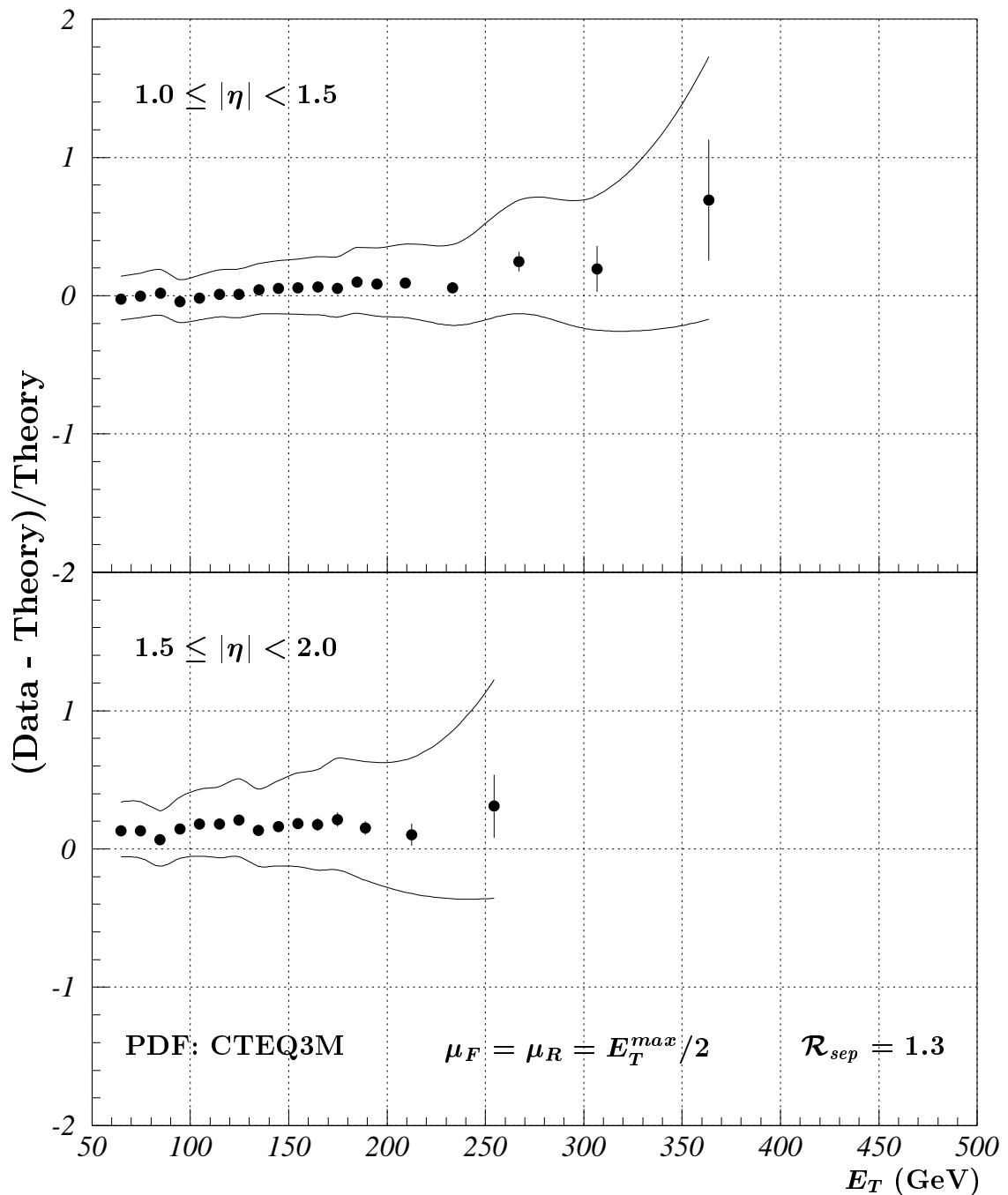


Figure 10.7: The comparison between the DØ single inclusive jet production cross sections, $\langle d^2\sigma/(dE_T d\eta) \rangle$, as a function of jet E_T in the two intermediate pseudorapidity regions and the α_s^3 QCD predictions calculated by JETRAD with the CTEQ3M PDF and the input parameters $\mu_R = \mu_F = E_T^{max}/2$ and $\mathcal{R}_{sep} = 1.3$.

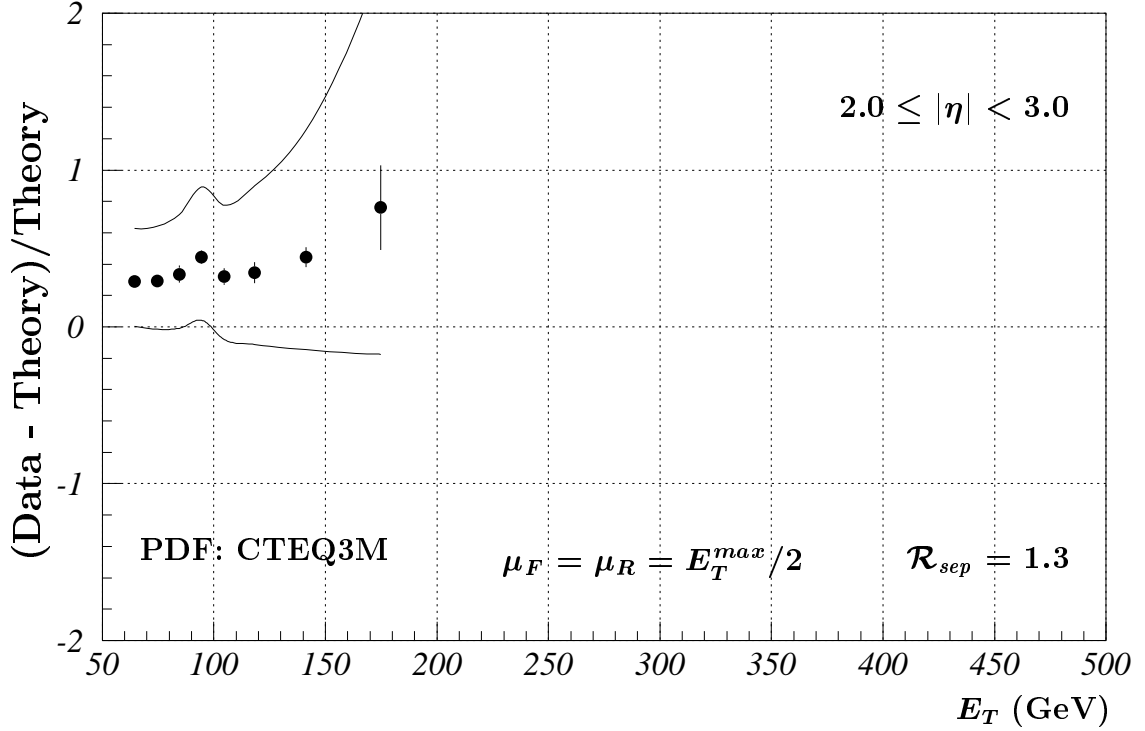


Figure 10.8: The comparison between the DØ single inclusive jet production cross section, $\langle d^2\sigma/(dE_T d\eta) \rangle$, as a function of jet E_T in the forward-most pseudorapidity region and the α_s^3 QCD prediction calculated by JETRAD with the CTEQ3M PDF and the input parameters $\mu_R = \mu_F = E_T^{max}/2$ and $\mathcal{R}_{sep} = 1.3$.

the data (D) and JETRAD theoretical predictions (T) normalized to the prediction (i.e. $(D-T)/T$) in *all* pseudorapidity regions considered along with the statistical error bars and experimental systematic uncertainty bands. The theoretical prediction in Figures 10.6–10.8 is generated with CTEQ3M PDF, with the renormalization and factorization scales set to $E_T^{max}/2$ and with the clustering parameter $\mathcal{R}_{sep} = 1.3$ —the choice of the input parameters that have become a standard in DØ. The data agrees with theoretical calculations within errors. Deviations from theory at highest E_T 's in the pseudorapidity region $0.5 \leq |\eta| < 1.0$ are not very significant given the large uncertainties.

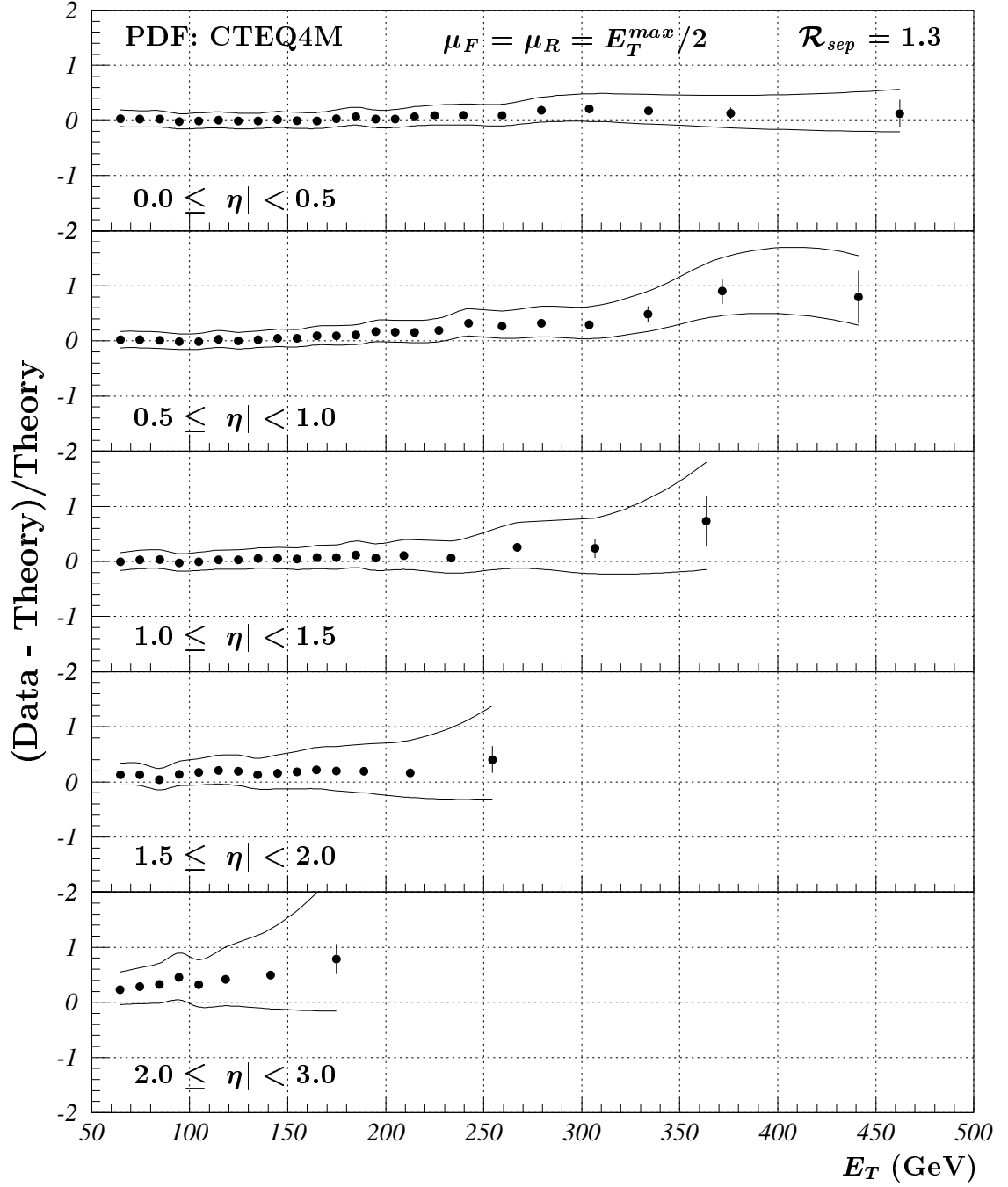


Figure 10.9: The comparison between the DØ single inclusive jet production cross sections, $\langle d^2\sigma/(dE_T d\eta) \rangle$, as a function of jet E_T in all five pseudorapidity regions (up to $|\eta| = 3.0$) and the α_s^3 QCD predictions calculated by JETRAD with the CTEQ4M PDF and the input parameters $\mu_R = \mu_F = E_T^{max}/2$ and $\mathcal{R}_{sep} = 1.3$.

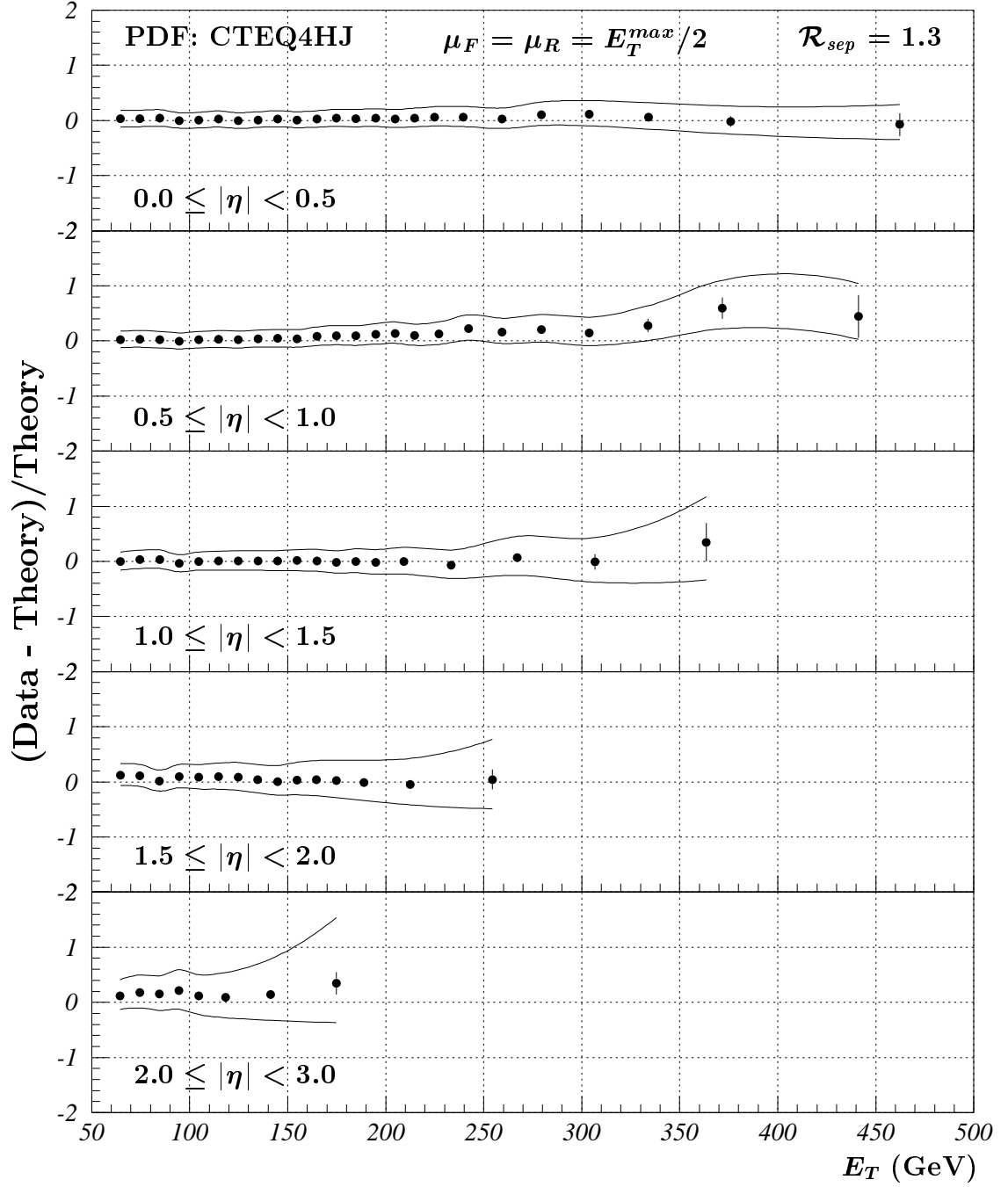


Figure 10.10: The comparison between the DØ single inclusive jet production cross sections, $\langle d^2\sigma/(dE_T d\eta) \rangle$, as a function of jet E_T in all five pseudorapidity regions (up to $|\eta| = 3.0$) and the α_s^3 QCD predictions calculated by JETRAD with the CTEQ4HJ PDF and the input parameters $\mu_R = \mu_F = E_T^{max}/2$ and $\mathcal{R}_{sep} = 1.3$.

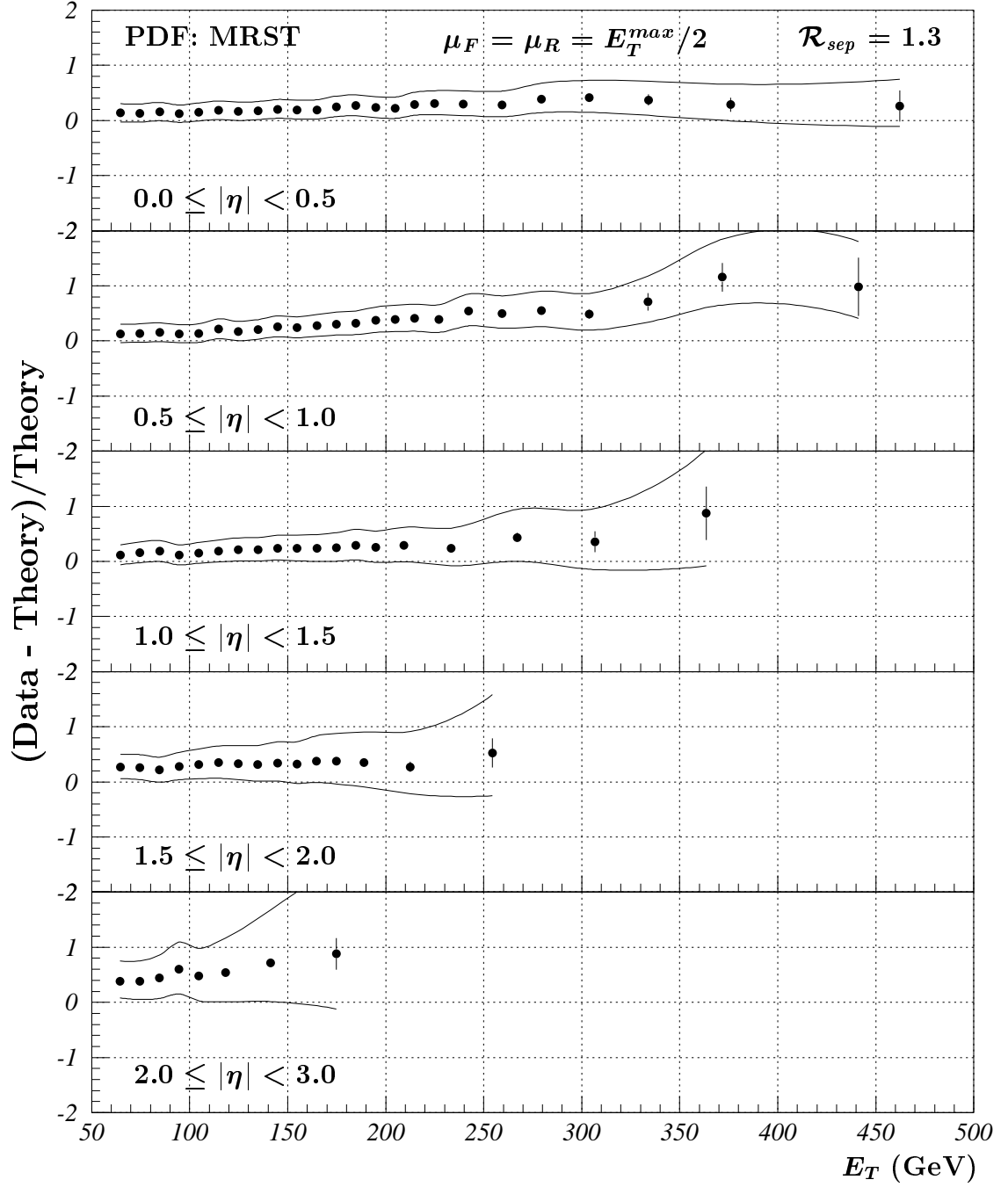


Figure 10.11: The comparison between the DØ single inclusive jet production cross sections, $\langle d^2\sigma/(dE_T d\eta) \rangle$, as a function of jet E_T in all five pseudorapidity regions (up to $|\eta| = 3.0$) and the α_s^3 QCD predictions calculated by JETRAD with the MRST PDF and the input parameters $\mu_R = \mu_F = E_T^{max}/2$ and $\mathcal{R}_{sep} = 1.3$.

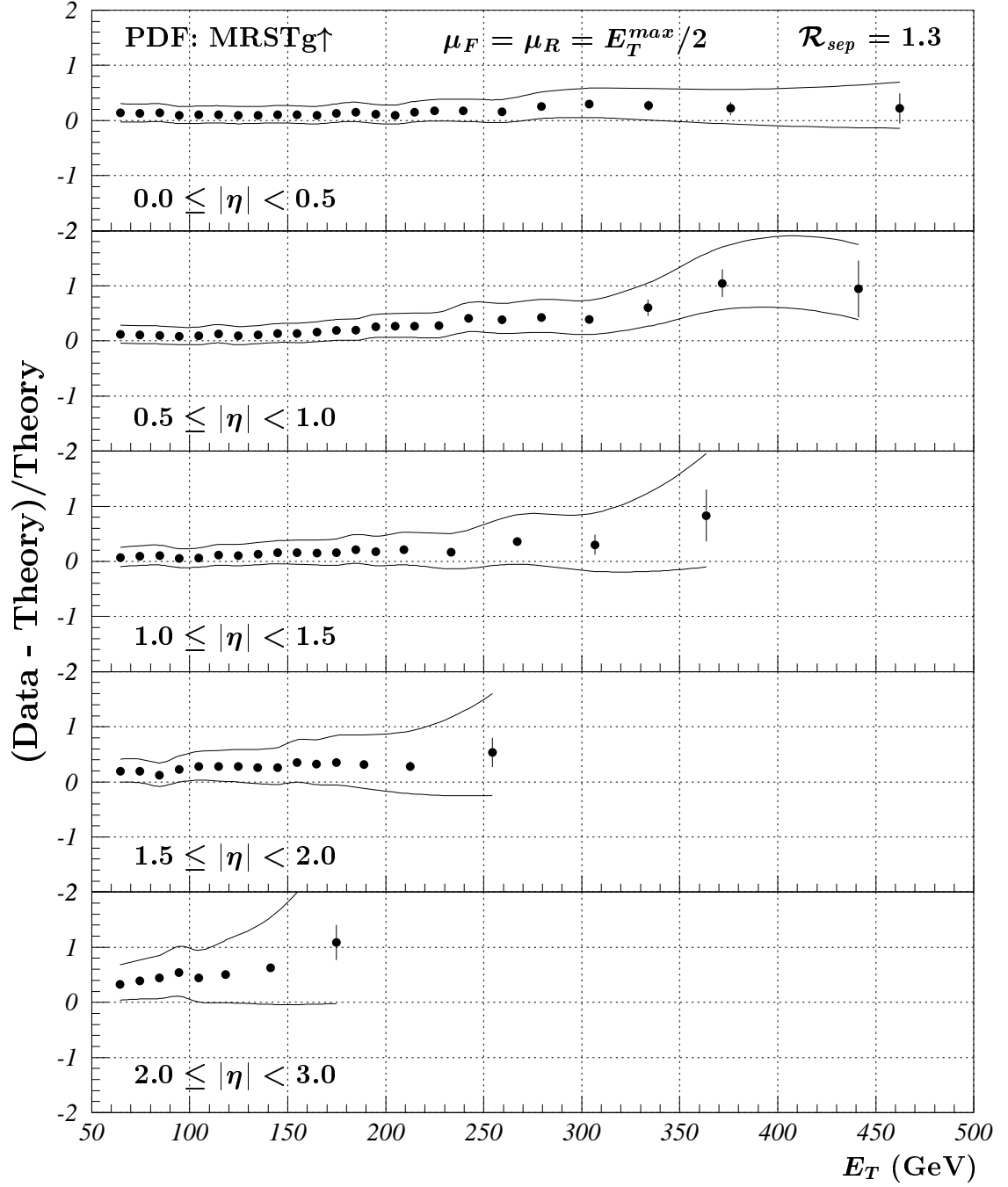


Figure 10.12: The comparison between the DØ single inclusive jet production cross sections, $\langle d^2\sigma/(dE_T d\eta) \rangle$, as a function of jet E_T in all five pseudorapidity regions (up to $|\eta| = 3.0$) and the α_s^3 QCD predictions calculated by JETRAD with the MRSTg \uparrow PDF and the input parameters $\mu_R = \mu_F = E_T^{max}/2$ and $\mathcal{R}_{sep} = 1.3$.

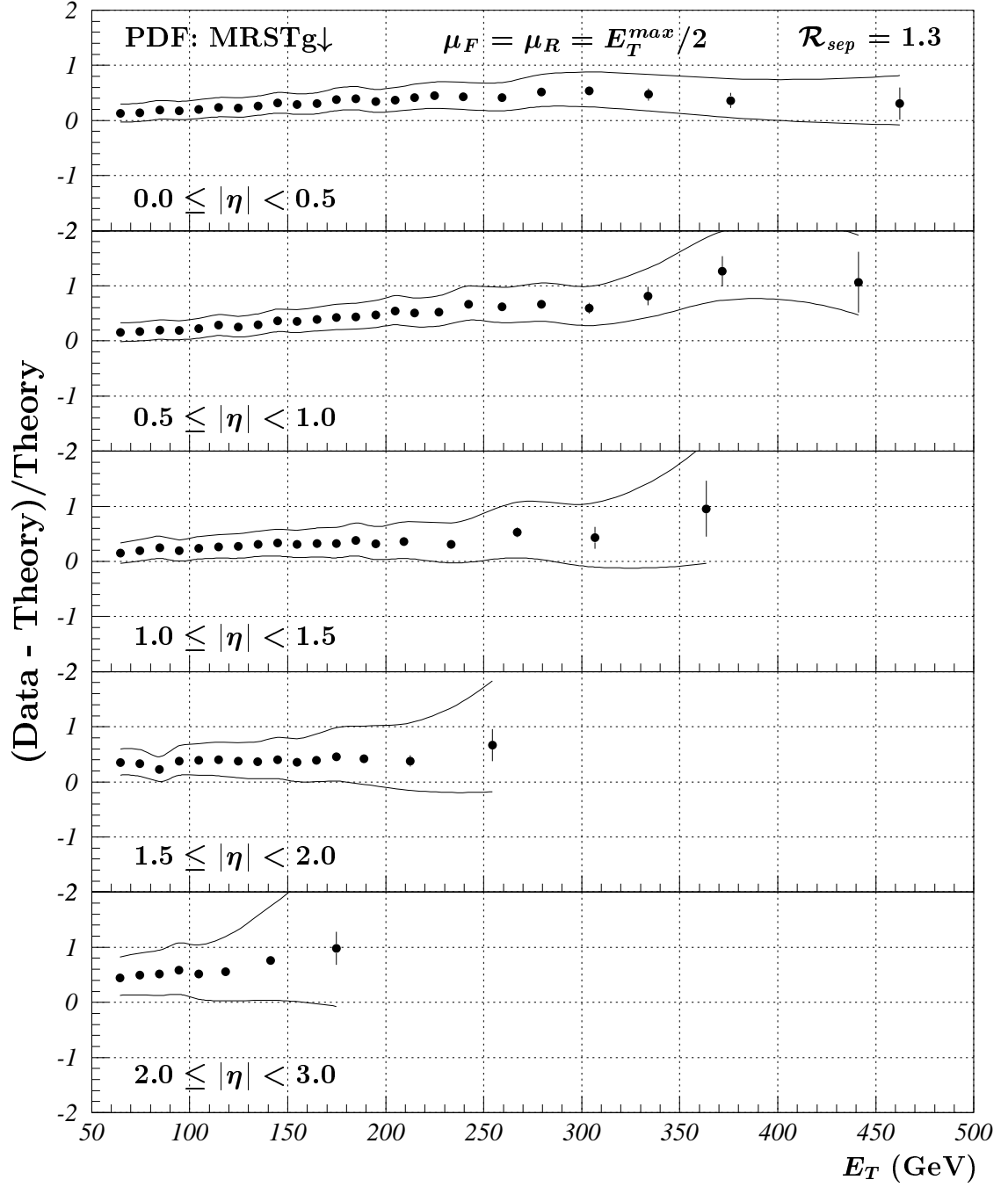


Figure 10.13: The comparison between the DØ single inclusive jet production cross sections, $\langle d^2\sigma/(dE_T d\eta) \rangle$, as a function of jet E_T in all five pseudorapidity regions (up to $|\eta| = 3.0$) and the α_s^3 QCD predictions calculated by JETRAD with the MRSTg↓ PDF and the input parameters $\mu_R = \mu_F = E_T^{max}/2$ and $\mathcal{R}_{sep} = 1.3$.

PDF	χ^2	χ^2/ndf	Probability (%)
CTEQ3M	183.32	2.04	2.40×10^{-6}
CTEQ4M	143.30	1.59	3.02×10^{-2}
CTEQ4HJ	54.11	0.60	99.90
MRST	126.39	1.40	0.69
MRSTg \uparrow	136.83	1.52	0.11
MRSTg \downarrow	177.93	1.98	9.82×10^{-6}

Table 10.6: Results of the χ^2 test for the full dynamic range.

PDF	χ^2	χ^2/ndf	Probability (%)
CTEQ3M	1.44	6.01×10^{-2}	100.00
CTEQ4M	1.02	4.23×10^{-2}	100.00
CTEQ4HJ	0.80	3.32×10^{-2}	100.00
MRST	14.27	0.59	94.04
MRSTg \uparrow	3.25	0.14	99.99
MRSTg \downarrow	37.16	1.55	4.22

Table 10.7: Results of the χ^2 test in the central ($|\eta| < 0.5$) region only.

Comparisons have also been made with all recent versions of the CTEQ and MRST families of PDF's which are presented in Figures 10.9–10.13. The visual agreement is the best for the CTEQ4HJ—the PDF tuned to the CDF central ($0.1 < |\eta| < 0.7$) inclusive jet cross section data which had shown an excess over the theory at the highest E_T 's when compared to other available PDF's.

A better quantitative measure of the agreement or disagreement in such comparisons is the χ^2 per degree of freedom calculated for the bin-by-bin differences between the data and theory. Determination of the full error matrix or, equivalently,

PDF	χ^2	χ^2/ndf	Probability (%)
CTEQ3M	77.97	1.62	0.40
CTEQ4M	66.78	1.39	3.77
CTEQ4HJ	25.61	0.53	99.67
MRST	104.05	2.17	5.11×10^{-4}
MRSTg \uparrow	71.15	1.48	1.66
MRSTg \downarrow	153.40	3.20	6.029×10^{-11}

Table 10.8: Results of the χ^2 test in the pseudorapidity region $|\eta| < 1.0$.

PDF	χ^2	χ^2/ndf	Probability (%)
CTEQ3M	84.26	1.26	7.55
CTEQ4M	69.81	1.04	38.33
CTEQ4HJ	29.47	0.44	99.99
MRST	110.56	1.65	6.46×10^{-2}
MRSTg \uparrow	76.55	1.14	19.88
MRSTg \downarrow	164.24	2.45	3.90×10^{-8}

Table 10.9: Results of the χ^2 test in the pseudorapidity region $|\eta| < 1.5$.

the full covariance matrix of the experimental uncertainties, allows comparisons to the theoretical predictions which have more discrimination power than the visual comparisons presented in Figures 10.6–10.13. The standard definition of χ^2 for such a comparison would be:

$$\chi^2 = \sum_{i,j} (D_i - T_i) \text{Cov}_{i,j}^{-1} (D_j - T_j), \quad (10.1)$$

with $(D_i - T_i)$ being the deviation of the measured cross section (D_i) from the theoretical prediction (T_i) in the i -th bin, and $\text{Cov}_{i,j}^{-1}$ being the inverse of the full covariance matrix of the measurement. There are 90 total η - E_T bins considered in

PDF	χ^2	χ^2/ndf	Probability (%)
CTEQ3M	124.69	1.52	0.17
CTEQ4M	102.52	1.25	6.22
CTEQ4HJ	37.02	0.45	99.99
MRST	117.53	1.43	0.62
MRSTg \uparrow	103.88	1.27	5.18
MRSTg \downarrow	171.43	2.09	2.82

Table 10.10: Results of the χ^2 test in the pseudorapidity region $|\eta| < 2.0$.

the measurement of the rapidity dependence of the inclusive jet cross section.

However, as discussed earlier in this chapter and in previous chapters, many of the systematic uncertainties affecting the normalization of the cross sections are partially or fully correlated across E_T and η . It is known that when correlated normalization error is included in the standard definition of the χ^2 , Eq. (10.1), a bias is introduced. This is known as Peelle’s Pertinent Puzzle [91]. The standard χ^2 definition then would prefer theoretical predictions that have a normalization below that of the data.

It has been demonstrated that a modified definition of χ^2 is needed to remove the bias [92]. When making such comparisons, the question we try to answer is: “How likely it is that a given theory could have produced the observed data?”. To also be consistent with this choice of a question we ask, we redefine the covariance matrix and assign the *fractional* experimental uncertainties to theoretical predictions, i.e. $\text{Cov}_{i,j} \rightarrow \text{Cov}_{i,j} \frac{T_i}{D_i} \frac{T_j}{D_j}$. Thus, instead of the standard χ^2 , we

consider the modified χ^2 and calculate it according to the following formula:

$$\chi^2 = \sum_{i,j} (D_i - T_i) \left[\text{Cov}_{i,j} \frac{T_i}{D_i} \frac{T_j}{D_j} \right]^{-1} (D_j - T_j). \quad (10.2)$$

In other words, we have chosen to perform χ^2 comparisons between the data and the theoretical predictions by using systematic uncertainties given by the product of the theoretical predictions and the measured fractional uncertainties because this method removes bias in the χ^2 test due to correlated systematic normalization uncertainties. We also note that in this way the test is more sensitive to shape differences between the data and theoretical predictions than to the differences in overall normalization.

The results of the χ^2 tests for the theoretical predictions generated with different PDF's are summarized in Table 10.6 for the full dynamical range of this measurement of the rapidity dependence of the inclusive single jet production cross section. CTEQ4HJ PDF exhibits the best agreement with the measured data with a nearly 100% probability of producing the observed data.

To address the question as to how significant the deviations at the highest E_T points in the $0.5 \leq |\eta| < 1.0$ region are, we calculated the joint χ^2 with and without the three highest E_T points from that region. The corresponding probability values changed by only a tenth of a percent as expected due to large experimental uncertainties associated with the measurement in this region of the phase space. It is hard to imagine a QCD process that might lead to such an excess in this one particular area of phase space. Perhaps this large deviation is due to our inadequate understanding of the detector systematics in this most poorly instrumented intercryostat region. On the other hand, we would like to point out that the extensive closure studies have not revealed any deviation of this order of magnitude

in our experimental measurement. Irrespective of the cause of this large deviation, however, our studies indicate that the χ^2 statistic is not sensitive to it.

We also repeated the χ^2 tests for different dynamical ranges starting from the central-most cross section ($|\eta| < 0.5$) and increasing the pseudorapidity reach by including adjacent, more forward η regions. The results of these studies are summarized in Tables 10.7–10.10. They indicate that the largest disagreement between the data and the theoretical predictions is observed in the pseudorapidity region $0.5 \leq |\eta| < 1.0$. However, the inclusion of higher η regions starts to recover the overall joint χ^2 values due to the many relatively well measured lower E_T data points which nominally agree with the theoretical predictions better in the other pseudorapidity regions than in the region $0.5 \leq |\eta| < 1.0$.

We note that the measurement of the inclusive jet cross section in the central ($|\eta| < 0.5$) pseudorapidity region alone does not provide enough discriminative power among theoretical predictions generated with different PDF's. However, by extending the measurement to higher η regions the discriminative power increases due to the increase in the size of the data sample and also because with many more degrees of freedom the comparison tests based on χ^2 statistics intrinsically become more discriminatory (as one can see from probability contours in the space of χ^2/ndf versus ndf).

10.3 Conclusions

We have made a new measurement of the rapidity dependence of the single inclusive jet production cross section in proton–antiproton collisions at the center-of-mass

energy of $\sqrt{s} = 1.8$ TeV with the DØ detector at the Fermilab Tevatron Collider. This measurement provides a stringent test of perturbative QCD over the large dynamic range accessible to DØ, significantly extending the previously available DØ and CDF inclusive jet cross section measurements which ended at $|\eta| = 0.7$ to jet pseudorapidities of 3.0.

Theoretical predictions calculated with different parton distribution functions are characterized by varying degrees of agreement with theory. The visual, qualitative comparisons between the data and the theoretical predictions with different PDF's do not provide grounds for strong discrimination among different sets of PDF's with the current experimental uncertainties. The quantitative tests based on the unbiased χ^2 statistics with full covariance matrix of the measurement for the particular choice of the parameters for calculating the theoretical predictions (the renormalization and regularization scales and the clustering parameter) indicate the preference for the CTEQ4HJ PDF. It is notable that we find good agreement—within experimental uncertainties—with the theoretical predictions based on CTEQ4HJ PDF over the full dynamic range.

Moreover, the measurement of jet cross sections very close to the beamline demonstrates our good understanding of the detector as well as the jet energy scale and other systematic corrections in nearly full solid angle coverage around the interaction region. The results of this analysis are applicable to both QCD tests and other physics analyses requiring a reliable understanding of the jets as dominant source of background or as tagging objects. This experience is invaluable not only for DØ Run 1 analyses but also for future studies to be carried out at the Tevatron upcoming run as well as the next generation Large Hadron Collider experiments.

REFERENCES

- [1] “Review of Particle Physics”, Euro. Phys. J. **C3**, 1 (1998).
- [2] P. Watkins, “The Story of the W and Z”, Cambridge University Press (1986).
- [3] G. Arnison *et al.*, Phys. Lett. **B123**, 115 (1983).
- [4] P. Bagnaia *et al.*, Phys. Lett. **B138**, 430 (1984);
J. Alitti *et al.*, Phys. Lett. **B257**, 232 (1991).
- [5] R. P. Crease and C. C. Mann, “The Second Creation”, Rutgers University Press, New Brunswick (1996).
- [6] T. D. Lee and C. N. Chang, Phys. Rev. **104**, 254 (1956).
- [7] C. S. Wu, E. Ambler, R. W. Hayward, D. D. Hoppes, and R. P. Hudson, Phys. Rev. **105**, 1413 (1957).
- [8] J. Schwinger, Ann. Phys. **2**, 407 (1957).
- [9] C. N. Yang and R. Mills, Phys. Rev. **96**, 191 (1954).
- [10] S. L. Glashow, Ph.D. Dissertation, Harvard University (1958).
- [11] S. L. Glashow, Nucl. Phys. **22**, 579 (1961).
- [12] A. Salam, J. C. Ward, Phys. Lett. **73**, 416 (1964).

- [13] J. Barden, L. N. Cooper, and J. R. Schrieffer, Phys. Rev. **106**, 162 (1956); *ibid.* **108**, 1175 (1957).
- [14] J. Goldstone, Nuovo Cimento **19**, 15 (1961).
- [15] P. W. Higgs, Phys. Rev. Lett. **12**, 132 (1964); *ibid.* **13**, 508 (1964).
- [16] S. Weinberg, Phys. Rev. Lett. **19**, 1264 (1967).
- [17] A. Salam, in “Elementary Particle Physics”, Nobel Symp. No. 8, ed. N. Svartholm, Almqvist and Wilsell, Stockholm (1968).
- [18] G. 't Hooft, Nucl. Phys. **B33**, 173 (1971); *ibid.* **B35**, 167 (1971).
- [19] G. Arnison *et al.*, Phys. Lett. **B122**, 103 (1983); *ibid.* **B126**, 398 (1983).
- [20] S. Glashow, J. Iliopoulos, and L. Maiani, Phys. Rev. **D2**, 1285 (1970).
- [21] M. Gell-Mann, Caltech report CTSL-20, *op. cit.*; reprinted in M. Gell-Mann and Y. Ne'eman, eds., “The Eightfold Way”, New York, W.A. Benjamin, 1964. Originally a long report written in 1961, the eightfold way was first published formerly as a three-page section at the end of a much longer paper: M. Gell-Mann, Phys. Rev. **125**, 1067 (1962).
- [22] M. Gell-Mann, Phys. Lett. **8**, 214 (1964).
- [23] G. Zweig, CERN preprint 8182/TH401, 17 January, 1964 (unpublished); *ibid.* 8419/TH412, 21 February 1964 (unpublished).
- [24] A. deShalit, H. Feshbach, “Theoretical Nuclear Physics”, Volume 1, “Nuclear Structure”, John Wiley & Sons (1974).

- [25] J. J. Aubert *et al.*, Phys. Rev. Lett. **33**, 1404 (1974).
- [26] J. E. Augustin *et al.*, Phys. Rev. Lett. **33**, 1406 (1974).
- [27] S. W. Herb *et al.*, Phys. Rev. Lett. **39**, 252 (1978).
- [28] F. Abe *et al.*, The CDF Collaboration, Phys. Rev. Lett. **74**, 2626 (1995).
- [29] B. Abbott *et al.*, The DØ Collaboration, Phys. Rev. Lett. **74**, 2632 (1995).
- [30] D. J. Gross and F. Wilczek, Phys. Rev. Lett. **30**, 1343 (1973).
- [31] H. D. Politzer, Phys. Rev. Lett. **30**, 1346 (1973).
- [32] S. Weinberg, “The Quantum Theory of Fields”, Cambridge University Press (1998).
- [33] V. D. Elvira, “Measurement of the Inclusive Jet Cross Sections at $\sqrt{s} = 1.8$ TeV with the DØ Detector”, Ph.D. Dissertation, University of Buenos Aires, Argentina (1994).
- [34] R. Feynman, “Photon-Hadron Interactions”, W. A. Benjamin, Reading, Massachusetts (1972).
- [35] V. N. Gribov, L. N. Lipatov, Sov. J. Nucl. Phys. **15**, 438 (1972); *ibid.* **15**, 675 (1972).
 Yu. L. Dokshitzer, Sov. Phys. JETP **46**, 641 (1977).
 G. Altarelli and G. Parizi, Nucl. Phys. **B126**, 298 (1972).
- [36] H. L. Lai *et al.*, The CTEQ Collaboration, “Global QCD Analysis and the CTEQ Parton Distributions”, Phys. Rev. **D51**, 4763 (1995).

- [37] A. D. Martin, R. G. Roberts, W. J. Stirling, and R. S. Thorne, “Parton Distributions: a New Global Analysis”, hep-ph/9803445 (1998).
- [38] V. D. Barger, R. J. N. Phillips, “Collider Physics”, Addison-Wesley Publishing Company (1987).
- [39] G. Marchesini *et al.*, Comp. Phys. Commun. **67**, 465 (1992). We used HERWIG versions 5.8 and 5.9.
- [40] T. Sjöstrand, Comp. Phys. Commun. **82**, 74 (1994). We used PYTHIA version 5.7.
- [41] E. Eichten, K. Lane and M. Peskin, Phys. Rev. Lett. **50**, 811 (1983).
- [42] P. J. Hiltz, “Scientific Temperaments”, Simon and Schuster, New York (1982).
- [43] J. Thompson, “Introduction to Colliding Beams at Fermilab”, Fermilab Tech. Memo, TM-1909 (1994).
- [44] D. H. Perkins, “Introduction to High Energy Physics”, Addison Wesley (1987).
- [45] The DØ Collaboration, “The DØ Detector”, Nucl. Instr. and Methods **A338** issue 2/3, 185 (1994).
- [46] G. C. Blazey, R. Hirosky, “The DØ Inclusive Cross Section”, DØ Note 3276.
- [47] G. Manning *et al.*, “DØ Software Documentation”, Calorimeter Reconstruction Section (1995).
- [48] N. J. Hadley, “DØ Algorithm for Jet Finding”, DØ Note 904.

- [49] M. K. Fatyga, “Trigger Efficiency Study Methods Using Single Jet Efficiencies”, DØ Note 3166.

K. Frame, T. Geld, M. K. Fatyga, “Trigger Efficiencies for Run 1B Inclusive Jet Triggers”, DØ Note 3178.
- [50] J. Huth *et al.*, in proceedings of “Research Directions for the Decade”, Snowmass 1990, ed. E. L. Berger, World Scientific, Singapore (1992).
- [51] S. D. Ellis and D. E. Soper, Phys. Rev. **D48**, 3160 (1993).
- [52] J. Guida *et al.*, “Calorimeter Studies”, DØ Note 3112.
- [53] L. Babukhadia *et al.*, “Hot Cells and Jets at DØ (AIDA Cell Restoration)”, DØ Note 3408.
- [54] J. Guida, “Calorimeter Hot Channel Study”, DØ Note 3080.
- [55] S. Fahey *et al.*, “Flagging Calorimeter Noisy Cells”, DØ Note 2379.
- [56] A. Boehnlein, “Changes Made to L2ETMISS and L2ETSUM During Run 1A”, DØ Note 1664.
- [57] A. Boehnlein, private communication.
- [58] Q. Li-Demarteau, private communication.
- [59] N. L. Grossman, “A Study of Hot Cells and Jets: Should We Add Hotcells Back into Events?”, DØ Note 2525.
- [60] A. L. Lyon, “A Search for Squarks and Gluinos Using the Jets and Missing Energy Signature at DØ”, Ph.D. Dissertation, University of Maryland (1997).

- [61] P. Grannis, “Specifications for the DØ Detector”, DØ Note 560.
- [62] I. A. Bertram *et al.*, “Single Jet Resolutions at DØ for Run 1”, DØ note 3414.
- [63] M. Paterno, private communication.
- [64] V. D. Elvira, “Jet η Bias and Resolution”, DØ Note 2173.
- [65] B. Abbott, “Effects of η and ϕ Definitions on Reconstructing Jets”, DØ Note 2769.
- [66] G. G. Di Loreto, “The Triple Differential Di-Jet Cross Section at $\sqrt{s} = 1.8$ TeV”, Ph.D. Dissertation, Michigan State University (1998).
- [67] L. Babukhadia,
[http : //www - d0.fnal.gov/ blevan/d0_private/incl/etabias/index.html](http://www-d0.fnal.gov/blevan/d0_private/incl/etabias/index.html).
- [68] L. Babukhadia, “Studies of Event/Jet Selection Criteria and their Efficiencies with DØ Run 1B Data”, DØ Note 3373 (talk presented at DØ QCD meeting 12 December 1997).
- [69] L. Babukhadia *et al.*, “Standard Jet Cuts and their Efficiencies for Run 1B DØ Collider Data”, DØ Note 3407.
- [70] M. G. Kendall and A. Stuart, “The Advanced Theory of Statistics”, Volume I, page 243, Charles Griffin and Co. Ltd., London (1969).
- [71] V. D. Elvira *et al.*, “A Study of Standard Jet Cuts and their Efficiencies Using DØ Collider Data”, DØ Note 1763.
- [72] M. Bhattacharjee *et al.*, “Efficiencies of the Standard Jet Cuts for Cone Sizes: 0.3, 0.5, 0.7”, DØ Note 2197.

- [73] A. Goussiou, “Jet Sample Selection at $\sqrt{s} = 630$ GeV”, DØ Note 3364.
- [74] B. Abbott *et al.*, The DØ Collaboration, “Determination of the Absolute Jet Energy Scale in the DØ Calorimeters”, Nucl. Instr. and Methods **A424**, 352 (1999).
- [75] L. Babukhadia *et al.*, “Method to Test the Jet Energy Scale Using Transverse Momentum Balance”, DØ Note 3554.
- [76] J. Kotcher, “Design, Performance, and Upgrade of the DØ Calorimeter”, FERMILAB-CONF-95-007-E, 15 (1995). Published in the proceedings of 1994 Beijing Calorimetry Symposium, Beijing, ed. P. R. Chian, 25 (1994).

U. Heintz, “A Measurement of the Calorimeter Response Using π^0 Decays”, DØ Note 2268.

M. Demarteau *et al.*, “Measurement of the W Mass”, DØ Note 2929.
- [77] A. Goussiou, “New Showering Correction for the Jet Energy Scale at DØ”, DØ Note 3606.
- [78] R. Brun and F. Carminati, “GEANT Detector Description and Simulation Tool”, CERN Program Library Long Writeup W5013 (1993)
- [79] B. Klima and C. Stewart, “PJET-Parton Jets in the Monte Carlo”, DØ Note 905.
- [80] M. Bhattacharjee *et al.*, “Jet Energy Resolutions”, DØ Note 2887.
- [81] L. Babukhadia *et al.*, “Studies of the Luminosity Dependence of the Run 1B Inclusive Jet Cross Sections at DØ”, DØ Note 3527.

- [82] I. Bertram, private communication.
- [83] J. Bantly *et al.*, “DØ Luminosity Monitor Constant for the 1994–1996 Tevatron Run”, DØ Note 3199.
- [84] J. Krane, private communication.
- [85] H. Schellman, “The Relation Between E_T Asymmetry, Jet Resolutions and Vertex Resolution”, DØ Note 3454.
- [86] F. James, “MINUIT Function Minimization and Error Analysis”, CERN Program Library Long Writeup D506, Version 94.1 (1994).
- [87] J. Krane, “The Ratio of Inclusive Jet Cross Sections at $\sqrt{s} = 630$ GeV and $\sqrt{s} = 1800$ GeV”, Ph.D. Dissertation, University of Nebraska (1998).
- [88] S. D. Ellis, Z. Kunszt, D. Soper, “One-Jet Inclusive Cross Section at Order α_s^3 . Quarks and Gluons.”, Phys. Rev. **D64**, 2121 (1990).
- [89] W. Giele, E. W. N. Glover, and D. A. Kosower, “The Two-Jet Differential Cross Section at $O(\alpha_s^3)$ in Hadron Collisions”, FERMILAB-PUB-94/070-T (1994). We use their program JETRAD.
- [90] B. Abbott *et al.*, “Fixed Cone Jet Definitions in DØ and R_{sep} ”, Fermilab-PUB-97/242-E (1997).
- [91] G. D’Agostini, “Probability and Measurement Uncertainty in Physics – a Bayesian Primer”, hep-ph/9512295 v3, 88 (1995).
- [92] I. A. Bertram, “A Study of the χ^2 Comparisons Used in the Inclusive Jet Analyses”, DØ Note 3644.